CENTRAL RESEARCH LIBRARY
DOCUMENT COLLECTION

133

MARTIN MARIETTA ENERGY SYSTEMS LIBRARIES
3 4456 0351161 6

ORNL-2802
Controlled Thermonuclear Processes
TID-4500 (15th ed.)

THERMONUCLEAR PROJECT SEMIANNUAL REPORT

FOR PERIOD ENDING JULY 31, 1959

CENTRAL RESEARCH LIBRARY
DOCUMENT COLLECTION
LIBRARY LOAN COPY
DO NOT TRANSFER TO ANOTHER PERSON
If you wish someone else to see this document, send in name with document and the library will arrange a loan.

OAK RIDGE NATIONAL LABORATORY
operated by
UNION CARBIDE CORPORATION
for the
U.S. ATOMIC ENERGY COMMISSION

Printed in USA. Price $2.75. Available from the

Office of Technical Services
Department of Commerce
Washington 25, D.C.

LEGAL NOTICE

This report was prepared as an account of Government sponsored work. Neither the United States, nor the Commission, nor any person acting on behalf of the Commission:

A. Makes any warranty or representation, expressed or implied, with respect to the accuracy, completeness, or usefulness of the information contained in this report, or that the use of any information, apparatus, method, or process disclosed in this report may not infringe privately owned rights; or

B. Assumes any liabilities with respect to the use of, or for damages resulting from the use of any information, apparatus, method, or process disclosed in this report.

As used in the above, "person acting on behalf of the Commission" includes any employee or contractor of the Commission, or employee of such contractor, to the extent that such employee or contractor of the Commission, or employee of such contractor prepares, disseminates, or provides access to, any information pursuant to his employment or contract with the Commission, or his employment with such contractor.

ORNL-2802
Controlled Thermonuclear Processes
TID-4500 (15th ed.)

Contract No. W-7405-eng-26

THERMONUCLEAR PROJECT SEMIANNUAL REPORT

For Period Ending July 31, 1959

DATE ISSUED

DEC 22 1959

OAK RIDGE NATIONAL LABORATORY
Oak Ridge, Tennessee
operated by
UNION CARBIDE CORPORATION
for the
U. S. ATOMIC ENERGY COMMISSION

MARTIN MARIETTA ENERGY SYSTEMS LIBRARIES

3 4456 0351161 6

CONTENTS

1. INTRODUCTION 1

2. SUMMARY 1

3. DCX OPERATION AND PERFORMANCE 3
   - 3.1 Modifications in Ion Source and Accelerator Tube 3
   - 3.2 Modifications in Arc and Vacuum Conditions 3
     - 3.2.1 Pumping System 3
     - 3.2.2 Electrodes and Baffles 3
     - 3.2.3 Dissociation Efficiency 3
   - 3.3 Observation of the Trapped Plasma 4
     - 3.3.1 Particle Detectors in DCX 4
     - 3.3.2 Spreading of the Trapped Plasma 4
     - 3.3.3 Mean Residence Times; Arc Loss 8
     - 3.3.4 Particle Accountability 9

4. VACUUM ARC RESEARCH 11
   - 4.1 D_2^+ and D_3^+ Dissociation Studies in the Carbon Arc 11
     - 4.1.1 Effect of Radial Distance of Arc from Beam 11
     - 4.1.2 Effect of Longitudinal Distance of Arc from Beam 12
     - 4.1.3 Effect of Ultraviolet and Radio Frequency Radiation on Beam Dissociation 13
     - 4.1.4 Simultaneous Measurement of Dissociation of D_2^+ and D_3^+ 14
   - 4.2 Trapping of High-Energy Ions Within an Arc Wall 15
     - 4.2.1 Arc Wall Experiments 15
     - 4.2.2 Multistage Grid Ion Source 25
   - 4.3 Long "PIG" Arc Discharges 25
   - 4.4 Falling Particle and Probe Studies 26
     - 4.4.1 Falling Particle Studies 26
     - 4.4.2 Probe Studies 29
     - 4.4.3 Ion Beam Modulation from Grid Source 29
   - 4.5 A Mass Spectrometric Analysis of the Carbon Arc 31
     - 4.5.1 Mass Spectrometer in the Long Solenoid Machine 32
     - 4.5.2 Mass Spectrometer in the Arc Research Facility 32
   - 4.6 Arc Transparency Measurement 37
   - 4.7 Total Radiation from a Short Arc as a Function of Magnetic Field Strength 38
   - 4.8 Radiation from a Long Arc as a Function of Magnetic Field Strength 38
   - 4.9 Effect of Local Variation of Magnetic Field Strength on Radiation from a Vacuum Carbon Arc 40
   - 4.10 Anode Withdrawal Experiments 41
   - 4.11 Radiation as a Function of Axial Position Along Arc in the LSF 43
   - 4.12 Voltage vs Current Relation for Vacuum Carbon Arc in LSF 44
   - 4.13 Microwave Diagnostics of a Carbon Arc and Hydrogen Plasma 46
     - 4.13.1 Carbon Arc Measurements 46
     - 4.13.2 DCX Plasma Measurements 47

4.14 Vacuum Properties of the Carbon Arc 48
4.14.1 Measurements of Arc and System Parameters 50
4.15 A Type of Hollow-Cathode Discharge 54
4.15.1 Apparatus 54
4.15.2 Experiments 56
4.16 Analysis of a Cavity Cathode Discharge in Carbon 59
4.17 Hydrogen Arc Development 65

5. ION SOURCE AND ACCELERATOR DEVELOPMENT 67
5.1 High-Current Von Ardenne Duo-Plasmatron Ion Source Development 67
5.1.1 Design Parameters 67
5.1.2 Anode-Plate Cooling 67
5.1.3 Operating Characteristics 68
5.2 High-Current Accelerator Tube Development 71

6. INSTRUMENTATION 75
6.1 High-Frequency Filter for the DCX 600-kv Power Supply 75
6.1.1 Theory of Operation 75
6.1.2 Circuit Design 77
6.2 Variable-Q, Variable-Frequency Filter Amplifier 79
6.2.1 Theory of Operation 79
6.2.2 Circuit Design 81
6.3 Oxide Sandwich Detector 82
6.3.1 Rejection of Semiconductors 82
6.3.2 Choice of Dielectric, Shield, and Base Materials 82
6.4 Microwave Diagnostics Utilizing the Faraday Effect 84
6.4.1 Equipment 85
6.4.2 Theory 85

7. THEORY 87
7.1 Absolute Containment of Ions in DCX 87
7.2 DCX Orbit Studies 88
7.3 Orbit Precession in DCX 92
7.4 Particle Orbits in a Nonazimuthally Symmetric Mirror Field 93
7.5 Deuteron and Electron Energy Distributions in DCX 93
7.6 Cross Section Calculation for Dissociation of D_2^+ by Carbon Arc 94
7.7 Diffusion of Plasma Particles Across a Magnetic Field 95
7.8 Coherent Radiation from a Plasma 95
7.9 Critical Current for Burnout in an OGRA-Type Device 96
7.10 Motion of a Neutralized Beam of Charged Particles Across a Magnetic Induction 99
7.10.1 The Equations of Motion 100
7.10.2 Drift Velocity and Density 102
7.10.3 Drift Velocity of a Weak Beam 102
7.10.4 Speculations Regarding the Motion of a Beam Across a Magnetic Induction 103

8. ENGINEERING SCIENCES GROUP 105
8.1 Computation of Magnetic Fields and Ion-Beam Trajectories 105
8.2 Graphical Methods for Designing Magnetic Fields and Ion-Beam Trajectories 107
8.2.1 Booster Coils for the Long Solenoid Facility and for DCX-1 107
8.2.2 Ion Trajectories and Graphical Determination of Ion Source Location 107
8.3 Design of Long Solenoids for Arc Studies 111
8.3.1 Copper Weight Diagram 111
8.3.2 Variation of Magnetic Field Strength in the Solenoid 112
8.3.3 Cooling Problems 112

9. CROSS SECTION EXPERIMENTS 114
9.1 High-Energy Cross Section Experiments (100–600-kev Ion Beam) 114
9.2 Crossed-Beam Cross Section Experiments (5–50-kev Ion Beam) 115

10. DIFFUSION OF DEUTERIUM IN COPPER 117
10.1 Experimental Procedure and Results 117

11. SPUTTERING AND SURFACE PHYSICS 120
11.1 New Equipment 120
11.1.1 Double Acceleration Ion Source 120
11.1.2 Single Acceleration Ion Source 120
11.1.3 Vacuum Analyzer 120
11.2 Sputtering Data 121
11.2.1 Helium on Aluminum Oxide 121
11.2.2 Helium on Copper 121
11.2.3 Argon on Copper 121
11.2.4 Miscellaneous Sputtering Data 122

12. METALLURGY 123
12.1 Outgassing of Graphite 123
12.2 Getter Testing 124
12.3 Valve and Flange Development 124

13. VACUUM TESTS 128
13.1 Diffusion Pump Performance 128
13.2 Tests of Vac-Ion Pump 129
13.3 Purging and Fractionation in a Diffusion Pump 130

14. DCX-2 131
14.1 DCX-2 Coil Design Exercise 131
14.2 Magnetic Coil Design for DCX-2 133
14.2.1 Short Review of Known Methods of Magnetic Field Synthesis 133
14.2.2 Use of Zonal Harmonics in the Design of Magnetic Mirror Fields 134
14.2.3 Influence of Nonuniform Current Density Distribution on the Machine Data 135

15. DESIGN AND CONSTRUCTION GROUP 136

THERMONUCLEAR PROJECT SEMIANNUAL REPORT

1. INTRODUCTION

A. H. Snell

During the past six months there has been substantial accomplishment both in the growth of our understanding of the processes that take place within DCX and in sundry ancillary matters pertaining to vacuum arcs, technique, the engineering of magnetic fields, instrumentation, orbit computation, Sherwood theory, and "down-to-earth" engineering.

---

2. SUMMARY

In respect to DCX, perhaps the greatest single advance has been an appreciation of the importance of the vacuum carbon arc as a loss mechanism (by charge exchange) for the trapped H^+ plasma. Loss in the arc and dissociation efficiency are both sensitive to electrode configuration; with the anode and its baffle assembly at the center of the anode-end mirror coil, the arc provides by far the most important loss mechanism. With the anode and its baffle retracted about 10 in. so that they are at the outer face of the anode-end mirror coil, conditions are much better: the mean residence time of the trapped ions is lengthened by a factor of 5, and the arc loss is then approximately equal to the loss by charge exchange in the residual gas at a pressure of 10^{-6} mm Hg. Under the condition of greater loss, the arc is presumably dense and is probably populated largely with C^+ and C^{++} ions; the molecular dissociation efficiency is about 30% for a single pass of the 600-kev H_2^+ beam. When loss is reduced by retraction of the anode and its baffle, the arc is probably less dense and may be populated mostly by C^{+++} and C^{4+} ions, but the dissociation efficiency is reduced to 8%. It should perhaps be remarked that the arc loss being observed is not in conflict with the limit set two years or more ago, namely, that fewer than 1 in 10^5 of the 300-kev H^+ ions that pass through the arc suffer a charge exchange therein; the loss now seen is just about at that limit.

Clearly, the arc loss must be removed from DCX; there is little to be gained by striving for better vacuums while it is present. Progress might be gained by moving the electrodes farther in the direction that has already been found to be favorable; this would require a lengthwise extension of the magnetic field of DCX. A more promising approach appears to be the introduction of orbital precession such that the trapped H^+ ions pass through the arc only in every tenth to twentieth orbital circuit. Not only would this reduce charge-exchange loss in the arc, but it would also reduce scattering and energy loss. This will be one of the first modifications to be tried (since it involves a simpler physical change), even though it promises a more modest gain than does moving the electrodes. A third possibility is to go to the hydrogen or deuterium arc, where the charge exchange should be zero; the technical problems appear, however, to be severe, and experience with deuterium arcs will first be accumulated in the PPF and DCX-EPA apparatus.

In auxiliary experimentation, a noteworthy advance has been made in knowledge of the secondary plasma that surrounds the column of a vacuum carbon arc. Experiments by molecular ion dissociation, microwave absorption, and ion extraction agree in giving information about the radial decrease in density. The rather substantial fringing ion population may be simply the result of ambipolar diffusion outward from the column; a comparison with theory is not yet complete.

The sideways momentum imparted to metallic granules when they are dropped into a vacuum

carbon arc has been measured and found to be roughly compatible with carbon ion densities and velocities that have been inferred from other work, that is, a peripheral rotational velocity of 3×10^5 cm/sec and a density of 10^{14} cm^{-3}.

A vacuum carbon arc has been run, albeit for a few minutes only, at a record low for the ambient pressure, namely, 5×10^{-8} mm Hg. Previously, the lowest ambient pressures had been 2×10^{-7} mm Hg. Development of the large, hollow cylindrical arcs has continued; D_2^+ ions at 30 kev have been injected into them, and a wrap-up of dissociated D^+ ions has been visually observed in the interior; again, in these first attempts, the wrap-up was produced only for a brief interval, but the accomplishment has been established nevertheless. The duoplasmatron ion source has been developed to the point of yielding 100 ma of ions at 70 kev. An algebraic theory of burnout in an OGRA-like machine has been developed which gives numerical results for OGRA itself that agree with those of the Russians, but the functional dependence of relevant quantities is found to be different. The research engineering in the Project has been particularly active, in the design of magnetic fields in apparatus to be built, in the calculation of orbit trajectories therein, and also in the testing of vacuum components. A substantial effort in mechanical and construction engineering has been required for the impending move of the Project to new quarters. The design of a new DCX apparatus (DCX-2) remains conceptual, but a magnetic field configuration has been developed that promises a large volume of uniform field in a flexible arrangement permitting injection and accumulation experiments that are impossible in DCX-1.

3. DCX OPERATION AND PERFORMANCE[1]

C. F. Barnett
J. L. Dunlap
R. S. Edwards
J. A. Ray
R. G. Reinhardt
E. R. Wells

3.1 MODIFICATIONS IN ION SOURCE AND ACCELERATOR TUBE

In the past six months, various changes have been made in the accelerator system that is used to inject the 600-kev H_2^+ ions into DCX. Reliability and performance of the ion source have been improved by modifying the associated power supplies. Modulation in amplitude had been present in the ion beam, and it had led to some uncertainty as to the meaning of the initial readings given by the detectors that were used to observe the decay of the trapped beam following cutoff of the input. Most of the modulation had been traced to the low-frequency ripple in the various ion-source power supplies. The ripple in the ion beams has now been reduced to less than 2%, and the initial amplitude readings of the detectors accordingly have greater reproducibility and significance. The accelerating tube has likewise been improved toward more stable performance. Higher breakdown voltages have been realized by replacing the aluminum electrodes with Inconel electrodes. The length and overlap of the electrodes have been increased so that the beam is now completely shielded from insulating surfaces. These changes have resulted in very stable electrical operation, and total beam currents of 18 ma have been measured at the base of the accelerator.

3.2 MODIFICATIONS IN ARC AND VACUUM CONDITIONS

3.2.1 PUMPING SYSTEM

The pumping system of the vacuum tank of DCX has been improved by the addition of two 14-in. Leybold diffusion pumps. These act upon the outer vacuum volume, giving an increase of net pumping speed from 600 liters/sec to 3000 liters/sec. In recent months, the liner region has been devoid of pumps except for the arc. Measurements of the arc pumping speed by the introduction of a known leak rate of air indicated that it acts with a speed of about 3000 liters/sec. The pressure differential between the inner and outer vacuum regions is approximately a factor of 60 at high pressures (i.e., 10^{-5} mm Hg), and it is a factor of 10 at lower pressures (i.e., 5×10^{-7} mm Hg). This difference suggests that the minimum pressure in the liner is determined by the rate of outgassing. With arc-pumping on the liner, use has been made of its radiant energy for outgassing. The arc is operated without water in the cooling tubes of the liner until the liner wall temperature reaches 400–500°C, at which time the arc is turned off and the liner is allowed slowly to cool. After two cycles of this procedure the liner surfaces seem to be adequately clean.

3.2.2 ELECTRODES AND BAFFLES

The carbon electrodes and baffles used in the past were "pre-purified" by treatment under an atmosphere of Cl_2 and CO_2 at a temperature of 1400°C. Carbons treated by this method have been replaced by carbons treated by National Carbon Company at 2500°C under a Cl_2 atmosphere. The initial rate of pressure decrease after striking the carbon arc is much greater with carbons from National Carbon Company, but there has been no noticeable change in the ultimate minimum pressure.

3.2.3 DISSOCIATION EFFICIENCY

Measurements made during the past six months indicated that the method which had been used in determining dissociation efficiency could lead to

[1]Report written in part by A. H. Snell.

large errors. The method had been to measure the exit H_2^+ beam current with arc on and off. The difference in these two quantities divided by the H_2^+ current with the arc off had been accepted as the dissociation efficiency, although it might vary between limits as wide as 5 and 40% for apparently identical arc conditions. A permanent, movable Faraday cup has now been installed so that the H^+ beam can be measured directly. Break-up efficiencies (now defined as the ratio of H^+ current to the sum of H^+ and exit arc-on H_2^+ current) now seldom exceed 8% under arc conditions similar to those previously used.

3.3 OBSERVATION OF THE TRAPPED PLASMA

3.3.1 PARTICLE DETECTORS IN DCX

Most of the observations of the trapped, circulating H^+ beam in DCX are made with detectors that are located at a radius of 11 in., so that they are well outside of the orbital region of the beam. Each detector consists of a thin foil backed by a collecting electrode. Most of the particles, whether charged or neutral, of sufficient energy to penetrate the foil emerge charged, so that a current is carried from foil to collector. This is the detector signal that is used. The incoming particles are presumed to be mostly H neutrals that are produced by charge exchange and fly tangentially from the circulating proton beam. When desired, the input H_2^+ beam to DCX can be cut off within a few microseconds, and the decay time of the trapped plasma can be observed by means of oscillographic recording.

Some readings have been obtained with foils 25 μin. thick (nickel), but in this report we will discuss measurements taken with foils 10 μin. thick (0.23 mg/cm^2, again nickel), and we take into consideration the transmission factor introduced by the supporting grid. In such a foil very nearly all incident H particles (neutrals or ions) that have energies exceeding 150 kev emerge as ions, but below 150 kev the fraction emerging as ions becomes progressively smaller.[2]

The location of the foils has been determined largely by the availability of ports in the DCX vacuum tank. Figures 3.3.1 and 3.3.2 show the locations, with detectors 1, 2, and 3 at the top, and Nos. 4 and 5 offset in azimuth from the vertical. Below, there is an "arc detector" situated azimuthally so as to register particles that have been neutralized in the arc, but axially in such a position as to avoid neutrals formed by dissociation of the injected beam. All of the foregoing detectors are $\frac{3}{4}$ in. wide. A "narrow detector," $\frac{1}{8}$ in. wide, is situated approximately 10° below horizontal on an arm that can be positioned at will in a direction parallel with the magnetic axis.

In obtaining the readings to be discussed, no detectors had entrance collimators. The angle of acceptance was wide both in the axial direction and in the circumferential direction, the limitation being set primarily by the effect of the oblique thickness of the foils.

3.3.2 SPREADING OF THE TRAPPED PLASMA

At the time of our last report we had observed that although the trapped H^+ ions remain in a tight torus (major radius 5.3 in.; minor radius about $\frac{3}{4}$ in. by visual estimation) so long as the pressure in the DCX vacuum tank is in the neighborhood of 10^{-5} mm Hg, nevertheless, as the pressure is reduced to 10^{-6} mm Hg or below, the volume occupied expands both axially and radially. Clearly, at 10^{-5} mm Hg, the protons suffer charge-exchange collisions and are lost before they have a chance to spread. In the presence of spread, the removal of peripheral obstacles, strangely enough, did not appreciably increase the mean residence time of the trapped protons.

The spreading has now been studied in a variety of ways, and at the time of writing, the observations still have some internal inconsistencies. The best that can be done seems to be to describe

[2] R. J. Kerr, R. A. Dandl, and C. F. Barnett, *Thermonuclear Project Semiann. Rep. Jan. 31, 1959*, ORNL-2693, p 4, Fig. 1.1.2.

UNCLASSIFIED
ORNL-LR-DWG 36526A

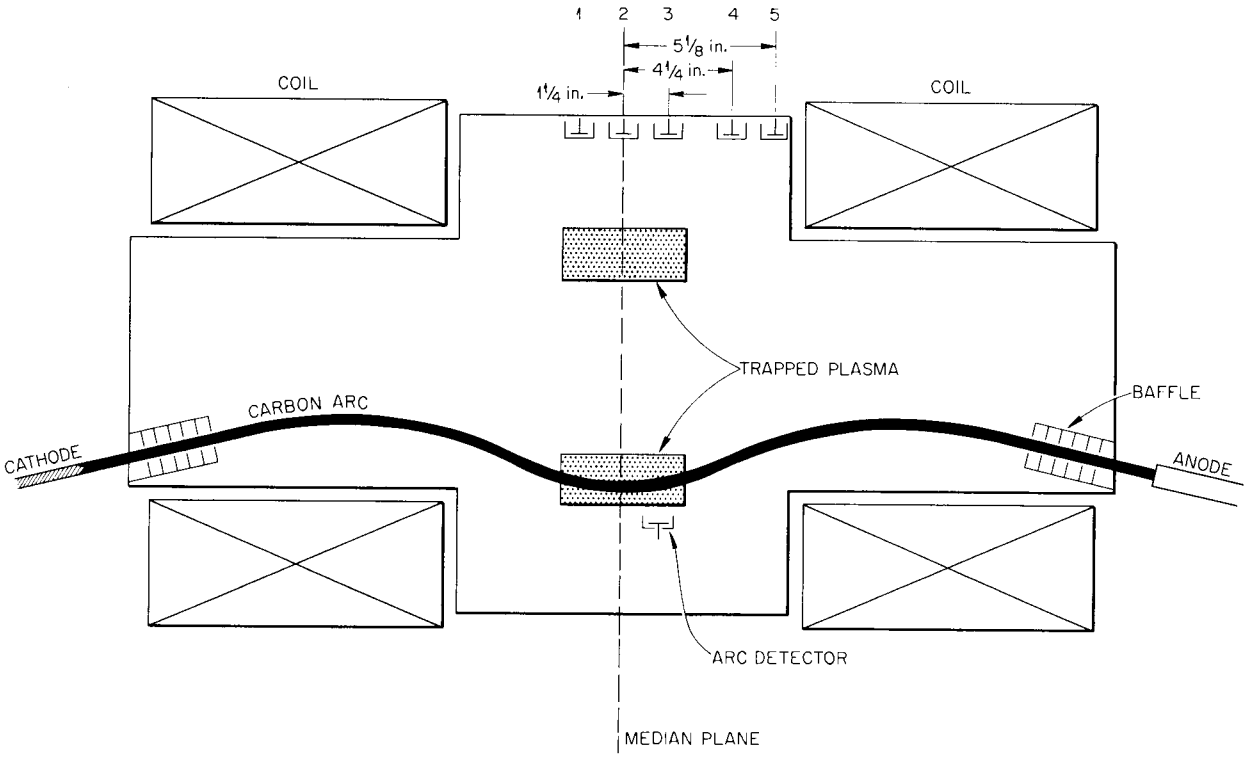

Fig. 3.3.1. Schematic Diagram of Neutral Particle Detectors.

UNCLASSIFIED
ORNL-LR-DWG 40092R

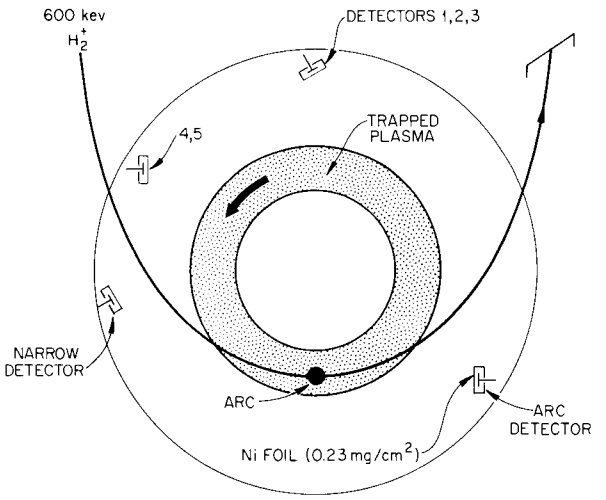

Fig. 3.3.2. Section in Median Plane of DCX, Showing Location of Detectors.

what is seen, in the spirit of a progress report, even though the explanation may be incomplete. Evidence concerning the spreading is both visual and instrumental.[3] Curve *A* of Fig. 3.3.3 shows the response of detectors 1, 2, 3, 4, and 5 at 1×10^{-6} mm Hg. The points represent the amplitude of the exponentially decaying current in each detector at the time of beam cutoff. A very short time component is found on the No. 2 detector, and inasmuch as it is probably associated with the input beam, this component is neglected in determining these curves. The distribution of detector responses suggests a rather wide distribution – although the curve should be interpreted with caution as a representation of either the spatial spread or the density distribution, because of the possibility of axial components of motion.

[3] *Ibid.*, Fig. 1.1.5.

The decrease in the H^+ population near the midplane is shown rather dramatically in Fig. 3.3.4, which was obtained with the narrow detector. The direct current readings are used for these curves. The maximum reading decreases from 320 mv at 5×10^{-5} mm Hg to 29 mv at 1×10^{-6} mm Hg for the same input current. Evidently the particle population moves largely to different locations at the lower pressure. It is observed, however, that the half widths of the curves increase only slightly as the pressure is lowered.

The doubly peaked shape of the curve of Fig. 3.3.4 is associated with an off-median-plane injection of the H_2^+ beam. The direction of injection can in fact be varied slightly by means of electrostatic deflecting plates, and Fig. 3.3.5 shows the result of injection from a direction somewhat north of the geometrical midplane of DCX: the two peaks merge into one, which is

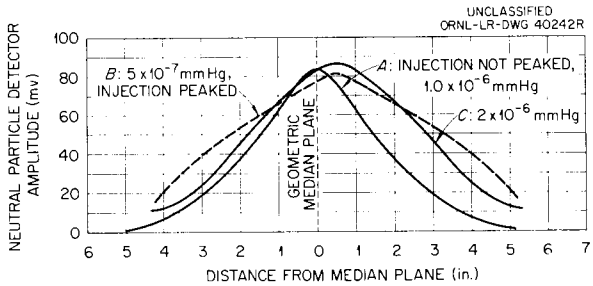

Fig. 3.3.3. Amplitude of Detector Signals as Function of Axial Position. Detectors $\frac{3}{4}$ in. wide; wide acceptance angle.

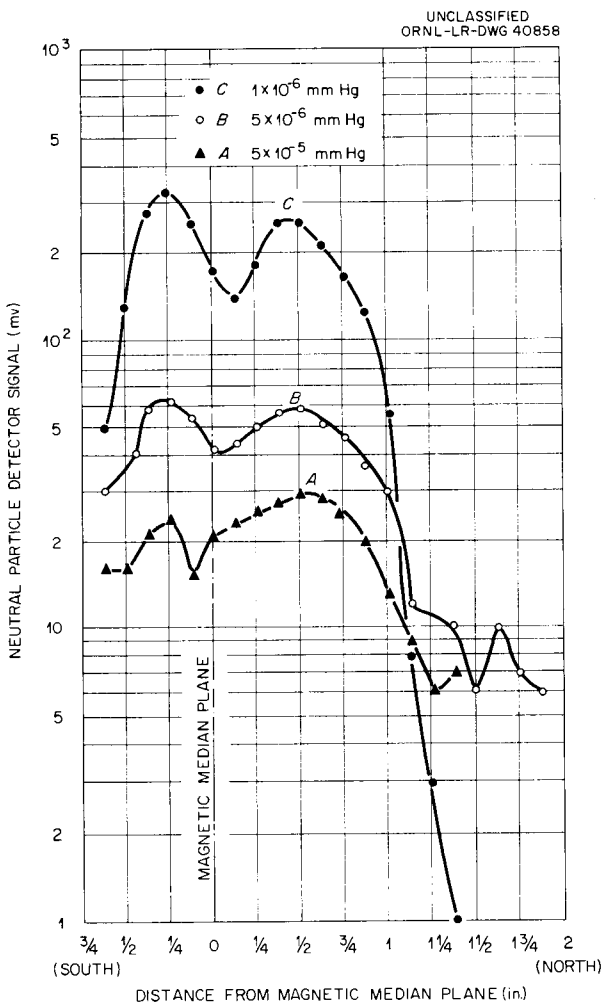

Fig. 3.3.4. Z Scan with $\frac{1}{8}$-in.-wide Neutral Particle Detector.

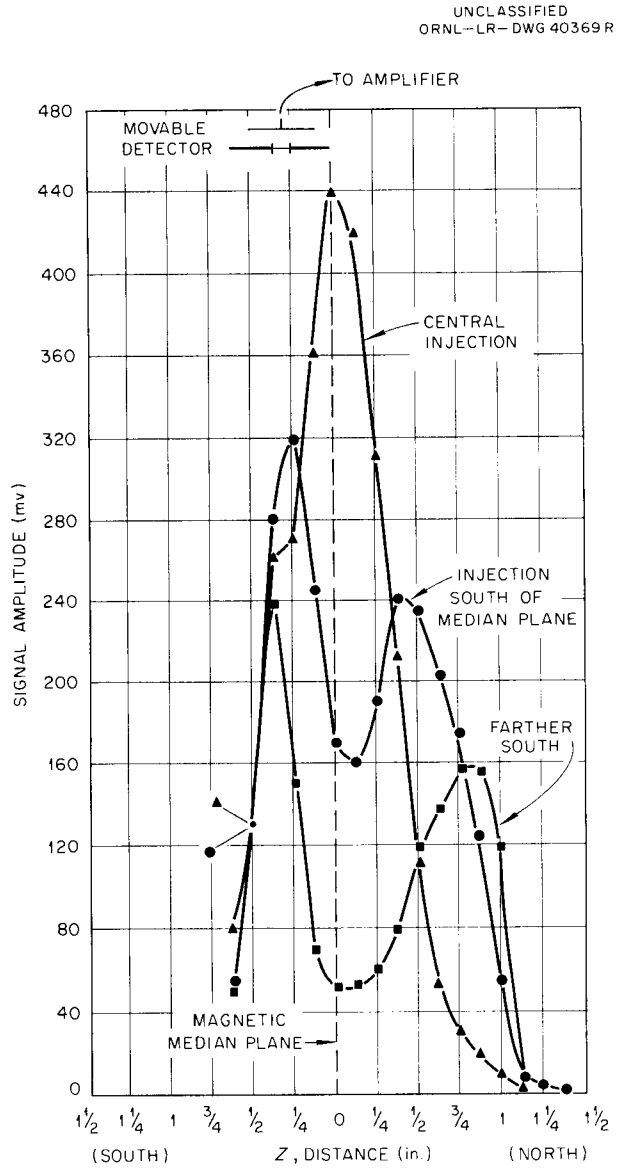

Fig. 3.3.5. Amplitude Response of Narrow Detector and Dependence upon Direction of Injected H_2^+ Beam.

narrower. This shows that the magnetic median plane does not coincide with the plane of injection. When injection takes place off the magnetic median plane the particles oscillate from side to side, and since they spend most of their time at the ends of this oscillatory motion they are most likely to suffer a charge exchange there.

If now one looks at the signal distribution of detectors 1, 2, 3, 4, and 5 under the injection condition of a single central peak, one obtains curves *B* and *C* of Fig. 3.3.3. These are again the amplitude of the slowly decaying signal after beam cutoff. Evidently the curves are asymmetric, suggesting a distribution of the trapped plasma that is symmetrical about the actual magnetic median plane. The observation is supported by results obtained when an obstruction or "paddle" is pushed into the plasma from the south end (Fig. 3.3.6). Observations have been made that indicate an interception of the plasma by the paddle at the south end when the edge of the latter is as much as $5\frac{1}{2}$ in. from the geometric median plane. Figure 3.3.7 summarizes the observations, indicating again the increase of spread with decreasing pressure. In this connection we run into one of the conflicts in the observations, because a set of data exists that gives the puzzling result that under the conditions prevailing in the experiment of Fig. 3.3.7,

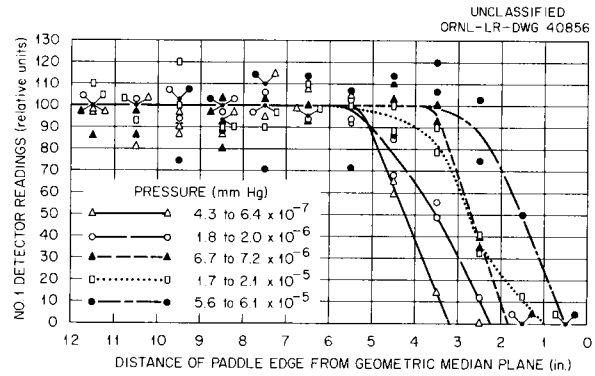

Fig. 3.3.7. Axial Spread of Trapped Plasma as a Function of Pressure.

the obstructing paddle produced practically no decrease in the mean residence time of the protons even when it was inserted sufficiently to cause a decrease in the amplitude of the detector signals by a factor of 2.

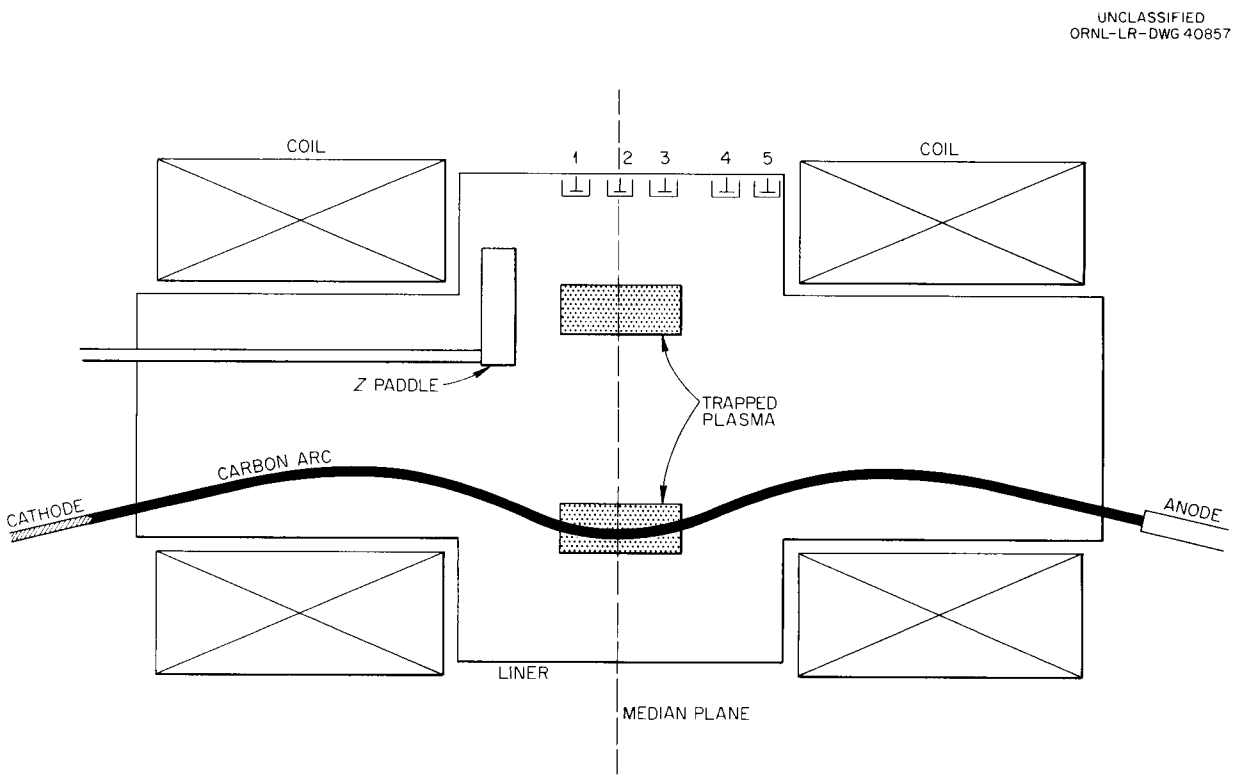

Fig. 3.3.6. Schematic Diagram of Position of Z Paddle.

Figure 3.3.8 shows the direct current data obtained from detector No. 1 (south $1\frac{1}{4}$ in.) as a function of paddle position for various input H_2^+ beam currents. The negligible variation of spreading leads to the important conclusion that the spreading of the plasma is not appreciably due to space charge. The cause of spreading must, therefore, be looked for in other directions.

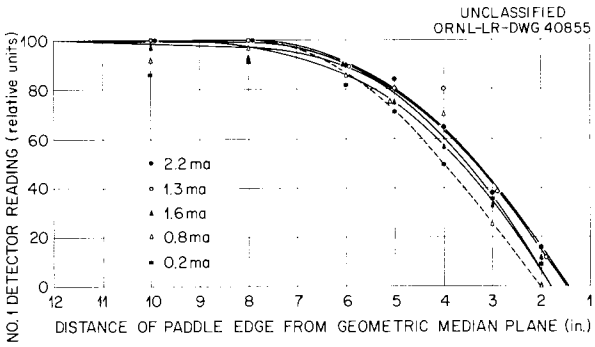

Fig. 3.3.8. Axial Spread of Plasma with Various Input Beam Currents.

3.3.3 MEAN RESIDENCE TIMES; ARC LOSS

An experiment was performed in which the decay time τ (time for $1/e$ decay of detector signal amplitude after injected beam cutoff) was investigated at pressures somewhat above 10^{-6} mm Hg in H_2 gas, with and without the carbon arc. The arc was operated in condition 3 (described below). This condition is the one giving minimum arc losses. The results are shown in Fig. 3.3.9. They suggest that at 10^{-6} mm Hg, the presence of the arc reduces the decay time from about 10 msec to about 5 msec. Evidently under some circumstances the arc can introduce a loss mechanism which adds to the loss by charge exchange in the residual gas.

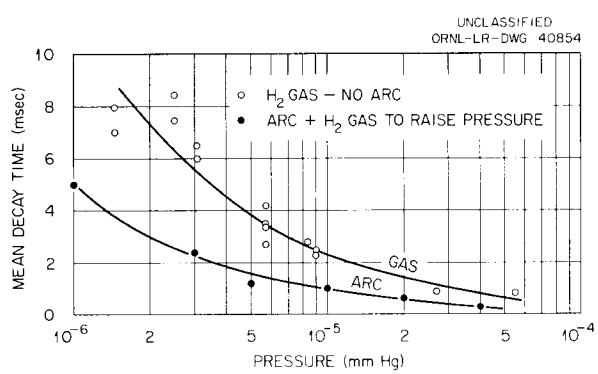

Fig. 3.3.9. Decay Time for Arc and Hydrogen Gas Dissociation (No. 2 Detector).

The gas breakup data of Fig. 3.3.9 could not be taken at lower pressures because the signal amplitude vanishes. It is significant to observe that spreading was essentially absent under the condition of gas breakup, despite the longer residence times.

Partly as a consequence of this observation, the arc detector indicated in Fig. 3.3.2 was installed. There followed a series of experiments in which this detector was used to assess the arc loss under various configurations of the arc electrodes and baffles. Changes in the positions of cathode and cathode baffle had little effect, but changes at the anode end had marked effects. In addition to changing the arc loss, the configuration at the anode end produced variations in the efficiency of dissociation of the primary H_2^+ ions, so the two effects had to be followed together. The main results of a considerable series of empirical investigations can be summarized as follows, the configuration of the cathode baffle being as in Fig. 3.3.1 throughout:

1. With a single anode baffle located at the center of the anode magnet mirror coil, and with the anode spaced about 1 in. from the baffle, H_2^+ dissociation efficiencies as high as 30–40% could be obtained, but the arc loss was severe and the mean containment times were low (1–2 msec). Figure 3.3.10 shows a

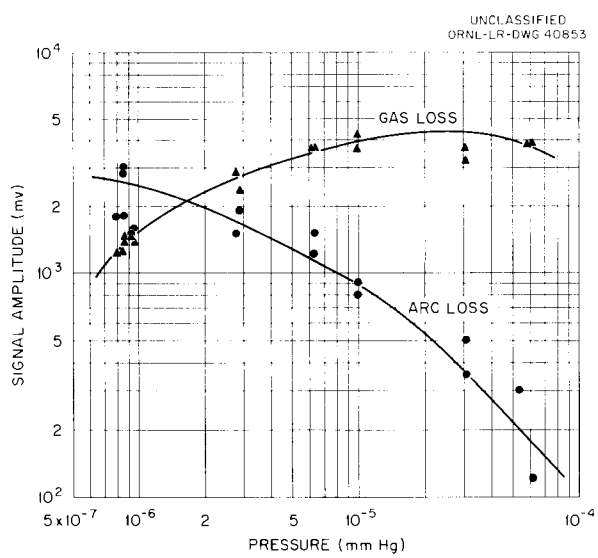

Fig. 3.3.10. Comparison of Arc Loss with Circumferential Gas Loss. Detector $1\frac{1}{4}$ in. from median plane; single anode baffle at center of coil.

comparison of the arc loss (lower curve) with the gas loss as integrated circumferentially at the location of detector 3. Evidently below 10^{-6} mm Hg, the arc loss exceeds the gas loss. Curve A of Fig. 3.3.11 shows the variation of $1/\tau$ as a function of pressure under this configuration. Evidently τ loses its sensitivity to pressure below about 5×10^{-6} mm Hg.

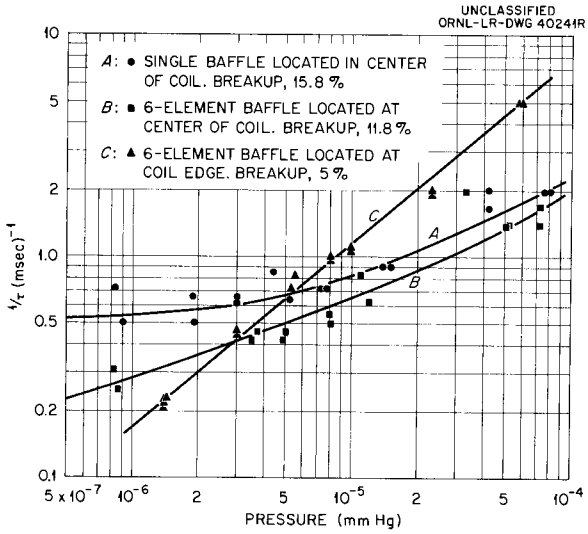

Fig. 3.3.11. $1/\tau$ as a Function of Pressure for Vorious Arc Configurations (No. 3 Detector).

2. With a six-element baffle located at the center of the anode-end magnet coil, the breakup falls to about 12% and the mean residence time increases 3–4 msec. Curve B of Fig. 3.3.11 shows, however, that there is a loss of sensitivity of $1/\tau$ to pressure that is more gradual than that of curve A.
3. When the six-element baffle and the anode were moved out to the coil edge (configuration shown in Fig. 3.3.1) the dissociation efficiency fell to about 8%, but the mean residence time increased to 5–6 msec. This configuration yielded curve C of Fig. 3.3.11. Evidently the $1/\tau$ curve can be expected to flatten out only at pressures considerably lower than 10^{-6} mm Hg. The circumferentially integrated gas loss is compared with the arc loss in Fig. 3.3.12. At 6×10^{-7} mm Hg, the gas loss still exceeds the arc loss.

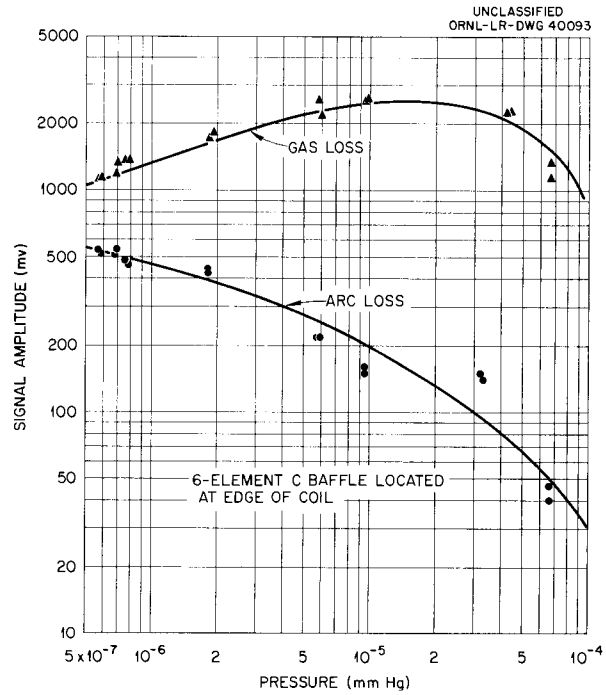

Fig. 3.3.12. Comparison of Arc Loss with Circumferentiol Gas Loss. Detector $1\frac{1}{4}$ in. from median plane; 6-element baffle at coil edge.

These observations are in general agreement with experience that has been gained with the carbon arcs in the long solenoid and in the DCX-EPA apparatus. At locations close to the anode, the arc density is presumably relatively high, and the ion population consists mainly of C^+ and C^{++}. Farther from the anode, the density may be reduced, and the population shifts largely to C^{+++} with an admixture of C^{4+}. Table 3.3.1 summarizes some spectroscopic observations that have been made by Werner and Skidmore on DCX for varying configurations of the anode and its baffle. In cases 1, 2, and 3 it appears that the dissociation efficiencies are approximately proportional to the total radiation of the C^+, C^{++}, and C^{+++} lines, suggesting that they depend upon ion density rather than upon the mean state of ionization.

3.3.4 PARTICLE ACCOUNTABILITY

The existence of data such as shown in Fig. 3.3.3, together with a knowledge of the arc loss, encourgages an assessment as to how well the detectors shown in Figs. 3.3.1 and 3.3.2 can

Table 3.3.1. Dissociation Efficiency and Carbon Ion Relative Abundance for Various Configurations of Anode and Baffle

Anode Configuration	Dissociation Efficiency (%)	Spectrometer Response (relative abundance)			Total Response to C^+, C^{++}, C^{+++} Lines (relative units)
		C^+	C^{++}	C^{+++}	
1. Single baffle at center of anode-end magnet coil. Anode 6 in. from baffle and stationary.	6.2	0.1	23.1	76.8	2,730
2. Single baffle ot center of anode-end coil. Anode 1 in. from baffle and rotating.	30	0.2	67.5	32.3	10,200
3. Single baffle at center of onode-end coil. Anode 1 in. from baffle and stationary.	15	0.3	46.1	53.6	6,210
4. Six-element baffle at edge of coil. Anode rotating.	4.8	0	6.5	93.5	
5. Six-element baffle at edge of coil. Anode stationary.	5.0	0	6.6	93.4	
6. Six-element boffle at edge of coil. Apertures in carbon baffles enlarged to $1\frac{1}{2}$-in. diameter. Anode rotating.	8.3	0	33.1	66.9	

account for the total input of H^+ ions into the plasma. An integration of the distributions of Fig. 3.3.3 has been carried out, and the arc losses have been added on the assumption that they are proportional to the ordinate of Fig. 3.3.3 along the entire axial extent of the plasma. In view of the incomplete coverage given by the detectors, and their insensitivity to particles that have suffered degradation in energy, it can hardly be expected that the particle accountability will be complete. The results of such a computation are shown in Fig. 3.3.13 for three anode configurations. Apparently, at 10^{-6} mm Hg the detectors can account for about half of the H^+ input rate, although the results can hardly be credited with much accuracy.

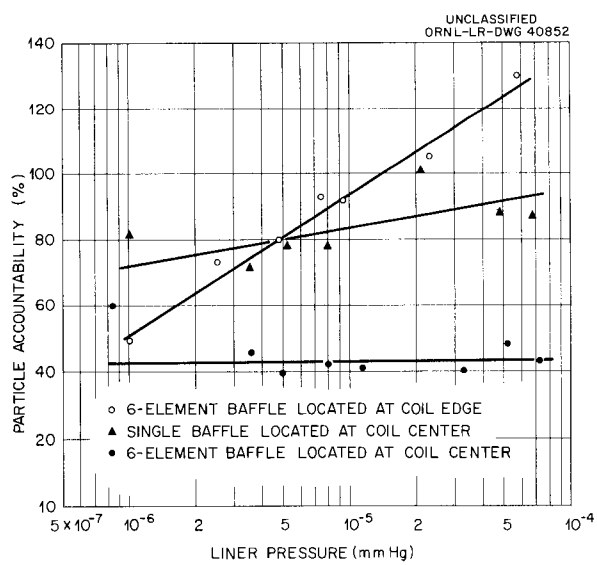

Fig. 3.3.13. Particle Accountability as a Function of Pressure.

4. VACUUM ARC RESEARCH

4.1 D_2^+ AND D_3^+ DISSOCIATION STUDIES IN THE CARBON ARC

J. S. Luce J. Meece O. Sharp

4.1.1 EFFECT OF RADIAL DISTANCE OF ARC FROM BEAM

For this work, a grid ion source used at Geneva was modified to provide a simple horizontal slit and good beam focus (0.060 × 3 in.) at 180° from the source slit. In some tests performed in a Beta tank, the beam was made to pass through a 0.010-in. slot at 180°, so that in the region where dissociation occurred, the beam was 0.030 in. thick. In the first test a 30-kev D_2^+ beam was passed 0.200 in. below the "edge" of the carbon arc; that is, below the boundary of the brightly luminous column defined by the size and shape of the cathode. Ten per cent dissociation was observed in the experiment. Several checks were made with movable probes to determine whether or not the beam was being deflected by magnetic or electrostatic forces as it passed the arc, and it was shown that the beam shape remained constant with the arc on and off. The rather surprising fact that breakup of a molecular ion beam could occur some distance from the core of the arc led to the construction of a movable assembly that would permit scanning by moving the arc through the beam as it remained in a fixed orbit. The arrangement is shown in Fig. 4.1.1. A machined carbon strip measuring 0.062 × 0.500 × 7 in. was mounted on the movable arc electrode assembly, in such a manner that the beam would strike on the narrow edge (see Fig. 4.1.2*a*). The strip was then used as a probe and moved through the beam, so that a profile of the beam could be obtained in terms of the coordinate of the moving electrode assembly. The strip was then cut to a shorter length, and the part that remained became the cathode of the arc (Fig. 4.1.2*b*). (In the uniform magnetic field of the Beta tank, the arc is straight and the coordinate of the cathode is the same as the coordinate of the arc.) Using this accurate fix for the relative positions of arc and beam, dissociation measurements were taken as a function of the intervening distance. Figures 4.1.3 and 4.1.4 give typical sets of the resulting data (the subtraction of dissociation due to residual gas in the vacuum tank is shown explicitly in Figs. 4.1.4*a* and *b*). Evidently dissociation of D_2^+ ions can take place in the fringes of the arc. The measurements also permit an evaluation of the relative probabilities of simple dissociation ($D_2^+ \rightarrow D^+ + D^0$) and dissociation with ionization

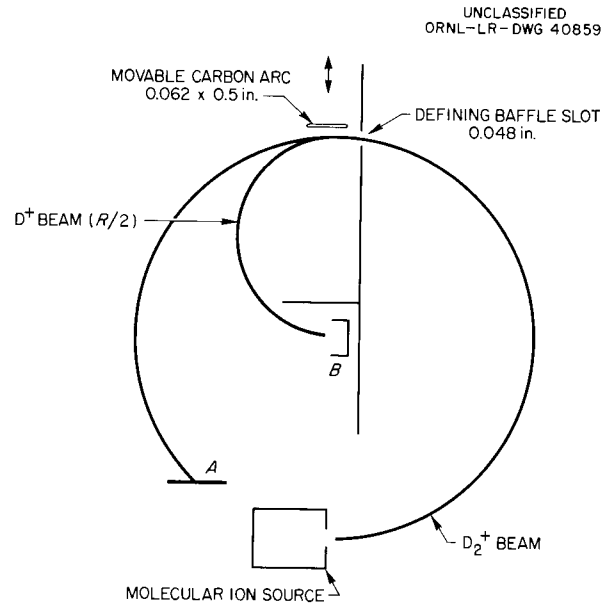

Fig. 4.1.1. Apparatus for Measuring Dissociation of D_2^+ as a Function of Arc Position.

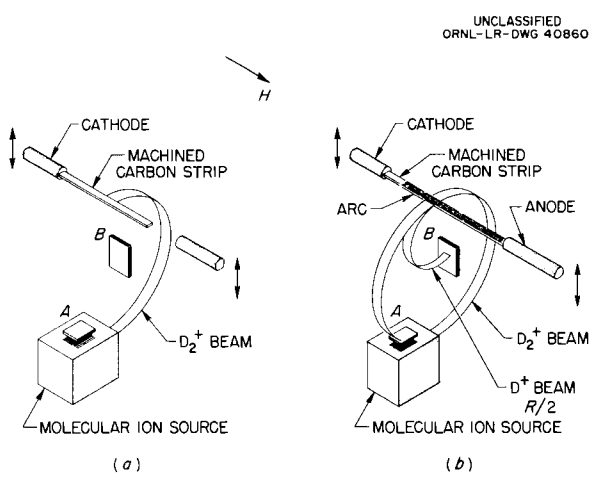

Fig. 4.1.2. Beam Scanning with Movable Cathode and Movable Arc.

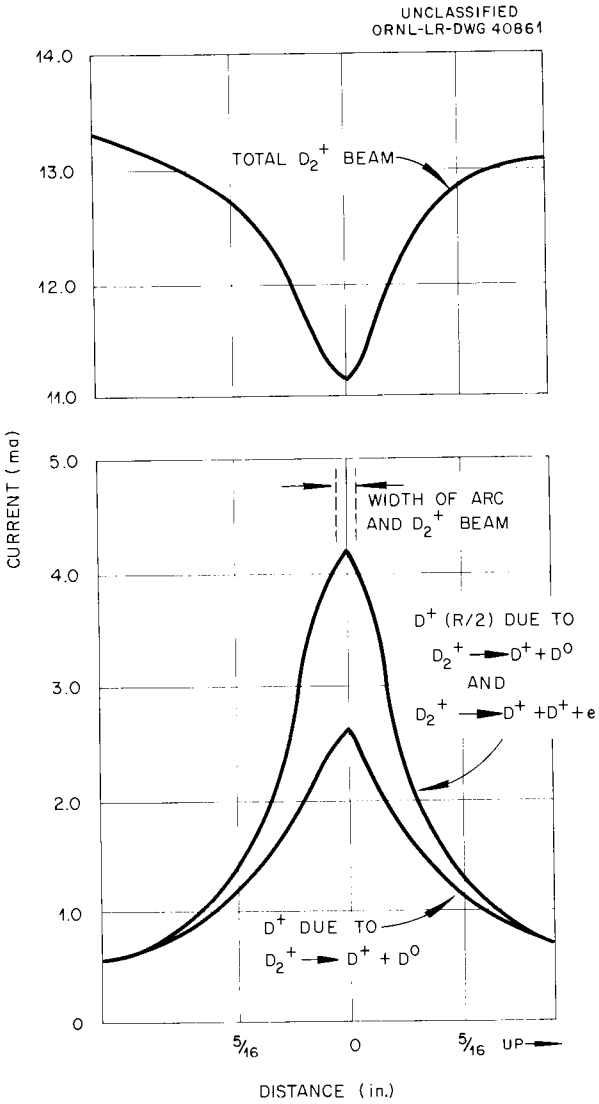

Fig. 4.1.3. Dissociation of D_2^+ as a Function of Arc Position.

($D_2^+ \rightarrow D^+ + D^+ + e$); an excess of summed collector current over input current (determined with the arc remotely positioned) is indicative of the latter process and can be evaluated from the data of Figs. 4.1.3 and 4.1.4*b*. Values for the ratio ($D_2^+ \rightarrow D^+ + D^0$)/($D_2^+ \rightarrow D^+ + D^+ + e$) were found to be about 1.5 when the beam was running through the center of the arc.

4.1.2 EFFECT OF LONGITUDINAL DISTANCE OF ARC FROM BEAM

The discovery that breakup also occurs outside the main arc boundary suggested several experiments. In one the D_2^+ beam was allowed to pass under the cathode, starting with a short arc displaced to one side (see top of Fig. 4.1.5). Dissociation was then measured as the cathode eroded past the beam. It was found that appreciable breakup occurred even though the arc was at some longitudinal distance from the beam. Breakup increased as the arc approached the location of the beam, and leveled off when the tip of the cathode had eroded 60% of the way through the width of the beam (bottom, Fig. 4.1.5). The tests were done with $\frac{3}{8}$-in. cylindrical cathodes and 0.062 × 0.500-in. flat cathodes. The shape of the curve remained constant, but with the cylindrical

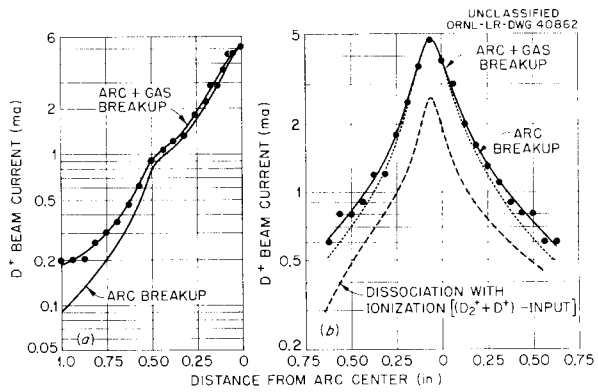

Fig. 4.1.4. (*a*, *b*) Dissociation of D_2^+ as a Function of Arc Position Showing Subtraction of Dissociation Due to Residual Gas.

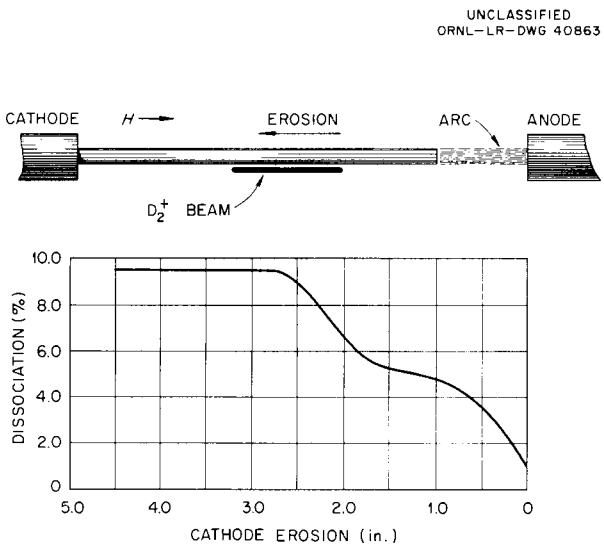

Fig. 4.1.5. Dissociation of D_2^+ Beam as a Function of Cathode Erosion.

cathode a maximum dissociation efficiency of 10% was recorded, while with the flat cathode the dissociation efficiency reached 30%.

The next series of tests employed flat carbon strips instead of an arc. These strips were heated to incandescence by passing 300 amp of d-c current at 20 v through them. No dissociation was observed under these conditions. It was found, however, that if the strips were operated until a crack appeared, 10% dissociation of the D_2^+ beam to D^+ was observed simultaneously with the formation of the crack (Fig. 4.1.6). At the same instant a large amount of hash appeared on an oscilloscope attached to the system. It was also

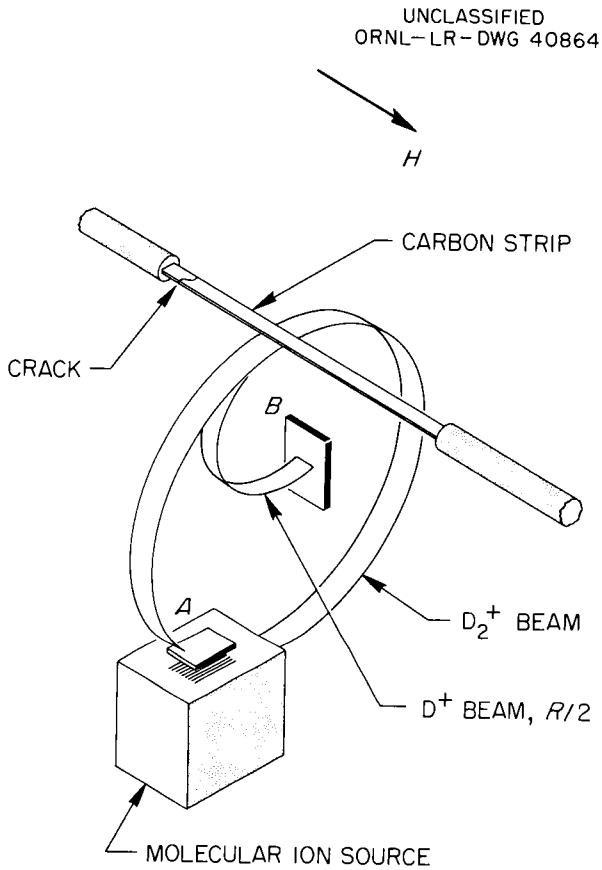

Fig. 4.1.6. Dissociation of D_2^+ Beam with Cracked Carbon Strip.

noticed that regardless of where the crack appeared, the results were the same. A device was then built that permitted current to flow either through a carbon strip alone or through the strip and a carbon arc in series in the manner shown in Fig. 4.1.7. Using the strip alone, heated to

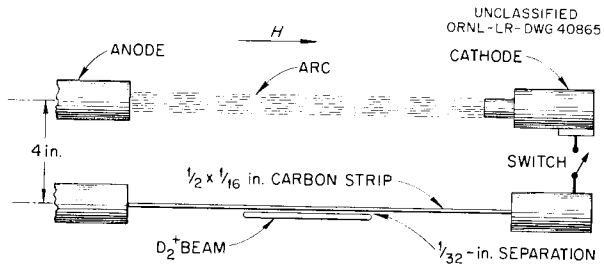

Fig. 4.1.7. Carbon Strip and Arc Combination Used in D_2^+ Dissociation Studies.

incandescence, no breakup occurred, but when the strip was operated in series with the arc using the same current (and with no crack in the strip), 10% breakup occurred.

4.1.3 EFFECT OF ULTRAVIOLET AND RADIO FREQUENCY RADIATION ON BEAM DISSOCIATION

While these experiments were of considerable interest they in no way helped to illuminate the mechanism that produces dissociation. The fact that breakup was occurring at some distance from the apparent arc led to an examination of possible roles of ultraviolet radiation, radio-frequency radiation, or a combination of these as active agents in producing the breakup. A definitive experiment was sought to clear up this point, first by making geometrical changes that would influence the amount of radiation falling on the beam. The result was negative; for example, a small, square arc and a wide, thin arc produced equal dissociation efficiencies. A definite result was finally obtained when a tantalum screen was placed between the arc and the beam (Fig. 4.1.8). Since the plasma is known to rotate about the arc core, its angle of incidence upon the screen would be small, and very little would be transmitted. On the other hand, this screen would be 90% transparent to optical radiation and, as was shown later, also relatively transparent to radio-frequency radiation. Several runs were made with this arrangement and all showed a very large drop in the intensity of the dissociated beam when the screen was interposed between the arc and the D_2^+ beam. Figure 4.1.9 gives data from a typical run.

It would seem logical to conclude from these tests that radiation does not cause appreciable dissociation of the molecular ions in any direct

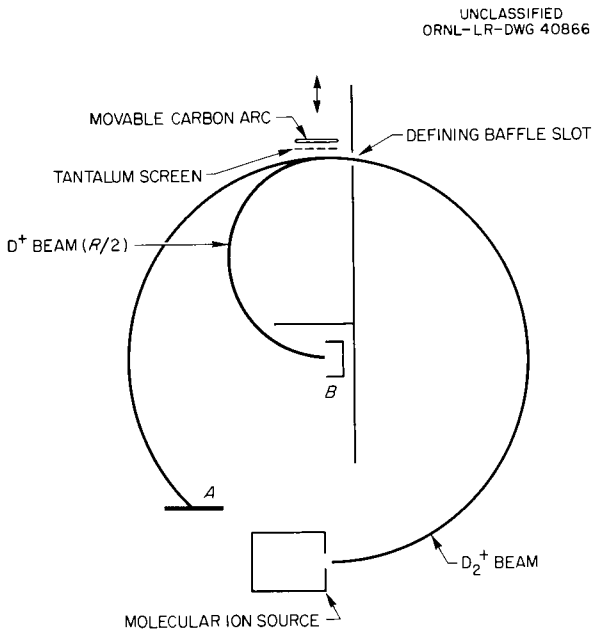

Fig. 4.1.8. Apparatus for Measuring Dissociation of D_2^+ Using a Tantalum Screen.

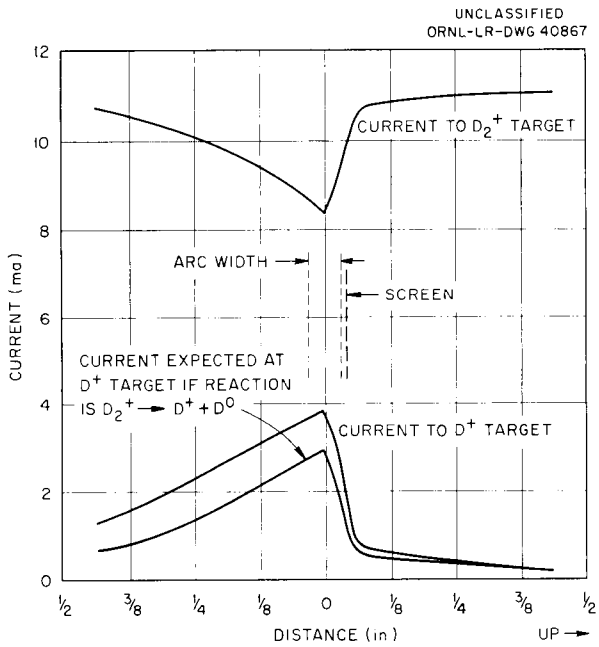

Fig. 4.1.9. Dissociation of D_2^+ Using a Tantalum Screen.

way. An indirect role of radio-frequency radiation is suggested by the cracked carbon strip and the arc-with-hot-carbon-strip experiments; perhaps the radiation aids in establishing a plasma condition conducive to breakup. These tests suggested that direct mass spectrometric and microwave measurements of plasma density in the region near the arc should be made. The measurements have been made, and sections 4.4 and 4.5 of this report indicate that the data confirm the existence of plasma outside the arc column.

4.1.4 SIMULTANEOUS MEASUREMENT OF DISSOCIATION OF D_2^+ AND D_3^+

For the final test series the apparatus was rebuilt so that the dissociation of both D_2^+ and D_3^+ could be measured in the same run with the same equipment (see Fig. 4.1.10). The only alteration made in these tests was to change the magnetic field from 3000 to 3700 gauss.

In the case of dissociation of D_3^+, the ratio of the strength of the dissociated D^+ beam to that of the D_2^+ beam averaged about 4/1. Tests were then made using hydrogen gas as the breakup target and the average between D^+ and D_2^+ was 3/1. These measurements are quite consistent with cross section measurements by Federenko. The data suggest that the process of dissociation in the carbon arc may be basically the same as that of dissociation in a neutral gas. Integration of the data from a number of runs shows that the ratio remains constant with changes in beam intensity, variations in pressure, and different arc currents.

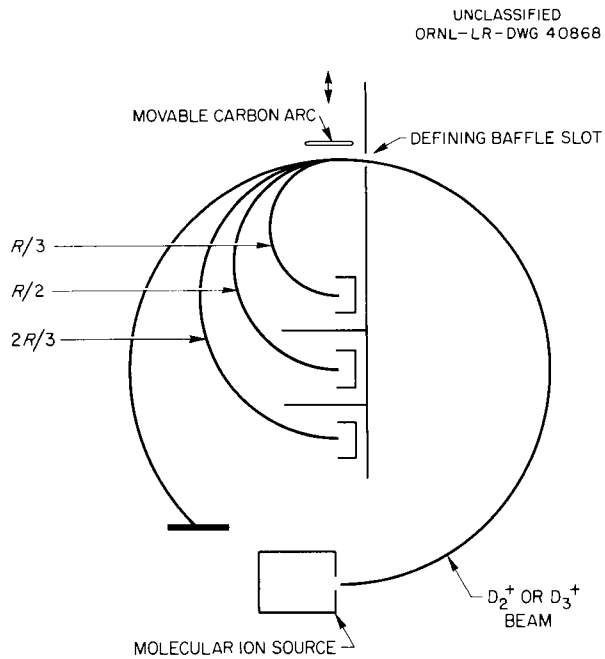

Fig. 4.1.10. Apparatus for Measuring Dissociation of D_2^+ and D_3^+.

4.2 TRAPPING OF HIGH-ENERGY IONS WITHIN AN ARC WALL

J. S. Luce

Magnetically confined direct-current arcs have been studied in the controlled fusion program at Oak Ridge.[1,2] These energetic, high-vacuum discharges were developed as an integral part of the DCX system, which provides trapping and storing of high-energy ions in an evacuated magnetic volume. Molecular deuterium ions are accelerated into the volume and dissociated to the atomic state by the arc.

An extension of the dissociation system has recently permitted operation of large-diameter cylindrical arcs with the resulting atomic ions trapped in the region enveloped by the wall of the cylindrical discharge. The arc wall can act as a barrier preventing neutral gas from reaching the trapped ions within, thereby reducing charge-exchange losses between low-energy neutrals and the trapped high-energy ions (Fig. 4.2.1).

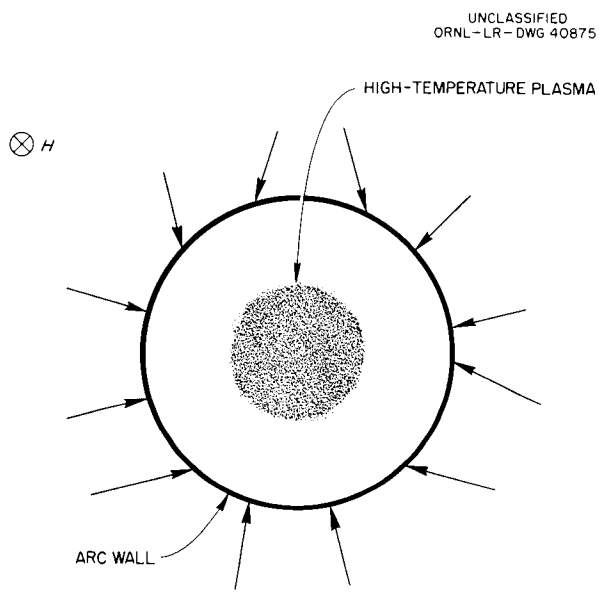

Fig. 4.2.1. Diagram Illustrating Inability of Low-Energy Neutrals to Penetrate Arc Wall Due to Ionization Effect.

Both deuterium and carbon arcs have been considered for these tests. Despite the higher Z of the carbon ions the work has been concentrated on hollow cylindrical carbon arcs. The strong ionizing power and gettering action of this discharge make its use very attractive. Calculations based on scaling the pumping measurements in DCX show that the discharge now under study should have a pumping speed greater than 100,000 liters/sec. The 15-in. arc planned for DCX-2 will have an estimated pumping speed of at least 250,000 liters/sec. Testing of these 15-in. and even larger-diameter arcs will require extensive modifications of one of the Geneva DCX machines. The tank will be extended in length, will have additional diffusion pumps and liquid nitrogen traps, and, more important, a set of coils which will produce a much higher magnetic field. A d-c power supply that provides a maximum of 10,000 amp at 350 v has been ordered for the arc power source.

No basic limitation has been encountered in producing large cylindrical carbon arcs and trapping high-energy ions inside the wall of the arc. The role of this system in the field of controlled fusion research is dependent upon success in producing ions in the arc with high average charge, the elimination of low-energy neutrals, and the establishment of the trapped ions in orbits well inside and away from the walls of the arc. Proper evaluation of the system will be made when the decay time of the trapped ions is measured.

4.2.1 ARC WALL EXPERIMENTS

Equipment

The first tests upon annular arc walls were carried out in a small facility. Hollow cylindrical carbon cathodes up to 3 in. in diameter were used. The best wall thickness appeared to be about 0.062 in.; thicknesses of more than 0.070 in. led to unstable arc operation; and thicknesses of less than 0.050 in. permitted erosion that was too rapid for a practical system. The experiments were later moved to the more roomy circumstances in the Geneva exhibit tank (now called DCX-EP), Fig. 4.2.2, and the arrangement used is illustrated

[1] C. F. Barnett *et al.*, "The Oak Ridge Thermonuclear Experiment," paper UN/P-344 presented at the Second United Nations International Conference on the Peaceful Uses of Atomic Energy, Geneva, Sept. 1–13, 1958.

[2] J. S. Luce, "Studies of Intense Gaseous Discharges," paper UN/P-1790 presented at the Second United Nations International Conference on the Peaceful Uses of Atomic Energy, Geneva, Sept. 1–13, 1958.

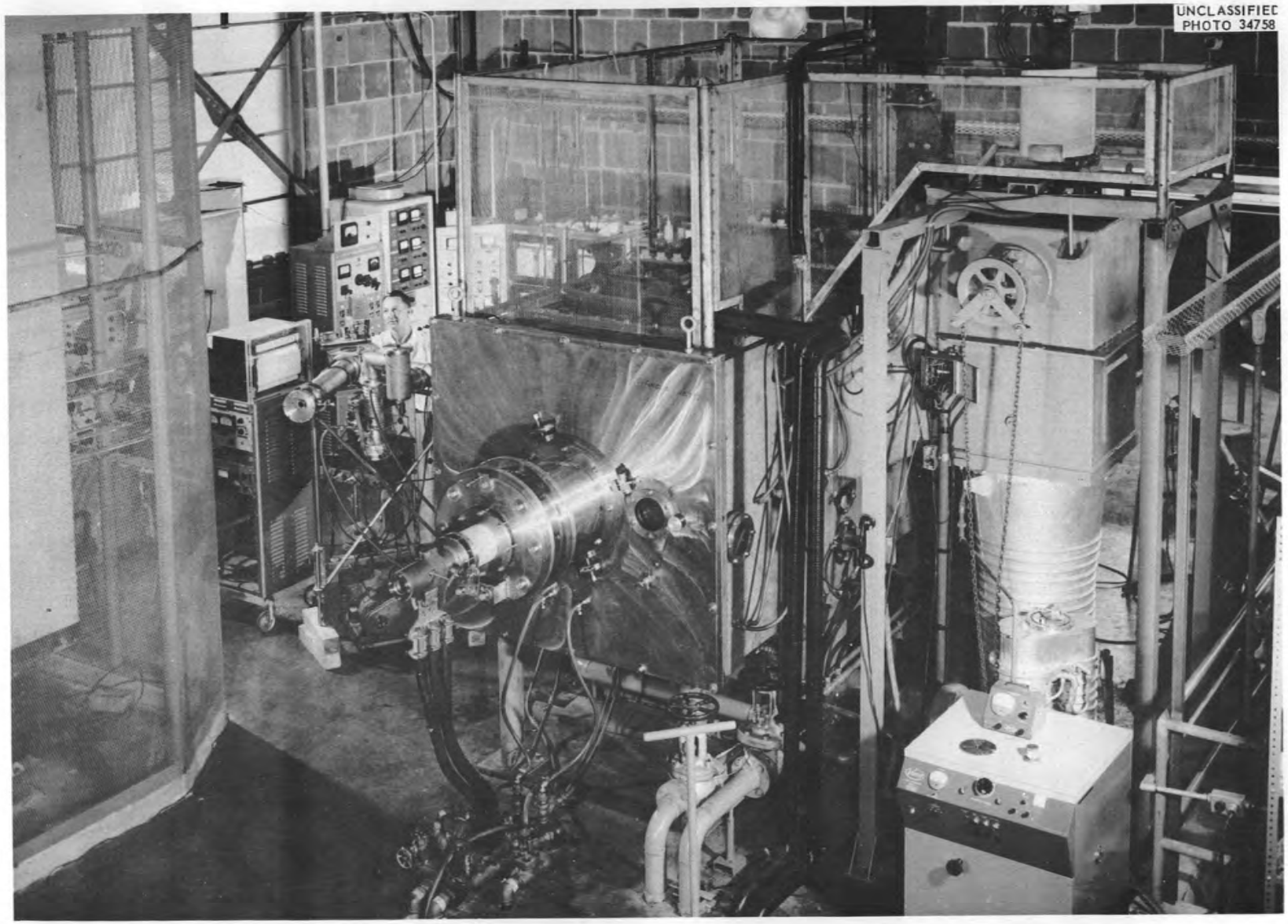

Fig. 4.2.2. Photo of DCX-EP.

in Fig. 4.2.3. To prevent carbon neutrals and carbon aggregates from reaching the inner region of the arc, it is necessary to provide inner cylindrical baffles. These baffles are placed so that they shade the inner region of the arc from the hot edges of both the cathode and anode. It is necessary to insulate the central section of the inner cathode baffle to prevent the arc striking from it (Fig. 4.2.4). The cathode assembly provides an annular space between the cathode and the inner baffle, to allow ionized material to pass out of the system, thus providing pumping at high speed from the strategic area. No annular space is provided at the anode since the ions flow away from the anode and toward the cathode (Fig. 4.2.5). The first tests were made with the cathode and anode at the center of the mirror coils. The arc was 7 in. across at its greatest diameter. The arc voltage was 160 v and the arc current 3600 amp. Little basic difficulty was encountered in these tests. The cylindrical shape is apparently a natural and stable operating mode for this discharge. Figure 4.2.6 is a photograph of a cylindrical arc 7 in. in diameter and 47 in. long.

Arc Homogeneity

One problem encountered in these tests was the formation of longitudinal striations, which left intervening thin sections of the arc wall. The formation of the striations was apparently connected with the limitation in magnetic field strength to 2500 gauss by the coils that were available. Brief tests at higher fields showed a reduction in the intensity of striations. The maximum field now used is limited to 3600 gauss, and new coils are being designed to provide higher fields. The diameter of the arc has been reduced to 5.6 in. which, in conjunction with the 3600-gauss field, has produced a more homogeneous arc wall.

Spectroscopic Analysis

Spectroscopic analysis of this arc wall shows it to be unsuitable for protecting a hot plasma, due to the presence of a large number of C^+ and C^{++} ions (Table 4.2.1). Trapped, high-energy D^+ ions can capture electrons from these carbon ions, particularly if they are in excited states. The velocity of the remaining outer-shell electrons is in the 3 to 5×10^8 cm/sec range. This matches the velocity of the trapped, 10-kev D^+ ions quite closely. In addition, the low mean-charge state of the carbon ions probably indicates the presence of some carbon neutrals that should be observable

Table 4.2.1. Relative Abundance of Carbon Ions in Hollow Carbon Arc with Anode at Center of Coil

Wavelength	Ion	Relative Abundance	Normalized to Line 1548
2478	C^0		
1930	C^0_E		
1335	C^+_R	60	9.5
2512	C^+_E	9	1.4
977	C^{++}_R	273	43.3
2296	C^{++}_E	288	45.7
1548	C^{+++}	630	100
2530	C^{+++}_E		

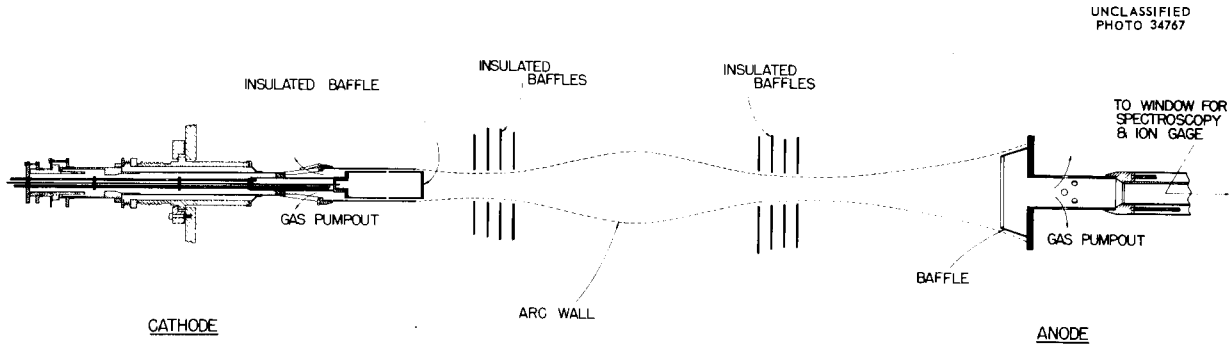

Fig. 4.2.3. Arc Wall Experiment.

UNCLASSIFIED
PHOTO 34757

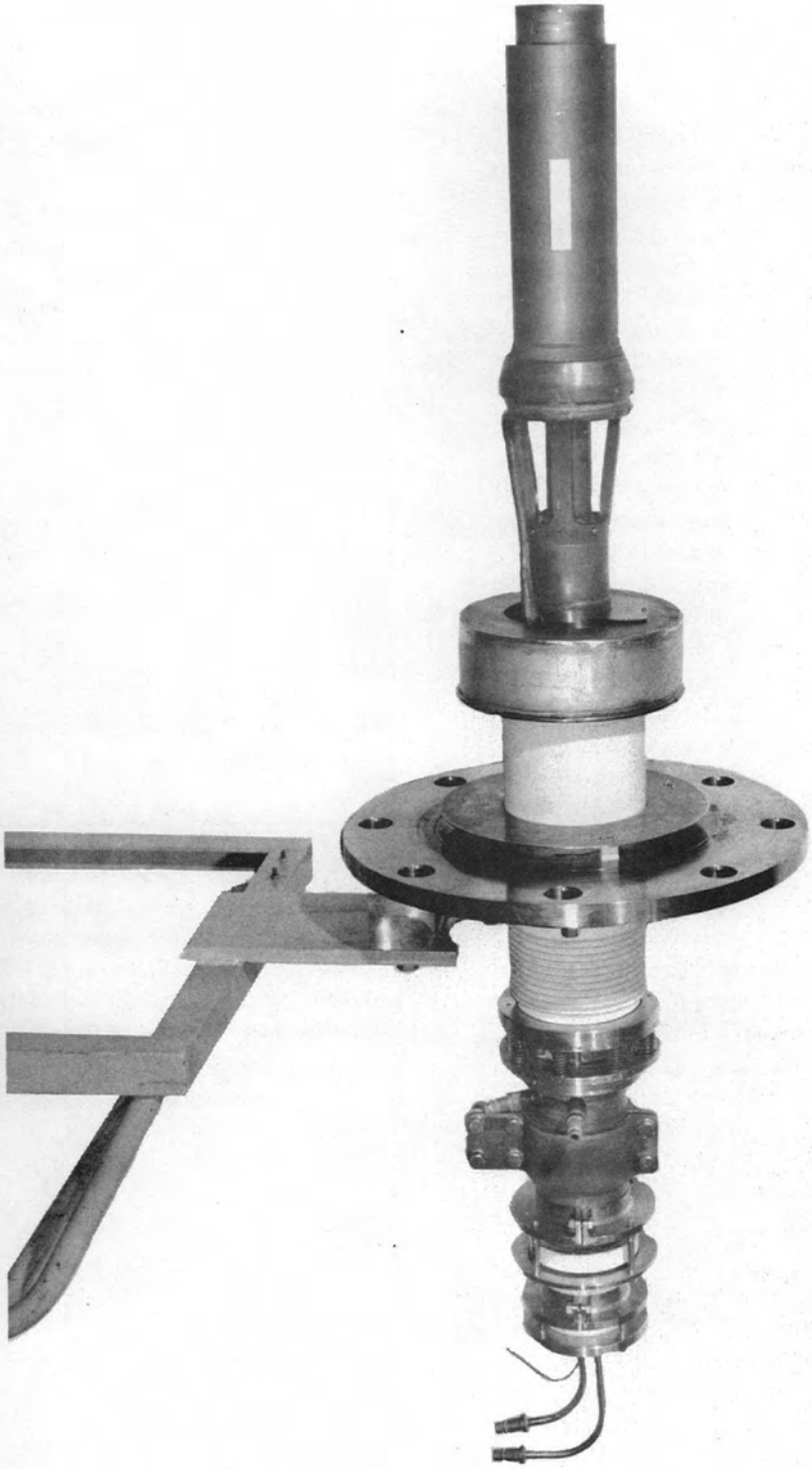

Fig. 4.2.4. Photo of Cathode Assembly.

UNCLASSIFIED
PHOTO 34760

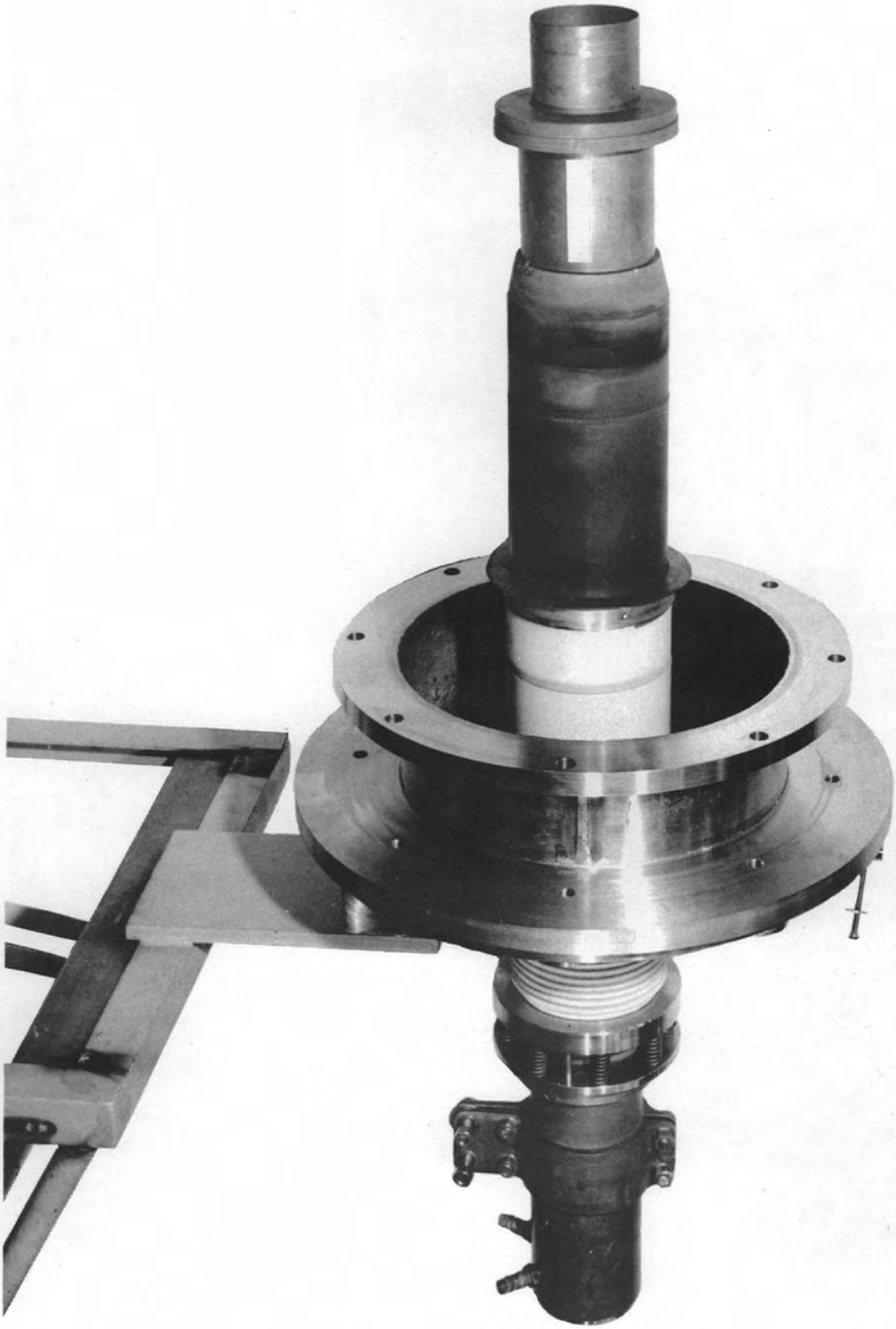

Fig. 4.2.5. Photo of Anode Assembly.

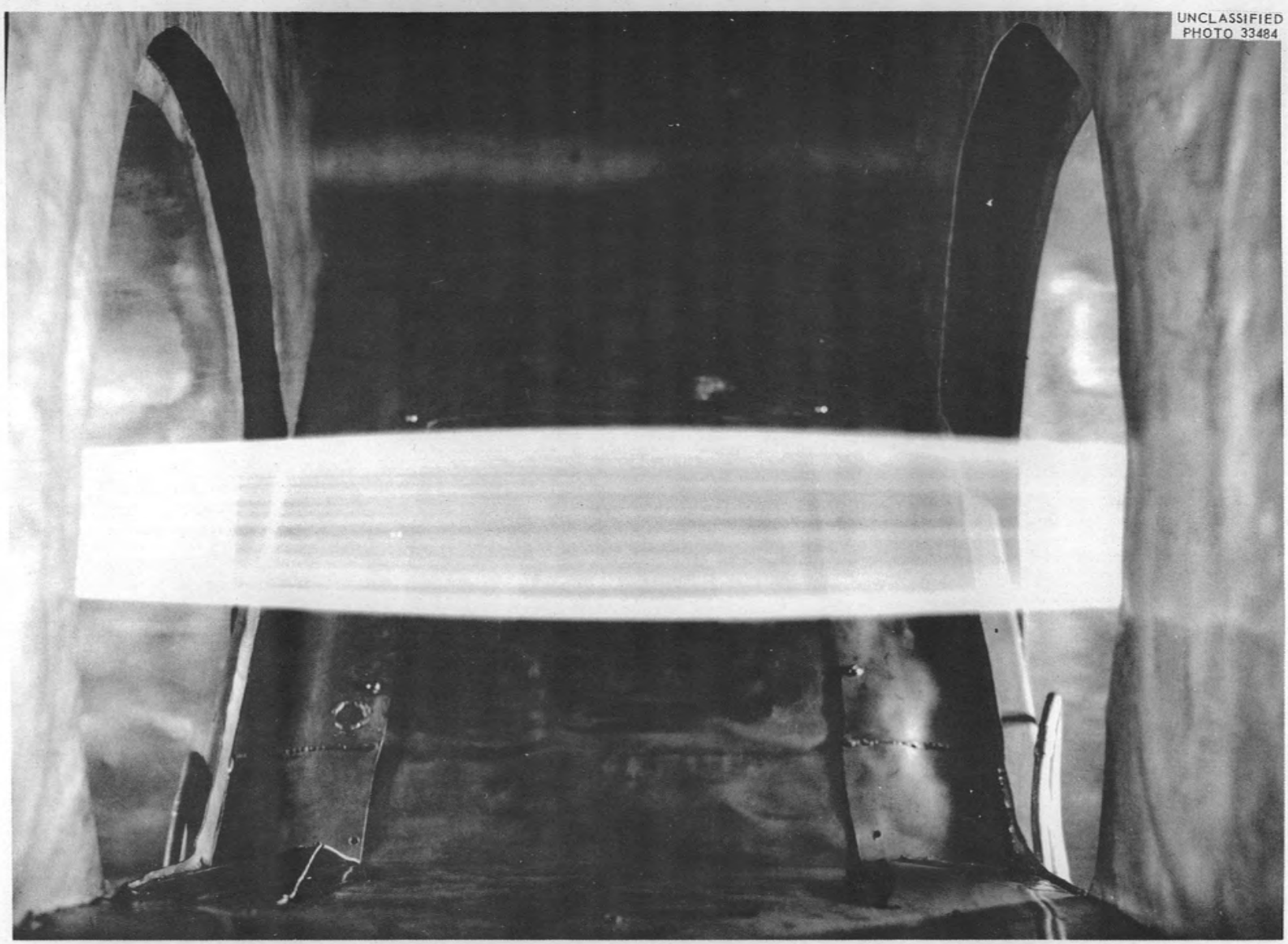

Fig. 4.2.6. Photo of Hollow Carbon Arc.

with longer exposures. Measurements in DCX show that about one ion in 10^5 is lost in the arc via charge exchange when trapped ions of 300-kev energy are used. With the 10-kev trapped ions used inside the arc wall the losses should be greater than in DCX if there is even a small amount of neutral gas present, since the cross section for charge exchange between the neutrals in the system and the D^+ ions peaks at approximately this energy. It seems clear that the injected molecular ions should have somewhat higher energy, particularly if multiple scattering is also considered. The trapped D^+ ions will, at least in early testing, pass through a plasma region with a carbon ion density in a range of 1 to 3×10^{13} particles/cc. Several plans are under study to cause the ions to spend more time near the center of the volume enclosed by the arc, where the plasma density is lowest. These include use of a rising magnetic field so that the trapped ions rotate in small orbits near the center of the hollow discharge and the use of a magnetic "bump" which may accomplish the same purpose. As many of the L electrons as possible should be removed from the carbon ions, since charge exchange between the high-velocity, tightly bound K electrons and trapped D^+ ions should be reduced.

Effect of Electrode Position

An attempt has been made to increase the mean-charge state of the carbon ions in the arc by moving the electrodes farther apart until they are outside the magnet coils. Figure 4.2.7 shows a typical wear pattern with the anode positioned 25 in. out from the coil center. At the present time the cathode is 10 in. from the center of one coil and the anode 38 in. from the center of the other, the total arc length being 8 ft. The magnetic field in the center of the coil is 7000 gauss and the field at the anode is 600 gauss. The appearance of the arc has improved to the extent that striations are almost eliminated. Preliminary spectroscopic data show a trend (Table 4.2.2) toward higher charge states of the carbon ions. Further improvement in the arc is expected when the new coils are available. These coils will more than double the present magnetic field. It has been shown that the average charge on the ions increases with increasing magnetic field.[3]

[3] J. F. Potts, private communication.

Table 4.2.2. Relative Abundance of Carbon Ions in Hollow Carbon Arc with Anode 33 in. Out from Center of Coil

Wavelength	Ion	Relative Abundance	Normalized to Line 1548
2478	C^0		
1930	C^0_E		
1335	C^+_R	1.8	0.54
2512	C^+_E		
977	C^{++}_R	76	23
2296	C^{++}_E	108	32.6
1548	C^{+++}	331	100
2530	C^{+++}_E	0.6	0.18

Trapping Experiments

Two tests have been made to see if a beam could actually be trapped within an arc wall. A 350-ma beam of D_2^+ at 26 kev was used in these tests, which were carried out in DCX-EP. The trapped beam was clearly visible inside the arc due to the presence of a large number of small carbon aggregates. The cylindrical baffles had been removed to provide carbon for this purpose. No meaningful measurements were made, the runs being of an exploratory nature. It was obvious that some of the ions were passing through the arc rather than remaining inside the wall. This condition is geometrically inherent when using D_2^+ ions unless a very large-diameter arc is used.

The smaller radius of D^+ resulting from dissociation of D_3^+ ($R/3$) led to a change from D_2^+, which provides a trapped radius of only $R/2$. No difficulty was encountered in producing 0.25 amp of D_3^+ ions, and currents up to 0.5 amp have been achieved for short periods of time. Figure 4.2.8 shows the arrangement of the arc wall, the ion source, the ion beams, and the beam targets using a primary beam of D_3^+. Thorough mixing of the trapped ions is achieved by causing them to rotate in orbits which have their centers ¼ in. off the magnetic axis. The resulting trajectories cause the ions to rotate through each other and to precess away from the region of dissociation,

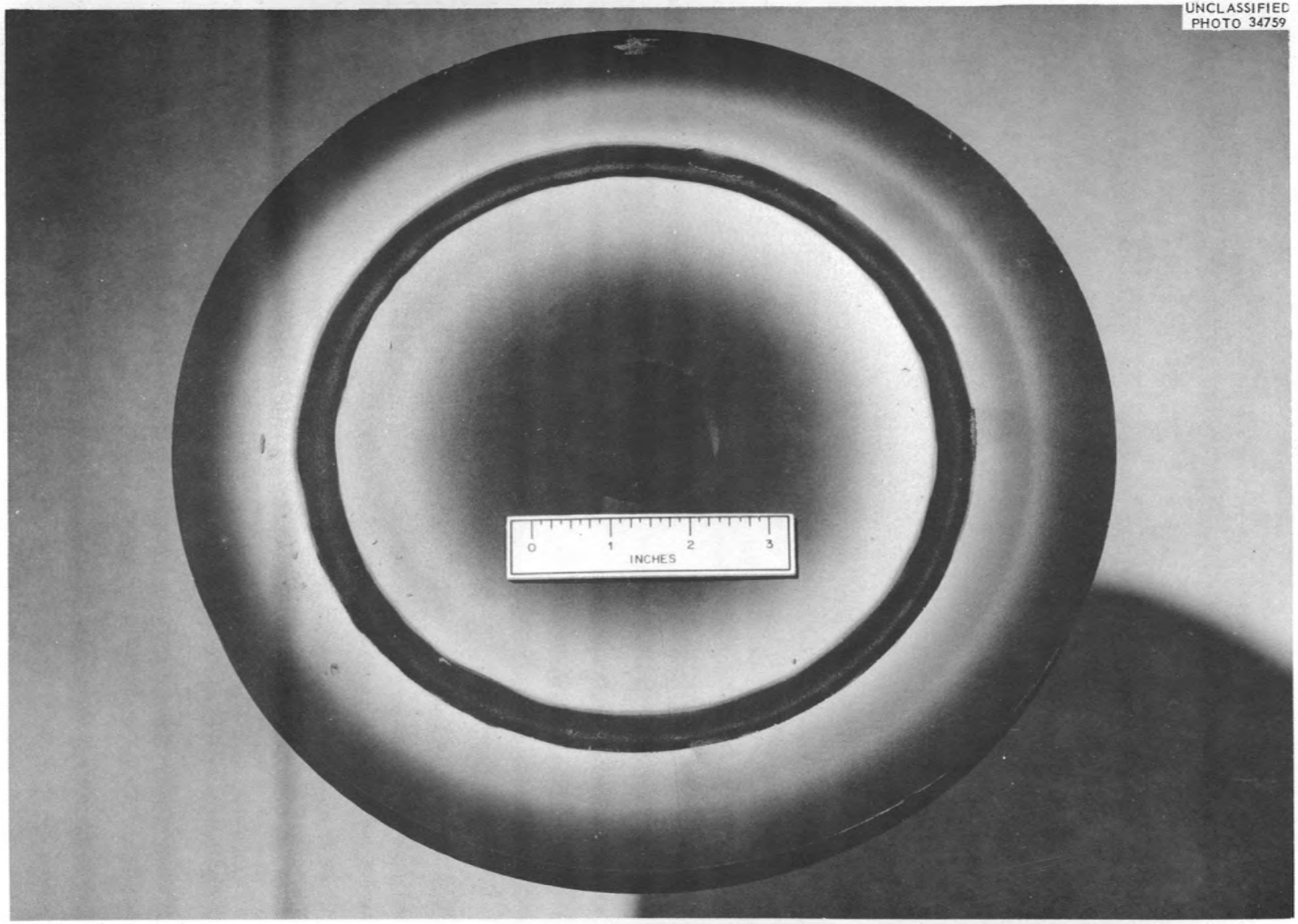

Fig. 4.2.7. Photo of Anode Wear Pattern.

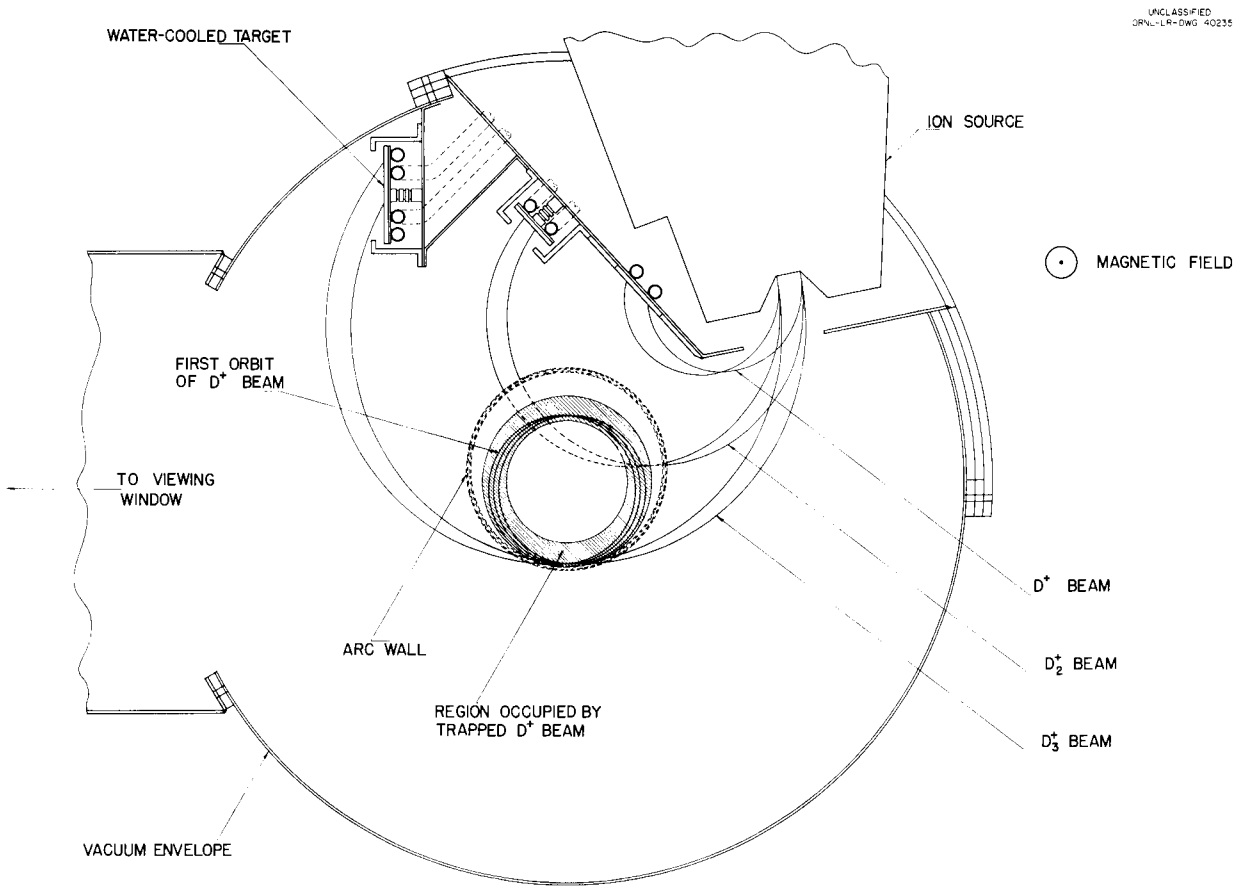

Fig. 4.2.8. Trapping of High-Energy Ions Within an Arc Wall.

which is close to the inner diameter of the arc wall. The ions spend most of their time in orbits some distance from the dense part of the wall.

Spectrographic Analysis and Neutron Detection

A mass spectrograph is being designed for analysis in addition to spectroscopic analysis of the ions in these hollow arcs. This instrument is of particular value in detecting C^{4+} ions since they cannot be seen optically unless they are in an excited state. It is extremely difficult to make direct measurements of the trapped ions inside the hollow arc, but one indirect method that seems attractive is to measure the decay time of the trapped ions with neutron detectors. A system is being prepared that is based on the decay of the neutron flux as the stored D^+ beam is lost, presumably by charge exchange. The neutrons result from the high-energy neutral deuterons striking deuterium occluded by the walls.

The DCX-EP device, with its present beam and target surfaces, emits approximately 50 neutrons/cm^2 in one second to one counter. The number of events observed per second will be raised to approximately 250 by increasing the number of counters to 5. An oscillographic arrangement is being prepared to record neutrons as a function of time during the interval when the injected beam is switched off. Arranging the device so that many such intervals can be recorded will make possible a plot of neutrons as a function of time. Using the count of 250 neutrons/sec with the repetition rate adjusted so that the average count is reduced by no more than a factor of 5, there should be 50 counts per decay interval per second. One hundred seconds yields 5000 counts, which should give a decay time of $T = t/\ln 2$ to

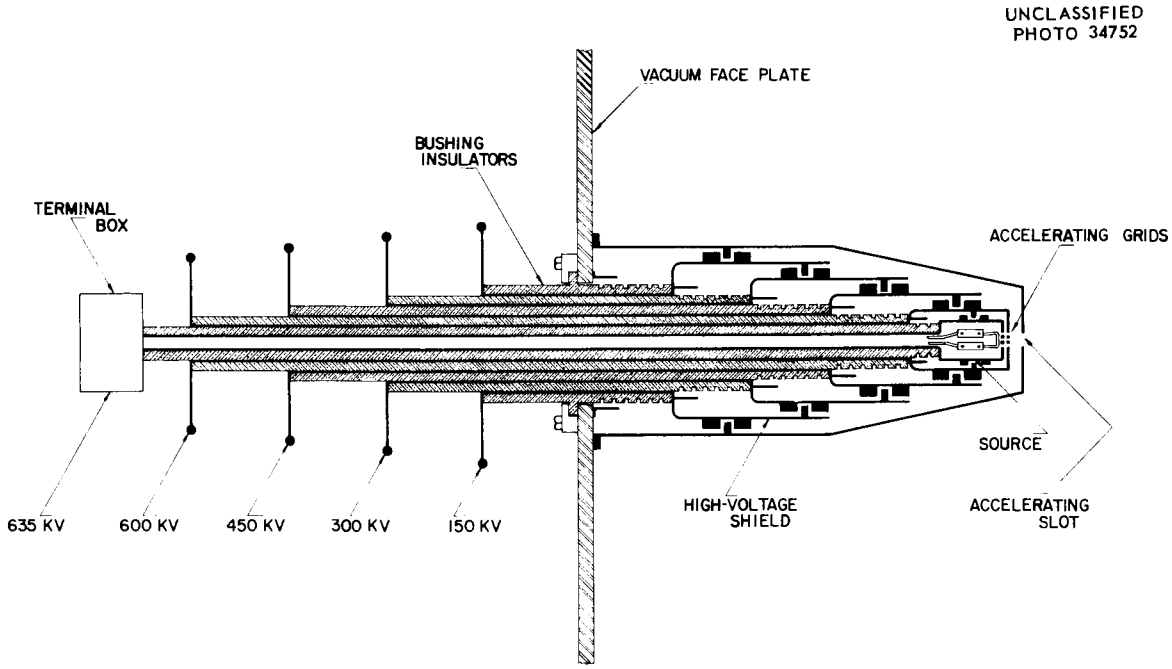

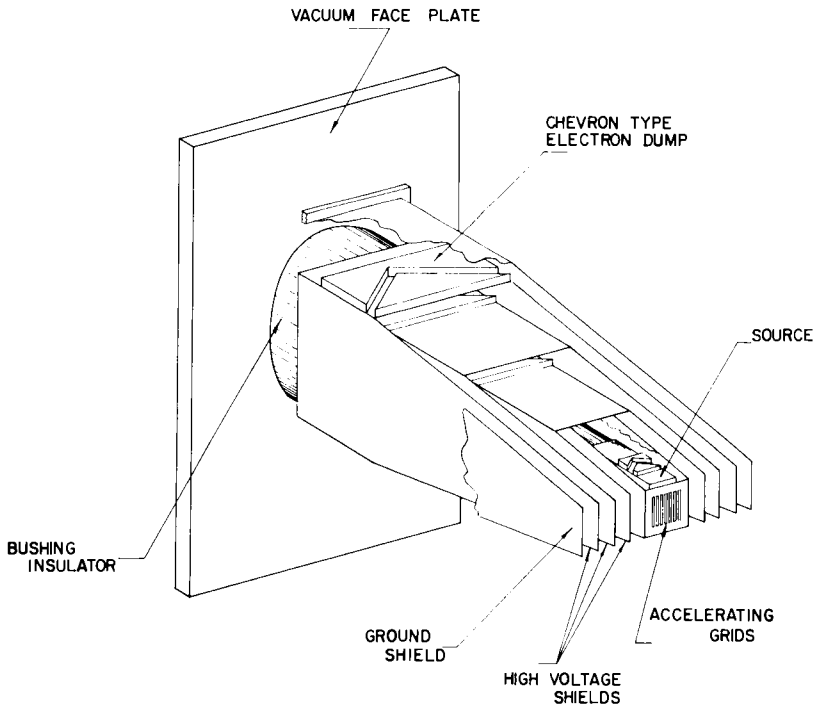

Fig. 4.2.9. Multistage High-Voltage Source.

$1/\sqrt{2500}$, or a variation of 2%, assuming an exponential decay.

4.2.2 MULTISTAGE GRID ION SOURCE

The grid sources used in these tests are being modified to provide higher-energy molecular ions. These sources are to be built in stages, so that the highest applied voltage will be in the 100- to 150-kv range per stage. The first source, now under construction, will have two stages – one at 30 kv, the second at about 100 kv. It is difficult to hold voltage above 30 kv on the first stage because of sparking in the region of initial acceleration, but acceleration in later stages is much easier. Preliminary tests have been made with a small assembly using 20 kv on the first stage and 60 kv on the second, providing 300 ma of D_2^+ at 80 kev with stable operation. The applied voltage of the second stage was limited to 60 kv by the power supply. If higher-energy ions are needed the net voltage can, in principle, be raised to a higher value by increasing the number of stages. Figure 4.2.9 shows a five-stage, 600-kv source under design study.

ACKNOWLEDGMENTS

General engineering and construction were directed by H. C. Hoy, assisted by R. L. Knight, G. F. Leichsenring, and several others. Operational assistance was provided by V. J. Meece, and modifications and general assembly of experiments were made by a group under O. D. Matlock. Magnetic-coil and ion-orbit calculations were done by W. F. Gauster and colleagues.

Diagnostic analysis and equipment were provided by the Spectroscopic Group under J. R. McNally, Jr., and the Diagnostics Group led by R. A. Dandl, assisted by C. H. Weaver; the mass spectrograph was designed by R. V. Neidigh. This diagnostic work was made possible by the cooperation of P. R. Bell.

4.3 LONG "PIG" ARC DISCHARGES

J. W. Flowers[1]

High-current PIG arcs in argon, helium, and deuterium (studied for possible use in molecular beam dissociation or as arc walls) were operated over a path length of 6 ft in a magnetic field of 5000 gauss, extending experiments previously reported for short PIG arcs.[2] Two points seem worth reporting. In the first instance the arc, including the cylindrical anode (Fig. 4.3.1 and ref 2, Fig. 20), was extended in length to approximately 6 ft, and when gas pressure was lowered during operation, a breakdown took place between the cathode and a spot on the anode adjacent to the reflector. This breakdown appeared to limit the extent to which the pressure could be lowered for an intense PIG discharge with a given anode structure. It probably is related to the visual "blowup" previously reported for the short discharges.

Secondly, for the successful operation of the long arc at relatively high pressure, plane shields previously used were not adequate to prevent breakdown and arc-back at the cathode and reflector. Before the long PIG arc could be operated under any condition consistent with the self-heated cathode and the available supply voltage, it was necessary to develop more effective shielding. A floating shield interlocking a radial extension on the cathode proved to be effective together with a similar shield at the reflector. This is shown in Fig. 4.3.1. With this shielding, desired arc paths could be initiated with gas feeding through the solenoid case instead of the favorable feed through the cathode.

A further manifestation of the low-pressure limitation for a long PIG discharge was indicated by increasing discharge current on approaching breakdown. The behavior in the region of breakdown suggests that many electrons pass readily

---

[1]Consultant, University of Florida.

[2]J. S. Luce, "Studies of Intense Gaseous Discharges," paper UN/P-1790 presented at the Second United Nations International Conference on the Peaceful Uses of Atomic Energy, Geneva, Sept. 1–13, 1958.

from the cathode to the far anode end, crossing the magnetic field. In the range of operation, discharge current could be varied between 10 and 200 amp and pressures ranged from 10^{-2} to 10^{-4} mm Hg. Maximum arc potential drop was 600 v.

UNCLASSIFIED
ORNL-LR-DWG 40869

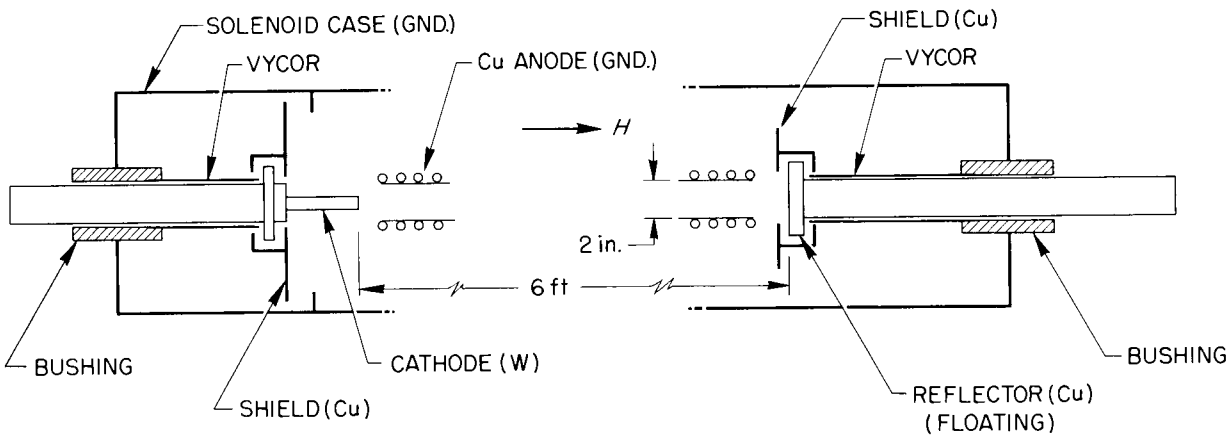

Fig. 4.3.1. Cathode Shields for Long PIG Arc.

4.4 FALLING PARTICLE AND PROBE STUDIES

4.4.1 FALLING PARTICLE STUDIES

C. W. Blue C. H. Weaver
H. S. Robertson

Figure 4.4.1 illustrates an experimental arrangement used to study the carbon arc by dropping molybdenum particles into it from above. The experiments were done in a Beta tank. The falling stream of particles was approximately 0.1 in. in diameter, and all particles were sized for diameters of 5 μ or less. The arc used was approximately 0.5 in. in diameter, and the distance from the visual edge to the upper turning point (indicated in Fig. 4.4.1) was approximately 0.25 in. Pressures were approximately 0.02 to 0.05 μ, except immediately after the arc was struck. At such times pressures of 1.0 μ were obtained momentarily, due to gas let in to facilitate striking. The arc current was approximately 250 amp and the magnetic field approximately 6000 gauss.

Three principal visual results were observed. First, for normal operating pressures of 0.02 to 0.05 μ, the stream of metal particles was heated to incandescence and thrown sideways through distances of several feet when dropped on the arc. The direction of the stream depended upon the direction of the magnetic field, as shown in detail *A-A* of Fig. 4.4.1. Since the magnet pole pieces prevented the taking of photographs of the phenomenon from the side, the angular region containing typical observed trajectories is shown by diagram; it lies between the dotted lines of Fig. 4.4.2. The fact that some particles can be thrown slightly upward should be noted. The solid lines show possible theoretical parabolic trajectories for two cases: when the particle retains its vertical velocity component as it is thrown sideways, and when it loses its vertical component of velocity before being thrown sideways. In both cases the assumption is made that all horizontal energy is imparted to the particle at the arc surface, and has a value corresponding to the horizontal velocities measured. These velocities were determined by means of motion

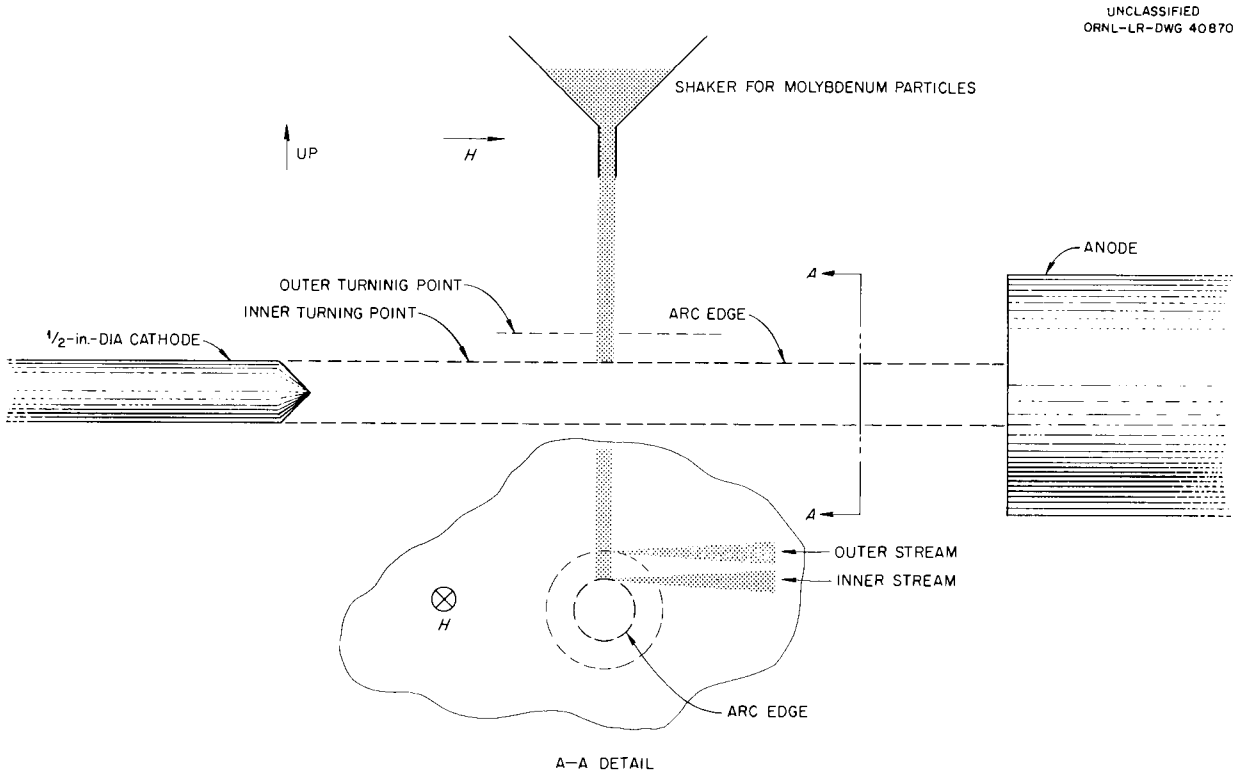

Fig. 4.4.1. Effect of Carbon Arc on Dropped Molybdenum Particles.

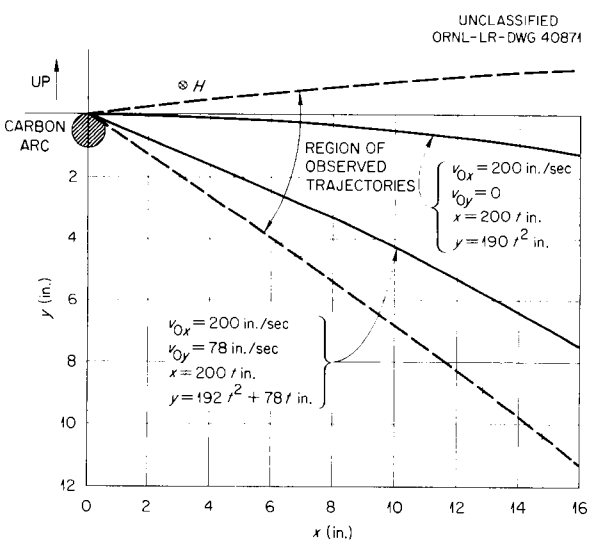

Fig. 4.4.2. Theoretical and Observed Molybdenum Particle Trajectories.

pictures taken from above the arc. A grid of known size was placed between the camera and the particle stream moving sideways, and a light pulse of known frequency was superimposed on the film as the pictures were taken. From this, it was determined that the particles had horizontal velocities up to 200 in./sec.

Secondly, it was observed that the molybdenum particles were actually thrown from the arc surface in two distinct layers, as shown in Fig. 4.4.1. The distance between turning points was about 0.25 in., and increased significantly with arc current. No exact measurements were made during this observation.

Thirdly, at the high pressures accompanying startup (several microns), it was observed that all particles were thrown along the arc toward the anode. As pressure decreased to typical operating values (0.1 μ), the particle streams returned to directions normal to the arc, as illustrated in Fig. 4.4.1.

A possible explanation of the first result can be made, based on the potential measurements of Potts.[1] From these measurements a model of the arc cross section can be formed as shown in Fig. 4.4.3. For a positive or negative ion or

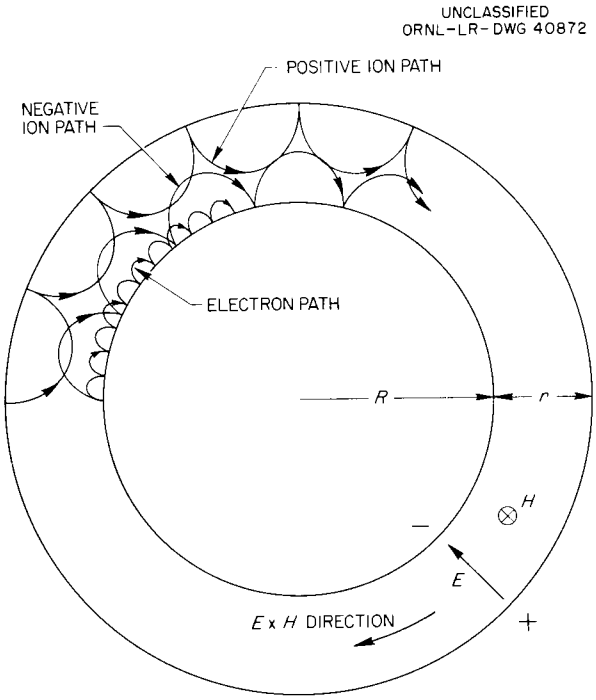

Fig. 4.4.3. Possible Surface Conditions in the Carbon Arc.

electron moving in the "scattering layer" around the outside of the arc, the $E \times B$ particle drift velocity[2] can be calculated. With a radial electric field in the scattering layer of about 18 v/cm, and an axial magnetic field of 6000 gauss, the drift velocity is given by:

$$v_\theta = \frac{E}{B} = \frac{1.8 \times 10^3 \text{ v/m}}{0.6 \text{ weber/m}^2}$$

$$= 3 \times 10^3 \text{ m/sec} = 3 \times 10^5 \text{ cm/sec} .$$

Carbon ions in this arc have been observed to have energies of about 10 ev, with speeds therefore of about 10^6 cm/sec.

The physical picture of the molybdenum scattering is as follows. Molybdenum particles falling into the arc effectively encounter a rotating plasma just outside the visual arc. Bombardment of the falling particles by plasma ions imparts tangential momentum to the particles, thereby deflecting them. At the scattering layer, the particles have acquired a free-fall velocity of 78 in./sec, or 200 cm/sec. The brightest of the deflected glowing particles, considered to have been deflected from the lower scattering layer closer to the arc and therefore to be those of most nearly the full 5-μ size, have horizontal velocities of 200 in./sec, or 500 cm/sec. If each ion transfers, on the average, momentum equal to mv_θ to a particle, then the total number of collisions necessary to impart this horizontal velocity to a particle is given by:

$$N = \frac{\frac{4}{3}\pi r^3 \rho V}{m v_\theta} ,$$

where r, ρ, and V are the radius, density, and horizontal velocity of the molybdenum particles, and m is the ion mass. For the observed numbers, with $r = 2.5 \times 10^{-4}$ cm and $\rho = 9$ g/cm^3, $N = 5 \times 10^{10}$ collisions. The total number of collisions is also given by: $N = nv\sigma T$, where n is the average ion density, v the average ion speed, σ the particle cross section, and T the time spent in the scattering layer. If σ is taken to be πr^2, the geometrical cross section, and v taken to be 10^6 cm/sec, corresponding to an ion energy of 10 ev, then an estimate of T leads to an estimate of n.

One basis for estimating T is as follows. Assume that the molybdenum particles consist of a mixture of 5-μ particles and very much smaller particles. Assume further that the top of the scattering layer is marked by the scattering of the very light particles, and that the observed upper layer corresponds to this scattering. Then one may estimate T as the time required for a 5-μ particle to fall from the upper scattering surface to the lower surface from which it is scattered. This distance, about 0.25 in., gives T as 3×10^{-3} sec.

Using this value, one obtains:

$$n = 10^{14} \text{ particles/cm}^3 .$$

Another estimate of T may be made from the visual observation that the incandescent particles

[1] J. F. Potts and C. H. Weaver, *Thermonuclear Project Semiann. Rep. Jan. 31, 1959*, ORNL-2693, p 44.

[2] L. Spitzer, *The Physics of Fully Ionized Gases*, p 3, Interscience, New York, 1956.

seem to exhibit a radius of curvature during deflection of about 1 mm, or that they are subject to bombardment for a path length of about 2 mm, during which time the horizontal deflection is 1 mm, and the horizontal velocity increases from zero to 500 cm/sec. The time required for this is 4×10^{-4} sec. Using this value for T, one obtains:

$$n = 5 \times 10^{14} \text{ particles/cm}^3 \ .$$

These values are not necessarily inconsistent, since it is expected that n increases as the arc axis is approached, and therefore the value of n will depend upon the radial distance over which the force is averaged.

Another explanation may be found for the presence of two distinct scattering surfaces. As reported in the next section, probe measurements show a time periodicity in the rotating arc plasma. This is probably associated with a rotating cylindrical asymmetry in the arc plasma, producing an inner and an outer envelope from which particles may be scattered. Such a rotating asymmetry has been observed in another type of arc.[3] If this is the case, probably the second estimate of T is more accurate, and the higher estimate of n may be more nearly correct: one difficulty in this hypothesis is that the particles would have to fall a distance of about 0.6 cm in about 1 μsec. Even if the particles acquire a reasonable electric charge, such speeds are improbable.

The existence of oscillatory electric fields introduces uncertainty in the calculation of v_θ, a quantity which is very difficult to measure anyway. It is conceivable that the falling-particle method, coupled with a good independent measurement of n, might lead indirectly to an estimate of v_θ and thus to the radial electric field. Several refinements in method are immediately evident and are apparently worthy of further consideration. For example, particle size and shape can be more accurately controlled, axial observation in improved geometry can be made, and scattering as a function of position, both axial and transverse, can be studied. A more accurate density profile might be obtained in a series of experiments in which the particle diameter is varied over a range from 1 to 10 μ, and the free-fall height may also be varied.

Space charge effects have been neglected in this crude analysis, although they may be quite important. As methods improve, a more careful analysis may be warranted, and it may be possible to examine such questions as the charge state, sheath thickness, rate of evaporation, rate of electron emission, and temperature of the falling particles.

It is interesting to note that the spectroscopic slant effect observed by McNally *et al.*[4] qualitatively checks with the rotating plasma model used here.

4.4.2 PROBE STUDIES

C. H. Weaver

Floating point probes of the type used by Neidigh[3] have been mounted for probing the region near the visual surface of the arc (outer turning point for the falling particle experiment, Fig. 4.4.1). Average voltages of several volts positive have been observed in this region, with a superposition of alternating voltages of several volts at discrete frequencies. Figure 4.4.4 shows the traces obtained on two probes placed 90° apart in azimuth around the arc. The phase shift is always opposite to that expected from a positive ion "bunch" in simple Larmor orbit around the arc, but agrees with $E \times H$ drift if the interior of the arc is assumed to be negative with respect to the exterior.

In addition, it was also determined that no phase shift existed between probes placed at equal azimuth along the arc, and that the signal on a probe increased in magnitude when the area of the probe was increased.

4.4.3 ION BEAM MODULATION FROM GRID SOURCE

C. H. Weaver

Measurements have been made to determine the instantaneous variations of current in the R and $R/3$ beams in the device used for D_3^+ ion breakup measurements (see Sec 4.1.4). Figure 4.4.5 shows

[3] R. V. Neidigh and C. H. Weaver, "The Effect of an Applied Pressure Gradient on a Magnetically Collimated Arc," paper presented at the Second United Nations International Conference on the Peaceful Uses of Atomic Energy, Geneva, Sept. 1–13, 1958.

[4] J. R. McNally, Jr., M. R. Skidmore, and G. K. Werner, *Thermonuclear Project Semiann. Rep. Jan. 31, 1959*, ORNL-2693, p 27.

UNCLASSIFIED
ORNL-LR-DWG 40873

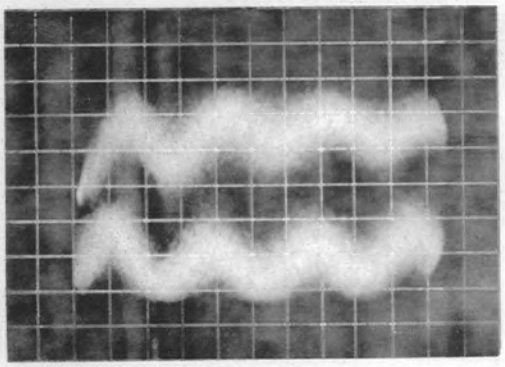

2 volts PER VERTICAL DIVISION
2 μsec PER HORIZONTAL DIVISION

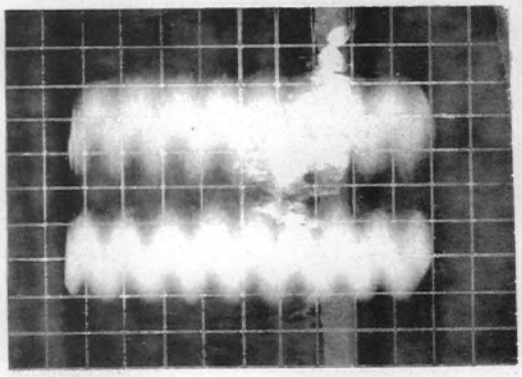

1 volt PER VERTICAL DIVISION
5 μsec PER HORIZONTAL DIVISION

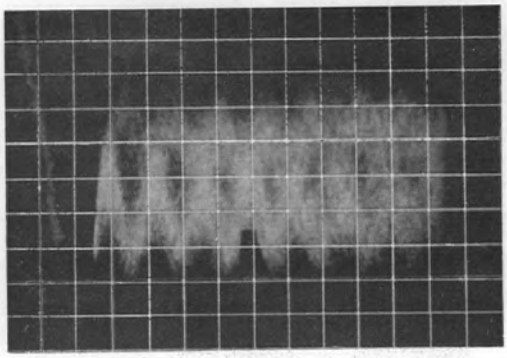

1 volt PER VERTICAL DIVISION
5 μsec PER HORIZONTAL DIVISION

Fig. 4.4.4. Point Probe Signals Near the Carbon Arc Surface. Traces are from probes separated 90° around the arc surface.

UNCLASSIFIED
ORNL-LR-DWG 40874

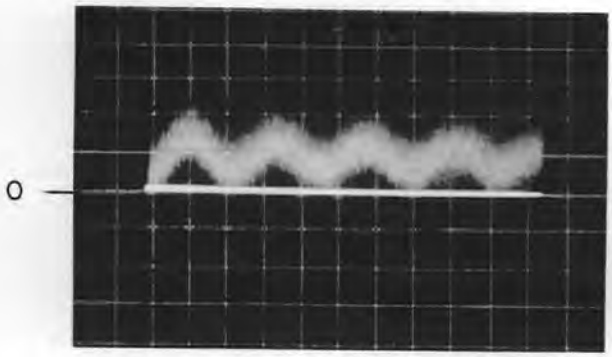

10 ma PER VERTICAL DIVISION
100 μsec PER HORIZONTAL DIVISION

Fig. 4.4.5. Variation in R Beam Current – Arc Off.

a typical signal on the R (D_3^+) collector with no arc; Fig. 4.4.6 shows simultaneous variations in both the R (D_3^+) and $R/3$ (D^+) beams with the arc on. Since the variations are essentially in phase, it is seen that this effect is of no consequence in breakup measurements using average values. However, it would appear that the effect might be significant in future diagnostic work on circulation of a trapped ion beam.

UNCLASSIFIED
ORNL-LR-DWG 42291

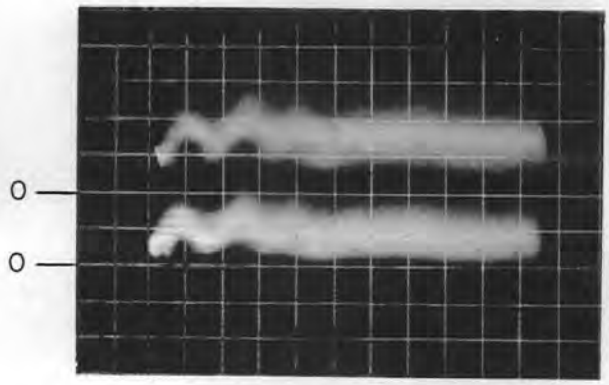

2 μsec PER HORIZONTAL DIVISION

UPPER TRACE – R BEAM
5 ma PER VERTICAL DIVISION

LOWER TRACE – R/3 BEAM
2 ma PER VERTICAL DIVISION

Fig. 4.4.6. Variations in R and $R/3$ Beam Currents – Arc On.

4.5 A MASS SPECTROMETRIC ANALYSIS OF THE CARBON ARC

R. V. Neidigh

Mass spectrometric analysis of the plasma surrounding the carbon arc has been made for the long arc in the long solenoid, and is being made for the short arc in the arc research facility. Apparatus for the same analysis in DCX-EPA is being constructed.

It should be emphasized that the data presented here are not the densities of the various ion species present in the carbon arc. At best a mass spectrometer yields only relative abundances. This analysis is further complicated by the intense radiation from the arc. The entrance slit to the mass spectrometer cannot exist in the arc but must be located in the plasma surrounding the arc. In addition this spectrometer extracts ions only from the immediate vicinity of its entrance slit, and it is not known how much its presence disturbs the plasma or the arc.

The motivation, however, is strong. The breakup of molecular ions is observed in the plasma surrounding the arc and can be shown experimentally to be independent of the radiation from the arc (see Sec 4.1.3). The electron density in this plasma can be determined experimentally by microwaves (see Sec 4.1.3). If charge neutrality is assumed and the mass spectrometer data believed to represent relative abundances of the ion species, then the average ion densities can be found. That this is only the average density is emphasized by the increasing evidence that there is bunching of the ions and electrons in the arc plasma (see Sec 4.4.1).

4.5.1 MASS SPECTROMETER IN THE LONG SOLENOID MACHINE

A mass spectrometer was installed at the midsection of the long solenoid. A schematic diagram of the instrument and the associated equipment is shown in Fig. 4.5.1. It was necessary to operate the arc off the axis of the solenoid to provide the necessary space for the mass spectrometer. The magnetic field on the axis of the solenoid is 6000 gauss maximum in the coils and 2600 gauss in the midsection. Completely satisfactory off-axis arcs were obtained by displacing the cathode from the solenoid axis and using an oversized anode. The arc was 67 in. long. Cathode diameter was $\frac{1}{2}$ in. Arc current was 250 amp. The collector of the mass spectrometer was $\frac{1}{8}$ in. wide, and it was driven back and forth over a 3-in. path by an automatic, constant-speed mechanism. The current to the collector was fed to a high-speed Bristol recorder.

Collector current as a function of position for a 3-kv accelerating potential and pressures of 2.0, 3.5, and 8.0×10^{-5} mm Hg, measured at the anode end of the solenoid, is shown in Fig. 4.5.2. C^{4+} and C^{+++} peaks are observed. The ratios of the C^{4+} total current (area under the curve) to the C^{+++} total current for the various pressures are:

Pressure (10^{-5} mm Hg)	Ratio C^{4+}/C^{+++}
2.0	1.7
3.5	0.7
8.0	0.3

A run with nitrogen peaks enhanced by bleeding nitrogen gas through the cathode to obtain a pressure of 3×10^{-4} mm Hg is shown also in Fig. 4.5.2.

Changing the accelerating potential puts other m/q arc components within the range of the probe mechanism. Scans at 2 kv yielded a peak which was not positively identified but may have been due to C^{++} or N^{++}. The ratio of the C^{+++} total current to the total current of this unknown was at least 10/1. Scans at 1 kv did not yield any peaks; it is possible that the spectrometer does not operate satisfactorily at accelerating potentials this low. Scans at 5 kv did not yield any evidence of C^{5+} or N^{5+}.

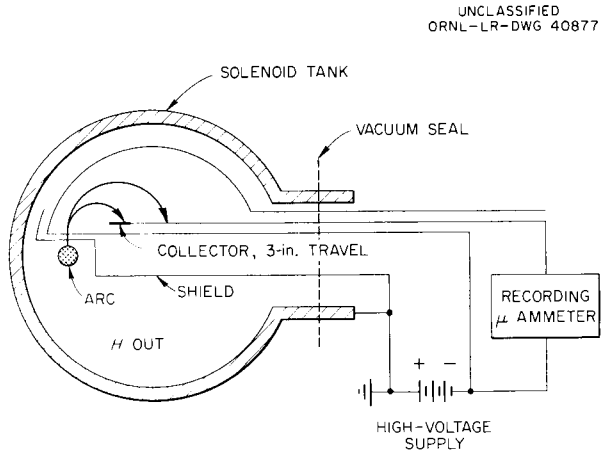

Fig. 4.5.1. Mass Spectrometer Installed in Carbon Arc Long Solenoid Machine.

4.5.2 MASS SPECTROMETER IN THE ARC RESEARCH FACILITY

The mass spectrometer in the Arc Research Facility is more versatile than that used in the long solenoid. The collector travel is 6 in., which for 5 kv accelerating potential and 3000 gauss magnetic field will include all the ion species which have m/q equal to or less than the C^+ ion. In addition, the distance from the entrance slit of the mass spectrometer to the edge of the arc can be adjusted during the run from 0 to $1\frac{1}{2}$ in. This makes possible an examination of the ion abundances as a function of the distance out from the arc.

The first data taken were for arc configuration similar to that used by Luce in the experiments to determine percentage breakup as a function of the distance from the arc (see Sec 4.1.1); that is, a flat cathode was used, $\frac{1}{16}$ by $\frac{5}{8}$ in. The arc current was 225 amp and the arc length varied from 4 in. at the beginning of the run to about 7 in. at the end. The data are plotted in Fig. 4.5.3.

The relative particle densities of the C^+ ions are plotted in Fig. 4.5.4 as a function of distance from the flat face of the arc as defined by the cathode shape. Field strengths of 3000, 4000, and 5000 gauss were used. Similar observations on C^{++} and C^{+++} are plotted in Figs. 4.5.5 and 4.5.6, respectively. The curves cannot be closely related to one another on the ordinate scale

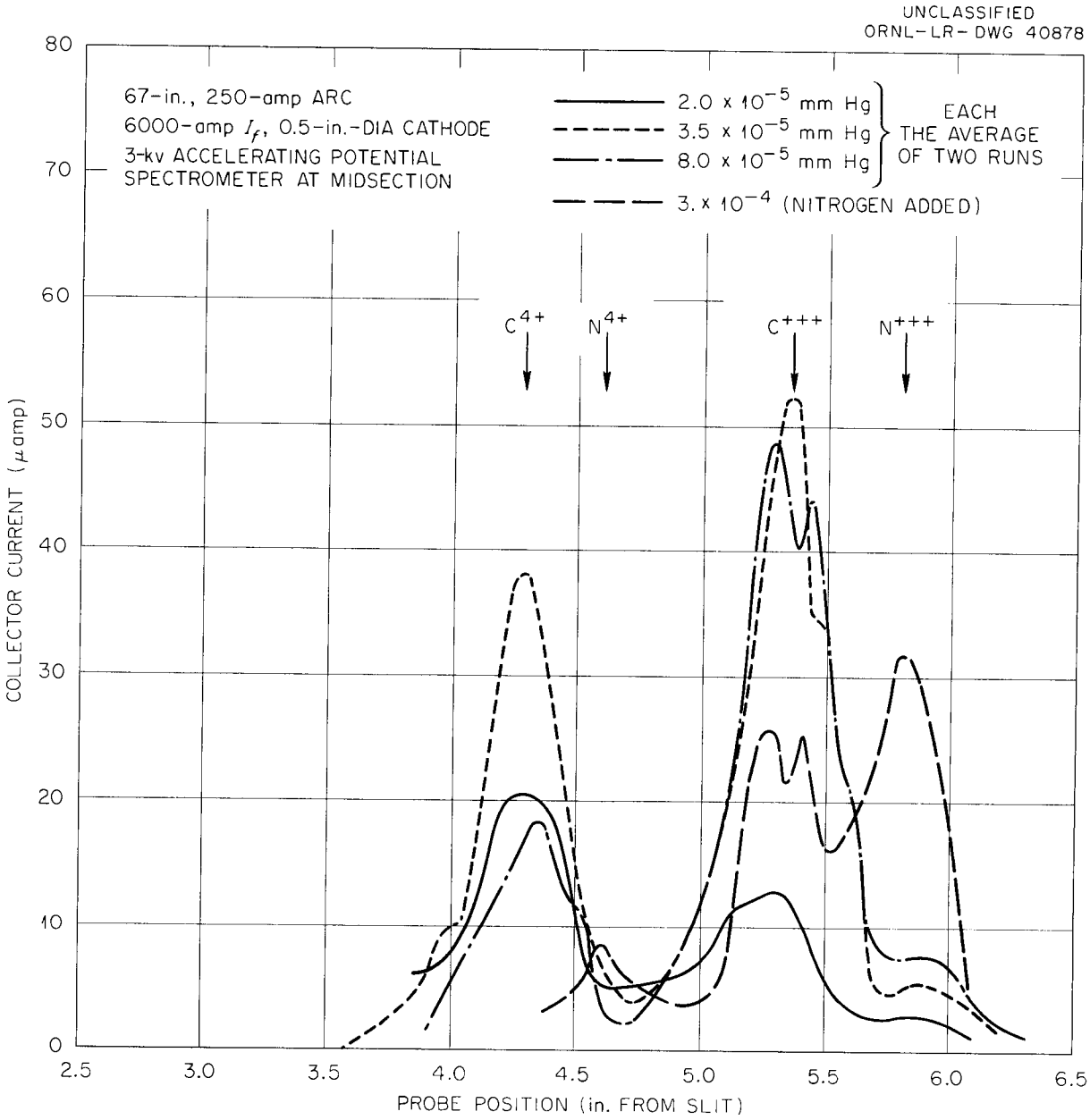

Fig. 4.5.2. Mass Spectrometer Data from the Carbon Arc Long Solenoid Machine. Note the depression of the C^{+++} and C^{4+} with the addition of nitrogen.

because the sampling efficiency of the slit of the mass spectrometer presumably varies for ions of different charge. (However, the slit is narrow compared with the Larmor diameter.) In addition, the accelerating potential of the mass spectrometer was increased at the higher magnetic field strengths to retain ion orbits of the same diameter.

Further data, taken at 3000 gauss with a hollow, round cathode $\frac{1}{4}$ in. in diameter and $\frac{1}{8}$ in. hole, are plotted in Fig. 4.5.7.

Two trends seem to be evident from the observations: (1) ions of low charge spread more widely than do ions of higher charge; (2) an increase of magnetic field reduces the spread.

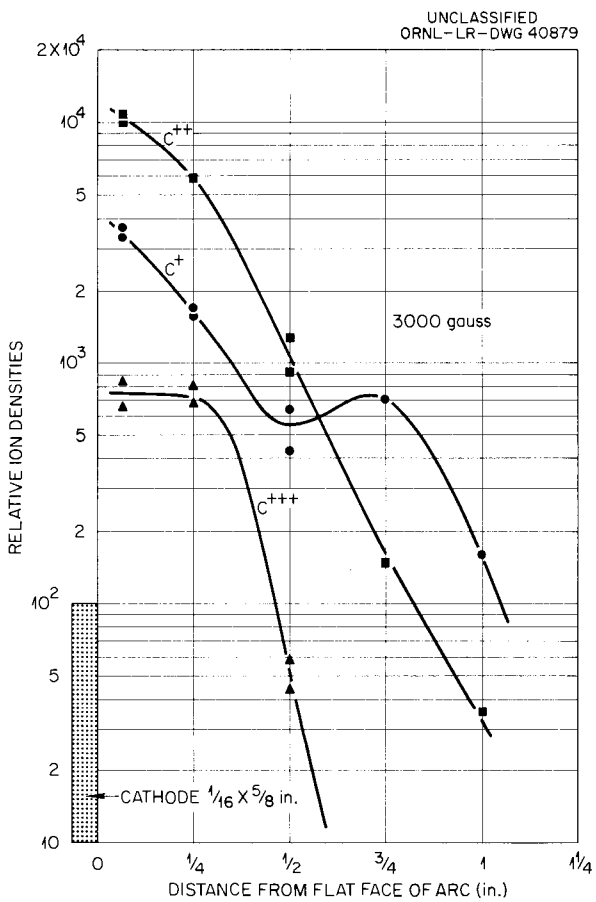

Fig. 4.5.3. Relative Ion Densities at Different Distances from the Flat Cathode Arc.

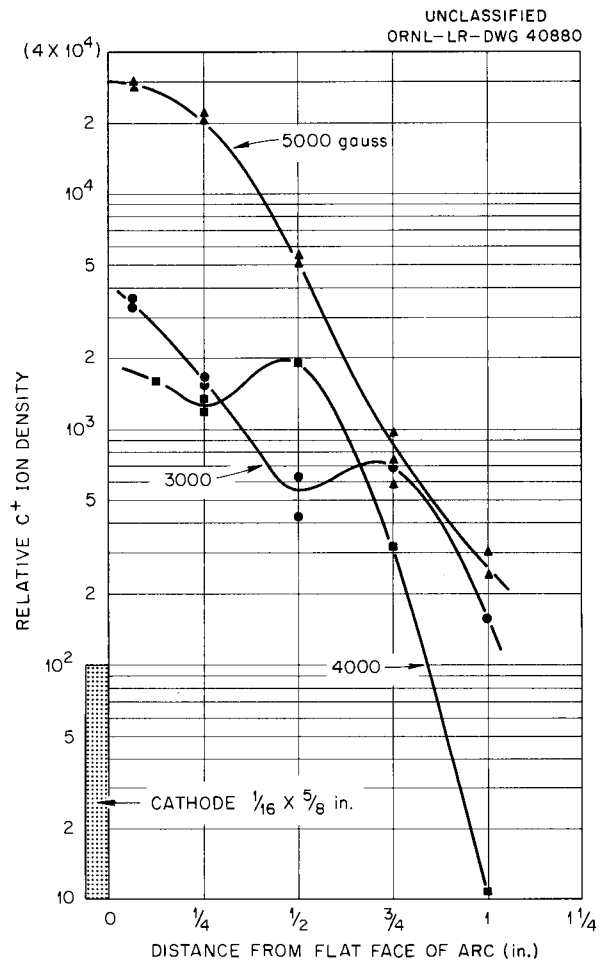

Fig. 4.5.4. C^+ Ion Distribution at 3, 4, and 5 kilogauss.

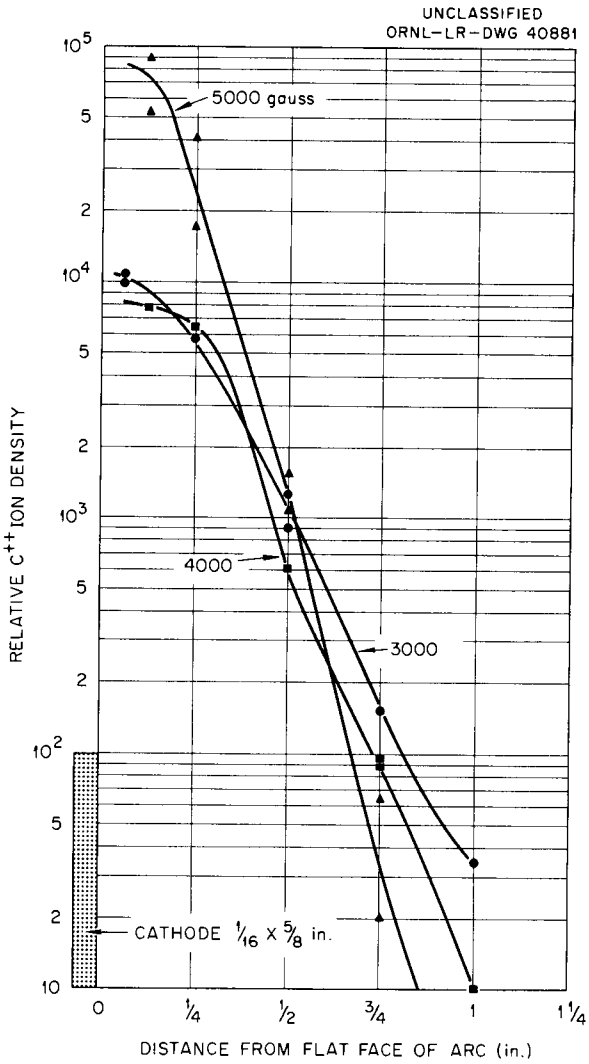

Fig. 4.5.5. C^{++} Ion Distribution at 3, 4, and 5 kilogauss.

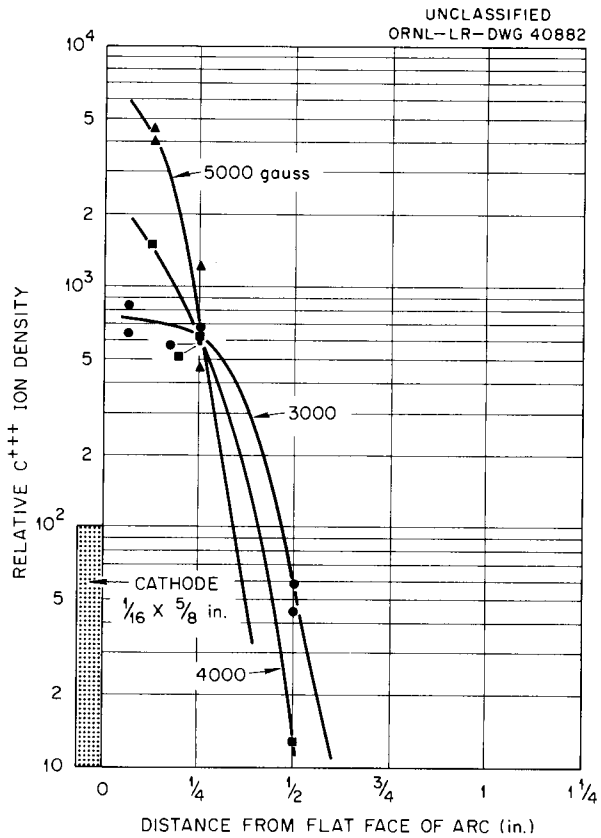

Fig. 4.5.6. C^{+++} Ion Distribution at 3, 4, and 5 kilogauss.

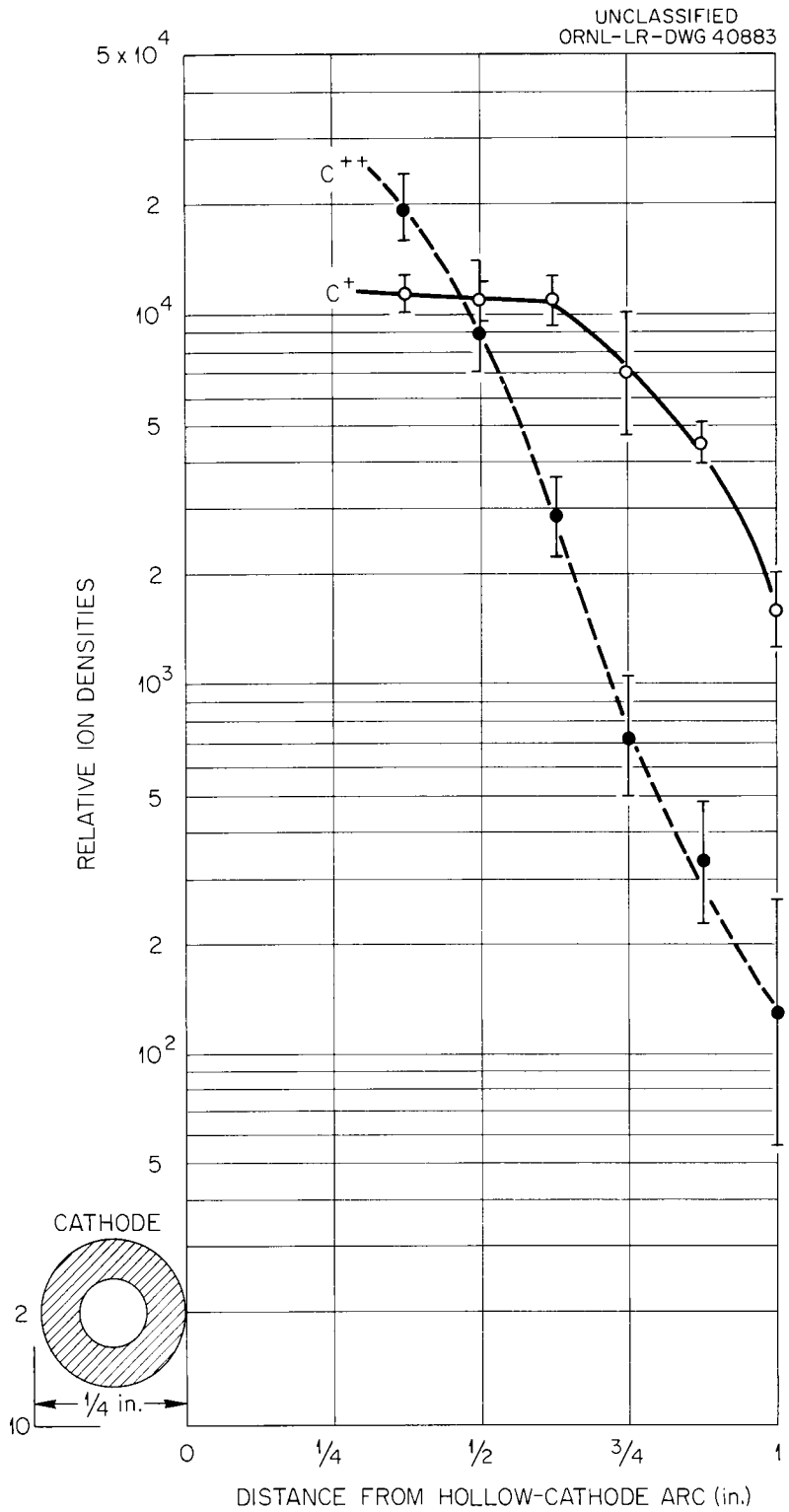

Fig. 4.5.7. Relative Ion Densities at Different Distances from the Round Cathode Arc.

4.6 ARC TRANSPARENCY MEASUREMENT

J. F. Potts R. E. Toucey P. M. Jenkins

Several experiments were performed with two short parallel arcs to determine the transparency of the vacuum carbon arc to its own radiation. These experiments were run in the calutron ion source research facility (Building 9735) making use of an arc assembly and a circular foil thermoelectric radiometer (CFR), both similar to descriptions previously given.[1]

The configuration used during these experiments is illustrated schematically in Fig. 4.6.1. The two arcs shared a common anode, but were operated from independent power supplies with individual gas feed and R-F welders to the respective cathodes for starting the arcs. Attempts to strike both arcs from a common supply met with failure.

The ¼-in.-dia cathodes were consumed rather rapidly. Arc length was approximately 4 in. at the beginning of a run and 6 in. at the end of a run. Originally, measurements were attempted with ½-in.-dia cathodes, but data were very inconsistent for reasons yet to be determined.

Radiometer readings were noted with only the transmitting arc on, with only the absorbing arc on, and with both arcs on. These readings were taken in all six possible sequences. Readings were lowered by as much as 50% toward the end of a run (longer arc). Figure 4.6.2 illustrates the transmission results obtained for constant current in the transmitting arc with varying current in the absorbing arc. The system parameters and method of computing per cent transmission are also shown in Fig. 4.6.2. The average of all data presented, disregarding absorbing arc current, indicates that the arc is 65% transparent. There was a suggested trend toward less transparency as absorbing arc current increased.

[1] J. F. Potts and C. H. Weaver, *Thermonuclear Project Semiann. Rep. Jan. 31, 1959*, ORNL-2693, p 45–50.

UNCLASSIFIED
ORNL-LR-DWG 40884

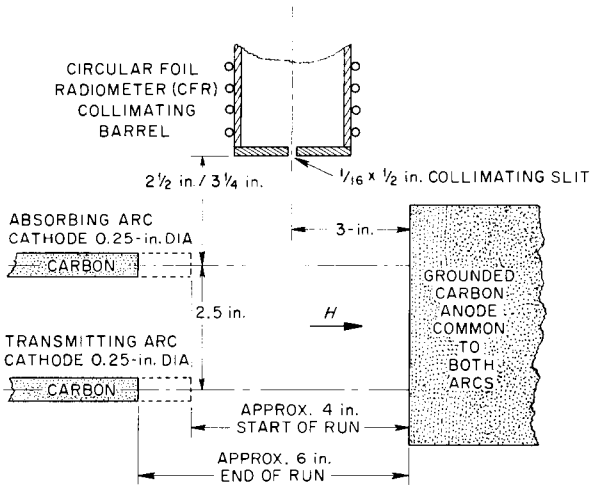

Fig. 4.6.1. Arc and Radiometer Configuration for Arc Transparency Measurement.

UNCLASSIFIED
ORNL-LR-DWG 40885

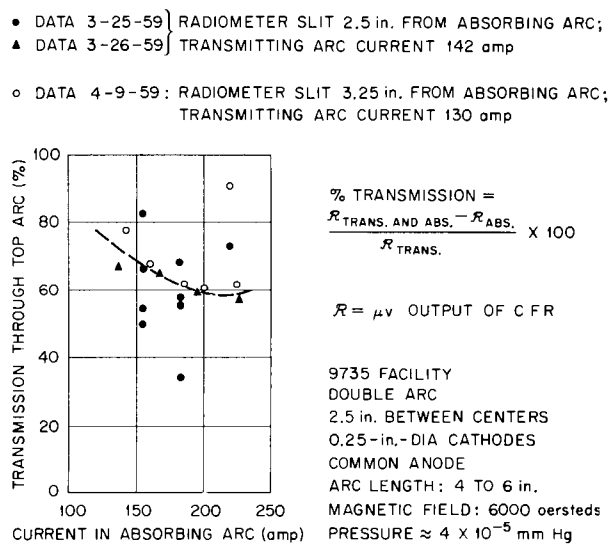

Fig. 4.6.2. Transmission of Arc Radiation vs Current of Absorbing Arc.

4.7 TOTAL RADIATION FROM A SHORT ARC AS A FUNCTION OF MAGNETIC FIELD STRENGTH

J. F. Potts R. E. Toucey P. M. Jenkins

Since the original data (ref 1, Sec 4.6) required normalization to constant current, other data have been obtained which verified the proportionality between total radiation (as measured by a circular foil radiometer) and collimating magnetic field strength. During the course of making the arc transparency measurements reported in the previous paragraph, the effect of magnetic field strength on radiated energy was again observed. These data are presented in Fig. 4.7.1. The two runs shown show the same slope but different zero-field intercepts. No known differences in experimental conditions were found to explain this difference.

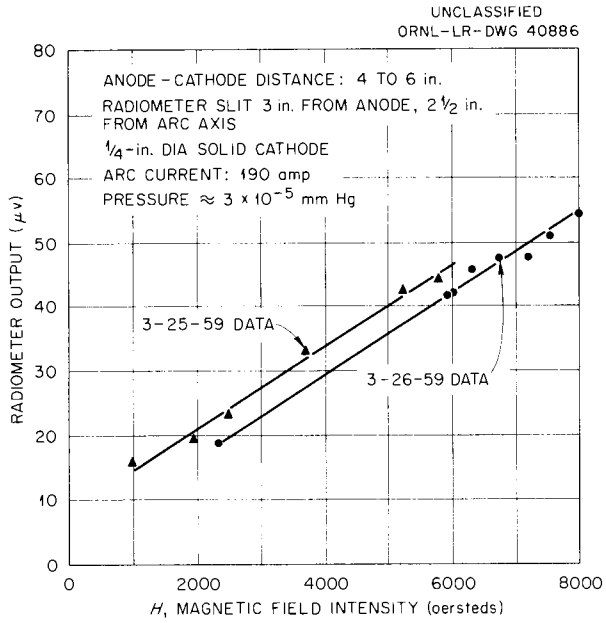

Fig. 4.7.1. Total Radiation from a Short Carbon Arc as a Function of Magnetic Field Intensity.

4.8 RADIATION FROM A LONG ARC AS A FUNCTION OF MAGNETIC FIELD STRENGTH

J. F. Potts M. R. Skidmore G. K. Werner R. E. Toucey

The Long Solenoid Facility (LSF) is shown schematically in Fig. 4.8.1, with a plot of axial variation in its magnetic flux density superimposed. The patch coil shown was not present during this experiment. A 72-in.-long carbon arc was run with a 4-in.-dia anode at position 30 in. A $\frac{1}{2}$-in.-dia solid cathode was at position 46 in. The arc current was maintained at 300 amp while the magnetic field was varied. The pressure remained unusually steady at a value of approximately 10^{-5} mm Hg during the experiment. The solenoid current was varied from 6500 to 2500 amp (the corresponding magnetic field strengths at the mirror maximum were 5800 and 2200 gauss, respectively).

Simultaneous measurements were made of total radiation with a circular foil radiometer and the intensity of the C^{+++}, 1548 Å line with a Seya spectrometer. Both instruments were monitoring a narrow transverse section of the arc at the

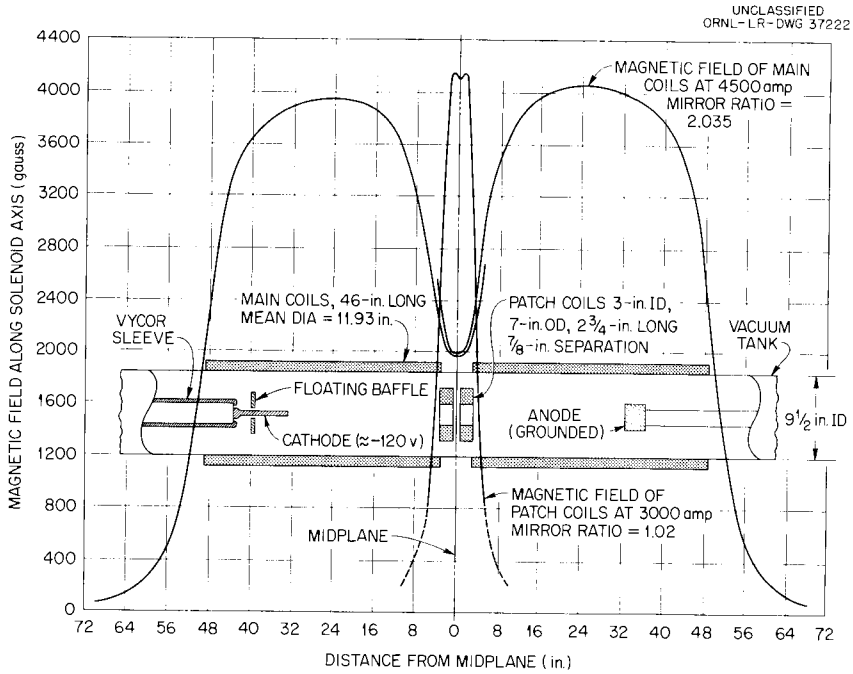

Fig. 4.8.1. Long Solenoid Facility (LSF).

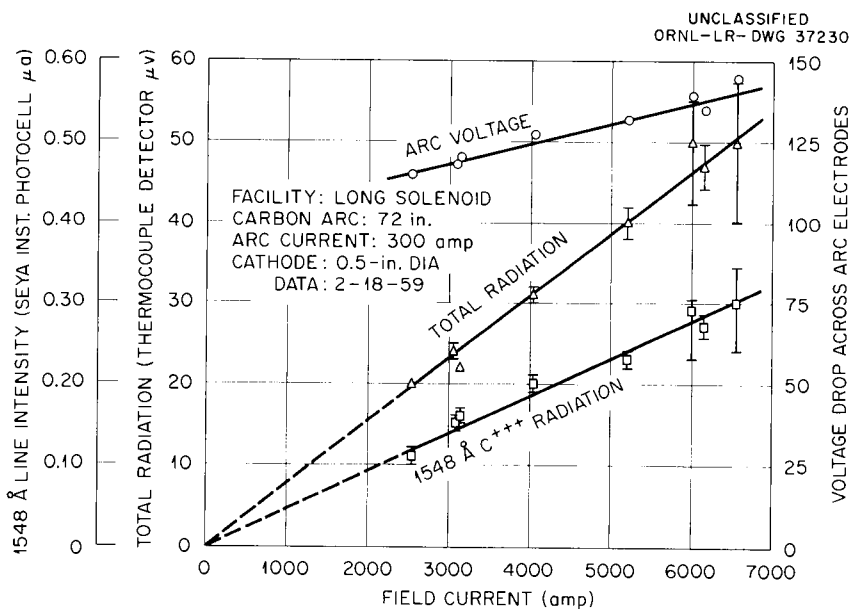

Fig. 4.8.2. Variation of Arc Voltage, Total, and C^{+++} 1548-Å Line Radiation with Magnetic Field.

midplane of the solenoid. The variation of total arc voltage was also monitored as a function of magnetic field strength. These results are shown in Fig. 4.8.2.

A linear relation is observed between radiation and magnetic field strength for a long arc, as was the case for a short arc. In the case of the long arc the relation extrapolates to zero radiation at zero magnetic field intensity, whereas the extrapolation for the short arc is to finite radiation at zero magnetic field intensity. We are, as yet, unable to explain the difference, much less give a full explanation for the linear relation.

4.9 EFFECT OF LOCAL VARIATION OF MAGNETIC FIELD STRENGTH ON RADIATION FROM A VACUUM CARBON ARC

R. E. Toucey P. M. Jenkins J. F. Potts

With patch coils inserted in the LSF tank as indicated in Fig. 4.8.1 of the previous section, the magnetic field was varied in the section of the arc that was being monitored by a circular foil radiometer, without disturbing other regions of the arc. The contribution of the patch coils to the total magnetic field is indicated in Fig. 4.8.1.

With a circular foil radiometer inserted under the patch coils and viewing the arc between these coils, information was obtained concerning the effect of this local variation of magnetic field on total radiation. The results of a typical run are shown in Fig. 4.9.1, wherein other pertinent data are also shown. Figure 4.9.2 shows the same data with total radiation plotted as a function of $1/H$. This illustrates that from around 2000 to

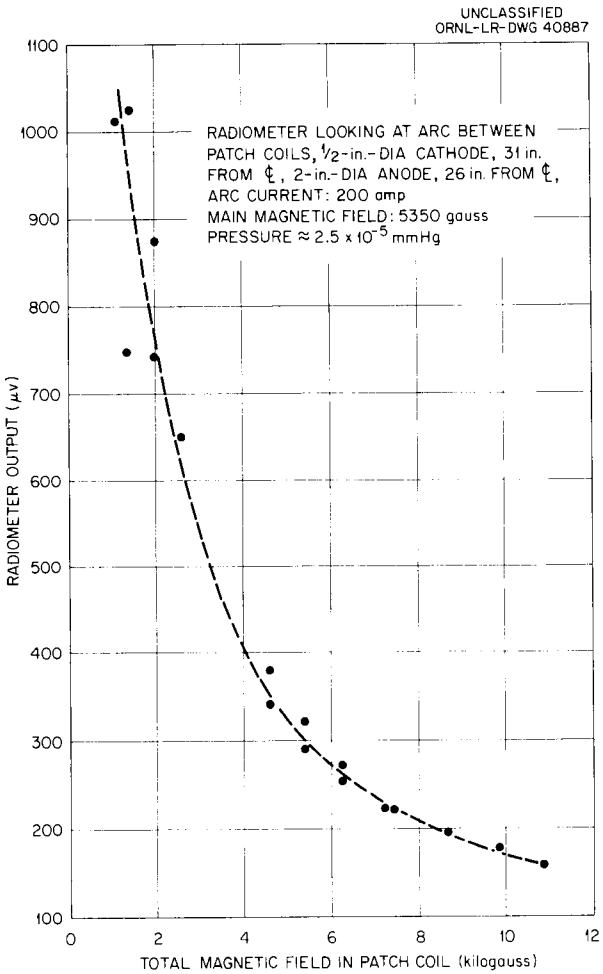

Fig. 4.9.1. Total Radiation as a Function of Local Magnetic Field at the Center of a Long Arc (Main Field Constant).

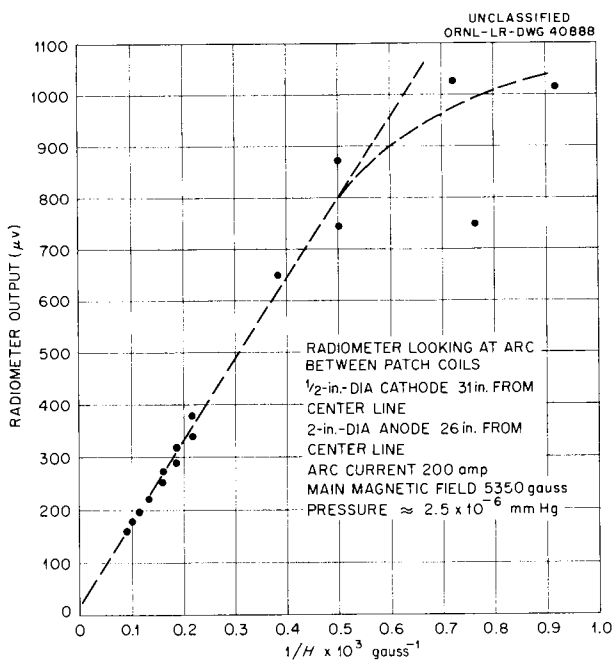

Fig. 4.9.2. Total Radiation vs Reciprocal of Local Magnetic Field at the Center of a Long Arc (Main Field Constant).

10,000 gauss local field, total radiation is proportional to $1/H$, for which we have as yet no good explanation.

In the hope of solving the paradox that radiation varies directly with total magnetic field but inversely with local magnetic field, two additional experiments were run making use of the patch coils. First, the cathode was moved into one of the patch coils with the anode in approximately the original position. The patch-coil current was varied with main solenoid current constant. The result of this run is shown in Fig. 4.9.3. Secondly, the anode was moved into one of the patch coils with the cathode in approximately the original position. The results with this configuration are shown in Fig. 4.9.4. Neither of these results indicates explicitly an explanation for either of the linear relations between magnetic field intensity and radiation at the arc center. The total arc length was reduced by a factor of 2 in these later experiments, but this reduction is not considered to be a serious factor. Furthermore, total radiation was monitored in the vicinity of the anode (electrodes as shown in Fig. 4.8.1) during changes of patch-coil current, and there was no noticeable effect on radiometer output.

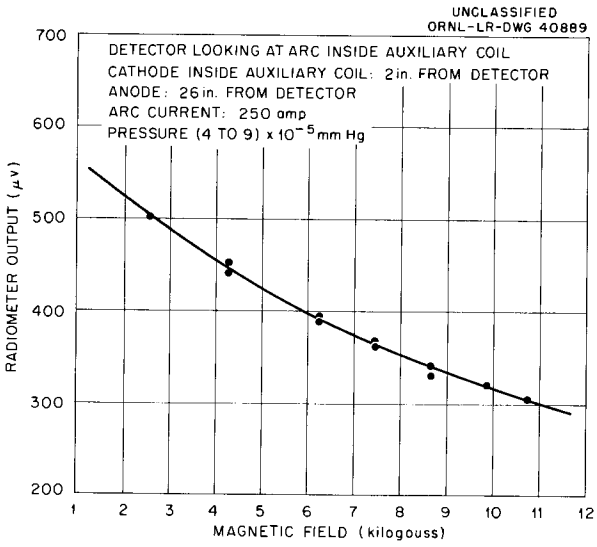

Fig. 4.9.3. Total Radiation as a Function of LSF Magnetic Field Variation in the Vicinity of the Cathode.

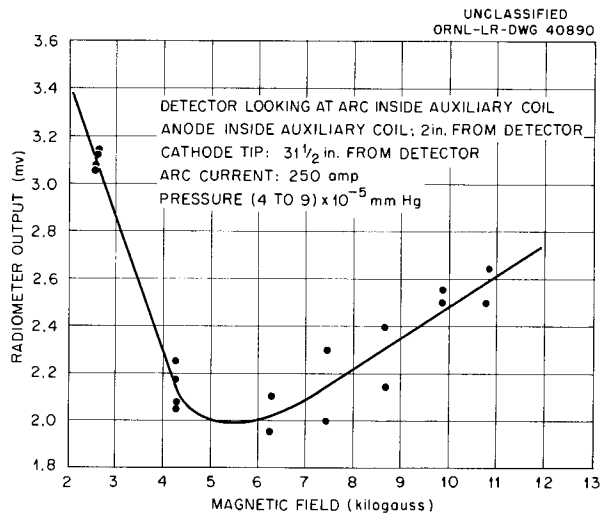

Fig. 4.9.4. Total Radiation as a Function of LSF Magnetic Field Variation in the Vicinity of the Anode.

4.10 ANODE WITHDRAWAL EXPERIMENTS

J. F. Potts
M. R. Skidmore
J. Dunlap
R. E. Toucey
G. K. Werner

The radiation from the center of a long vacuum carbon arc was observed as the anode was withdrawn into the reduced magnetic field at the solenoid end (Fig. 4.8.1). This was another of the series of experiments conducted to further understanding of the relation between the arc performance and magnetic field configuration. The total radiation was monitored with a thermoelectric radiometer and the radiation spectrum was resolved with the Seya spectrometer. Both instruments were monitoring a narrow transverse section of the arc at the midplane of the solenoid. The spectrum was scanned at each of several anode positions. Results of the average of a number of runs are shown in Fig. 4.10.1. The scaling factors for the Seya data are not known, so the relation between energy distribution of the various resonance lines and total radiation is arbitrary. The raw data were

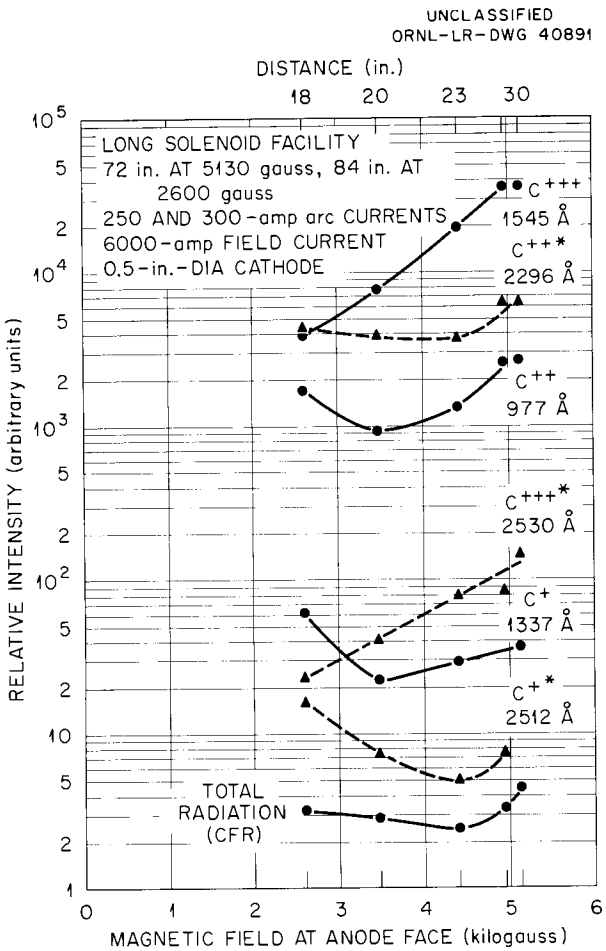

Fig. 4.10.1. Averaged LSF Anode Withdrawal Data.

corrected for differences in spectrometer slit widths and photocell sensitivity, but not for spectrometer efficiency as a function of wavelength. It should be noted that the total radiation goes through a minimum, as do all the recorded carbon resonance lines, except for the 1548 Å resonance line of C^{+++}, which indicates a continuous increase of intensity with anode-face magnetic field strength (this appears to be contrary to the results noted by Luce in Sec 4.2.1, Tables 4.2.1 and 4.2.2; however, explanation of the discrepancy will depend upon further analysis of the circumstances of the experiments).

As the anode is withdrawn into the region of a weaker magnetic field, the lines of force which the arc follows diverge. The arc strikes a larger area on the anode face and the anode hot-spot temperature is reduced. Consequently, less carbon is evaporated.

The anode hot-spot temperature was monitored with an optical pyrometer. It was observed that a small circular disk at the center of the anode spot was 20 to 40°C cooler than the outer edges. The edge temperature and the corresponding vapor pressure of carbon as a function of magnetic field intensity are shown in Fig. 4.10.2.

If the total effect of anode withdrawal were simply to starve the arc, these data of Fig. 4.10.1 would be contradictory to data on rotating and water-cooled anode experiments. However, anode withdrawal accomplishes more than just starving the arc; the arc length is certainly changed and other, more complicated factors may be present.

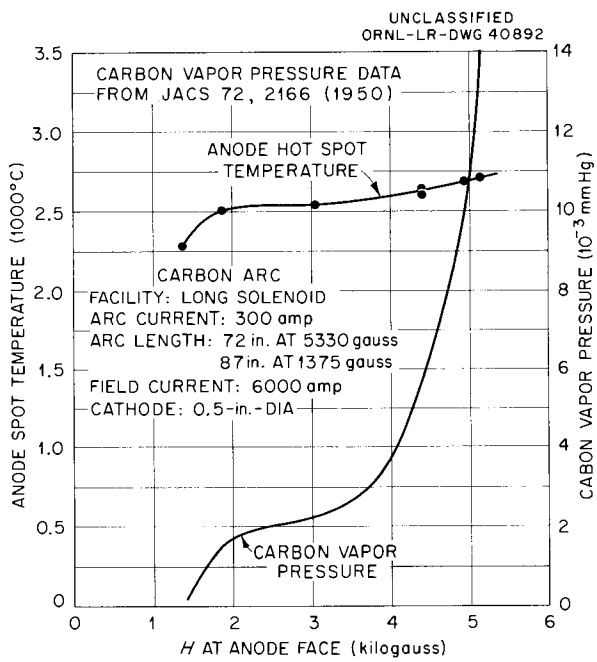

Fig. 4.10.2. Variation of Anode Temperature and Vapor Pressure in LSF Anode Withdrawal Experiments.

4.11 RADIATION AS A FUNCTION OF AXIAL POSITION ALONG ARC IN THE LSF

J. F. Potts R. E. Toucey

The variation of total radiation along a vacuum carbon arc as a function of axial position of the thermoelectric radiometer was observed over the anode region of an arc in the LSF (see Fig. 4.8.1) with only the main solenoid energized. The results are shown in Fig. 4.11.1. Similar results were obtained with additional collimation on the radiometer which yielded essentially the same curve but with reduced signal. These results are shown in Fig. 4.11.2. Also shown in Fig. 4.11.2 is the effect of adding current in the patch coils at the solenoid center. The change was within the spread of the data, and so the effect was considered negligible.

Some preliminary data have been obtained concerning the axial variation of radiation in the vicinity of the solenoid midplane. These results are shown in Fig. 4.11.3. The radiometer was not well collimated during this run, and mechanical difficulties prevented exploring the entire arc length. A later measurement of axial variation of radiation, wherein traversing difficulties had been overcome, is shown in Fig. 4.11.4, but poor vacuum during this run minimized the value of the data. It is noteworthy that the hump in the radiation curve at the LSF midplane (Fig. 4.11.4) corresponds to the decrease in magnetic field in that region (see Fig. 4.8.1), which is in agreement with the $1/H$ relation shown in Fig. 4.9.1.

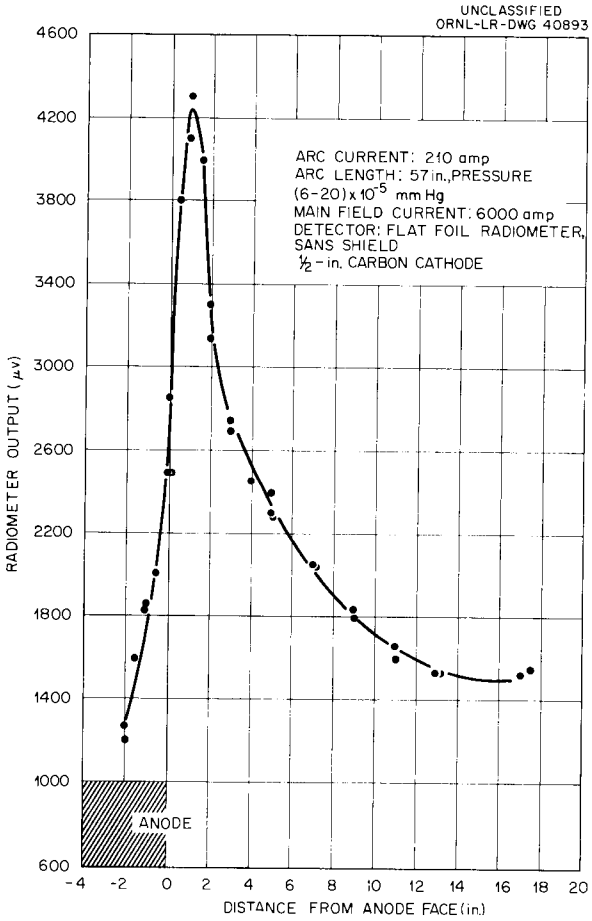

Fig. 4.11.1. Total Radiation vs Distance Along LSF Arc – First Run.

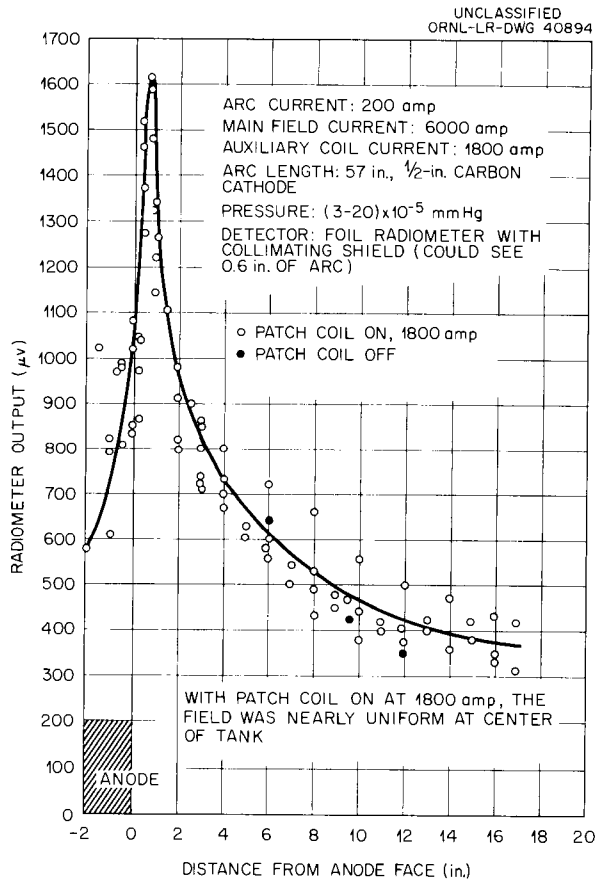

Fig. 4.11.2. Total Radiation vs Distance Along Arc – Second Run.

More complete data on axial variation of radiation in long arcs will be forthcoming as experimental difficulties are overcome.

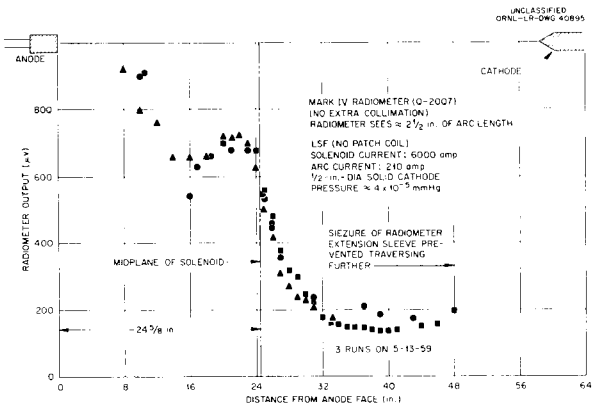

Fig. 4.11.3. Total Radiation vs Distance Along Arc – Third Run.

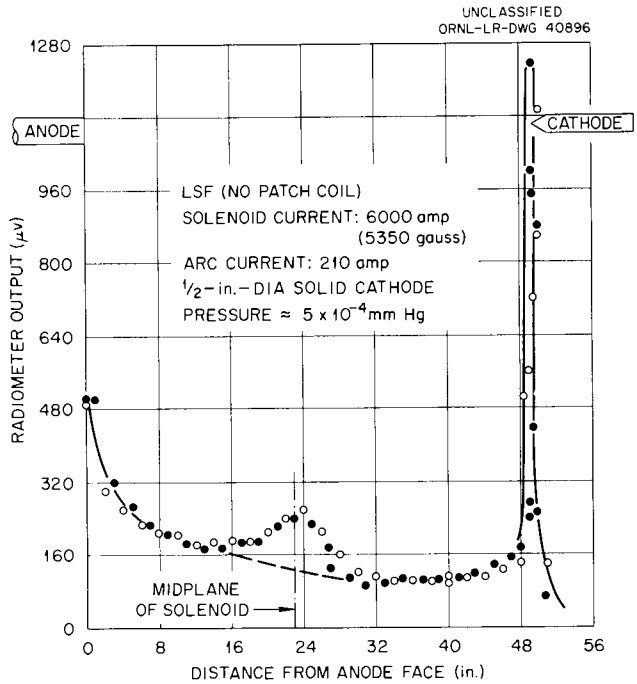

Fig. 4.11.4. Total Radiation vs Distance Along Arc – Fourth Run.

4.12 VOLTAGE vs CURRENT RELATION FOR VACUUM CARBON ARC IN LSF

J. F. Potts R. E. Toucey J. Dunlap

Typical current-voltage curves for a 74-in.-long arc in the LSF with 1-in.-dia cathodes and 4-in.-dia anodes are shown in Fig. 4.12.1. Curves are given for both solid and hollow (⅞ in. ID) cathodes. A similar curve for a ½-in. solid cathode is shown in Fig. 4.12.2.

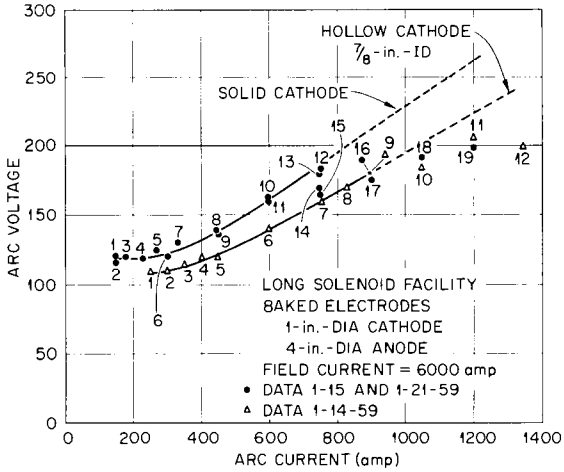

POINT NO.	PRESSURES (mm Hg) • DATA	△ DATA
1	3×10^{-5}	8×10^{-6}
2	4×10^{-5}	1×10^{-5}
3	5×10^{-5}	9×10^{-6}
4	3×10^{-5}	1×10^{-5}
5	5×10^{-5}	5×10^{-5}
6	3×10^{-5}	2.5×10^{-5}
7	5×10^{-5}	3.0×10^{-5}
8	6×10^{-5}	1.1×10^{-4}
9	3×10^{-5}	5.0×10^{-5}
10	3×10^{-5}	1.4×10^{-4}
11	1.4×10^{-4}	2.5×10^{-4}
12	3.0×10^{-5}	2.5×10^{-4}
13	3.4×10^{-4}	
14	2.6×10^{-4}	
15	2.2×10^{-4}	
16	4.0×10^{-4}	
17	6.0×10^{-5}	
18	1.4×10^{-4}	
19	2.0×10^{-4}	

Fig. 4.12.1. Arc Voltage–Current Relation for 1-in.-dia Cathodes.

In each case it was impossible to maintain an arc at current values below the lowest points shown for each case. Two features of these curves should be noted:

1. The arc voltage levels off at low current values.
2. High pressure depresses arc voltage at a given arc current.

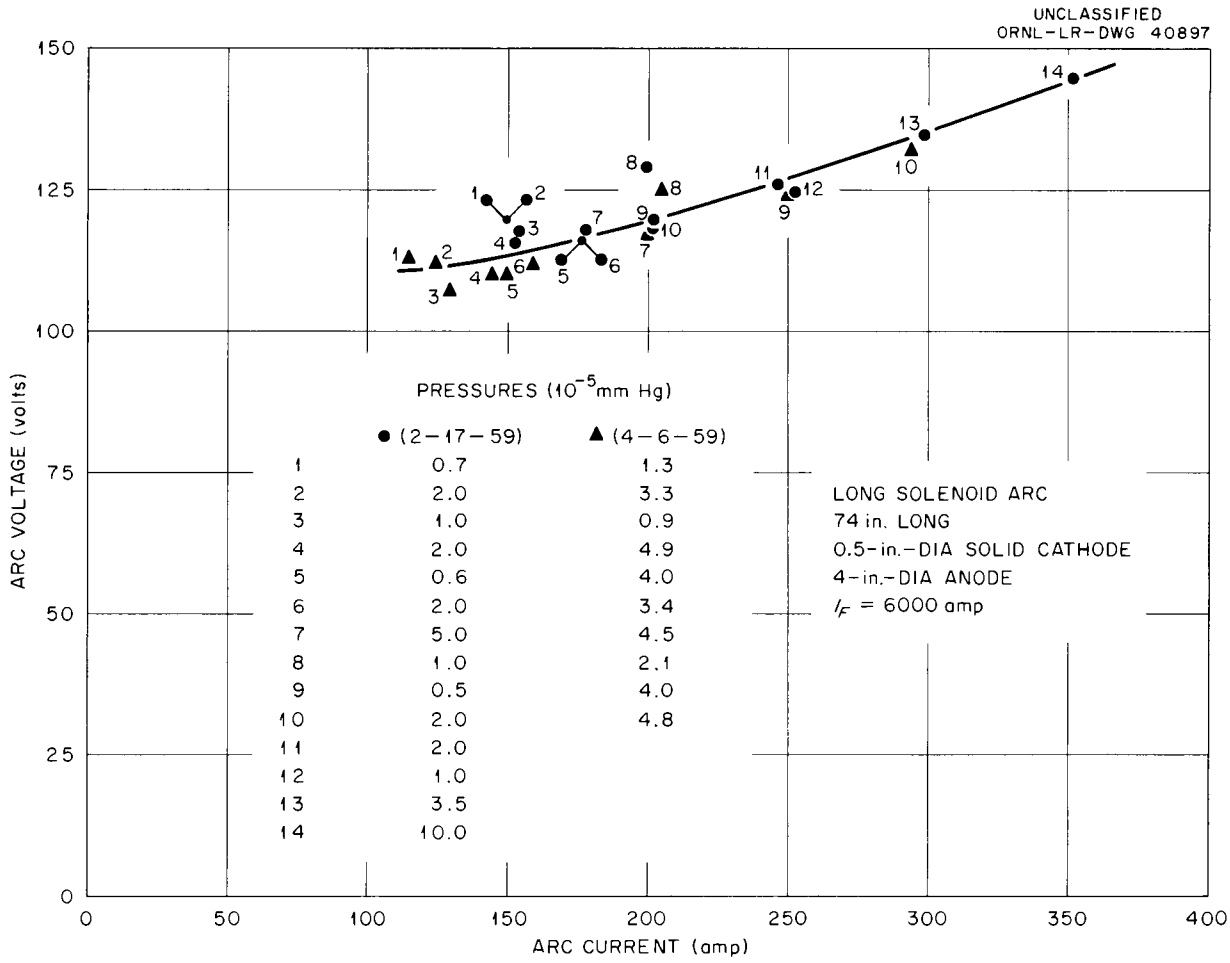

Fig. 4.12.2. Arc Voltage–Current Relation for ½-in.-dia Cathodes.

4.13 MICROWAVE DIAGNOSTICS OF A CARBON ARC AND HYDROGEN PLASMA

H. O. Eason, Jr.

4.13.1 CARBON ARC MEASUREMENTS

An experiment was performed in an attempt to measure the extent of the dense region of a carbon arc similar to that used in pre-DCX breakup experiments. This experiment was performed in a calutron track, and involved moving a 6-in.-long carbon arc through a focused 4-mm microwave beam. Attenuation was measured as a function of arc position, and the resulting attenuation profile then compared to that produced by known obstacles moving through the beam. Since a 4-mm beam cannot propagate through that region of the arc in which the electron density, n_e, is greater than 6×10^{13} electrons/cm^3, the attenuation profile should be similar to that produced by a conducting surface enclosing a like region. It is to be expected that this simple approximation is somewhat in error because of the probable absence of a sharp boundary at this density in the arc and also because of interference and mismatch resulting from the dielectric properties of the arc in surrounding regions of lower density. These effects would increase the attenuation in the boundary regions of the arc, and the apparent obstacle size, therefore, would represent more accurately a region of density greater than perhaps 3×10^{13} particles/cm^3 for which the effective index of refraction is ≥ 0.7.

The results of two runs made with the apparatus under different conditions are shown in Fig. 4.13.1. The arc cathodes were of $\frac{1}{16}$- by $\frac{5}{8}$-in. rectangular cross section with microwave propagation occurring along an axis parallel to the $\frac{5}{8}$-in. dimension of the cathode. This axis was at a constant distance of $4\frac{1}{2}$ in. from the arc anode. Also shown in Fig. 4.13.1 are the attenuation profiles produced by a carbon rod of cross section identical to that of the cathode as well as that produced by a copper surface of the cross section indicated. On the basis of these results, it was concluded that the density of this arc exceeded 3×10^{13} particles/cm^3 over a region extending $\frac{3}{4}$ in. from the projected cathode boundary. The results were essentially identical for both combinations of pressure and magnetic field. Similar measurements at lower frequencies are anticipated with this apparatus if the focusing of the lenses proves adequate. The combination of measurements is then expected to define the density profile of the arc.

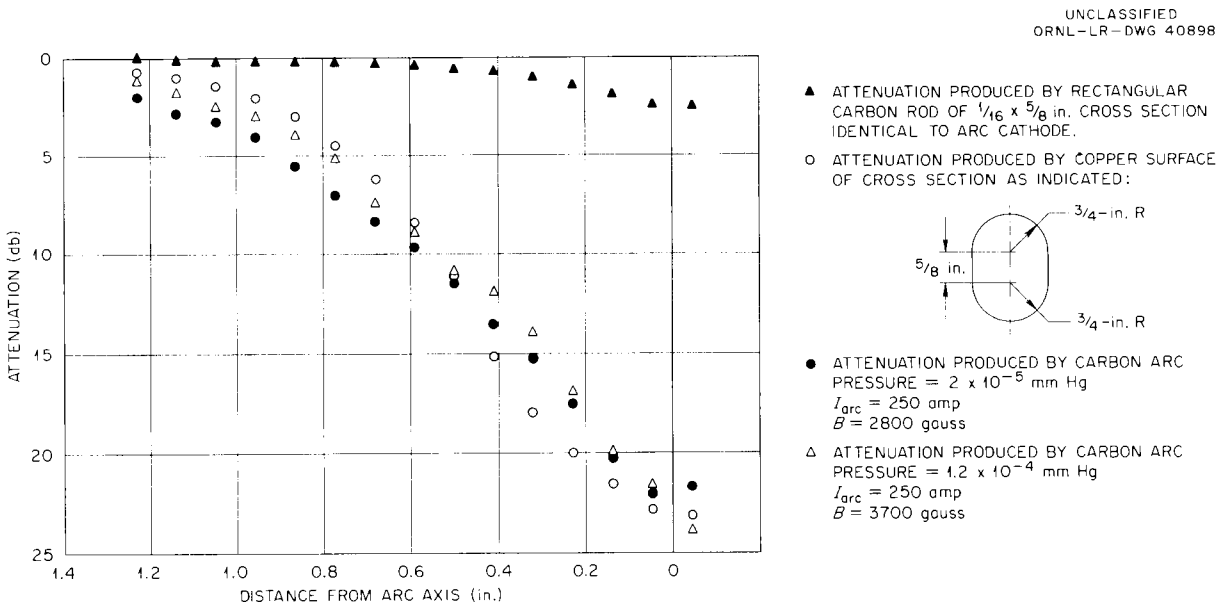

Fig. 4.13.1. Attenuation vs Position for Various Obstacles Moved Through a Focused 71.4-kmc Microwave Beam.

No attempts to obtain a more accurate measure of the average density of the carbon arc were made during this period due to lack of availability of the necessary components for measuring phase shift at 140 kmc. It is anticipated that these components will become available commercially in the near future. An attempt was made to produce power at 210 kmc using a beyond-cutoff waveguide filter to remove the 140-kmc output of the crystal multiplier; however, the resulting output was only 7 db above noise when operating directly into a detector, and was therefore insufficient for making transmission measurements on the arc.

A 2-mm crystal detector of construction similar to the crystal multiplier[1] was fabricated and tested during this period. Its sensitivity when adjusted was approximately 10 db above that of the commercial 4-mm crystal and taper combination used previously. The increased detection sensitivity will provide a much greater dynamic range for the 2-mm system.

4.13.2 DCX PLASMA MEASUREMENTS

Further attempts were made during this period to determine the density of the trapped hydrogen plasma ring in DCX using the 24,000-Mc interferometer. Again no phase-shift indications were observed under normal operation even though the minimum density which could be detected was approximately 1×10^{10} electrons/cm^3. Density measurements were then attempted at higher-than-normal pressures using an argon leak to increase the pressure in DCX. First indications of a density of 1×10^{10} electrons/cm^3 were obtained when the liner pressure reached 4×10^{-5} mm Hg, and the density continued to increase with increasing pressure to an estimated 1×10^{12} electrons/cm^3 at a pressure of 5×10^{-3} mm Hg. This measurement was then repeated with the arc turned off, using breakup on the background gas to produce ions which could be trapped. The results of density measurements for this condition were identical to those obtained with the arc on.

Further attempts to obtain a quantitative measure of density as a function of pressure and background gas using gas breakup were unsuccessful due to excessive heating of the interferometer test path from the disk of H^+ ions. It was also ascertained that when the arc was turned on in the absence of an input beam, an immediate phase shift occurred, along with a marked increase in the observed noise level. These effects were found to be due to changes in the standing-wave pattern in the liner caused by the presence and random motions of the arc itself.

This knowledge prompted the design of an improved interferometer test path, which is illustrated diagramatically in Fig. 4.13.2. This apparatus consists of a pair of horn-fed, 5-in.-dia

[1] H. O. Eason, *Thermonuclear Project Semiann. Rep. Jan. 31, 1959*, ORNL-2693, p 38.

UNCLASSIFIED
ORNL-LR-DWG 40899

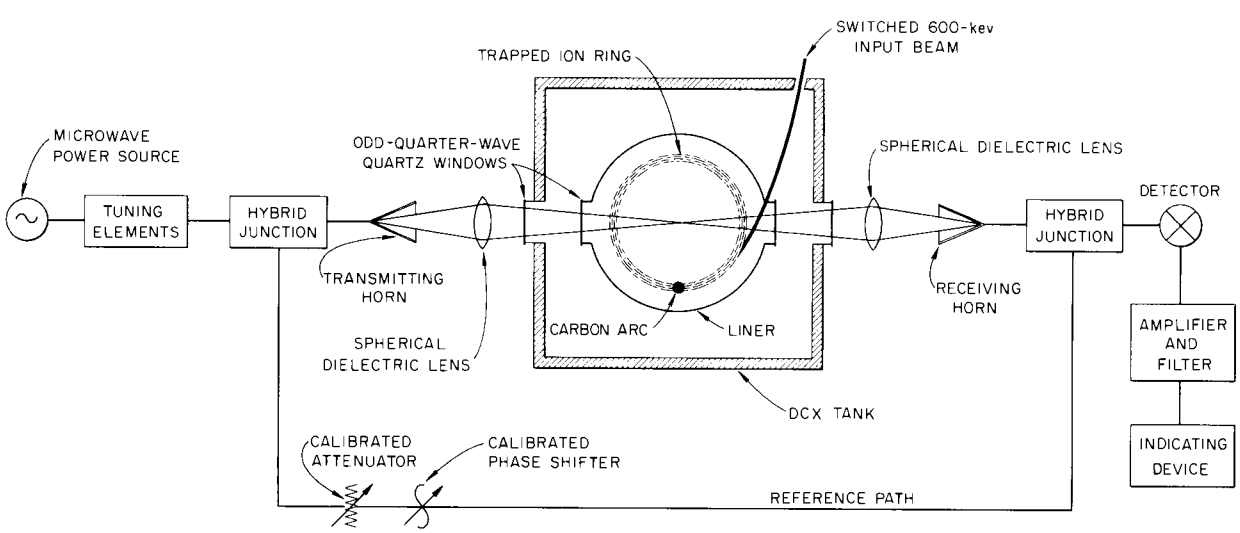

Fig. 4.13.2. Microwave Interferometer for DCX Density Measurements.

polystyrene lenses mounted on opposite sides of the DCX tank. The lenses are corrected for thickness and spherical aberration. Odd-half-wave quartz windows provide access for transmission across the entire differential vacuum system of the machine. The microwave beam thus passes through the trapped ring twice, doubling the sensitivity in this respect over that of the unit previously used. In addition, the focusing effect greatly increases the efficiency of transmission, thereby reducing the amplitude of standing waves inside the machine and the effect of the carbon arc thereon. This apparatus offers no obstruction which could interfere with spreading in the z direction or density buildup of the trapped ring. Since the horns and lenses are rigidly attached to the sides of the DCX machine, thermal and vibrational noise and drifts should be largely eliminated. Also, since the microwave beam is focused at the center of the trapped ring, and this point lies outside the plasma itself, no difficulty is anticipated from the 180° phase shift which occurs here.

The system is designed to operate in the 8-mm band rather than the 1.25-cm band to take advantage of the better focusing and beam confinement obtainable at the shorter wavelength. Also, if increased power input is necessary, the system can be powered by the Elliot B579 20-w klystron. The penalty paid in loss of sensitivity in using a higher frequency is small, being proportional to the frequency ratio for a given system, assuming a given minimum detectable phase shift.

This system has been constructed and is presently undergoing bench tests prior to installation and operation on the DCX machine. Focusing appears to be satisfactory, and further tests will be made to determine the minimum detectable phase shift using synchronous detection in conjunction with switching of the DCX ion beam input.

4.14 VACUUM PROPERTIES OF THE CARBON ARC

R. J. Mackin, Jr.

The attainment of a pressure near 10^{-8} mm Hg in the presence of a carbon or other energetic arc is essential to the achievement of burnout with deuterons in DCX in its present form. The development of a system in which this is possible may have ramifications for the thermonuclear field as a whole, since the radiation from a 300-amp carbon arc is comparable to or greater than that expected from the plasma in a working reactor.

Between March 5 and June 3, 1959, the PPF[1] (PIG-Pump Facility) was used for experiments whose aim was the determination of the base pressure attainable in the presence of the carbon arc. This program has since been temporarily set aside in favor of development work on a hydrogen gas arc, so what is reported here will be essentially a progress report on an incomplete experiment, one which is still in a fairly unrefined form. All the conclusions drawn from the data are therefore tentative, and some may be expected to be wrong.

For these experiments, the PPF was operated as a three-region vacuum system (Fig. 4.14.1). The central region was pumped by two liquid-nitrogen-trapped 10-in. oil diffusion pumps with a combined speed of 1000 liters/sec.[1] Each end region was pumped by a trapped 6-in. pump with a speed of 250 liters/sec. In addition, during arc operation, the arc constituted an ion pump in the central region[2] (feeding virtually all of its gas output into the cathode region) and as a surface pump in the cathode region. The total arc length was 3 ft, with 2 ft in the central region. The arc was operated off-axis.

[1] *Thermonuclear Project Semiann. Rep. Jan. 31, 1959*, ORNL-2693, chap. 4.

[2] R. J. Mackin, Jr., *Controlled Thermonuclear Conference Held at Washington, D.C., Feb. 3–5, 1958*, TID-7558, p 331.

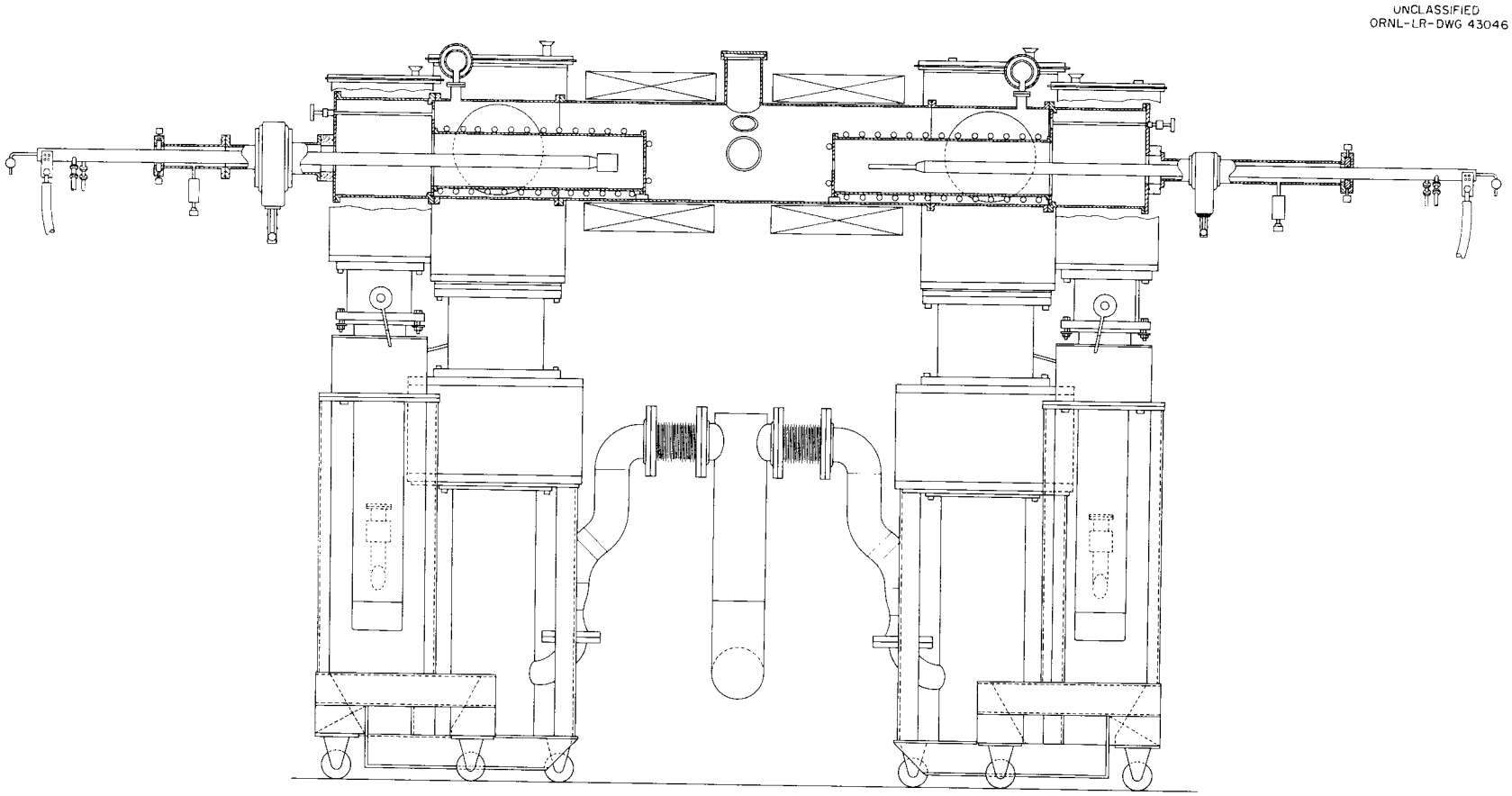

Fig. 4.14.1. PIG-Plate Facility – Side Elevation.

A brief list of certain properties of the arc may be useful for giving some perspective to the descriptions of experiments to follow. In the PPF magnetic field (2.5 kilogauss, midplane; 5 kilogauss maximum) the arc was customarily run at 300 amp, which required between 120 and 130 v, depending upon the state of the anode crater and upon the baffle configurations separating the respective regions. The dynamic resistance was 0.1 ohm. The electrode temperatures at the operating points were about 2700°C (anode) and 2400°C (cathode).[3]

The arc emits hard ultraviolet radiation at a rate which is customarily given as 300 w/in. based on a measurement at one point. Recent data,[4] however, reveal a considerable variation along the arc length. Furthermore, black-body radiation from the electrodes and other obvious forms of energy consumption can account for less than 10% of the input power; hence the average value might be closer to 900 w/in. For 8-ev photons (corresponding to the resonance radiation of C IV, believed to be the dominant component of the radiation), this amounts to 7×10^{20} photons per second per inch.

The problem of achieving an ultrahigh vacuum in the presence of the arc is mainly that of overcoming the gas-evolving effects of the radiation, but whether what is involved ultimately is merely the surface temperature of the walls or direct atomic desorption by individual photons cannot yet be stated.

The experiments reported here all involved the active participation of R. M. Warner and C. Michelson. Considerable assistance was given by R. A. Gibbons, C. W. Wright, and T. F. Rayburn.

4.14.1 MEASUREMENTS OF ARC AND SYSTEM PARAMETERS

The most noteworthy result of the program to date has been the achievement of a pressure of 5.5×10^{-8} mm Hg in the presence of a 250-amp carbon arc. This pressure was reached after 17 hr of intermittent operation, spread over four days, during which time the system was held under vacuum. Details of this extended arc run will be given in the next section.

A few relevant results of experiments leading up to it will be given here. The letters a, c, and k will refer to the anode, center, and cathode regions, respectively. The adjoining regions, in most experiments, were connected by openings (1.5-in.-dia) whose conductance in the absence of the arc was 130 liters/sec.

Pumping Speeds for Three PPF Regions

By comparing pressures with various pump valves open and closed, the arc-pumping speeds, S, of the individual regions could be determined relative to the diffusion pumps. The results, in liters/sec, for the residual gas in the system at 10^{-6} mm Hg (assuming diffusion pumping speed equal to that for nitrogen) are:

$$S_a = 450 \ ,$$

$$S_c = 2500 \ ,$$

$$S_k = 150 \qquad \text{(all valves closed).}$$

The pumping in the cathode region is (ultimately) by adsorption, although ionization and/or dissociation in the arc is believed to be an initial step in the process. This assertion is based on the observation that, for measured amounts of input gas (e.g., nitrogen), S_k is a factor of 3 to 5 higher when the gas is fed in through the cathode itself than when it is fed in through a valve at the chamber wall.

For argon, S_k was found by following the rate at which the pressure decreased after it had been raised by the addition of a small amount of argon gas. The figure was

$$S_k = 2 \text{ liters/sec} \ .$$

Ratio of Conductance to Pumping Speed

By comparing pressure increments in adjoining regions, the ratio of conductance, C, to pumping speed, S, has been obtained for several gases. For instance,

$$C_{kc}/S_c \text{ (argon)} = 3 \times 10^{-3} \ ,$$

$$C_{ac}/S_c \text{ (argon)} = 3 \times 10^{-2} \ ,$$

$$C_{kc}/S_c \text{ (nitrogen)} = 7 \times 10^{-4} \ ,$$

$$C_{ac}/S_c \text{ (nitrogen)} = 7 \times 10^{-3} \ ,$$

$$C_{kc}/S_c \text{ (deuterium)} = 7 \times 10^{-3} \ ,$$

$$C_{ac}/S_c \text{ (deuterium)} = 1.7 \times 10^{-2} \ .$$

[3] J. L. Dunlap, private communication.

[4] J. F. Potts and R. E. Toucey, private communication; also *Thermonuclear Project Semiann. Rep. Jan. 31, 1959*, ORNL-2693, sec 2.6.

The nitrogen and deuterium data were taken with the center region pumped by the arc alone. All the data were found to be only moderately reproducible.

Experiments suggest that the effective conductance of an aperture may be sharply diminished by the presence of a strongly ionizing arc passing through it. The order of magnitude difference between the anode and cathode conductances quoted above is interpreted as indicating that the mean electron energy in the arc is lower in the region 6 in. away from the anode than in that 6 in. away from the cathode. If this is true, however, the observed pumping speed in the anode region (30% of which may be attributed to conductance into the center region) is higher than might be expected from ionization pumping alone.

Pressure Bursts

During one run it was noticed that spontaneous pressure "bursts" in the anode region were reproduced in the center region. From the relative amplitudes of the pressure changes, it was possible to calculate the C/S for the gas of which these bursts were composed. For a 1.5-in. hole in the partition dividing the two regions, it was found that

$$C_{ac}/S_c \text{ (burst)} = 1 \times 10^{-1} \ .$$

When this hole was replaced by a 1.38-in. tube 3 in. long which protruded into the central region and which theoretically should have reduced the conductance by a factor of 4, the result was

$$C_{ac}/S_c \text{ (burst, tube)} = 5 \times 10^{-2} \ .$$

The indicated attenuation factor is thus 0.5. The difference from the theoretical value may be experimental error or possibly the result of "beaming" of the burst gas through the aperture. There is thus no evidence of attenuation by ionization out to 9 in. from the anode.

Effect of Oxygen on Pressure. – Attempts to measure C/S for oxygen were complicated by its interactions in the vacuum chamber. When oxygen was bled into the cathode region, p_k rose quickly to a near-constant value, while p_c showed a quick rise followed by one with a mean time of about 1.5 min. Simultaneously, the arc voltage decreased from 130 to 117 v. The apparent value of C_{kc}/S_c (oxygen) increased from 1×10^{-2} to 3.5×10^{-2}. When the gas bleed was cut off, the pressure decay showed a mean time of 1.5 min.

The pressure-burst records were examined and many of the bursts found to have a 1.5-min time constant associated with them. It was concluded that oxygen was very likely a major constituent of these bursts.

It was also noted that when oxygen was bled into the anode region of the tank in the vicinity (within 18 in.) of the RG-75 ionization gage the gage's emission dropped immediately by a factor of 5. When oxygen was bled in near the anode itself (separated from the gage by a 24-in.-long tube coated with evaporated carbon), this did not happen. Nor did any of the other gages in the system show emission anomalies during oxygen bleed experiments. The inference may be drawn that conversion to some gaseous oxide of carbon occurs with high efficiency in the anode chamber.

EXTENDED ARC-RUN EXPERIMENT

Procedure

The extended arc experiment which resulted in pressures below 10^{-7} mm Hg will be described in some detail. The pressures were monitored by two ion gages on the central region and one on each end region. A third gage on the central region, whose collector electrode was partly exposed to the arc, was operated, filament off, as a phototube. Photoelectron currents ranging between 0.2 and 1.5 μamp gave a continuous measure of the arc's radiation intensity. While the spectral sensitivity of such a device makes its use open to question, it was found that a fair over-all correlation existed between its readings and the temperature of the chamber wall, a more direct but less immediately responsive indicator of the radiation intensity.

The chamber was not baked before the run, and initial pressures (in units of 10^{-6} mm Hg) in the three regions were

$$p_c = 0.72 \text{ and } 1.5 \ ,$$

$$p_a = 3.2 \ ,$$

$$p_k = 2.2 \ .$$

The nitrogen traps were filled after 2 hr of arc operation and kept filled thereafter. After 7 hr of arc operation, the arc-off pressures (in units of

10^{-8} mm Hg) were

$$p_c = 1.1 \text{ and } 2.4 \ ,$$

$$p_a = 8.1 \ ,$$

$$p_r = 7.3 \ .$$

The p_c values are equal to the lowest which have been achieved by a 300–400°C bakeout with the arc fixtures in place.

The operation of the arc was imperfect for a number of reasons. The magnetic field strength was marginal for operation under a less than ideal configuration, leading to arc instability or extinction when an overly deep anode crater was made or when the arc column was too close to a baffle edge. The cathode was not aligned along a magnetic field line, so that as it burned back the arc's position changed. In the central chamber this resulted in less intense radiation on the nearest part of the wall (about 2 in. away at the closest point) and at the anode it resulted in a gradual burning along the side of the anode crater. The cathode was customarily moved forward 1 in. at the end of every half hour (roughly the burning rate). After every 2 or 3 hr, the anode was shifted so that a new crater was begun. The rate of anode burning was found to be just 1 in./hr.

After 5 to 7 in. of cathode consumption and/or the completion of 4 anode craters, it was necessary to replace the electrodes. This was done through air locks so that the vacuum was maintained.

Since some runs were terminated by arc instabilities, the entire operation consisted of a series of runs varying from 30 min to 3 hr 45 min in length. These were separated by intervals varying from a few minutes to four days.

The electrodes (National Carbon Company grade ATJ) were prepared after machining by baking for 12 hr in a chlorine atmosphere at 1400°C (2600°C would have been preferred) and for 4 hr in vacuum at 1000°C.

Experimental Results

The pressure records were somewhat irregular. In addition to the usual "noise" which ranged in amplitude from 2 to 20% of the average reading, there were pressure pulses or steps associated with each electrode adjustment and occasional pulses (varying in size up to several times 10^{-5} mm Hg) associated with erratic arc behavior. Some of the latter decayed in a few seconds; others required as much as 20 min for their effects to disappear at low pressures.

In spite of these excursions, it was possible to make several correlations between averaged pressure, radiation, and temperature data. The relationships varied from run to run but were fairly consistent within a run. The following features give an idea of the characteristic pressure pattern and permit some inferences regarding wall cleanup.

Pressure Record. – When the arc was struck for the first run (using nitrogen as the striking gas), the pressures rose to several tenths of a micron but began to drop quickly. After about 30 min they began to follow an exponential curve with about 60 min required for the pressure to drop by ½. At the time the new slope was established the pressures (in units of 10^{-6} mm Hg) were

$$p_c = 1.5 \text{ and } 2.5 \ ,$$

$$p_a = 9 \ ,$$

$$p_k = 7 \ .$$

In subsequent runs, the time to settle into the exponential curve varied between 6 and 15 min and the corresponding central-region pressure (with traps filled) lay between 2 and 5×10^{-7} mm Hg. The exponentials had pressure-halving times between 60 and 80 min.

Of the three runs which were long enough that the extrapolated curve would have carried the pressure below 1×10^{-7}, all entered that region but departed from the extrapolation. The values were (in units of 10^{-8} mm Hg)

Predicted	Observed
5.8	9.6
7.2	8.1
1.6	7.4

In the cases of significant departure, it appeared that the effects of pressure pulses (of more or less fixed size and increasing frequency) came into equilibrium with the (presumed) cleanup effect responsible for the pressure drop rather than that a true base pressure was reached. For instance, in the last run a pressure of 8×10^{-8} mm Hg was reached after 65 min of operation, but no subsequent pulse-free interval in the remaining 2 hr 40 min was long enough for the pressure to go much lower.

Incidentally, there was general agreement between the two gages reading the central region's pressure. In the early part of the first run, the ratio of their readings was 1.35. It drifted slowly downward as the runs progressed, going as low as 0.85 but generally lying between 0.9 and 1.1.

The gages in the electrode regions showed the same behavior as those in the central region in the early part of the run (including the same slope), but eventually leveled off. The equilibrium anode pressure lay in the region of 5×10^{-7} mm Hg and the cathode pressure in the region of 1×10^{-6} mm Hg. Both pressures at times reached values lower than these by a factor of 2.

Gas leakage from the electrode regions is believed, on the basis of several observations, to have contributed less than 50% of the central region influx down to the lowest pressures observed. The anode region was isolated from the center by a $1\frac{3}{8}$-in.-ID tube 3 in. long and the cathode region by a $1\frac{1}{2}$-in. hole.

Correlations Between Radiation and Wall Temperature. – Equilibrium values of the current (I, microamperes) measured by the gage that was reading as a photometer showed a moderately good correlation with the wall temperature (T, °C) which took the form

$$I = \frac{a}{200}(T - 10) \quad ,$$

where a took values lying between 0.75 and 1.5 for the various runs.

The wall temperature was measured on the outside of the chamber near the arc's point of closest approach. It varied between 80 and 170°C but usually stayed in the range between 100 and 150°C. The lack of correlation between instantaneous values other than equilibrium was, in general, attributable either to the time lag in the temperature response to a radiation change or to the change in the arc's position relative to the wall.

Pressure Conditions. – Central-region pressure readings (after the equilibrium pressure slope was established) were found to be correlated with equilibrium wall temperature values and with instantaneous photometer readings, except during pulses. These correlations held reasonably well over a given run but varied from run to run. The variations were erratic but generally in the direction of lower pressure at a given radiation level, indicating a progressive wall-cleaning effect even after several hours.

The correlations were again approximately linear over the range observed ($p_c < 10^{-6}$ mm Hg). For one intermediate run, the correlation took the form (for p_c in units of 10^{-7} mm Hg, I in μamp, and T in °C)

$$p_c = 1.1\,(I - 0.45) \quad ,$$

or

$$p_c = 0.045\,(T - 80) \quad .$$

The deviations from these curves were less than 15% in pressure when pressure bursts were excluded.

The data contained hints that when the wall temperature departed from its correlation with the photometer reading the pressure retained its correlation with the wall temperature. This was repeatedly observed (for pressures down to 8×10^{-8} mm Hg) when a cathode movement brought the arc nearer to the wall, raising the local temperature but not changing the photometer reading. The inference is that still lower pressures will have to be reached before direct photon ejection of gas from the walls is a dominant effect.

Pumping Speed and Gas Evolution. – Closing and opening the valves to the pumps on the central region raised and lowered the pressures there by amounts varying between 20 and 40%. The average of 10 observations was 29%. The implied pumping speed for the arc (taking the pumps' speed as 1000 liters/sec) is 3500 liters/sec. The observations were all made at pressures near 2×10^{-7} mm Hg.

Taking the total pumping speed on the central region as 4500 liters/sec permits a calculation of the rate of gas evolution. During the first hour of the first run, an apparent 100 atmospheric cm^3 of gas was evolved. Since this large amount did not reappear in subsequent runs, it probably consisted of pump oil, which migrated to the arc's vicinity from all surfaces above the Freon-cooled traps, a total surface area of about 10^5 cm^2. Assuming this to be the case and taking the gage sensitivity factor of pump oil as 13 (ref 5), the

[5] H. G. Nöller, G. Reich, and W. Bächler, *4th Vacuum Symposium Transactions*, p 6, Pergamon Press, New York, 1957.

true volume was 7.7 cm^3, corresponding to about 1.5×10^{15} molecules/cm^2.

In 2 hr of a subsequent run, an apparent 5 cm^3 was evolved, corresponding (for unity gage sensitivity) to 1×10^{15} molecules/cm^2, or several monolayers of adsorbed gas.

In the last run, a pressure of 1×10^{-7} mm Hg was reached after 55 min which saw the evolution of about 3×10^{14} molecules/cm^2. After this point, the system appeared merely to hold its own against the gas influx in the form of large bursts. Decreased pressure sensitivity to wall-temperature variations in the later stages of this run suggested that the walls were cleaner than at any other time during the experiment.

Conclusions

It has been found possible by making an extended arc run to achieve pressures of 7.5×10^{-8} mm Hg in the presence of a 300-amp carbon arc and 5.5×10^{-8} mm Hg in the presence of a 250-amp arc. At pressures down to 8×10^{-8} mm, indications were that wall temperature was still an important factor in determining gas evolution. Observations of decreased pressure sensitivity to wall temperature changes indicated progressive wall cleanup from run to run and even within one long run. Extraneous effects, mostly associated with erratic behavior of the arc, prevented unambiguous interpretation of much of the data. Frequent pressure pulses are believed to have played a major role in determining the limiting pressure in the final run.

Recommendations

Since this is a report on work in progress, albeit shelved temporarily, it is not out of place to describe equipment and procedure developments regarded as desirable. Uniform cathode feed is essential and uniform anode motion desirable. The wall temperature should be measured inside (although a true surface temperature is as yet unmeasurable); and a more sensitive phototube as well as a fast thermocouple radiation detector should be provided. A stronger set of magnet coils is under construction, which is expected to provide enhanced arc stability, and there are several changes in cathode design which promise to lead in this direction. A more adequate baking program for the electrodes is being set up by the laboratory. Somewhat better isolation of the central region is both desirable and easily achieved in the stronger field. A copper liner has been constructed which will be capable of being baked at 650°C by arc heating and which will constitute a fourth region pumped only by the arc.

In earlier experiments, a prior bakeout (without liner) was shown to save about an hour or two in getting to the low 10^{-7}-mm range of pressures. Extended runs after bakeout, at higher currents, with and without diffusion pumps, should be made. If the low 10^{-8}-mm region can be reached, some fairly interesting and fundamental experiments should be possible.

4.15 A TYPE OF HOLLOW-CATHODE DISCHARGE

C. Michelson

4.15.1 APPARATUS

The small-arc apparatus shown in Fig. 4.15.1 was designed to facilitate the study of small gas- and carbon-arc discharges in a multiple-region vacuum under the influence of various magnetic field configurations. The pumping system for this apparatus consisted of three CEC MCF-300 oil diffusion pumps with water-cooled baffles and quarter-swing isolating valves. Forepumping was provided by a Welch Duo-Seal model 1402 mechanical vacuum pump. The entire vacuum chamber was fabricated from 4-in. nominal Pyrex glass pipe. Standard mild-steel flanges were used where the magnetic field distortion was permissible. Flanges at critical field locations were fabricated from brass plate. The central vacuum chamber was fabricated from a standard glass cross by extending two of its legs an additional 3 in. to permit magnet coil movements. The pumping manifolds at the ends were standard glass tees with necks added for ion-tube mounting. The pumping manifold for the central chamber was a standard glass tee. The letdown

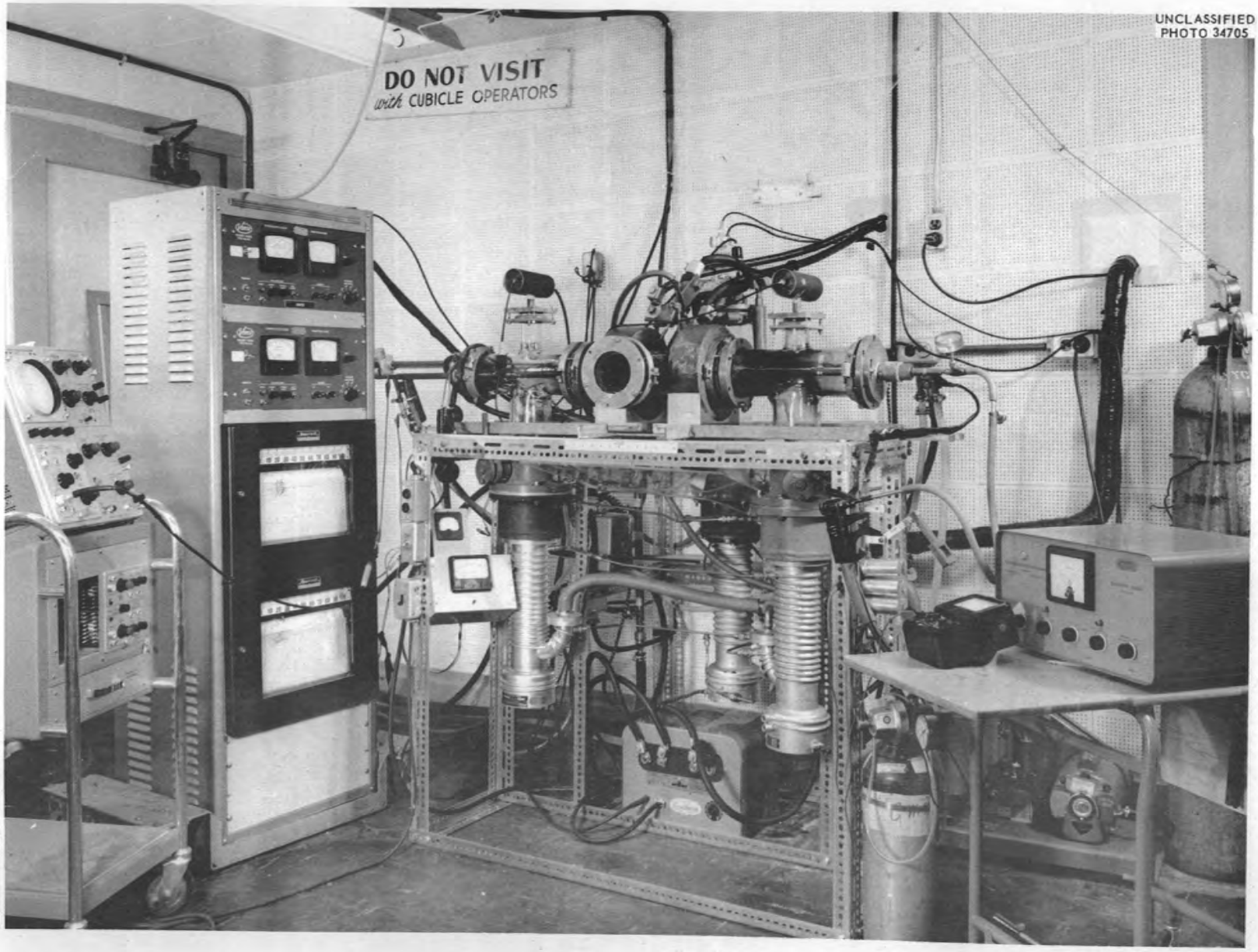

Fig. 4.15.1. Small Arc Apparatus.

valve, roughing valve, thermocouple gage, and ion gage were attached to the blank-off plate on this manifold. All glass joints were vacuum-sealed with $\frac{1}{8}$-in. neoprene O-rings. A $\frac{1}{4}$-in. thick Lucite shield was placed over the top, front, and bottom of the apparatus to protect against implosion.

A magnetic mirror field was established in the central vacuum chamber by two field coils, each consisting of 72 turns of $\frac{1}{4} \times \frac{1}{4}$ in. square hollow copper conductor. A series bank of three 6-v, 500-amp rectifiers supplied the field current to the series-connected coils. The normal operating current of 250 amp established a mirror field of 840 gauss at the center of the apparatus with a mirror ratio of 1.5. The coil spacing was 8.5 in. center to center. Although most arc experiments were run in a straight-through mirror configuration, the apparatus was designed to test also the feasibility of arc operation in a tightly curving magnetic field such as that obtained by a right-angle arrangement of the mirror coils. For this experiment, which has not yet been performed, one field coil will be placed over the front leg of the central vacuum chamber.

The water-cooled electrode holders for this arc apparatus were $\frac{3}{4}$ in. in diameter. Gas feed lines were provided to permit gas injection into either electrode. A dual vacuum-coupling and Teflon-insulator arrangement was used to electrically insulate the holder and to permit electrode movement during operation. No vacuum lock system was considered necessary because the apparatus could be let down and re-evacuated in a few minutes.

A water-cooled cylindrical copper liner was used during most arc experiments. Viewing was accomplished through the glass plate used to cap off the front leg of the central vacuum chamber. An axial slot was cut in the liner along the line of sight from the window. During most experiments the arc length was maintained at 4–5 in.

Rectifier and rotary types of welding equipment were used for the arc power supply. A standard high-frequency welding starter was used to initiate the arc. In most cases, the starting gas was argon.

4.15.2 EXPERIMENTS

Characteristics of Cavity Discharge

One of the first experiments begun in the apparatus described above was a study of the limitations on scaling down the various parameters of the Luce carbon arc. In the course of these experiments during late June, there was discovered an unusual sort of discharge which appeared to run between a large solid carbon anode and the interior of a small hollow carbon cathode through which argon gas was fed. (The cathode was a $\frac{3}{32}$-in.-dia cylinder, 2 in. long, with a $\frac{3}{64}$-in. axial hole. The discharge was about 4 in. long.) It was observed that in situations where $\frac{3}{8}$ in. or more of the cathode was heated to bright incandescence by increasing the discharge current, the gas discharge changed from a series of unstable filaments running off the cathode tip, to a well-behaved collimated plasma terminating inside the cathode hole about $\frac{1}{4}$ in. back from the tip. The terminating point appeared as a $\frac{1}{8}$-in.-wide incandescent band. This discharge, as originally observed, was characterized by high impedance (typically $V/I = 70/15$, where V is in volts and I in amperes), by radio-frequency noise generation an order of magnitude greater than that of the arc run off the tip, and by operation with the background pressure around 2×10^{-4} mm Hg. It appeared to be essentially a scaled-down version of the Luce-Bell deuterium arc.[1] Subsequent experiments have revealed further points of similarity and some differences.

Although high impedance was first thought of as characterizing the hollow-cathode discharge, it was later found to be only characteristic of one segment of a broad range of operation. The discharge was found to be operable over a broad range of currents, showing a V/I characteristic with a slightly negative slope starting at $V/I \approx 50v/50a$ and extending to higher currents. Discharges up to 200 amp (25,000 amp/cm^2) were run without difficulty for periods up to 15 min. Off-axis operation was also tried successfully, as was operation without gas input at currents above 150 amp. Without gas input,

[1] P. R. Bell and J. S. Luce, *The ORNL Thermonuclear Program*, ORNL-2457, Appendix I (Jan. 31, 1958); J. S. Luce, *Studies of Intense Gaseous Discharges*, UN-1790, Geneva Conference Paper (1958).

the discharge ran alternately in the cavity and on the cathode face.

Experiments on the hollow-cathode discharge are continuing. Possible applications include use as a dissociating arc in DCX and as a continuous plasma source for containment studies.

D. J. Rose, consultant from MIT, observed a resemblance to the "cavity cathode" glow discharge developed at Bell Telephone Laboratories.[2] Several experiments suggested by him have tended both to enhance the similarity and to indicate fundamental differences. The next section of this report is an article by Rose in which he outlines a theory of operation for this new hollow-cathode discharge.

One of the remarkable characteristics of the hollow-cathode type of discharge is its stability as compared to the filamentary type of discharge. The latter runs as a series of filaments terminating on the cathode as small, randomly wandering, incandescent spots. These cathode spots rapidly erode the cathode surface. The voltage and current of the filamentary arc vary constantly. By comparison, the hollow-cathode discharge is characterized by negligible loss of cathode material and no detectable voltage-current variations except for the r-f noise.

During the first few minutes of operation in a cylindrical hole, the hollow-cathode discharge redistributes carbon so as to form a more nearly spherical cavity. The cavity formed in a $\frac{1}{4}$-in. cathode is shown in Fig. 4.15.2 (thumb tack shown for size reference). This cavity was observed after 30 min of operation of a discharge which was run at 66 v and 15 amp. The system pressure was 0.5 μ. After the experiment the electrode was potted in epoxy resin and sectioned along the axis. Other electrode cavities are shown in the next section.

Experiments showed that the initiation and operation of the hollow-cathode discharge were largely unaffected by the choice of anode material or configuration. A 2-in.-dia solid cylindrical carbon anode was selected for most subsequent experiments, for convenience, although copper was also used.

[2] A. D. White, *J. Appl. Phys.* 30, 5, 711–19 (1959).

Effect of Cathode Configuration

The cathode configuration was found to be critical in detail for obtaining consistent cavity cathode operation. For discharges operating at 50 amp or more, it was found possible to use carbon cathodes up to $\frac{1}{4}$ in. OD with axial holes up to $\frac{1}{8}$ in. in diameter. At lower currents the large cathodes could not be heated sufficiently to obtain the cavity-type discharge. For consistent cavity operation at lower currents a cathode with about $\frac{1}{8}$ in. OD with a $\frac{1}{16}$-in. hole proved very satisfactory. This smaller cathode also operated satisfactorily at higher currents but its life was limited by the thin walls. Successful cavity operation was not attainable with cathode holes smaller than $\frac{3}{64}$ in. A $\frac{5}{32}$-in. molybdenum cathode was tried without success. No further effort was made to investigate other cathode materials.

One interesting observation was made regarding the transition which occurred when the cavity discharge burned through the cathode wall. This was found to occur about every 15 min for a $\frac{1}{8}$-in. cathode ($\frac{1}{16}$-in. hole) operating at discharge currents of 15 to 20 amp. As the cavity wall became thin it cracked and released its gas out the side. At this time, the r-f noise became dominated by oscillations at a discrete frequency between 0.3 and 2 Mc. The cavity discharge eventually broke into a filamentary-type discharge (upon which the discrete oscillations disappeared) and proceeded to erode the carbon surface. After a few seconds, the old cavity tore away and the discharge either re-entered the hollow cathode or went out.

Effect of Magnetic Field

A few experiments were conducted to determine the effect of the magnetic field on the hollow-cathode discharge. Remarkably enough, it was found that the field could be turned off entirely with no marked difference noted in the current and voltage. Although the discharge spread out to fill the entire volume, the cathode showed no visible change in temperature distribution. The chamber liner was electrically insulated during field-off operation. In general, the magnetic field appeared only to act as a collimator of the gas discharge. This point is being investigated further.

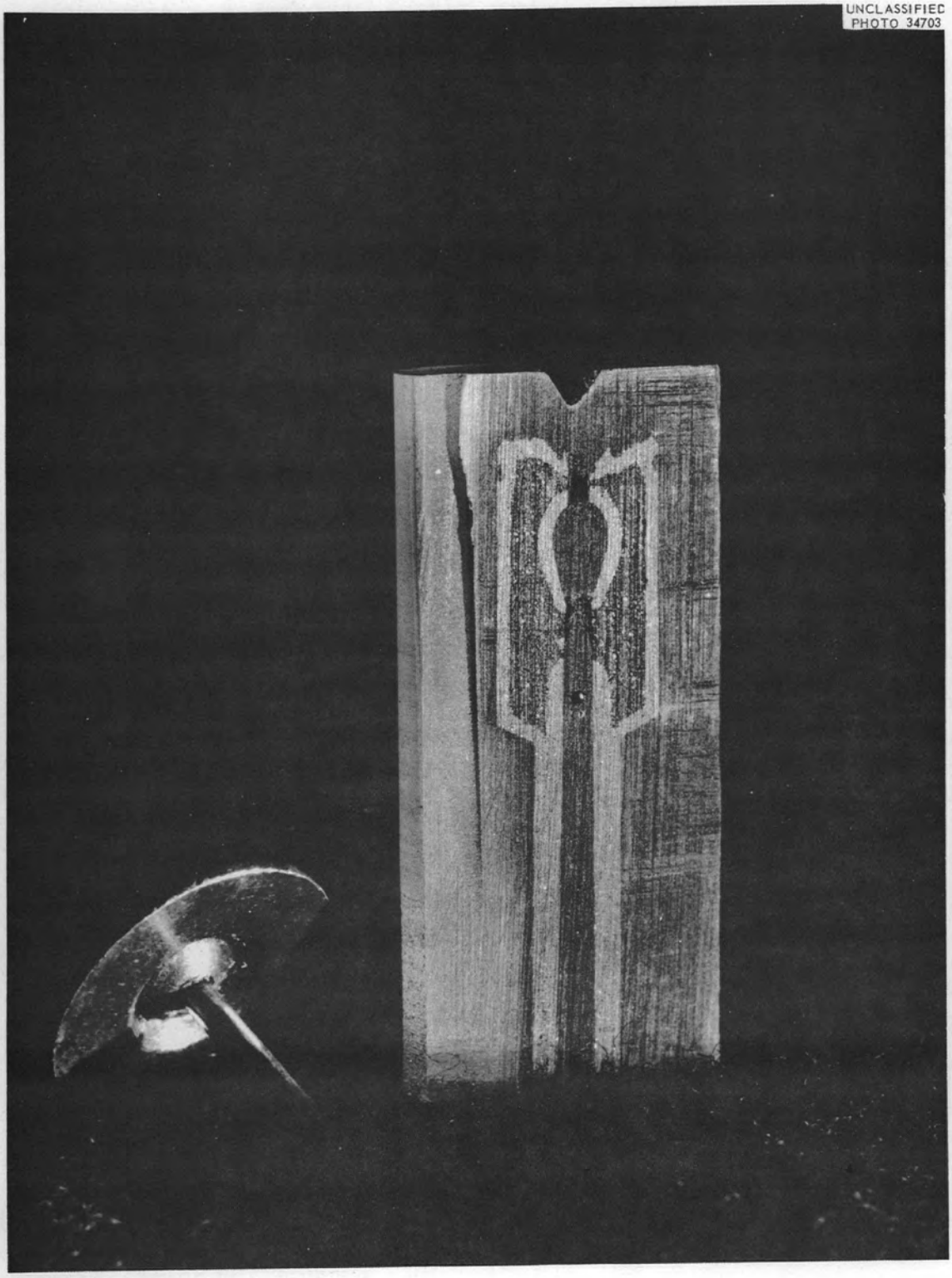

Fig. 4.15.2. Center-Line Section of Cavity Cathode.

4.16. ANALYSIS OF A CAVITY CATHODE DISCHARGE IN CARBON

D. J. Rose

OBSERVATION

A mode of discharge operation with carbon cathode recently discovered here and reported in the previous section may be related to one already known to operate in refractory metal cathodes.[1] Experimental work is presently being carried out, principally by C. Michelson. At present, data are too fragmentary for serious analysis.

Very briefly, the initial observation was that a $\frac{1}{8}$-in.-dia cathode with a $\frac{1}{16}$-in. axially bored hole was placed in an axial magnetic induction ≈ 800 gauss. Argon gas was fed into the vacuum chamber through the cathode, and the main discharge chamber was pumped. Then with a suitable gas flow, giving a chamber pressure of the order of a few times 10^{-4} mm Hg, a discharge could be maintained which terminated on the inside of the cathode hole, typically $\frac{1}{8}$–$\frac{1}{4}$ in. inside. Since then, the range of current, pressure, and cathode configuration has been partly investigated, and currents up to 200 amp have been obtained in this mode.

It is proposed that this discharge is similar in many respects to the type described in ref 1, about which a good deal is known. Briefly, the cavity cathode forms when a hole is drilled in a refractory metal, as shown dashed in Fig. 4.16.1. Under suitable conditions of rare-gas pressure, and for a current exceeding a minimum value, the discharge runs inside, sputters the metal to form an equilibrium shape (shown solid), and runs in that shape for an extraordinarily long time. In the typical application described by White, a 0.030-in.-dia niobium cavity, with an ambient gas pressure of 100 mm Hg, will run for 12,000 hr at a current of 10 ma, with almost no detectable aging. This current is small, but when one remembers that the current density on the interior of the cavity is ≈ 0.5 amp/cm^2, one realizes that this is a remarkably long life. In practice, White formed his cavities to the correct shape by a hobbing method, once the shape had been determined by initial aging experiments.

[1] A. D. White, *J. Appl. Phys.* 30, 711–19 (1959).

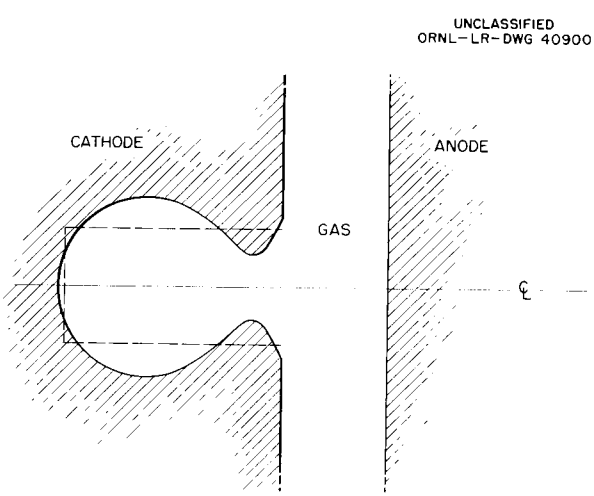

Fig. 4.16.1. Cavity Cathode Configuration with Metal Electrodes.

Qualitatively the same effect is observed in the present instance. Figure 4.16.2 shows the result of resectioning a cathode after about 8 min operation at about 15 amp. The part shown dotted was not indexed carefully in the axial direction, and the front was also damaged by filamentary arcs formed during the initial attempt to persuade the discharge to run inside. Figure 4.16.3 shows another cavity formed by 31 min operation at 15 amp. This cavity failed at 31 min, with a blow-out on one side of the orifice.

Although the two cavities have somewhat different shape (note also the initial holes were different), the two volumes were almost identical. Thus a forming period plus a period of quasi-stable operation is indicated. Rough measurement of the carbon loss shows that $\approx 5 \times 10^{-4}$ cm^3 of carbon was eroded per ampere-hour, averaged over the life of the cathode of Fig. 4.16.3.

Besides the similarity in shape, there were some other similarities:

1. This discharge made in carbon ran as well with no magnetic induction as with 800 gauss (maximum available). To be sure, the induction collimated the external plasma, but that is incidental. Since $\omega_b \approx 1.4 \times 10^{10}$/sec at 800 gauss, one presumes that the electron collision frequency ν_c was higher than this. Thus a pressure of several millimeters inside the cavity is indirectly indicated. This checks with experience quoted in ref 1, where the pressure for a cavity of such a size would be tens of millimeters.

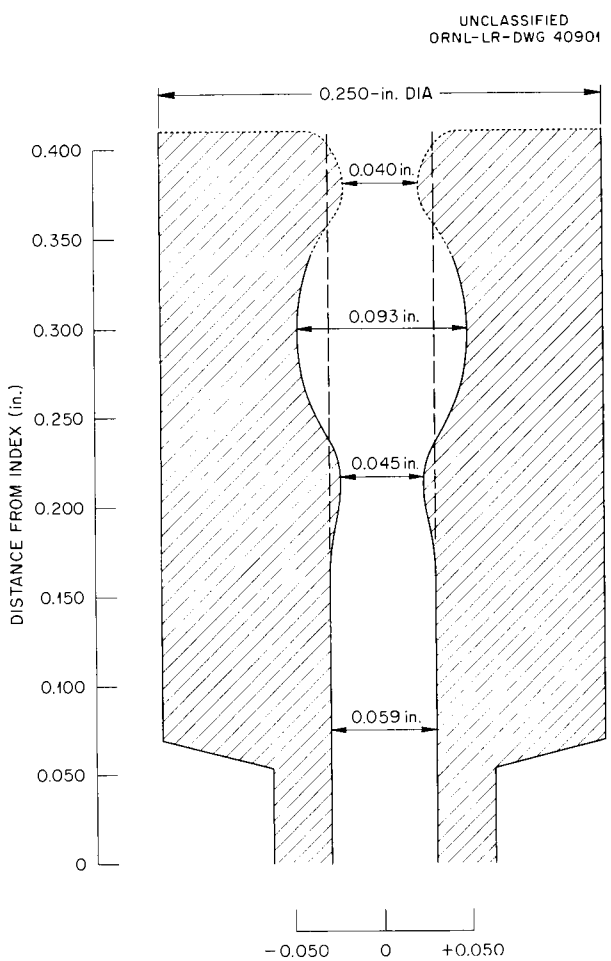

Fig. 4.16.2. Cavity Formed by 8-min, 15-amp Discharge.

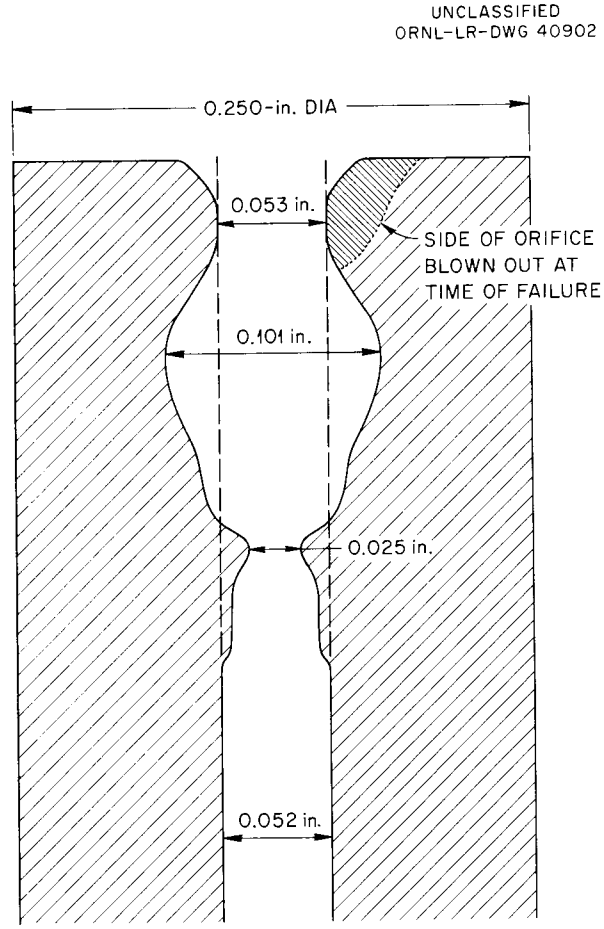

Fig. 4.16.3. Cavity Formed by 31-min, 15-amp Discharge.

2. Further qualitative evidence that the pressure was high inside is the fact that if the discharge was turned off, a burst of gas entered the vacuum system, as if the gas locked up in the cavity and lead-in tube were escaping. This point is being checked by insertion of a pressure gage in the cathode flow line.

3. At currents ≈ 15 amp, voltage was ≈ 65 v, more characteristic of a glow discharge than an arc. At higher current, the voltage dropped, and this circumstance will be discussed below. More detailed observations are reported by C. Michelson in the previous section.

PROPOSED MECHANISM OF THE DISCHARGE

The analogy with the cold cavity cathode discharge, for which some theoretical interpretation exists,[2] suggests a line of reasoning to apply to the present discharge. It is felt that the distinction between "glow" and "arc" is rather meaningless here and that we have a transition phenomenon.

It is proposed that the charge density inside the cavity is sufficiently high that a voltage sheath forms close to the cavity wall. This sheath is so thin that an electron emitted from the surface falls through the sheath and is injected into the substantially field-free region of the cavity without having significant collisions. The potential across the cavity will therefore appear qualitatively as shown in Fig. 4.16.4.

This point may be established by a qualitative argument. Suppose the ions formed in the cavity return to the cathode by ambipolar diffusion. Then

[2] W. P. Allis, *Proc. 3rd International Conf. on Ionization Phenomena in Gases*, Venice, 1957.

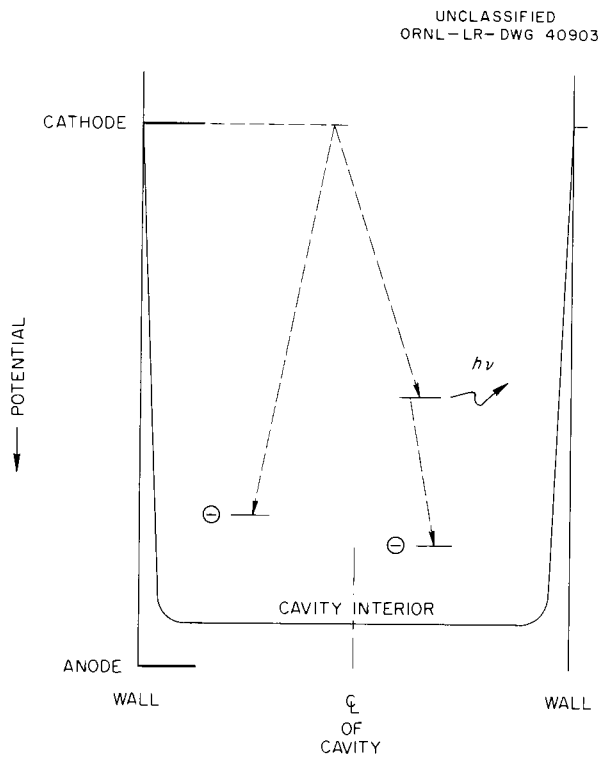

Fig. 4.16.4. Schematic Potential Distribution Across Cathode.

the current density j is:

$$j = -eD_a \nabla n \ , \tag{1}$$

where e is the electronic charge, D_a is the ambipolar diffusion constant, and n is the density. In a spherical volume, approximated here, the density distribution is given by the diffusion equation, and one finds:

$$n_{\pm} = n_0 \frac{\sin(\pi r/r_0)}{(\pi r/r_0)} \ , \tag{2}$$

where n_0 is the central density, and r_0 is the cavity radius. Thus at the boundary, $r = r_0$, one has:

$$j = \frac{e D_a n_0}{r_0} \ . \tag{3}$$

One may approximate:

$$D_a \approx \frac{D_-}{\mu_-} \mu_+ \ , \tag{4}$$

if the ion energy is much less than that of the electrons. Here "–" and "+" refer to electrons and ions, respectively, and μ is mobility.

One must guess at numbers to put in. Experience with metal cathodes gives $(D_-/\mu_-) \approx 1$ ev (two-thirds of mean energy). For μ_+, we will take 150 cm^2/v-sec, corresponding to a pressure of several mm Hg. The observed current, ≈ 15 amp, corresponds to about 80 amp/cm^2 over the interior, but let us be modest and presume that only 10% arises from ion current. Then one finds, with $r_0 = 0.125$ cm, that $n_0 \approx 4 \times 10^{16}$/cm^3. This is an intriguingly high charge density and may be somewhat in error. At the same time, it should be pointed out that the current density in the orifice is about 2000 amp/cm^2, at this current of 15 amp.

At the boundary of such a plasma, a sheath of thickness t will form, determined very roughly by:

$$V = \frac{e}{\epsilon_0} n_+ t^2 \ , \tag{5}$$

where V is the voltage developed and ϵ_0 is the dielectric constant of space. If $V = 50$ v, one then obtains $t \approx 3 \times 10^{-4}$ mm. To be sure, the calculation is not very good, partly because the gas inside must be highly ionized and normal diffusion theory does not properly apply. However, there are several orders of magnitude to spare here, and the assumption of a thin sheath as shown in Fig. 4.16.4 appears reasonable.

Returning now to the injected electron, it will travel about in the cavity, with negligible chance of escaping, until it has lost its energy by ionization or excitation. Thus it forms a low-energy "shower," and one such possible sequence is depicted on Fig. 4.16.4. In the case shown there, the electron (with an initial energy of about 50 v) ionizes a gas atom, giving one electron at too low energy to do anything, and the second which then is depicted as causing an excitation. Other sequences are possible, such as the production of metastable atoms which may be ionized on subsequent impact by low-energy electrons, etc.

McClure has shown[3] that in low-energy showers of this sort, the number of ion pairs produced is small. That is, in argon, at the voltages encountered here, the yield is no more than one ion

[3] B. T. McClure, Bell Telephone Laboratories, unpublished data.

per injected electron, and the yield falls rapidly with decreasing injection voltage. Under the best of circumstances, one can hardly expect more than one ion and one metstable atom to be produced, for effective use in further secondary processes.

The secondary mechanism here must be different from that obtaining in cold metal cavities. There, the voltage is higher (100 v for neon in Mo cavities), and the secondary emission coefficient γ_i for either ions or metstables is about 0.24. Thus, with stringent economy, the discharge may operate. In the present case, we need an effective γ_i of 0.5 or more, and it is known that γ_i for graphite at room temperature is vastly smaller. There appear to be only three possibilities; either:

1. The secondary emission coefficient γ_i is much enhanced at the high cathode temperature.
2. The secondary emission coefficient is much enhanced by the high field.
3. The cathode interior is heated to a level yielding thermionic emission.

In respect to these mechanisms, preliminary observation of the exterior of the cathode shows a temperature $\geqq 2150°K$. It is not yet possible to determine the temperature inside. As current increases, the cathode becomes visibly hotter. Then any one of the mechanisms above could give a falling voltage-current characteristic, as observed.

There is not enough information at hand to choose definitely between the alternatives. In regard to (1) above, nothing is known, although it would not be difficult to determine in an experiment designed for the purpose. In regard to (2), the previous suspect calculations lead to a field $\approx 1.3 \times 10^6$ v/cm, about enough for emission. In addition, the high temperature will raise a significant number of electrons near the vacuum level, thus enhancing the effect. An ion may then approach the cathode, and liberate one or several electrons, by depressing the potential barrier. This process might be amenable to calculation.

In regard to (3), application of the emission equation:

$$j_- = 5.9T^2 \exp(-4.57 \times 10^4/T) \ , \qquad (6)$$

corresponding to a work function of 3.93 ev, gives: 3000°K, 10.5 amp/cm^2; 3300°K, 62 amp/cm^2; 3500°K, 153 amp/cm^2; 4000°K, 1070 amp/cm^2. Thus to account for the high emission, a temperature $\geqq 3300°K$ is indicated. This appears somewhat unlikely. Incidentally, the vapor pressure of carbon at 3300°K has been estimated[4] to be about 0.25 mm Hg, corresponding to a departure rate of about 10^6 atom layers/sec, or about 0.1 mm/sec. One might think that the cathode would vanish in about 10 sec and therefore that such temperatures are precluded. This is not so, for the area of the two orifices in Fig. 4.16.3 is only about 5% of the cavity area. In addition, it will be shown below that a neutral atom has little chance of reaching the orifice before being ionized and returned to the interior surface.

It is interesting to write down an equation governing the temperature inside. Figure 4.16.5 shows some of the quantities of interest. The cathode is at $V = 0$, anode at $V = V_a$; and inside the cavity and through the orifice the potential is approximately constant at the sheath potential V_s. The total energy input is iV_a, and the energy dissipated in the exterior column is $i(V_a - V_s)$. In addition, assuming that most of the external current is carried by electrons, there is a flux of energy $n \langle v_- \rangle \langle mv^2/2 \rangle$ carried off by the electrons. But this is just $i \langle u_- \rangle$, where $\langle u_- \rangle$ is the average electron energy in electron volts. The rest of the energy is deposited inside the cavity, except for the negligible fraction of the radiation escaping from the orifice. Then the energy input to the cathode is $i(V_s - \langle u_- \rangle)$.

If the energy is deposited uniformly over the interior, where the current density is j, one must solve for the heat flux Γ and temperature T, with:

$$\Gamma = -K \nabla T \ , \qquad (7)$$

$$\nabla \cdot \Gamma = 0 \ , \qquad (8)$$

[4] A. L. Marshall and F. J. Norton, *J. Am. Chem. Soc.* 72, 2166 (1950).

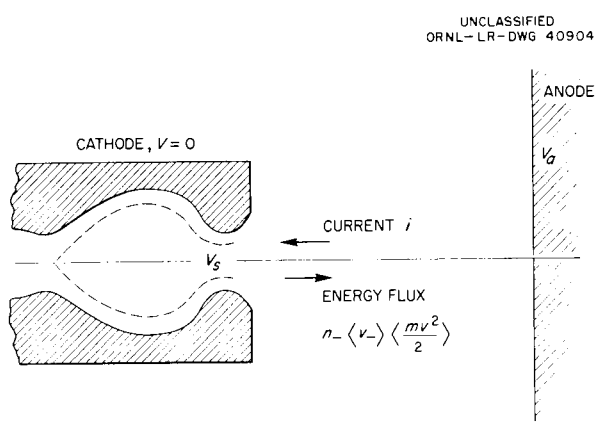

Fig. 4.16.5. Quantities Entering into Calculation of Energy Deposition of Cavity Cathode.

where K is the thermal conductivity, and with the boundary condition:

$$\int_{\text{outside}} \sigma T^4 \, da = i(V_s - \langle u_- \rangle) \ , \qquad (9)$$

where σ is the Stefan-Boltzmann constant. A solution could not be obtained for the shape used. For a cavity spherical inside and out, the solution is:

$$T_1 = \left[\frac{j(V_s - \langle u \rangle)}{\sigma} \right]^{1/4} \left(\frac{r_1}{r_2} \right)^{1/2} + \frac{j(V_s - \langle u \rangle) r_1}{K} \ln \left(\frac{r_2}{r_1} \right) \qquad (10)$$

$$\equiv T_2 + \Delta T_{1-2} \ .$$

Here subscripts 1 and 2 refer to the inner and outer surfaces. Conductivity K may be a function of temperature, complicating the situation. Apart from this, if one could measure T_1 and T_2, for example, some information could be obtained about

$$V_s - \langle u \rangle \approx V_s \ .$$

Incidentally, if interior temperature T_1 is an important parameter, wall thickness is important but simple scaling laws will not apply. For example, in Eq. (10), increasing the wall thickness (increasing r_2/r_1) will tend to raise the interior temperature because of the thermal impedance and to lower the temperature because of the increased radiating area. Preliminary observations of these cavities in their present configuration indicate that $T_2 \gg \Delta T_{1-2}$. In that case, increasing the wall thickness lowers the temperature. It is observed that this discharge anode strikes well in a ¼-in.-OD cathode, but not in a ½-in.-OD cathode.

Finally, let us see if the presumption of high gas density inside the cavity is reasonable, by estimating the chance of a neutral being ionized and returned, before escaping through the orifice. We assume in the following discussion that the ions and neutrals are in thermal equilibrium, and inquire into the diffusion of a neutral atom through the plasma. Since the density of neutrals is not known, and that of ions is only guessed at, the development is somewhat circuitous.

The number of fast electrons entering a unit volume of the cavity per second is $i_-/e\mho$, where $\mho$ is here the volume, and i_- the cathode electron current. These electrons are degraded in energy by excitation and ionization, and we will presume that each electron makes one ion pair. But also per unit volume, the rate of ionization is $n_0 \nu_{in}$, where ν_{in} is the frequency of ionization of a neutral atom, and n_0 is here the neutral density. Thus:

$$\frac{i_-}{e\mho} = n_0 \nu_{in} \ . \qquad (11)$$

The rate at which a neutral diffuses to the wall of the cavity is:

$$\nu_D = \frac{D}{\Lambda^2} \ , \qquad (12)$$

where D is the diffusion coefficient and Λ is the diffusion length. Since only a fraction f ($\approx 5\%$) of the cavity surface is taken up by the orifice, then the escape rate ν_e is given by:

$$\nu_e = \frac{fD}{\Lambda^2} \ . \qquad (13)$$

We are interested in the ratio of two frequencies ν_e and ν_{in}, because the chance of a neutral escaping as such is exp $(-\nu_{in}/\nu_e)$. Thus we must evaluate:

$$\frac{\nu_{in}}{\nu_e} = \frac{i_- \Lambda^2}{e\mho n_0 fD} \ . \qquad (14)$$

The diffusion coefficient D is given formally by:

$$D = \left\langle \frac{v^2}{3\nu_c} \right\rangle \ , \qquad (15)$$

where v is velocity, and ν_c is the collision frequency. Here, one must count collisions of a neutral both with other neutrals and with the ions. Since by assumption the quantity $\langle v^2 \rangle$ is the same for all particles, we can without great error just add the two averaged frequencies; that is, the total diffusion coefficient will be given by:

$$\frac{1}{D} = \frac{1}{D_{00}} + \frac{1}{D_{0+}} \ , \qquad (16)$$

where D_{00} is the self-diffusion coefficient of the neutrals and D_{0+} is the diffusion coefficient of

neutrals with ions. Thus it is convenient to write:

$$\frac{1}{D} = \frac{1}{D_{00}}\left(1 + \frac{D_{00}}{D_{0+}}\right) . \qquad (17)$$

For the neutral component, we use the data given by Present[5] for argon at atmospheric pressure. If the collision cross section is independent of temperature, $D/T^{3/2}$ should be independent of temperature. Figure 4.16.6 shows the data over the limited range listed in the reference. The

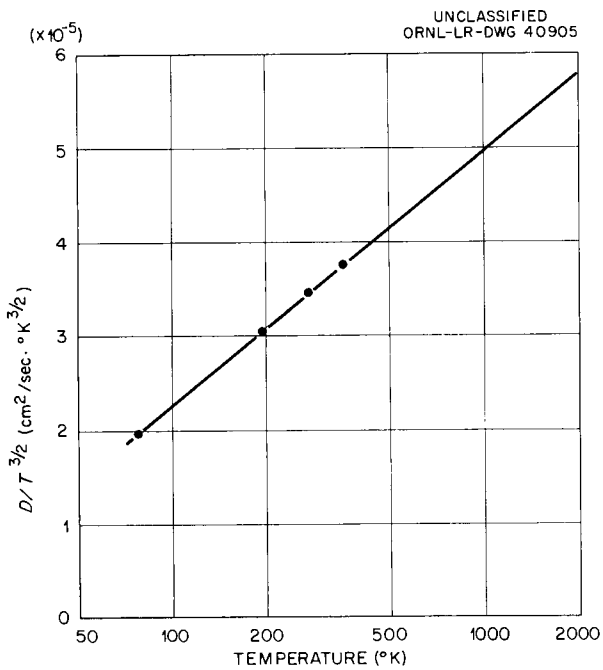

Fig. 4.16.6. Self-Diffusion Coefficient of Neutral Argon. $D/T^{3/2}$ vs temperature (°K) for 1 atm pressure.

quantity is not constant but can be extrapolated accurately enough for the present purposes. To the degree that argon is a perfect gas, one may write for our condition of gas density n and temperature T:

$$D_{T,n} \equiv D_{00} = \left(\frac{D_{T,\mathrm{atm}}}{T^{3/2}}\right) T^{1/2} \left(\frac{273L}{n_0}\right) , \qquad (18)$$

where $L = 2.69 \times 10^{19}/\mathrm{cm}^3$ is Loschmidt's number and n_0 is the neutral gas density in the experiment.

[5] R. D. Present, *Kinetic Theory of Gases*, p 263, McGraw-Hill, New York, 1958.

For the diffusion of a neutral in the ions, we note that for the same equilibrium temperature, the diffusion coefficient D_{0+} of a neutral in an ion density n_+ should be the same as the coefficient D_{+0} of an ion in a neutral density n_0. This latter is known from the mobility μ_+ of argon ions in neutral argon.[6] At 0°C, 760 mm Hg, $\mu_+ = 1.67\ \mathrm{cm}^2/\mathrm{v\text{-}sec}$. Since $D_+ = \mu_+(kT/e)$, one has $D_+ = 0.0435\ \mathrm{cm}^2/\mathrm{sec}$ at standard conditions. Since not much is known about the temperature dependence, we assume a simple perfect gas and write:

$$D_{0+} = \left(D_{+0}\right)_{\mathrm{stp}} \left(\frac{L}{n_+}\right)\left(\frac{T}{273}\right)^{1/2} \qquad (19)$$

corresponding to a hard sphere.

The ratio D_{00}/D_{0+} is now:

$$\frac{D_{00}}{D_{0+}} = \frac{(D_{T,\mathrm{atm}}/T^{3/2})\, T^{1/2}\,(273)^{3/2}\, n_+}{\left(D_{+0}\right)_{\mathrm{stp}}\, n_0} . \qquad (20)$$

The quantity $(D_{T,\mathrm{atm}}/T^{3/2})$ is plotted in Fig. 4.16.6. Assuming 2000°K, one has:

$$\frac{D_{00}}{D_{0+}} = 6.0\,\frac{n_+}{n_0} . \qquad (21)$$

Finally, after some insertions, Eq. (14) becomes:

$$\frac{\nu_{in}}{\nu_e} = 1.65\, i_- \left(1 + 6\,\frac{n_+}{n_0}\right) . \qquad (22)$$

Here, we have assumed 2000°K, a volume of $10^{-2}\ \mathrm{cm}^3$, and a diffusion length $\Lambda = 0.05$ cm.

So far we have not had to guess at either the electron current or the neutral gas density. If the electron current is half the total, then for a current of 15 amp, we have:

$$\frac{\nu_{in}}{\nu_e} = 10.7\left(1 + 6\,\frac{n_+}{n_0}\right) . \qquad (23)$$

Thus even without the ions being present, a neutral has little chance of escaping before being ionized.

[6] L. B. Loeb, *Basic Processes of Gaseous Electronics*, p 92, University of California Press, Berkeley, 1955.

Earlier calculations showed $n_+ \approx 4 \times 10^{16}/\text{cm}^3$. In that case, the ion contribution is large, unless n_0 is high. Presumably this very effect of high ν_{in}/ν_e forces n_0 to be high enough that an equilibrium solution determined in part by Eq. (23) obtains in the cavity.

4.17 HYDROGEN ARC DEVELOPMENT

R. J. Mackin, Jr.

During the month of July, the PPF was used for exploratory experiments directed toward the development of a high-vacuum hydrogen arc. The approach had its origin in the "high ionization efficiency" idea of the Luce-Bell hollow anode[1] experiments of 1957. The electrode configuration was one suggested independently by J. S. Luce and the author. It consisted of a capped anode (Fig. 4.17.1), into which gas could be bled, and an ordinary carbon cathode. The arc was operated in a three-region vacuum system.

The first run was made with a simple carbon cap whose front face was 1.5 in. from the anode face. Operation as a carbon arc was satisfactorily stable after the cap was burned through, and it was noted that the arc radiation, as indicated by both the photometer and the wall temperature, was about one-half that observed with an uncapped anode.

[1]P. R. Bell and J. S. Luce, *The ORNL Thermonuclear Program*, ORNL-2457, Appendix I (Jan. 15, 1958).

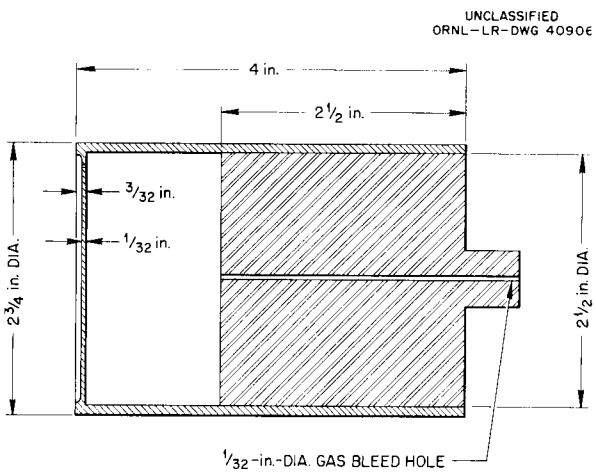

Fig. 4.17.1. Capped Anode Used in the Production of a High-Vacuum Hydrogen Arc.

Molecular ion breakup efficiency with a capped anode has been measured in DCX and found to be about 60% of that with a simple anode.[2] This suggests that reduced ion density is responsible for the reduced radiation.

The major result of the first experimental run was that there was no significant difference in the arc's behavior whether gas was bled into the anode or into a valve at the rear of the anode region. This is what would be expected in the light of earlier data (see Sec 4.14.1) which suggested that the arc's ionizing power is comparatively slight within a few inches of the anode.

Incidental observations of some importance were:

1. The cathode region pressure was raised to 1 μ without increasing the center pressure above 10^{-5} mm.
2. The arc's surface-pumping speed in the cathode region (see Sec 4.14) began to saturate (i.e., decrease) as the gas input was raised above 1 cm^3/sec. That quantity of gas molecules is about one-half of the carbon input to the cathode region by ion drift along the carbon arc and presumably comparable to what would be expected in an energetic gas arc. The arc's pumping is thus not expected to be very helpful when a real gas arc is achieved. It was possible to keep all pumps valved off with a gas input of 2 cm^3/sec, but the cathode pressure was about 15 μ and occasionally surged above 50 μ.
3. A 15% current increase during a gas run caused an overwhelming influx of gas (10–50 cm^3/sec, judging from the rate of rise of the fore-pressure). This presumably resulted from the release of stored gas in the carbon-coated chamber walls, a phenomenon which may cause some problems if this type of arc is used for long periods of time.

[2]J. L. Dunlap, private communication.

A second run was made with an anode whose cap contained a series of four baffle plates spaced 1 in. apart (Fig. 4.17.2). With this electrode it was possible to demonstrate substantial differences in the arc behavior (e.g., color, voltage, and radiation level) depending upon whether the gas was bled into a valve at the wall or through the anode. For anode feed, the cathode-to-anode pressure ratio p_k/p_a varied between 1 and 4. For wall feed it was between $\frac{1}{7}$ and $\frac{1}{3}$. The implication is that there was greater gas transport in the former case by a factor between 5 and 10.

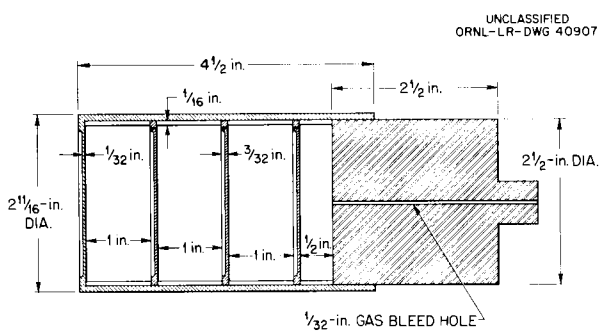

Fig. 4.17.2. Baffled Anode Used in the Production of a High-Vacuum Hydrogen Arc.

Analysis of the sets of pressure data for the two feed points together with the corresponding gas feed rates permitted a gas-ionizing efficiency for the anode to be calculated. For wall feed, the ratio of feed rate (Q_w) to anode-region pressure rise (p_w) gave the speed with which that region was being pumped. Using this pumping speed, it was possible to calculate the fraction of the anode feed which entered the anode region instead of (presumably) being carried away by the arc. The ionizing efficiency, ϵ, thus was found to be:

$$\epsilon = 1 - \frac{Q_w}{p_w} \frac{p_a}{Q_a} .$$

For the anode of Fig. 4.17.2, $\epsilon \approx 35\%$.

A third run was made whose purpose was to compare arc behavior when gas was bled into the cathode with that for anode feed. The surprising result was that there were no essential differences in behavior, and it is tentatively concluded that for gas flows large enough to be interesting, the high pressure in the vicinity of the cathode dominates the behavior of the arc.

It was found that during the experiments the hydrogen pressure in the fore-vacuum manifold became so high that hydrogen leaked back through the diffusion pumps into the central and anode regions. This was cured by feeding the output of the diffusion pump on the cathode region into an individual forepump.

Incidentally, the arc became a very pale (not faint) blue during gas operation and was surrounded by a red halo. The wall temperature indicated that even at the highest gas inputs, the radiation level was still nearly half that of a carbon arc, far from the almost radiation-free condition expected of a pure, completely ionized hydrogen arc.

The need for high pumping speed in the cathode region has, from the first, been recognized as probably the most stringent requirement for operating a high-vacuum gas arc. It had been hoped that the arc's surface pumping would go far toward satisfying that need, but (as mentioned above) it appears to saturate at too low a level. In the course of these experiments, attempts were made to do titanium pumping by evaporating titanium metal, first in the arc and then in the back-streaming plasma behind the cathode (where deposition on cold surfaces would predominate). Although lots of titanium was vaporized, there was no hint of any pumping action. It is suspected that the rapid formation of titanium carbide removes most of the titanium which might otherwise pump.

A manifold is being constructed which will permit replacing the cathode-region pump of the PPF with a 20-in. pump. The pumping speed of such a pump for hydrogen has been found[3] to be 9000 liters/sec. For a 5-cm^3/sec input, this should hold the cathode pressure below 0.5 μ.

These experiments were conducted with the participation of R. M. Warner, R. A. Gibbons, T. F. Rayburn, and R. L. Fredrickson.

[3] O. C. Yonts, private communication.

5. ION SOURCE AND ACCELERATOR DEVELOPMENT

R. C. Davis
R. R. Hall
G. G. Kelley
N. H. Lazar
E. C. Moore
O. B. Morgan
R. F. Stratton

This group has been concerned since the last report with (1) a study of the duo-plasmatron ion source directed toward higher ion output current and (2) the development of a 600-kv accelerator tube for ion beams of up to 500 ma.

At the time of this report an ion current of about 100 ma at 70 kv has been obtained. This increase was made possible by proper shaping of the electrodes in the extraction region and by improved cooling of the source.

The accelerator tube and pumping manifold are in the late stages of construction.

5.1 HIGH-CURRENT VON ARDENNE DUO-PLASMATRON ION SOURCE DEVELOPMENT

In preparation for the injection of higher ion currents into a DCX machine, a goal has been established to build a duo-plasmatron[1] ion source that will produce 0.5 amp of molecular ions. Using a modification of a source designed by C. D. Moak of the Physics Division, with the anode plate shown in Fig. 5.1.1, a total of 110 ma of ion current at 70 kv has been obtained. Both assembled and disassembled views of this source are shown in Figs. 5.1.2 and 5.1.3. Higher-current sources are being built.

5.1.1 DESIGN PARAMETERS

Some of the most important parameters in designing the Von Ardenne ion source for a specific output current are the physical dimensions of the tungsten insert for the anode. This insert, as shown in Fig. 5.1.1, consists of a small aperture which regulates the rate of gas and plasma diffusion from the source and an inverted cup which determines the area of the plasma surface from which ions will be extracted. The diameter of the cup is determined by consideration of the ion optics in the extraction region. The electrodes are shaped to create an electric field in the region whose radial component just cancels the radial field of the space charge in the beam.[2] Current density is determined, then, by the accelerating voltage and electrode spacing. For singly charged ions:

$$I = \frac{1.71 \times 10^{-7} \phi^{3/2} A^{-1/2}}{z^2}, \qquad (1)$$

where I is output current in amperes, ϕ is the accelerating potential difference in volts, z is the effective axial spacing of the electrodes in units of r_0 (the initial beam radius), and A is the mass number. The cup should be just slightly larger than the beam to prevent defocusing fields near the plasma surface. The current density cannot be increased indefinitely, however, by reducing z. The limit is reached when z is made comparable to $2r_0$, at which point the potential along the axis will not increase proportionately as the physical dimensions are decreased, and curvature of the potential lines will result in defocusing fields.

5.1.2 ANODE-PLATE COOLING

One of the initial problems encountered in building a high-current (>50 ma) source was to determine a method of cooling the anode plate to permit large arc currents. The first satisfactory solution to this problem, Fig. 5.1.1, consisted of a tungsten insert brazed to a mild steel anode with four high-velocity oil cooling jets. Later, it was found more satisfactory to shrink-fit the tungsten insert into the plate. This type of cooling has been adequate for arc currents of 0–9 amp. One objection to this

[1] M. von Ardenne, *Tabellen der Elektronenphysik, Ionenphysik und Übermikroskopie*, VEB Deutscher Verlag der Wissenschaften, Berlin, 1956.

[2] J. R. Pierce, *Theory & Design of Electron Beams*, D. Van Nostrand, New York, 1954.

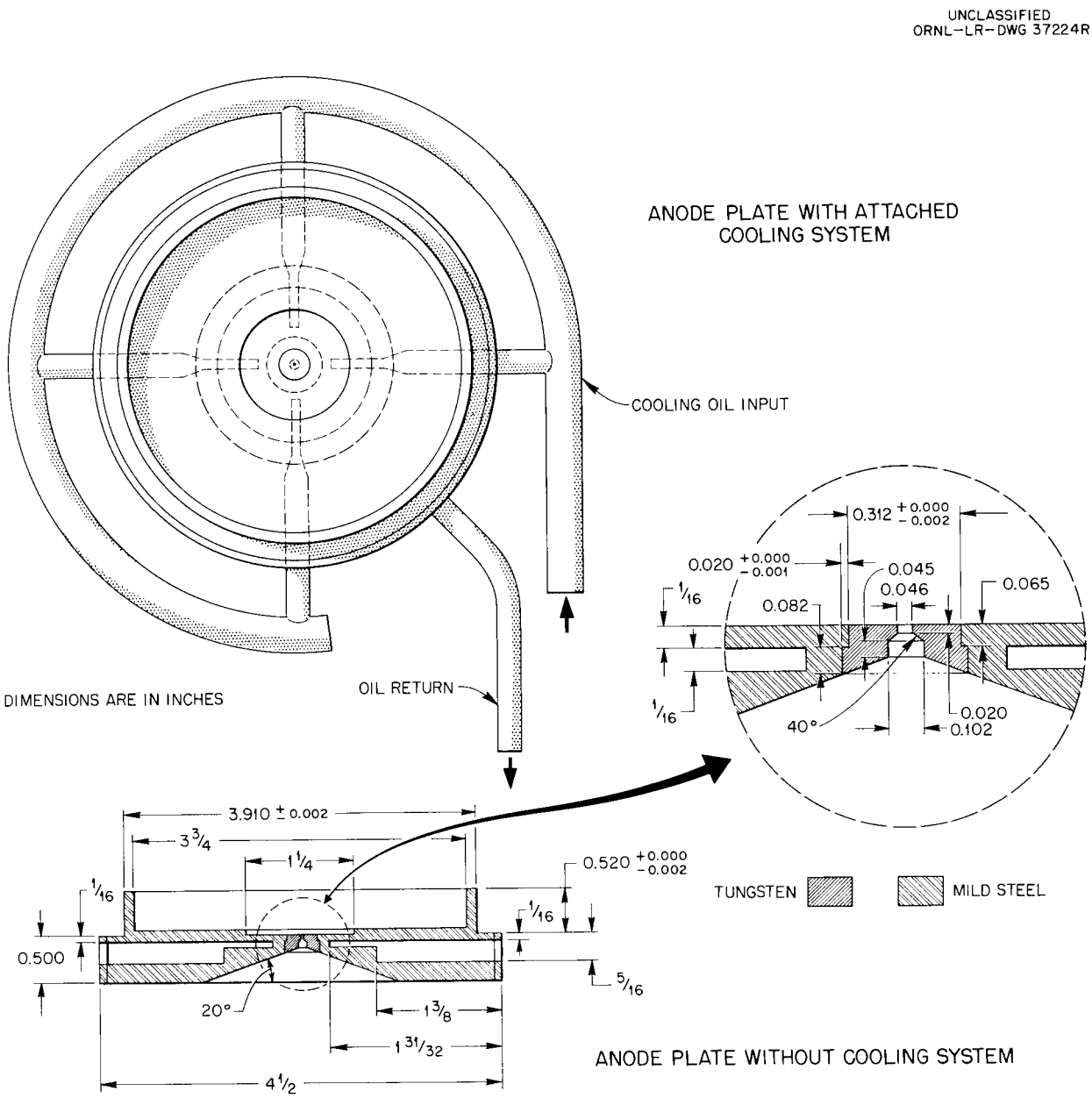

Fig. 5.1.1. Duo-Plasmatron Ion Source Anode Details.

cooling system is that a leak in the oil connections adjacent to the source may expose the neoprene O-rings, used for vacuum sealing, to the cooling oil. Since these O-rings are not impervious to this oil, contamination of the source volume has frequently occurred. Therefore, a self-contained water cooling system is being considered.

5.1.3 OPERATING CHARACTERISTICS

Some of the operating characteristics of a source with the anode plate shown in Fig. 5.1.1 are given in Fig. 5.1.4. These curves are all based on data taken with an accelerator voltage of 60 kv. For the 0.046-in. aperture and 0.102-in. cup shown in the anode plate of Fig. 5.1.1, the maximum total

UNCLASSIFIED
PHOTO 34644

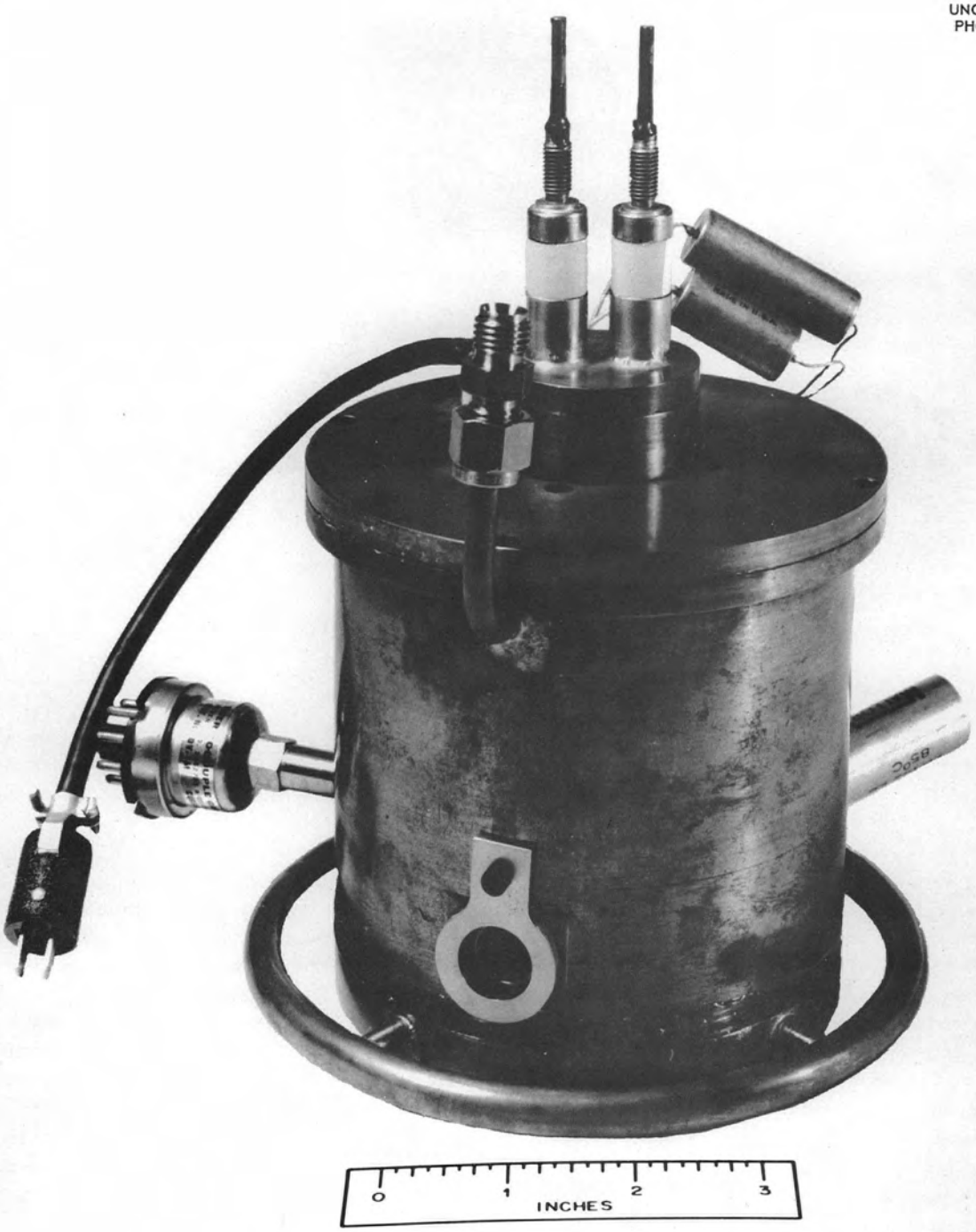

Fig. 5.1.2. Assembled View of a Duo-Plasmatron Ion Source.

Fig. 5.1.3. Disassembled View of a Duo-Plasmatron Ion Source. Top and bottom.

ion current was about 100 ma. This current was obtained with a central-electrode-to-anode spacing of 0.060 in. and an accelerating voltage of 70 kv at an anode-to-accelerator spacing of 0.140 in.

In an attempt to determine the gas efficiency of the source described in Figs. 5.1.1 and 5.1.4, the leak rate of hydrogen gas through the 0.046-in. aperture was determined as a function of the source pressure, as indicated by a thermocouple gage for the range of 50–150 μ Hg. Without changing the calibration of the gage, the maximum output current from the source was determined as a function of pressure. For a source pressure of 75 μ, corresponding to a leak rate of 1.29 atm cm^3 of hydrogen per minute, the maximum total ion current obtained was 75 ma. From mass analysis of the beam for the same source pressure but for lower arc current and accelerating voltages, approximately 75% of the ions extracted are H_2^+, 12% H^+, and 13% H_3^+. This information indicates a source efficiency of 81%. This efficiency would not be correct if the ratio of H^+, H_2^+, and H_3^+ for a constant source pressure varied significantly at higher output currents. Facilities have been built for the mass analysis of a source at higher output currents and are about to be put into use.

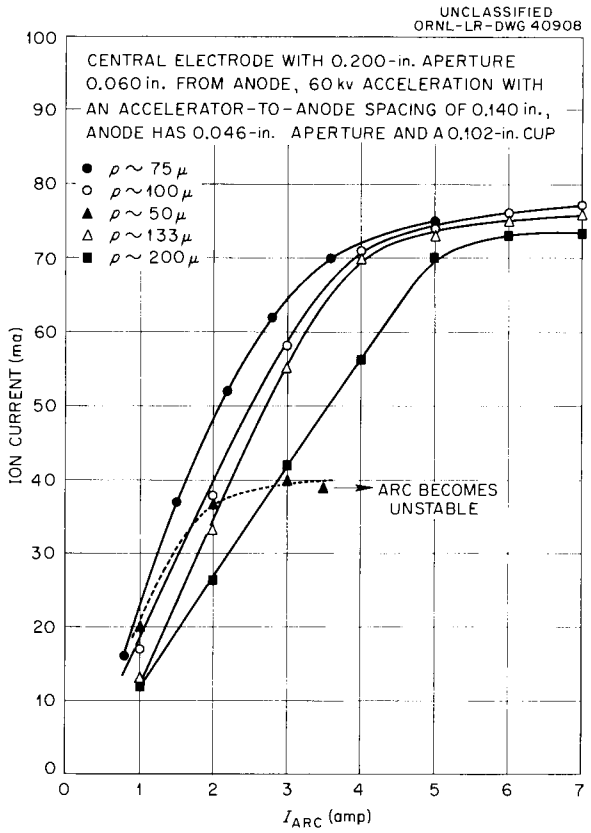

Fig. 5.1.4. Output Current as a Function of Arc Current at Indicated Source Pressures for a Duo-Plasmatron Ion Source.

5.2 HIGH-CURRENT ACCELERATOR TUBE DEVELOPMENT

An accelerator tube has been designed and is being constructed which will be able to handle ion currents of up to 0.5 amp. The design of the system was determined by considerations of the space-charge forces in these high-current beams. After acceleration, the beam must travel through a region of high pumping speed, through the DCX coil regions, and to the arc. This distance cannot be conveniently decreased to less than 5 ft. It is also necessary that the beam diameter at the arc be less than 1 in. in order to obtain the maximum dissociation efficiency. To meet these requirements, two solutions seemed feasible. (1) The beam may be space-charge neutralized over its entire path length after acceleration. (2) It may be permitted to expand sufficiently in the accelerator tube by its natural divergence so that appreciable further expansion does not take place. Electromagnetic lenses may then be used to focus the beam to the necessary shape at the arc. The latter solution was accepted as the more practical one.

The accelerator tube details are shown in Fig. 5.2.1 and a sketch of the system is shown in Fig. 5.2.2. The maximum internal electrical gradients between electrodes are 150 kv/in.

As a result of the experience with the present accelerator tube on DCX, it was felt that the insulators should be extremely well shielded from direct view of the beam. In this system the insulator is isolated from the beam by at least two

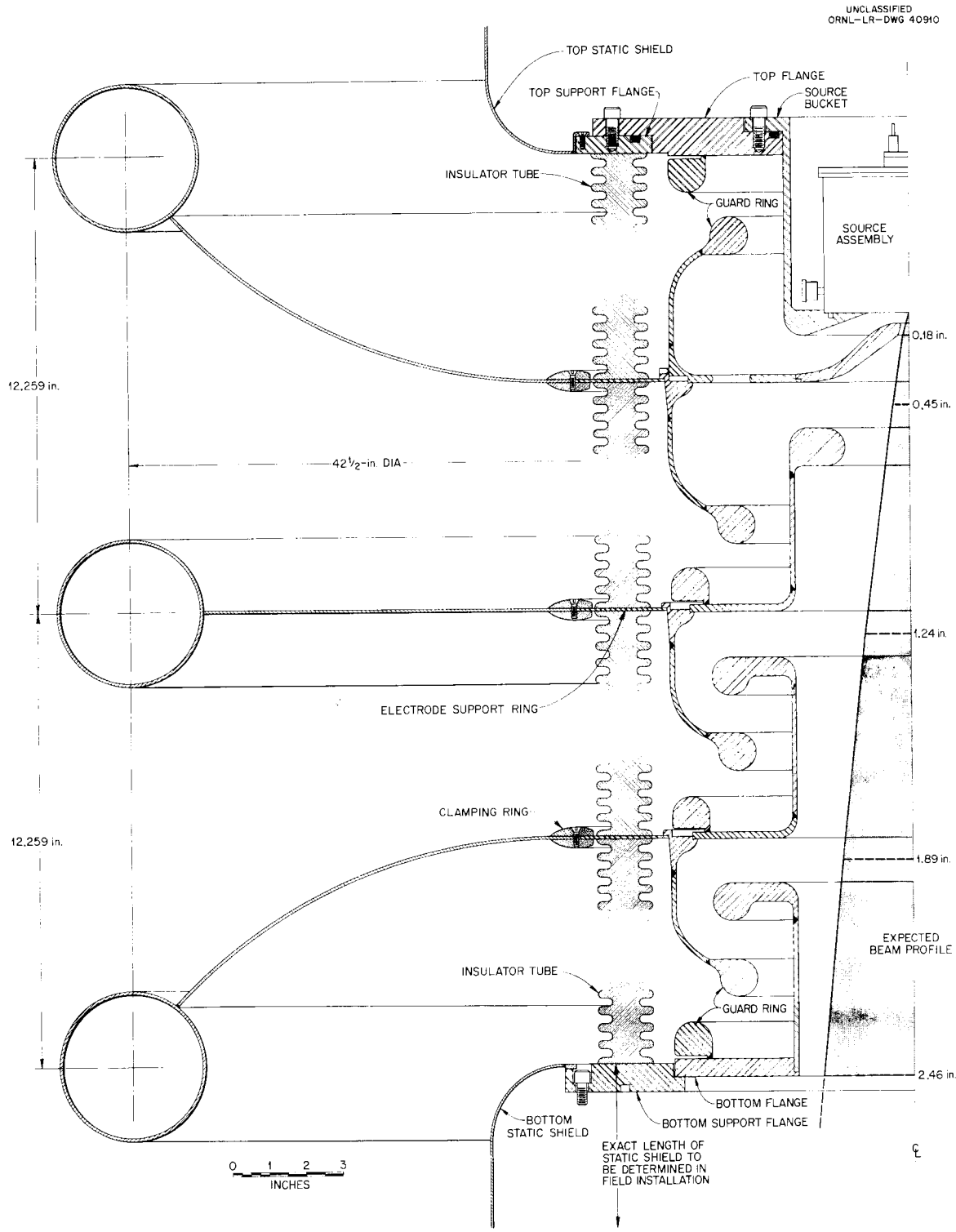

Fig. 5.2.1. Cross-Sectional View of Accelerator Tube. The beam radius is shown assuming 10° initial divergence.

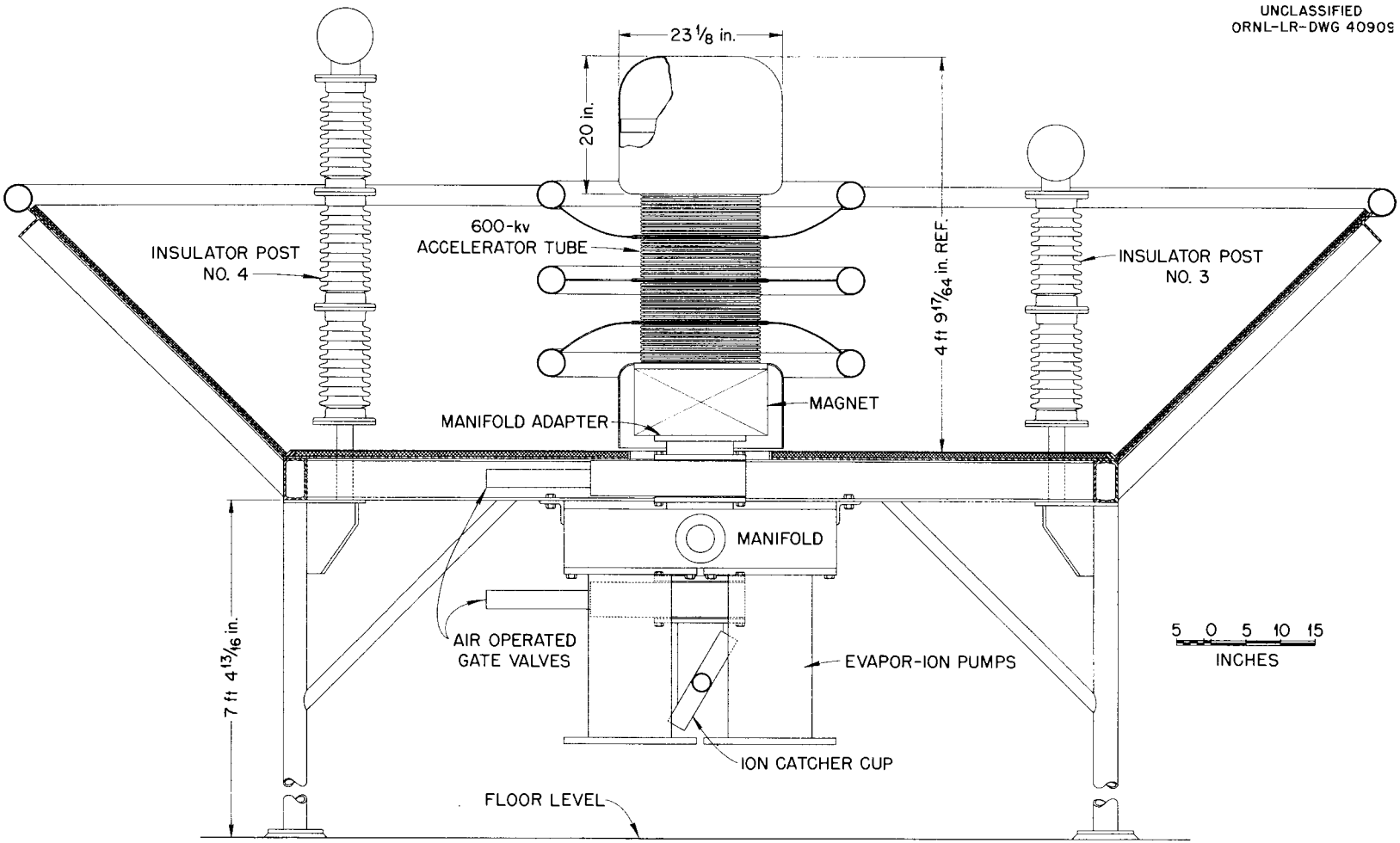

Fig. 5.2.2. Elevation View of Accelerator System Showing Positions of Accelerator Tube, Solenoidal Lens, Vacuum Manifold, and Evapor-Ion Pumps.

"bounces." The insulators will be sealed together with vinyl in a special aligning jig. The source will be positioned in the bottom of the reentrant piece at the top of the tube and a vacuum seal made against an O-ring.

Consideration was given to the possibility of magnetically analyzing the beam in the high-voltage terminal to remove the unwanted H_1^+, H_3^+, and H^0 components. In this respect, several major problems arise. To obtain good enough resolution with modest magnetic fields the beam must be handled at ~50 kv. To avoid disastrously large space-charge expansion it must, then, be neutralized during its analysis and along its path up to the accelerator itself. Sufficient pumping speed must be provided to handle the unwanted components. The pumping capacity must be ~0.1 mm liter/sec or 10^4 liters/sec at 10^{-5} mm Hg, a difficult achievement in the necessarily restricted space. Further, the lens action of the analyzing magnet places severe restrictions on the energy variations in the 50-kv, 0.5-amp power supply (also raised to 600 kv) in order that the object position for the "accelerator lens" be relatively stable. As a result, it was decided that beam analysis should take place at ground potential in the DCX field.

The accelerator electrodes are made from highly polished, nickel-plated stainless steel. The overall path length of the beam in the tube will be only 18 in. The beam will be accelerated to 300 kev in the first 3 in. so that space-charge blowup at low velocities can be minimized. The focal lengths of the lenses associated with the electrode gaps are all very much longer than the spacings. As a result, there will be, essentially, no focusing of the beam by the lenses at the accelerating gaps. The expected beam envelope is shown in Fig. 5.2.1 with the initial divergence from the 150-kv accelerator assumed to be 10°. It is hoped that this figure may be improved on because of the higher accelerating potential in this system compared with that used by Von Ardenne in ref 1 in the previous section. The beam diameter at the bottom of the accelerator tube under these conditions would be ~5 in. This beam will then immediately enter a solenoid magnet with a minimum 16-in. focal length which is being purchased from Pacific Electric Motor Company, Oakland, California. This company will also provide a 50-kw motor generator set to power the magnet. The lens will focus the beam to 0.4 of its diameter at the position of "maximum casting distance."[1] At this point, the beam is parallel. A pair of quadripole magnetic lenses will then focus this beam at the position of the arc in DCX. These quadripoles will have a minimum focal length (combined) of 20 in., and are also being purchased from Pacific Electric Motor Company.

The pumping system must handle the gas flow due to the beam for preliminary experiments (0.5 ma = 0.1 mm Hg-liter/sec). In order to reduce the organic molecule contamination of the system, four Evapor-Ion pumps, manufactured by Consolidated Electrodynamics Corporation, Rochester, N.Y., will be used. These will provide a pumping speed of ~30,000 liters/sec for hydrogen in the manifold. The pressure in the tube is expected to be $\sim 10^{-5}$ mm Hg.

The design of the first accelerator electrode was made on the same principles as described in Sec 5.1. However, if it is found that we can hold a higher voltage across the gap than indicated at present, higher currents may be feasible with the present system.

[1] C. D. Moak *et al.*, *Rev. Sci. Instr.* (to be published).

6. INSTRUMENTATION

6.1 HIGH-FREQUENCY FILTER FOR THE DCX 600-kv POWER SUPPLY

F. T. May

A filter circuit has been designed and built by the Thermonuclear Diagnostics Group to improve the regulation of the DCX 600-kv power supply. The filter will make any instantaneous step voltage in the power supply appear as an exponential rise, with a time constant of 1 sec, at the point that determines the accelerating potential for the input ion beam into DCX. The resulting 1-sec rise is slow enough to be regulated by the transistor regulator previously described.[1] Therefore, high-frequency fluctuations that previously would have saturated the derivative amplifiers in the regulator can be regulated with the filter in the regulation loop. The filter circuit is clamped to follow large voltage excursions of the high-voltage set and will automatically put itself into operation at any d-c level with a dynamic range of ±15 kv.

A low-voltage analog of the filter was built to check the theory and proved to be quite satisfactory. The final model has been built and will be given a trial run at 50 kv as soon as the test equipment required is ready. The plans are to then install the filter on top of the Cockcroft-Walton 600-kv power-supply stack.

6.1.1 THEORY OF OPERATION

A block diagram of the filter, Fig. 6.1.1, will be used to derive the response of the output to a step input. The analysis follows from the diagram and is developed through the equations:

$$i_2 = \frac{E - E_g - E_0}{R_1} , \qquad (1)$$

$$i_3 = \frac{E_g + E_r}{R_2} , \qquad (2)$$

$$i_1 + i_2 = i_3 , \qquad (3)$$

$$\beta E_0 = \int \frac{i_1 dt}{C} + E_g + E_0 , \qquad (4)$$

$$E_0 = i_4 R_4 , \qquad (5)$$

and

$$E = -uAE_g + i_4(r_p + R_4) . \qquad (6)$$

Combining Eqs. (1), (2), (3), and (4) yields:

$$\beta E_0 = \frac{1}{C}\int\left(\frac{E_g + E_r}{R_2} + \frac{E_g + E_0 - E}{R_1}\right) dt + E_g + E_0 . \qquad (7)$$

Then from Eqs. (5) and (6):

$$E_g = \frac{E_0 - E}{uA} , \qquad (8)$$

where

$$R_4 \gg r_p .$$

[1] F. T. May, *Thermonuclear Project Semiann. Rep. Jan. 31, 1959*, ORNL-2693, p 57–58.

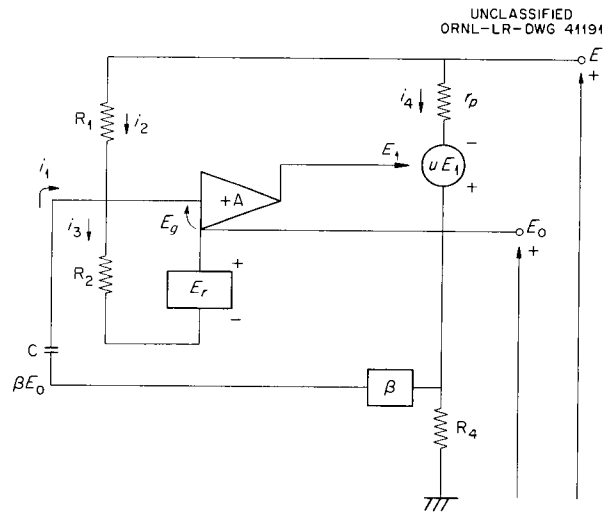

Fig. 6.1.1. Block Diagram of High-Frequency Filter for DCX 600-kv Power Supply.

Combining Eqs. (7) and (8) then gives:

$$\beta E_0 = \frac{1}{C}\int\left[\left(\frac{E_0 - E}{uA}\right)\left(\frac{1}{R_2}+\frac{1}{R_1}\right)+\frac{E_r}{R_2}+ + \frac{E_0 - E}{R_1}\right]dt + \frac{E_0 - E}{uA} + E_0 \ . \quad (9)$$

Taking the derivative of both sides of (9) results in:

$$\dot{E}_0\left(\beta - 1 - \frac{1}{uA}\right) = = (E_0 - E)\left[\frac{1}{uA}\left(\frac{1}{CR_1}+\frac{1}{CR_2}\right)+\frac{1}{CR_1}\right] + + \frac{E_r}{R_2} - \frac{\dot{E}}{uA} \ . \quad (10)$$

Assuming $|1/uA| \ll |\beta - 1|$ and $uAT_2 \gg T_1$, where $T_1 = R_1 C$ and $T_2 = R_2 C$, reduces Eq. (10) to:

$$\dot{E}_0(\beta - 1) = E_0 - E\left(\frac{1}{T_1}\right) + \frac{E_r}{T_2} - \frac{\dot{E}}{uA} \ . \quad (11)$$

From Eq. (11)

$$\dot{E}_0 - E_0\frac{1}{T_1(\beta - 1)} = \frac{-E}{T_1(\beta - 1)} + + \frac{E_r}{T_2(\beta - 1)} - \frac{\dot{E}}{uA(\beta - 1)} \ . \quad (12)$$

Equation (12) is the simplified notation for the time relations of the applied high voltage, E, and the output voltage, E_0, that is seen by the DCX accelerator tube. To study the time response, a step function, V, is applied to E. Using Laplace transforms the resulting equation is:

$$E_{0(s)}\left[S - \frac{1}{T_1(\beta - 1)}\right] = = -E_{(s)}\left[\frac{S}{uA(\beta - 1)} + \frac{1}{T_1(\beta - 1)}\right] + + \frac{E_r}{T_2(\beta - 1)S} + E_{0(+0)} + \frac{E_{(+0)}}{uA(\beta - 1)} \ . \quad (13)$$

With the initial conditions:

$$E_{0(+0)} = E - E_r\frac{T_1}{T_2} \ , \quad (14)$$

$$E_{(+0)} = E \ , \quad (15)$$

and the final applied voltage $(E + V)$, Eq. (13) becomes:

$$E_{0(s)} = \frac{-(E+V)\left[\frac{S}{uA(\beta - 1)} + \frac{1}{T_1(\beta - 1)}\right] + \frac{E_r}{T_2(\beta - 1)} + S(E - E_r)\frac{T_1}{T_2} + \frac{ES}{uA(\beta - 1)}}{S\left[S - \frac{1}{T_1(\beta - 1)}\right]} \ . \quad (16)$$

From this, using partial fractions and inverse Laplace transforms:

$$E_{0(t)} = E + V - E_r\frac{R_1}{R_2} - V\exp\frac{t}{T_1(\beta - 1)} \ , \quad (17)$$

where again

$$\left|\frac{1}{uA(\beta - 1)}\right| \ll |1| \ .$$

Defining

$$\alpha = \frac{R_1}{R_2} = \frac{T_1}{T_2} \ ,$$

and substituting

$$T_1 = R_1 C = R_2 C\left(\frac{R_1}{R_2}\right) = R_2 C\alpha \ ,$$

the time constant of the response is

$$T_r = R_2 C \alpha(\beta - 1) \ , \qquad (18)$$

as shown in Fig. 6.1.2.

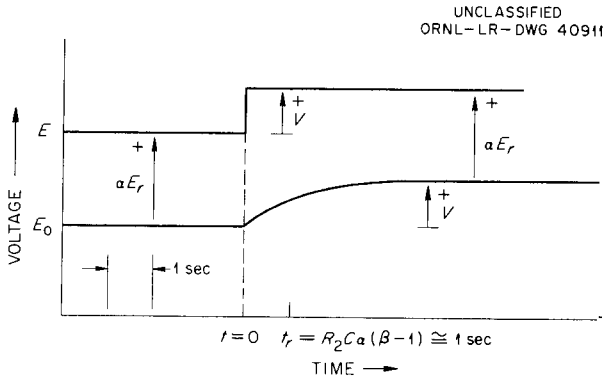

Fig. 6.1.2. Response of Output Voltage, E_0, to a Step Voltage, V.

6.1.2 CIRCUIT DESIGN

Taking into consideration the restrictions imposed in the foregoing theory, the circuit in Fig. 6.1.3 was designed. The entire apparatus is built on three separate aluminum boxes. One chassis has an unregulated 1.7-kv power supply for the 4-125A tube and another one has a regulated ±300-v power supply for E_r and the lower-voltage vacuum tubes. The main circuitry is on the third chassis and includes, in addition to the filtering circuit, a clamping circuit that protects the circuit and allows it to follow large changes. The clamping circuit utilizes the 12AT7 triodes and the 6AL5 diodes and is driven from the precision resistor string that goes from the plate of the input 6AU6 to the grid of the 4-125A.

The actual values of the terms referred to in the analysis are:

$$\beta = \frac{750 \text{ meg}}{752.5 \text{ meg}} = \frac{300}{301} \ ,$$

$$\beta - 1 = -\frac{1}{301} \ ,$$

$$E_r = 300 \text{ v} \ ,$$

$$\alpha = \frac{60 \text{ meg}}{1 \text{ meg}} = 60 \ ,$$

$$R_4 = 750 \text{ meg} \ ,$$

$$R_1 = 60 \text{ meg} \ ,$$

$$C = 0.1 \ \mu\text{f} \ ,$$

$$R_2 C = 51 \times 10^6 \times 10^{-7} = 5.1 \text{ sec} \ ,$$

$$T_r = 5.1 \times 60 \times \frac{1}{301} \simeq 1 \text{ sec response time} \ .$$

An interesting arrangement that should be noted is the use of the 50-meg resistor on the input grid of the 6AU6. This resistor allows the input time constant R_2C to use the total 51 megs for R_2 while the $\alpha = R_1/R_2$ uses only the 1 meg for R_2. This was necessary for practical reasons since for a long response, ~1 sec, R_2 must be of the order of 50 meg. However, to have an α of the desired 60, then R_1 would have to be 3000 megs. This is completely impractical; therefore, the arrangement shown was used. The voltage αE_r, 18 kv, will normally be across the high-voltage GL-6C21, which is a 35-kv tube. This voltage rating will easily allow for a reasonable swing of ±15 kv. The spark gap shown is set, of course, to protect against large swings, especially when the high-voltage set is turned on with the full 20 v from the transistor regulator on the field coil of the motor generator set.

Now that the equipment has been built, all that remains is the final checkout and then installation in the regulation loop. When completed, the regulation capabilities of the loop will extend to much higher frequencies than previously possible, and therefore the input ions into DCX will be more nearly monoenergetic.

UNCLASSIFIED
ORNL-LR-DWG 40912

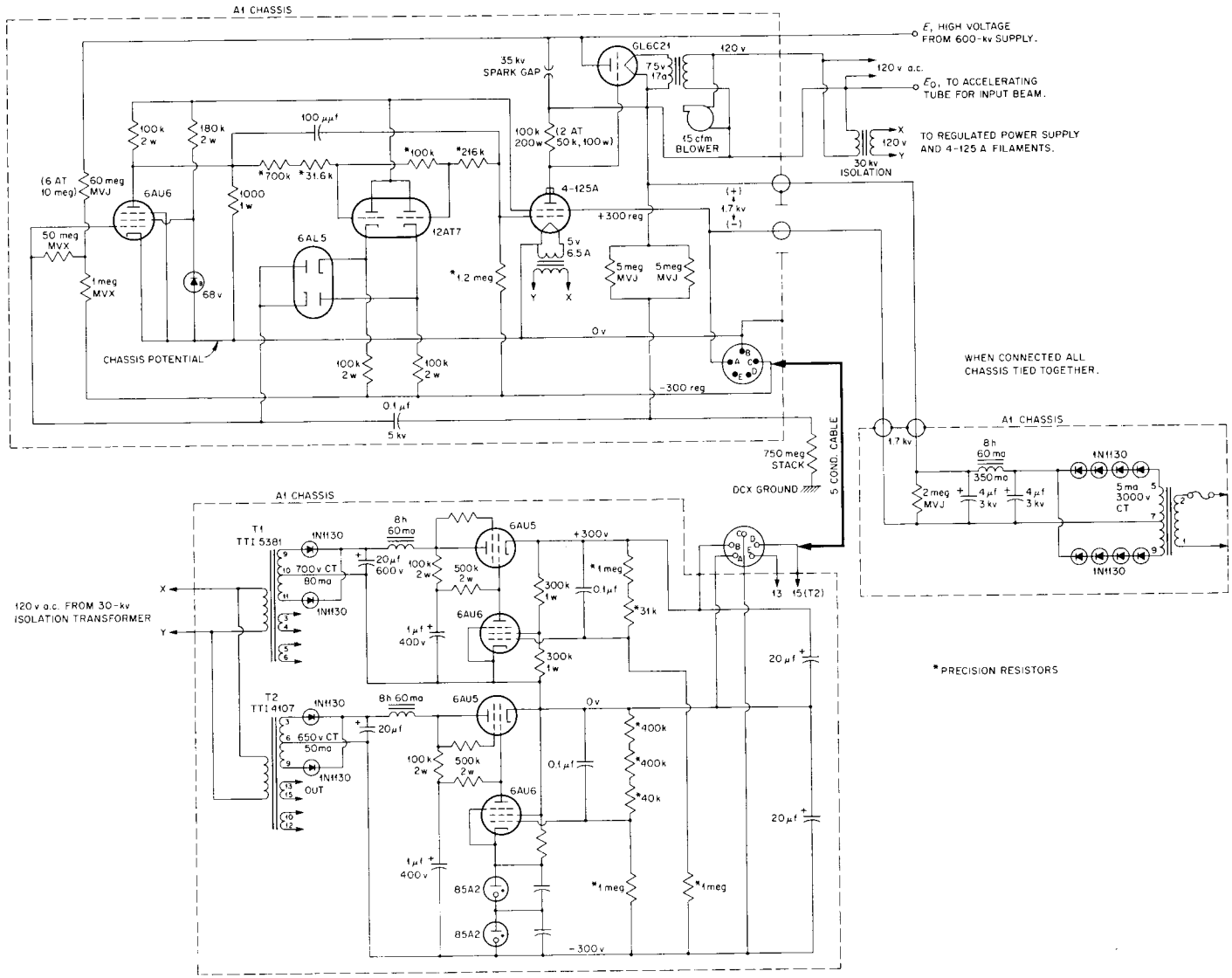

Fig. 6.1.3. Complete Circuit Diagram of High-Frequency Filter for DCX 600-kv Power Supply.

6.2 VARIABLE-Q, VARIABLE-FREQUENCY FILTER AMPLIFIER

F. T. May

A variable-Q, variable-frequency filter amplifier has been developed by the Thermonuclear Diagnostics Group to facilitate synchronous detection of signals from several Sherwood diagnostics tools. The filter is built around three basic transistorized amplifier blocks. A Q of greater than 1500 has been attained at a resonant frequency, f_o, of 1000 cps. The ability to attain such high Q and have control over both Q and f_o makes this filter far superior to any conventional LC filter.

The primary purpose of the circuit is improvement of the signal-to-noise ratio in the microwave detection equipment. The present plans are to build ten of these amplifiers and a summing amplifier to be used to detect a signal from a square-wave modulation of the input beam into DCX. In this application the Q will be of the order of 100, and the resonant frequencies will be the fundamental and the next nine harmonics of the modulating square wave. This will, in effect, take the Fourier analysis of the signal, eliminating the noise which lies outside the filters' passbands, and then will recombine the frequencies in the summing amplifier to reproduce the signal. This method permits the filtering of a repetitive non-sinusoidal signal with a minimum of wave-form distortion. Due to the decreased noise bandwidth the resulting signal-to-noise ratio is greatly improved over that obtainable with a simple low-pass filter of bandwidth sufficient to pass the desired signal with equivalent distortion. This will allow for much better microwave data, which in turn means a better device for density measurements.

6.2.1 THEORY OF OPERATION

The operation of the filter can be best explained by comparing the analysis of the block diagrams of Figs. 6.2.1 and 6.2.2. The transfer function for Fig. 6.2.1 is Z(feedback)/Z(input), which is:

$$\frac{e_0}{e_1} = \frac{(R/r) + (PL/r)}{P^2LC + PRC + 1} , \qquad (1)$$

where P is the Laplace operator.

In Fig. 6.2.2, the loop must be analyzed to get e_0/e_1. The first step is shown in Fig. 6.2.3, where the three basic amplifiers have been replaced by their individual transfer functions, which are again Z(feedback)/Z(input). With the following definitions $T = RC$, $\alpha = R_2/R_1 \simeq 1$, and β = (voltage feedback ratio on 3) ≤ 1, a loop equation can now be written:

$$\left[e_0\left(-\frac{1}{PT+\beta}\right) + e_1\right]\left(-\frac{1}{PT}\right)(-\alpha) = e_0 , \qquad (2)$$

UNCLASSIFIED
ORNL-LR-DWG 42313

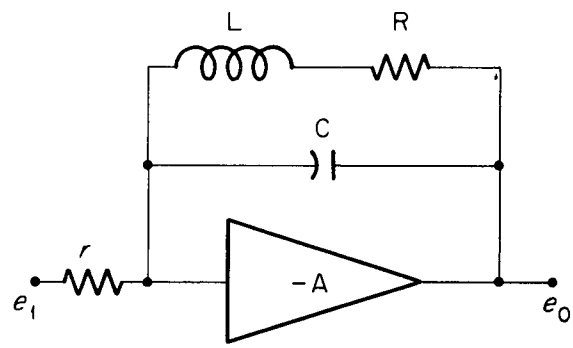

Fig. 6.2.1. Block Diagram of a Filter Circuit Using Inductance to Determine Q.

UNCLASSIFIED
ORNL-LR-DWG 42314

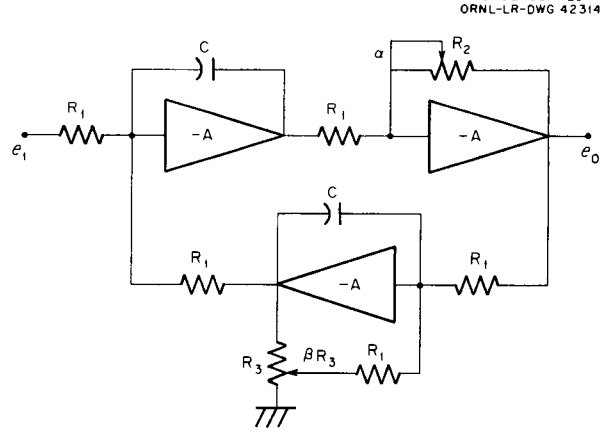

Fig. 6.2.2. Block Diagram of the New Filter Amplifier with Variable Q and f_0.

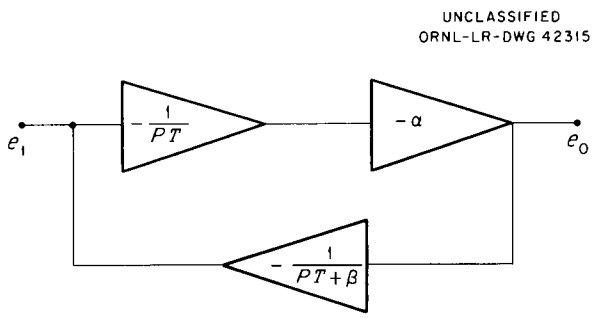

Fig. 6.2.3. Simplified Block Diagram of New Filter Amplifier Showing Transfer Functions of the Three Basic Operational Amplifiers. Here $T = RC$, $\alpha = R_2/R_1 \cong 1$, and β (voltage feedback ratio on R_3) $\cong 1$.

from which

$$e_1 = e_0\left(\frac{PT}{\alpha} + \frac{1}{PT+\beta}\right) , \tag{3}$$

giving the transfer function

$$\frac{e_0}{e_1} = \frac{\beta + PT}{(P^2T^2/\alpha) + (PT\beta/\alpha) + 1} . \tag{4}$$

Equation (4) is now in the same form as Eq. (1). To find the relationship of the constants first equate the denominators:

$$P^2LC + PRC + 1 = P^2\frac{T^2}{\alpha} + PT\frac{\beta}{\alpha} + 1 , \tag{5}$$

which yields

$$\frac{T^2}{\alpha} = LC , \tag{6}$$

$$\frac{T\beta}{\alpha} = RC ; \tag{7}$$

then equate numerators giving:

$$\frac{R}{r} + P\frac{L}{r} = \beta + PT , \tag{8}$$

$$\beta = \frac{R}{r} , \tag{9}$$

$$T = \frac{L}{r} . \tag{10}$$

Eliminating r from Eqs. (9) and (10) gives:

$$\frac{\beta}{T} = \frac{R}{L} . \tag{11}$$

Now from (6), (7), and (11) the desired relations are found by substituting the common filter equations:

$$f_o = \frac{1}{2\pi\sqrt{LC}} , \tag{12}$$

and

$$Q = \frac{2\pi f_o L}{R} . \tag{13}$$

Direct substitution yields:

$$f_o = \frac{\sqrt{\alpha}}{2\pi T} , \tag{14}$$

which is the resonant frequency, and

$$Q = \frac{\sqrt{\alpha}}{\beta} , \tag{15}$$

which is the Q of the filter. Other familiar filter terms can now be expressed in terms of the new parameters, such as:

$$\text{Bandwidth} = \frac{\beta}{T} , \tag{16}$$

$$\text{Gain at } f_o = \frac{\alpha}{\beta} . \tag{17}$$

Also, the limits on the highest possible gain and Q are set by the open loop gain of the operational amplifiers. Taking into consideration the finite gain, these limits are found to be approximately:

$$Q_{max} \cong G_{max} \cong \frac{A}{4} . \tag{18}$$

Since α and β can be varied, it can be seen from (14) and (15) that f_o can be set with α, and then the desired Q can be chosen with β. The f_o is first closely picked with T, which actually means picking C, and then α allows for the fine adjustment.

6.2.2 CIRCUIT DESIGN

A circuit has been designed using transistors since they provide sufficient open loop gain with adequate frequency response and require very little space for the entire set of ten filters. The circuit diagram is shown in Fig. 6.2.4. With the phase-advance networks that were employed for stability, the frequency response was reduced to a few thousand cps. However, since the fundamental square wave that will be used is 50 cps, the tenth harmonic will still have enough gain for satisfactory operation. The silicon diode coupling in the amplifiers is employed to set the collector-to-emitter voltage of the interstage transistors at –0.7 v, which puts them in a linear operating region. Also, since this permits direct coupling, the d-c levels for the entire loop can be set with the biasing resistors on the individual amplifier block's input bases.

Although this circuit does have the quality required to provide good filtering, it is questionable as to the ability to reproduce a good matched set for the desired number of harmonics. The biasing, for example, will vary as transistors are replaced, and the frequency response is marginal for higher harmonics that may later be desired. With this in mind, more work is being done to design a more desirable transistorized operational amplifier that will fulfill this need and can be used in other applications. When the new amplifier design is completed, the set of ten filters will be built and incorporated in the microwave density-detection apparatus.

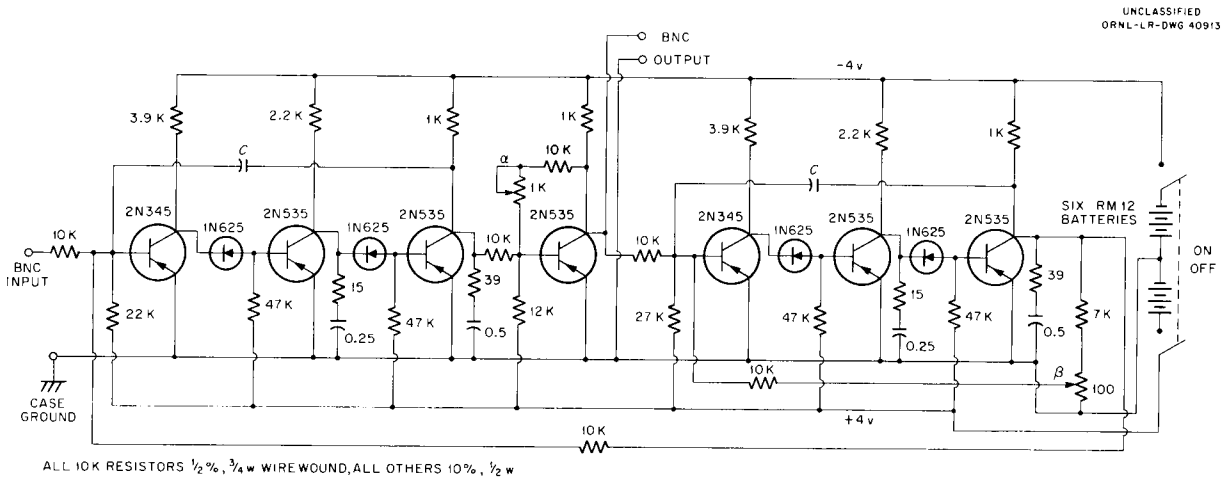

Fig. 6.2.4. Complete Circuit Diagram of a Filter Amplifier. C is chosen for the desired f_0 by the equation

$$C = \frac{1}{2\pi f_0 \times 10^4} = 15.9 \times 10^{-6} \frac{1}{f_0} .$$

6.3 OXIDE SANDWICH DETECTOR

M. C. Becker
R. A. Strehlow
R. J. Kerr
R. A. Dandl

The problem of measuring ions spiraling out of the mirrors of DCX has pointed to the need for a particle detector which does not have inactive edges. Particles on the verge of being lost at the mirrors will make very small progress along the field during a cyclotron revolution. Consequently, with any presently available detector having its necessary shield structure, the ions are all captured in an insensitive area. A solid-state detector of cylindrical or wedge shape consisting of a base charge-collector plate covered with a thin layer of solid dielectric and overlaid with a thin opaque film of metal, for optical and electrical shielding, might meet the need described above (Fig. 6.3.1). Its insensitive edge thickness could be only a few thousand angstroms (ΔZ in Fig. 6.3.1).

This detector would be applicable for detection of neutral particles as well as ions since most neutral particles will become charged upon penetrating the shield layer and appear at the collector plate as ions. It should have more durability than neutral detectors using self-supporting metal foils, and should be fairly easy to produce with a variety of base-plate configurations ranging from flat plates and wedges to cylinders or even spheres.

UNCLASSIFIED
ORNL—LR—DWG 40914

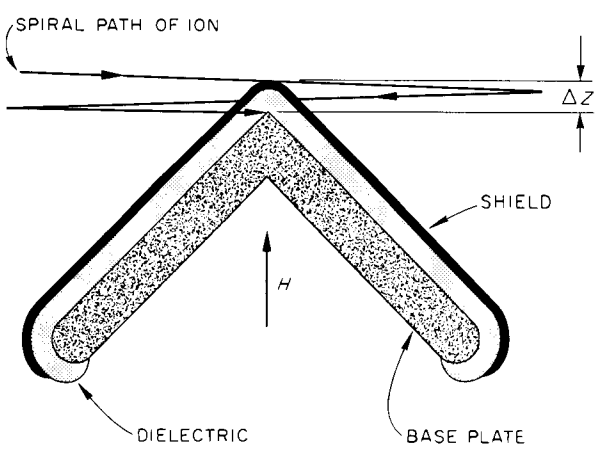

Fig. 6.3.1. Cross Section of Solid State "Oxide Sandwich" Detector Intercepting an Ion in a Magnetic Field.

6.3.1 REJECTION OF SEMICONDUCTORS

Semiconductor counters have been found very useful in some applications.[1] But although they should be useful in Sherwood diagnostics, they will not solve the present problem. They are very difficult to produce in the sizes needed (~10 cm^2 and up), requiring single crystals of high purity. Semiconductor counters are sensitive to light, both visible and ultraviolet, and very sensitive to radiation damage and temperature change. They would be difficult to calibrate in terms of an incident flux of particles.

6.3.2 CHOICE OF DIELECTRIC, SHIELD, AND BASE MATERIALS

We are attempting to develop a solid-state detector that will meet the qualifications already outlined. The base material employed is aluminum, with an Al_2O_3 dielectric layer. Shield layers of gold and aluminum are being tested. Alumina has high resistivity and fairly low dielectric constant, which are required for its use as the dielectric layer. Present transistor amplifiers have equivalent input noise of 10^{-9} amp so that the detector leakage current should be $<10^{-9}$ amp. The resistivity of alumina is listed[2] as high as 10^{14} ohm-cm. This means that an area of 10 cm^2 could be made as thin as 10^{-4} cm and still be usable with an ~1-v collection potential on the detector. It turns out that anodized layers have been produced which actually show about two orders of magnitude greater resistivity than the handbook value so that a layer of alumina 2×10^{-5} cm thick and 10 cm^2 in area has a resistance of about 10^{10} ohms. The dielectric constant of

[1] F. J. Walter *et al.*, *A Study of Germanium Surface Barrier Counters*, ORNL CF-58-11-99 (November 1958).

[2] C. D. Hodgman, R. C. Weast, and S. M. Selby, *Handbook of Chemistry and Physics*, p 2525, Chemical Rubber Publishing Company, Cleveland, 1958.

Al_2O_3, 5.5 (ref 3), means that a detector sandwich with area of 10 cm^2 and thickness of 3×10^{-5} cm has a capacity of 0.017 μf. This gives an RC time of 0.17 msec with the present transistor amplifiers which have 10^4 ohms input resistance. Transients up to 10^{-3} sec in duration can then be followed closely. A practical detector, which will be called the oxide sandwich, might then have a 10-cm^2 aluminum base plate overlaid with a 3000-Å layer of Al_2O_3 and completed with a shield layer of about 1000 Å of aluminum. The total surface density of material an incident particle would be required to penetrate would then be 132 $\mu g/cm^2$. By comparison, a 10-μin. nickel foil, such as those in the present DCX neutral particle detectors, has a surface density of 226 $\mu g/cm^2$.

Method of Fabrication

The first method of making the Al_2O_3 layer was high-temperature oxidation of aluminum in a furnace. Growth of oxide was very slow at temperatures below the softening point of aluminum. The next method was anodization in 10% H_2SO_4 electrolyte. The films produced by this method were thick enough, but they were porous because alumina is soluble in sulfuric acid. These films also had low resistance. Next, anodization was again tried, but in ammonium citrate electrolyte in a method similar to that used by Hauser and Werner[4] to make strong nonporous films. Alumina is not soluble in an electrolyte of this type (adjusted to pH 3.5–6.0), and a barrier layer type of oxide film is formed whose thickness is determined by the applied potential. Growth of the film stops in the ammonium citrate when the thickness reaches 14 Å/v. By using polished foils of commercial purity it was possible to obtain films 2800 Å (11 μin.) thick with a resistance of a few times 10^{10} ohms. Resistance of thinner films did not decrease linearly with thickness, but was about $\frac{1}{10}$ of that of the 2800-Å films. This nonlinearity of resistance with film thickness may be caused by pores and cracks, which were observed by an optical microscope.

The next step was to put anodic films on base plates suitable for use as detectors. Highly polished surfaces are necessary. E. H. Long, of the Metallurgy Division, solved the problem of polishing aluminum plates to the required smoothness. The plates are polished mechanically with Syntron vibratory polishers using water slurries of successively finer abrasives, the last being Linde B. If the plate is pure enough the final polishing is done electrolytically in $HClO_4$. Impurities cause pitting in the electropolishing process, and therefore plates of less pure material (2S) were given a final polishing mechanically with MgO abrasive on velvet.

After being polished, the plates are anodized to 2800 Å in citrate electrolyte. Particular care is now being used to eliminate structural imperfections in the oxide. Two necessary precautions are the use of very low growth rates, and stirring to maintain uniform electrolyte concentration. In addition, all aluminum used is 99.996% pure. After the aluminum is anodized, the sandwich is completed by evaporating an ~1000-Å film of gold or aluminum on the oxide layer. A few of such oxide sandwiches showed 4×10^9 ohms resistance for areas of ~10 cm^2. The rejection rate has been high. Present sandwiches are easily damaged and do not have long life. Absorption of water or lack of sufficient washing of electrolyte may be responsible for the short lifetimes.

A finished plate with dielectric resistance of 4×10^9 ohms, connected with battery and electrometer, as shown in Fig. 6.3.2, was irradiated with 5.3-Mev alpha particles. With $\sim 2.5 \times 10^5$ particles/sec penetrating the film the measured current was 2×10^{-10} amp or 12×10^8 electrons/sec. This is a charge multiplication factor of $\cong$ 2500. The energy loss for an alpha particle which penetrates 3000 Å of alumina is 68 kev. The energy gap between valence and conduction

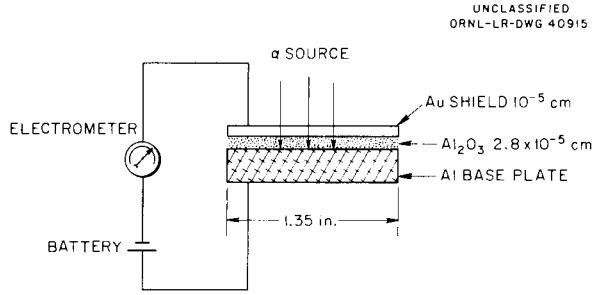

Fig. 6.3.2. Test Setup for Oxide Sandwich Detector.

[3] G. Haas and A. P. Bradford, *J. Opt. Soc. Am.* **44**, 810–15 (1954).

[4] U. Hauser and K. Werner, *Rev. Sci. Instr.* **29**, 380–82 (1958).

electron bands in alumina is ~8 ev (ref 5). If one assumes 20 ev average energy for the formation of each secondary electron by the alpha particle, then a total of 3400 electrons should be formed by each alpha as it penetrates the dielectric. The mean free path of these secondaries is quite long in an insulator, and so it is not unreasonable to expect that most of them would be collected by the metal plates. This would account for the charge multiplication factor. However, the direction of current flow was not a function of the polarity of the applied potential. The exterior electron current due to the alpha irradiation was always from the gold to the aluminum base plate. This phenomenon is difficult to explain, and steps are being taken to study it further. The first step was to make a symmetrical oxide sandwich consisting of 2800 Å of aluminum oxide between two layers of aluminum, each 1000 Å thick. A glass plate was used as a base. Alpha-induced current in this sandwich seemed to flow with applied potential, though surface effects of some of the uncoated Al_2O_3 made results hard to evaluate. A new sandwich is being fabricated with all dielectric surfaces shielded.

The primary effort at present is being directed toward preparation of oxide sandwich samples suitable for testing with a beam of energetic protons. These are being made with polished aluminum base plates and also with aluminum films evaporated on glass as base plates.

[5] N. B. Hannay, *Semiconductors*, Reinhold, New York, 1959.

6.4 MICROWAVE DIAGNOSTICS UTILIZING THE FARADAY EFFECT

H. W. Shields H. O. Eason T. K. Fowler

Equipment is being constructed for density measurements in DCX utilizing Faraday rotation of microwaves (application of this method to DCX was suggested by R. A. Dandl). With this method it may be possible to measure electron densities as low as $N \sim 10^9$ particles/cm^3 and to measure the electron collision frequency, ν, as well. The first rotation measurements will be made in DCX on plasmas obtained from gas breakup, since it is convenient to install the gear in ports normally occupied by the carbon arc.

Microwaves are to be propagated through the plasma parallel to the principal component of the magnetic field, B_z, along the symmetry axis, rather than across the field with $\vec{E} \times \vec{B} = 0$ as in conventional phase-shift measurements of density. The method hinges on the fact that in this case the initially plane wave separates into right and left circularly polarized components (designated − and + here) which propagate with different (complex) indices of refraction, n_- and n_+, since one wave rotates with the sense of the electron cyclotron motion and the other with that of the ions. The two circular waves, initially of the same phase and amplitude, thus emerge from the plasma with different phase and amplitude and recombine to form an elliptical wave which, if absorption is negligible, is almost plane polarized but rotated by an angle θ with respect to the original plane of polarization.

It is the rotation θ which is to be measured, θ being proportional to N. The rotation is greatly enhanced by resonances at microwave frequencies ω near the cyclotron frequencies of both ions and electrons. We intend to work at the higher of the two, the electron resonance (Ku band), in order that the wavelength be less than plasma dimensions. Of course, in the highly nonuniform magnetic field of DCX, cyclotron resonance can be maintained over only a short path length, just an inch or two around the heart of the plasma at the midplane. Even so, in a given plasma the rotation angle obtainable is greater than the phase shift of the conventional method by a factor greater than

$$\sqrt{\omega/(\omega_0 - \omega)} \ ,$$

ω_0 being the electron cyclotron frequency at the midplane. This factor can easily be made ~10 without violating the auxiliary requirement, to be discussed, that $\omega < \omega_0 - \nu$. Then a density $N = 10^9$ particles/cm^3 would produce a measurable rotation $\theta \sim 1°$, as compared with a phase shift ~0.1° which would be swamped by the background.

6.4.1 EQUIPMENT

The microwave circuit designed to make the Faraday rotation measurements is a simple transmission system employing the plane polarization of the TE_{01m} mode in a rectangular wave guide as a polarization analyzer. Plane electromagnetic waves radiated from a rectangular horn will pass through the plasma and be received with a second rectangular horn. The receiving horn and connecting guide can be rotated about the axis of the guide and horn, and will be set so that the polarization of waves propagated in the guide will be at an angle of 90° with the polarization of waves radiated from the microwave source. Unless the radiated energy is rotated by the plasma, it will not propagate through the receiving horn and guide. When the plane of polarization of transmitted energy is rotated, the receiving unit will be rotated manually, and the amount of rotation necessary to minimize the energy reaching a crystal detector will be read from a protractor.

6.4.2 THEORY

If the ratio of amplitudes of the two circular components of the elliptically polarized wave reaching the receiver is a and their phase difference is δ, the ratio, R, of intensity along the minor axis of the ellipse to that along its major axis is easily found to be

$$R = \left(\frac{1-a}{1+a}\right)^2 , \qquad (1)$$

and the rotation of the major axis with respect to the polarization of the initial plane wave is

$$\theta = \frac{\delta}{2} \qquad (2)$$

to first order in δ. The quantities a and δ are related to n_- and n_+ by

$$\delta = 2\theta = \int dz \frac{2\pi\omega}{c} \mathrm{Re}(n_- - n_+) , \qquad (3)$$

$$a = \frac{1-\sqrt{R}}{1+\sqrt{R}} = \exp \int dz \frac{2\pi\omega}{c} \mathrm{Im}(n_- - n_+) , \qquad (4)$$

and

$$n_\pm^2 = 1 - \frac{\omega_p^2/\omega}{\omega \pm \omega_c - i\nu} \text{ (ref 1)} , \qquad (5)$$

where ω_p is the plasma frequency, proportional to $\sqrt{N}$, and ω_c is the electron cyclotron frequency, which in the nonuniform DCX field varies with the distance z from the midplane approximately as

$$\omega_c = \frac{3}{2}\omega_0 \left(1 - \frac{1}{3}\cos\frac{2\pi z}{L}\right) , \qquad (6)$$

L being the distance between mirrors.

The integrations in Eqs. (3) and (4) extend over the path length through the plasma. For plasmas thin enough so that ω_c can be treated as constant, the evaluation of θ is immediate. We shall therefore limit detailed attention to cases when integration is essential, probably the more usual situation in DCX when the plasma density is so low that the rotation method is required to measure it.

We consider first the case $\omega < \omega_0 - \nu$. Then, if also $\omega_p^2/\omega(\omega_0 - \omega) < 1$, $d\theta$ in Eq. (3) becomes

$$d\theta \cong dz \frac{\pi\omega}{c} \frac{\omega_p^2}{\omega^2} \frac{1}{2}\left(\frac{\omega}{\omega_c - \omega} + \frac{\omega}{\omega_c + \omega}\right) . \qquad (7)$$

Integrating this and a similar approximation for Eq. (4) yields

$$\theta \cong \frac{\pi}{2} \frac{L\omega}{c} \frac{\omega_p^2}{\omega^2} \sqrt{\frac{\omega}{\omega_0 - \omega}} \quad \begin{pmatrix}\text{Off resonance} \\ \omega < \omega_0 - \nu\end{pmatrix} , \qquad (8)$$

$$\frac{1-\sqrt{R}}{1+\sqrt{R}} \cong \exp\left(-\frac{\nu}{\omega_0 - \omega}\theta\right) . \qquad (9)$$

Note that θ is independent of ν. Also, because of the midplane resonance, the exact path length does not appear if $\omega_c - \omega$ at the end of the path is a few times its minimum value, the midplane value.

---

[1] This is the zero-temperature dispersion relation of J. E. Drummond, *Phys. Rev.* 112, 1460 (1958). Ion motion is neglected, since we work at $\omega \sim \omega_0$. At high temperatures, thermal motion would introduce absorption in addition to the collision damping which has been included, and the measurement of ν described here would become a measurement of these combined effects. However, in DCX we are well outside Drummond's criterion for important temperature effects, namely,

$$\left(\frac{\sqrt{mkT}}{eB/c}\right)_{\text{electron}} \gtrsim \omega/n_\pm c .$$

For B of the order of the DCX field, the latter can be satisfied only for densities such that $n \gg 1$. In DCX, $n_\pm \sim 1$, even at resonance.

In DCX, this means a few inches of path. The measurement yields an average value of N heavily weighted by its values near the midplane.

Equation (8) is our principal result and exhibits the resonance enhancement factor claimed above. Note that the enhancement is gained at the expense of sharpness in the definition of the polarization; that is, from Eq. (9), the greater θ is, the greater is R and hence the more circular is the wave. However, for rotations of a few degrees, $R \sim 0$, and the wave, essentially plane, has a sharply defined polarization direction.

We now consider the case $\omega = \omega_0$. In this case, to evaluate Eqs. (3) and (4) we use the approximations of Eq. (7), etc., over that portion of the path where $\omega \lesssim \omega_0 - \nu$, and in the principal resonance region near the midplane, where $\omega_0 - \omega < \nu$, we let $\omega_c = \omega = \omega_0$. As it turns out, the strong resonance occurs over a path length so short that it contributes little either to θ or to R, so that the results are much like Eqs. (8) and (9), except that θ now depends on ν:

$$\theta \simeq \frac{L\omega}{c}\frac{\omega_p^2}{\omega^2}\sqrt{\frac{\omega}{\nu}} \quad \begin{pmatrix} \text{On resonance} \\ \omega = \omega_0 \end{pmatrix} , \quad (10)$$

$$\frac{1-\sqrt{R}}{1+\sqrt{R}} \simeq \exp(-2\theta) \ . \quad (11)$$

Thus, if ω_p can be measured using Eq. (8) with $\omega < \omega_0 - \nu$, a measurement independent of ν, one can then move onto resonance, $\omega = \omega_0$, to measure ν from Eq. (10). Experimental difficulties with these coupled measurements include the fluctuation of N with time in DCX. This fluctuation also makes difficult an obvious experimental scheme for ensuring that one is clear of ν-dependence in measuring N: in principle, one could know he is in the region of validity of the ν-independent Eq. (8) by scanning in ω to see if the function $\theta(\omega)$ has the dependence on ω predicted by Eq. (8), which is quite different from that of Eq. (10).

Finally, we note that throughout the derivation it has been implicitly assumed that the magnetic field has only one component, B_z, whereas in fact the nonuniform field has a radial component, B_r, also. However, under the conditions of interest, wherein the wave remains approximately plane with only a slight rotation of polarization, the effect of B_r can be eliminated simply by launching the wave parallel to the symmetry axis with the electric vector radial. Even at higher densities where the wave is a fatter ellipse, B_r can effectively be eliminated by working in resonance with the component of cyclotron motion due to B_z, which is quite different from that due to B_r near the midplane, where $B_r \to 0$.

7. THEORY

7.1 ABSOLUTE CONTAINMENT OF IONS IN DCX

T. K. Fowler M. Rankin

The study of orbits of single ions in the azimuthally symmetric DCX magnetic field has been continued[1] and a detailed report concerning the absolute containment (containment by virtue of the conservation of energy and the canonical angular momentum) of ions encircling the symmetry axis of the field has been issued.[2] In summary, the report presents a derivation of the absolute containment criterion together with plots of the regions in space and momentum space to which absolutely contained particles are confined. The plot of spatial confinement regions for 300-kev deuterons has been reproduced in Fig. 7.1.1. The plot is two-dimensional because of the azimuthal symmetry; r and z are cylindrical coordinates defined with respect to the magnetic symmetry axis, the center of the machine lying at $r = 0$, $z = 0$. The different curves apply to particles with different canonical angular momentum, p_θ, particles of given p_θ being confined within the contour corresponding to that value. Curves have been labeled both by p_θ/p (p being the deuteron momentum) and by the corresponding angle by which a newly injected ion must be scattered to have this value of p_θ. The largest contour shown, corresponding to particles which have been scattered at 42°, just reaches the magnetic mirrors and thus defines the critical scattering angle. Particles scattered at larger angles can escape through the mirrors.

[1] *Thermonuclear Project Semiann. Rep. Jan. 31, 1959*, ORNL-2693, sec 1.3.1.

[2] T. K. Fowler and M. Rankin, *Containment Properties of DCX*, ORNL CF-59-6-32 (June 15, 1959).

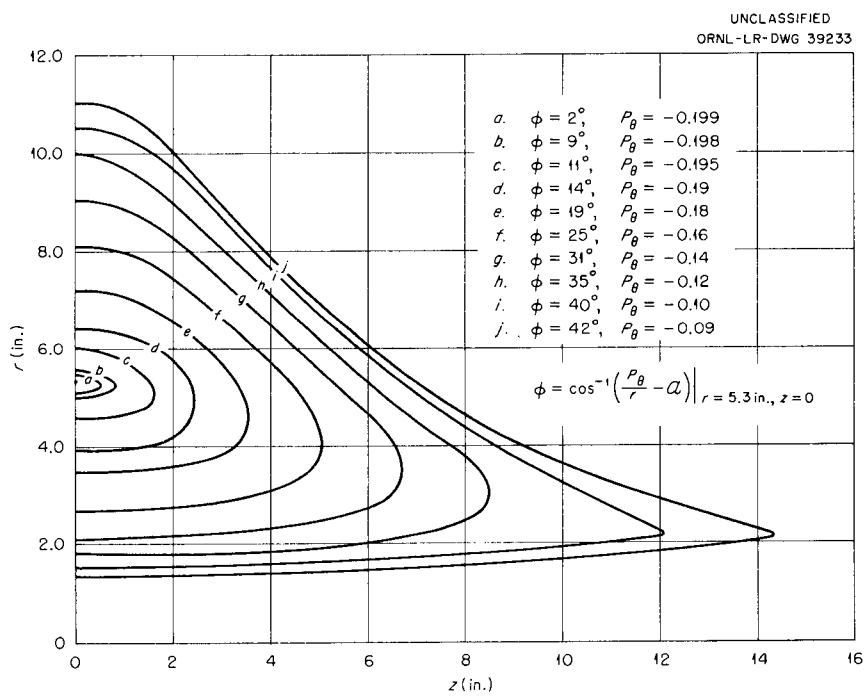

Fig. 7.1.1. Regions in Space Occupied by an Ion Absolutely Contained in DCX as a Function of Its Canonical Angular Momentum.

7.2 DCX ORBIT STUDIES

M. Rankin T. K. Fowler G. R. North

Various aspects of orbit properties were studied by means of codes programed for the Oracle. Included were those of: a particle initially at a mirror, periodic orbits, plots of midplane crossing conditions, interchange of r and z energy, azimuthal variation of orbits, and integration of time-independent orbit equations.

PARTICLE INITIALLY AT MIRROR

A series of Oracle runs was made in which a particle was initially considered as placed in an escaped position and its path followed backward into the interior of the machine. Slight variations in r_0 and $(P_z)_0$ (P_z and P_r represent fractions of the total momentum) were made in these cases. Some of these particles were reflected at the opposite mirror; some escaped. Conditions of these orbits at the midplane were studied. It was found that $P_z \sim 0.7$ (and P_r negative) were frequent midplane conditions just before escape.

PERIODIC ORBITS

An orbit which has a reflection point on the $(P_\theta/r - \mathfrak{A}) = -1$ curve (i.e., reflects with no P_r or P_z) and which crosses the midplane with $P_r = 0$ is a "one-pass periodic" orbit and is thus contained. Such orbits were quickly located with a short addition to the orbit code. Neighbors of two distinct periodic orbits found for $P_\theta = -0.09$ ft behaved quite differently. Near a periodic orbit having a reflection point at $r = 0.342$ ft no periodicity was seen. However, quasi-periodic orbits were found in the neighborhood of the periodic orbit reflecting at $r = 0.57$ ft. One of these, covering a range of about 2 in. in its midplane crossings, is shown in Fig. 7.2.1. Other, more complex, types of periodic orbits also exist; one with "three-pass periodicity" was found.

PLOTS OF MIDPLANE CROSSING CONDITIONS

To look for predictable patterns in orbits, many graphs were drawn from orbit data. At first these were drawn as λ, $|P_z|$ graphs[1] in polar coordinates, where

$$\lambda \equiv \tan^{-1} \frac{mr\dot{\theta}}{P_r} .$$

However, orbits with negative P_θ are not uniquely defined in this space, since r is a double-valued function of $mr\dot{\theta}$. Hence we now plot curves of midplane crossing conditions in an η, r polar coordinate system, where

$$\eta \equiv \tan^{-1} \frac{P_z}{P_r} .$$

A point in this space uniquely determines an orbit. Once a closed curve is established in η, r space, the complete history of the particle is known.

For a given P_θ, the η, r space is divided into a permissible and a forbidden region by energy considerations. For the equilibrium orbit of DCX ($P_\theta = -0.205$ ft) the permissible region is a single

[1] A. Garren *et al.*, "Non-Adiabatic Effects in Single Particle Orbits," in *Proceedings of Controlled Thermonuclear Reactions Conference*, TID-7536, Part 2, p 170 (September 1957).

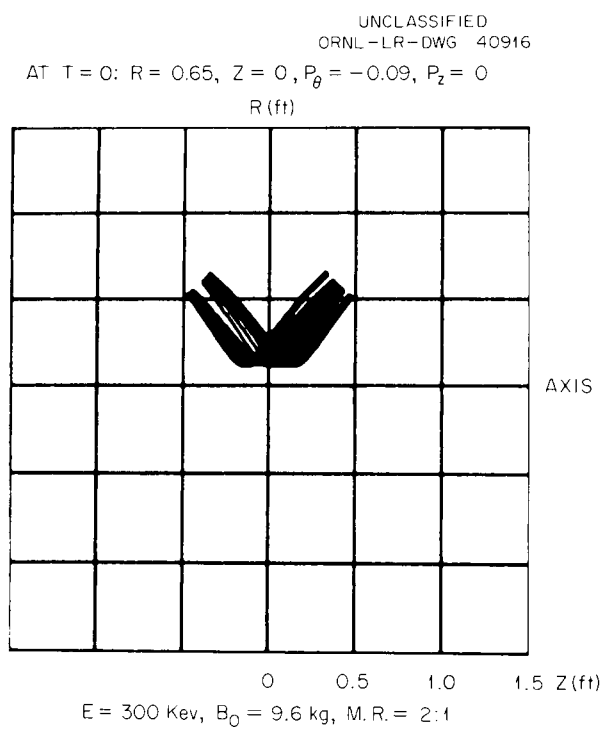

Fig. 7.2.1. Oracle Run of a Quasi-Periodic Ion Orbit in DCX.

point. As P_θ departs slightly from this value, the permissible zone enlarges and we see regular patterns form in the plots. By slowly varying P_θ we were able to observe pattern changes and also the introduction of much more complex patterns. These are illustrated in Figs. 7.2.2, 7.2.3, and 7.2.4. In all these cases $r_0 = 5.3$ in., $z_0 = 0$, and the curves are labeled by the initial value given to P_z at that point.

All the cases considered thus far have been for absolutely contained particles. It is hoped that by learning the behavior and changes in behavior of these particles we will be able to extend this study to nonabsolutely contained particles and discern patterns in their orbits.

INTERCHANGE OF r AND z ENERGY

A series of orbit runs with $P_\theta = -0.10$ was made with varying initial z momenta. It was found that with $(P_z)_0 \geqq 0.25$, interchange of r and z energy occurred quite rapidly. Figure 7.2.5 shows an

UNCLASSIFIED
ORNL-LR-DWG 40917

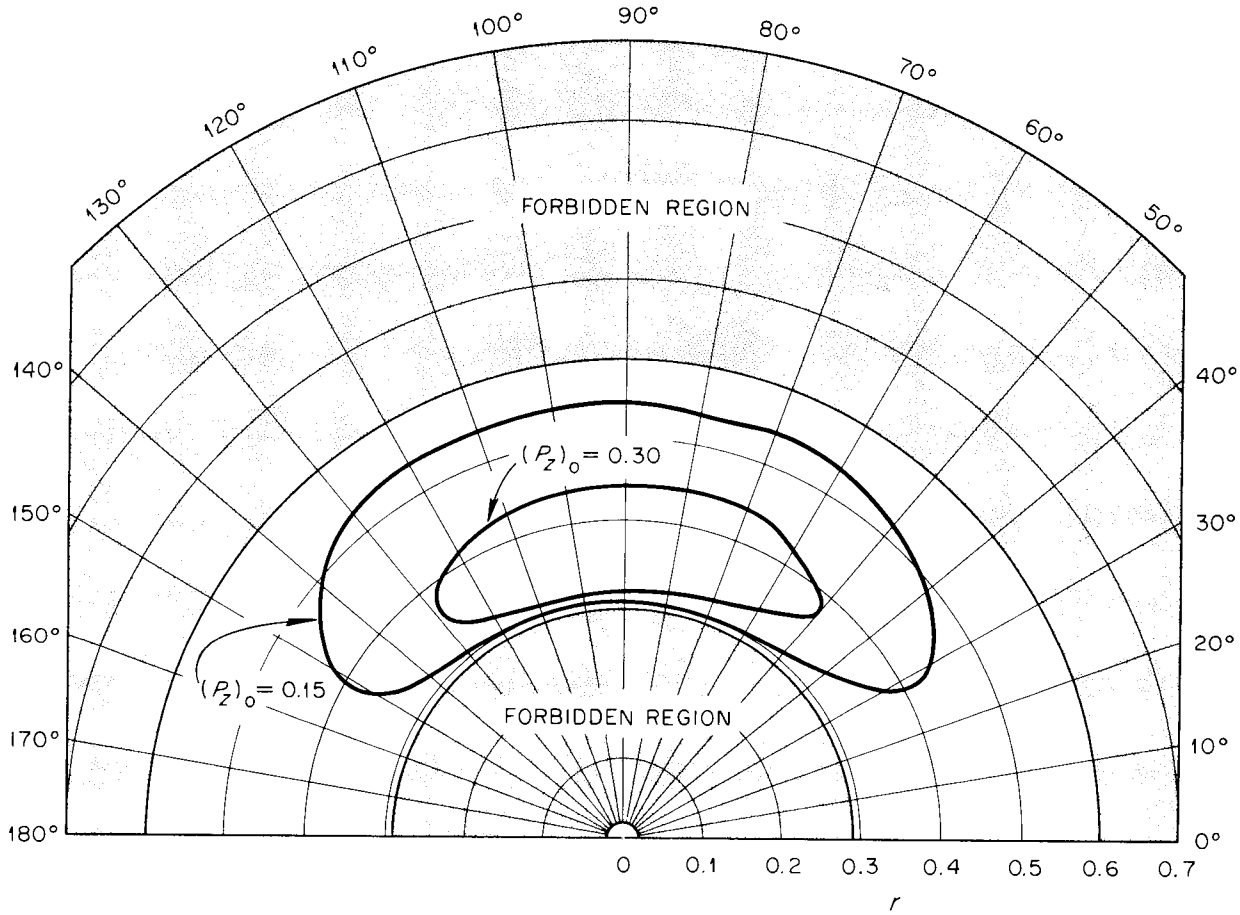

Fig. 7.2.2. Plot of $\eta - r$ for $P_\theta = -0.182$.

UNCLASSIFIED
ORNL-LR-DWG 40918

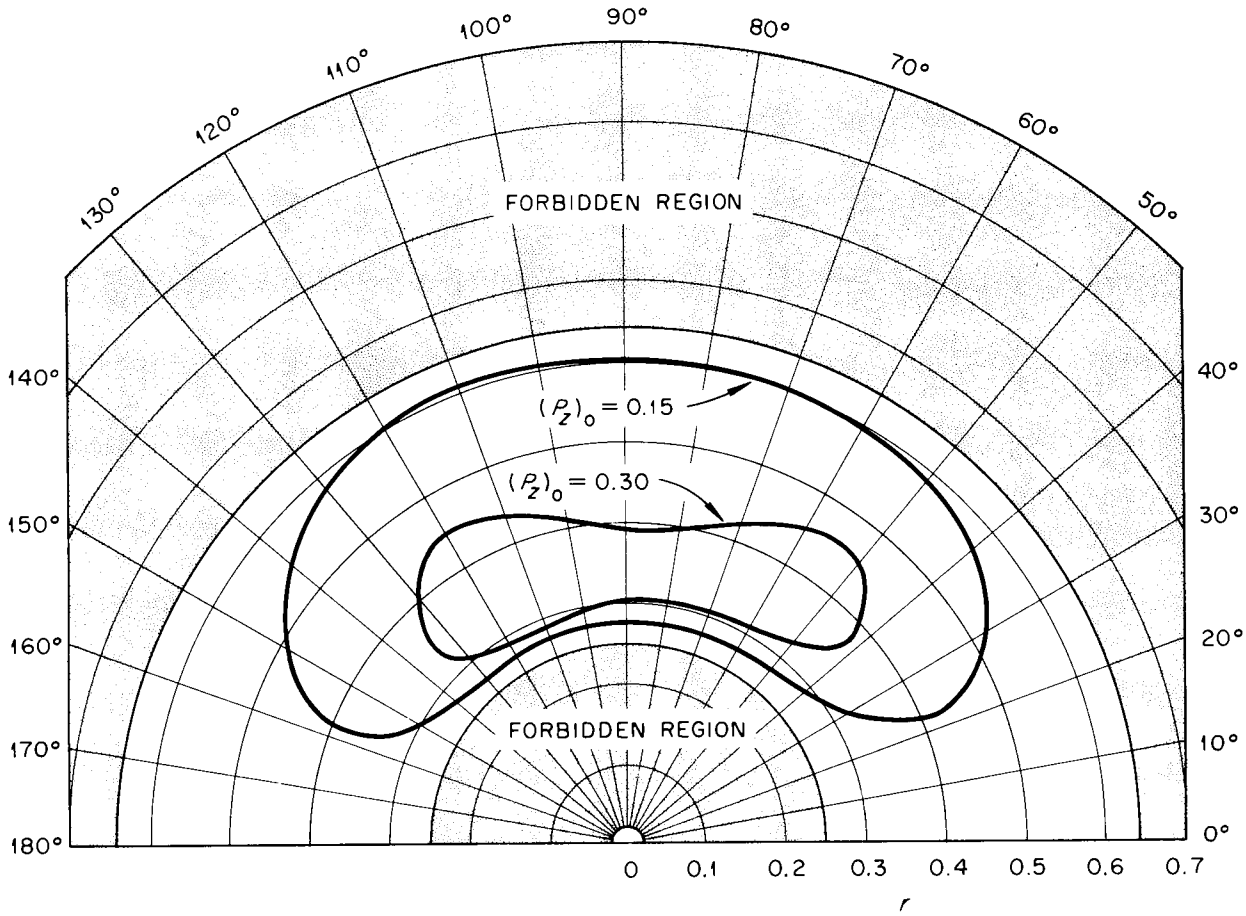

Fig. 7.2.3. Plot of $\eta - r$ for $P_\theta = -0.17$.

orbit run on the Oracle for a time corresponding to 3.5 μsec; the absolute containment region for this particle is seen to be well filled by this time. For $(P_z)_0 \leq 0.20$ Oracle runs were not long enough to show any such ergodic behavior.

AZIMUTHAL VARIATION OF ORBITS

At the suggestion of E. D. Shipley an addition was made to the orbit code to monitor θ motion. Studies to look for any grouping of θ values at reflection points have begun.

INTEGRATION OF TIME-INDEPENDENT ORBIT EQUATIONS

A code to integrate the time-independent equations of motion for a particle in DCX was written. However, initial runs with this code did not indicate any significant computing time advantage over the time-dependent code. It will be further investigated as time permits.

UNCLASSIFIED
ORNL—LR—DWG 40919

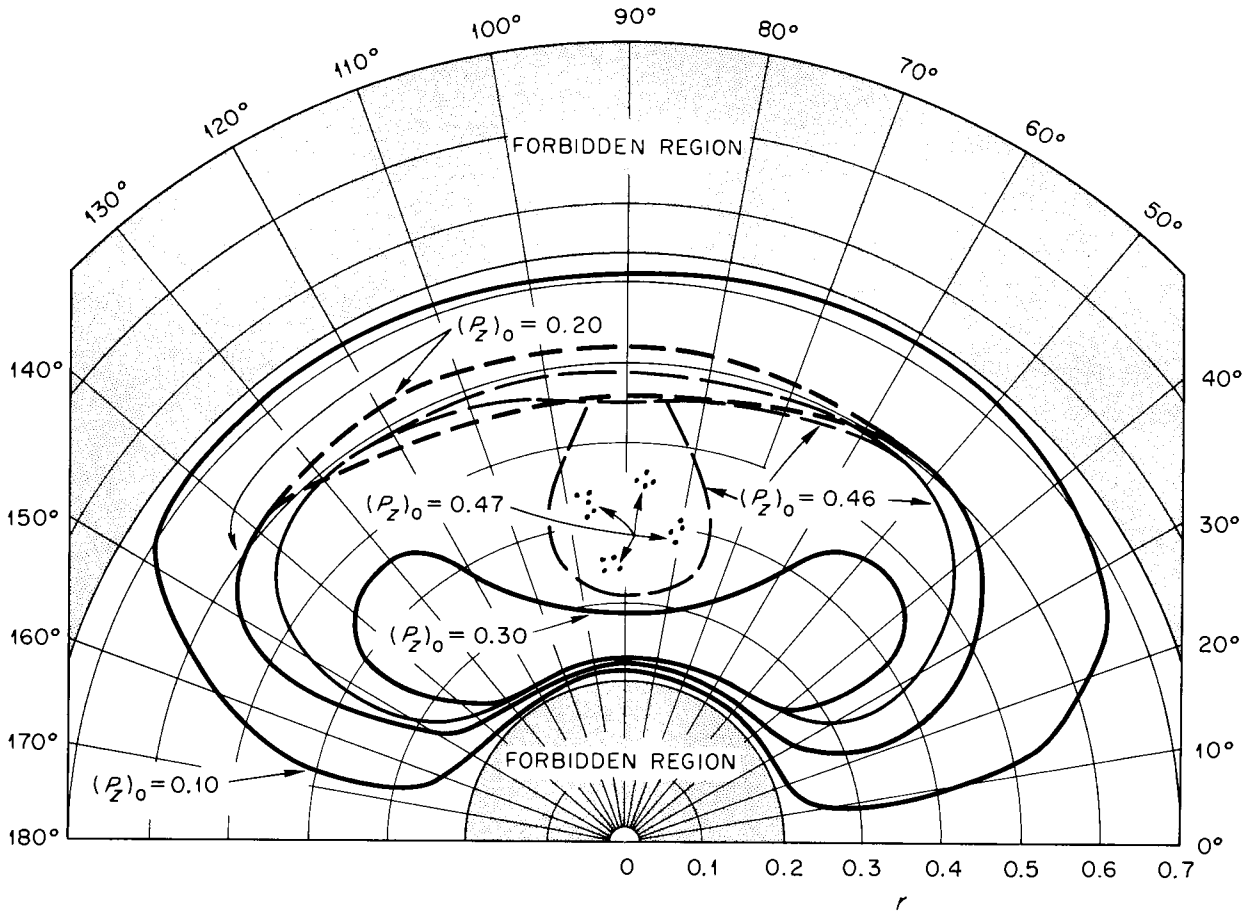

Fig. 7.2.4. Plot of $\eta - r$ for $P_\theta = -0.15$.

UNCLASSIFIED
ORNL-LR-DWG 40368

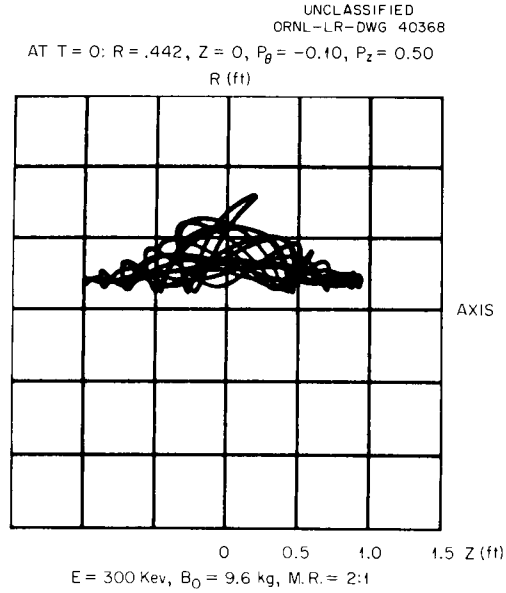

Fig. 7.2.5. Oracle Run of an Ion Orbit in DCX for a Time Corresponding to 3.5 μsec.

7.3 ORBIT PRECESSION IN DCX

T. K. Fowler

It has sometimes been suggested that in DCX undesirable effects of the carbon arc upon trapped ions (e.g., charge exchange) could be largely eliminated by deliberately causing the ions to precess to such a degree that they miss the arc most of the time. However, recent findings indicating that DCX mirror effectiveness is limited to "absolute containment" strongly curtail the amount of initial precession that can be tolerated. The larger the precession, the smaller the scattering necessary to transfer the ion to an orbit not absolutely contained. Specifically, if r_0 is the radius of the symmetric injection orbit, and X is the displacement of the guiding center of a precessing ion from the symmetry axis, an ion for which $X > r_0$ is lost immediately. Thus, we may limit attention to the condition $X \ll r_0$, in which case the following simple considerations are valid.

Consider motion in the midplane only. This is the most favorable case for missing the arc, since off the midplane the absolute containment regions become narrower in the r dimension. In the present approximation, the ion motion is a circle, radius r_0, with the center at $r = X$ (see Fig. 7.3.1). In a reference system in which the guiding center is at rest and the arc rotates, the arc motion sweeps out an annulus of width W, the diameter of the arc. Because when $X/r_0 \ll 1$ the frequency of arc rotation (i.e., the precession frequency) is much less than the frequency of ion rotation (the Larmor frequency), the ion may be assumed to encounter the arc once each ion revolution whenever the arc path intersects the ion orbit. This occurs a fraction $2\phi/2\pi$ of the time, ϕ being the intersection angle defined in Fig. 7.3.1. Then, the fraction f of time the particle spends *inside* the arc is:

$$f = \frac{W}{2\pi r_0}\,\frac{2\phi}{2\pi}\ , \qquad (1)$$

and g, the factor of decrease in f due to precession, is:

$$g = \frac{\phi}{\pi}\ . \qquad (2)$$

From the geometry of Fig. 7.3.1 it follows that:

$$\phi = \theta_- - \theta_+\ ,$$

$$\theta_\pm = \cos^{-1}\left\{\pm\frac{W}{2X}\,\frac{\left[1 \pm \left(\frac{X^2}{Wr_0} + \frac{W}{4r_0}\right)\right]}{\left(1 \pm \frac{W}{2r_0}\right)}\right\}\ , \qquad (3)$$

or, approximately, for $X/r_0 \ll 1$,

$$\phi = \cos^{-1}\left(-\frac{W}{2X}\right) - \cos^{-1}\left(\frac{W}{2X}\right)\ . \qquad (4)$$

Equation (4) has meaning only if $X \geqq \frac{1}{2}W$. For smaller displacements of the guiding center, the particle orbit always lies within the annulus swept out by the arc (i.e., $g = 1$). Approximation (4) gives the exact result in the two extreme limits $X = \frac{1}{2}W$, where $\phi = \pi$ and $g = 1$, and $X \to \infty$, where $\phi \to 0$ and $g \to 0$.

Typical values of X/W which can be tolerated might be <3, corresponding to $g > 0.1$.

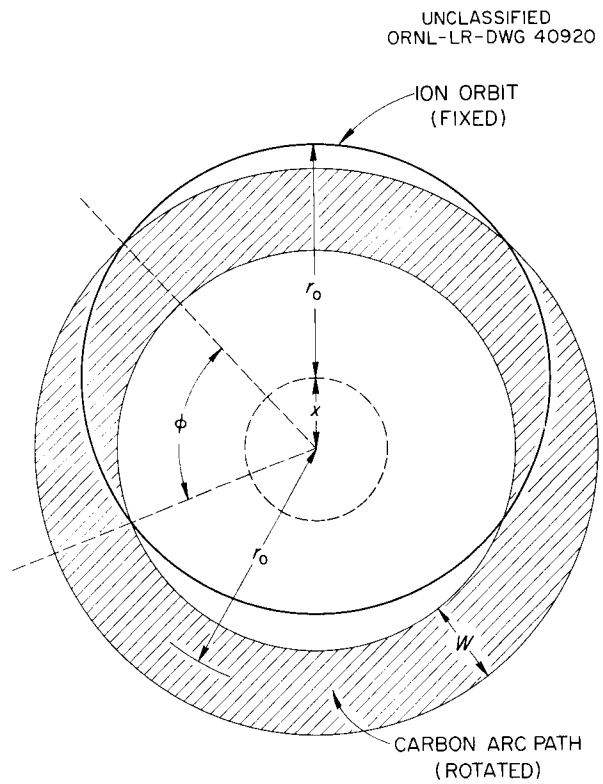

Fig. 7.3.1. Orbit Precession in DCX. Ion orbit arbitrarily fixed and arc path rotated to illustrate ϕ.

7.4 PARTICLE ORBITS IN A NONAZIMUTHALLY SYMMETRIC MIRROR FIELD

R. G. Alsmiller, Jr.

It has been shown by several authors that there is a class of single-particle orbits in an azimuthally symmetric mirror field which are absolutely contained.[1] The proof of this statement depends essentially on the symmetry (i.e., p_θ = const), and it is not known how slight deviations from symmetry will affect these absolutely contained orbits.

In order to obtain an estimate of the effects due to deviations from symmetry, p_θ is being calculated numerically by perturbation theory. If H_1 is the perturbing Hamiltonian we have the equation

$$\dot{p}_\theta = -\frac{\partial H_1}{\partial \theta} .$$

The perturbation approximation consists in integrating this equation by using the unperturbed orbit to evaluate the right-hand side of the equation as a function of time.

As a perturbation the field from a straight-line current parallel to but displaced from the z axis is used. This perturbation is to correspond roughly to the carbon arc, which probably produces the largest deviation from symmetry in DCX.

There is considerable doubt as to whether this calculation will yield any significant information both because the perturbation theory is valid only for small times and because the numerical integration can be carried out only for small times. On the other hand, the perturbation calculation adds very little complexity to the unperturbed orbit calculation; and thus it seems reasonable to obtain what information we can in this manner.

[1] M. Rankin and T. K. Fowler, *Thermonuclear Project Semiann. Rep. Jan. 31, 1959*, ORNL-2693, p 18.

7.5 DEUTERON AND ELECTRON ENERGY DISTRIBUTIONS IN DCX

T. K. Fowler M. Rankin

A previously discussed IBM-704 code[1,2] designed to solve coupled Fokker-Planck transport equations for the energy distributions of ions and electrons in DCX has been found to be too slow, and is being revised. The difficulty in the original code, which followed the distributions in time through the transient phase toward a steady state, lay in the fact that ion and electron relaxations occur at greatly different rates. Within time steps short enough to properly handle changes in the coldest part of the electron distribution, virtually nothing happened to the ions. The new code, which salvages most of the old including the difference scheme discussed in ref 2, circumvents this problem by solving directly for the steady state. Since the equations are nonlinear, an iterative scheme of solution is being attempted. Efforts to determine in advance the convergence of the procedure have not proved decisive.

[1] *Thermonuclear Project Semiann. Rep. Jan. 31, 1959*, ORNL-2693, sec 1.4.

[2] T. K. Fowler, M. Rankin, and A. Siman, *Boundary Conditions and Conservation Properties of FOPP, A Plasma Fokker-Planck Code*, ORNL CF-59-2-75 (Feb. 27, 1959).

7.6 CROSS SECTION CALCULATION FOR DISSOCIATION OF D_2^+ BY CARBON ARC

R. G. Alsmiller, Jr.

The cross section for the dissociation of the D_2^+ molecule by a particle of charge ze has been calculated. The calculation is carried out in the Born approximation using exact two-center wave functions, the Franck-Condon principle, and a classical average over molecular orientations.

The calculated cross sections divided by z^2 are shown in Fig. 7.6.1. Shown in the figure are the cross section for the excitation of the first excited state, $1s\sigma_g \rightarrow 2p\pi_u$ transition; the cross section for the excitation of the second excited state, $1s\sigma_g \rightarrow 2p\sigma_u$ transition; and the sum of these cross sections, which is approximately the total dissociation cross section. Also shown in Fig. 7.6.1 are experimental results obtained from the dissociation of H_2^+ and D_2^+ by a vacuum carbon arc.

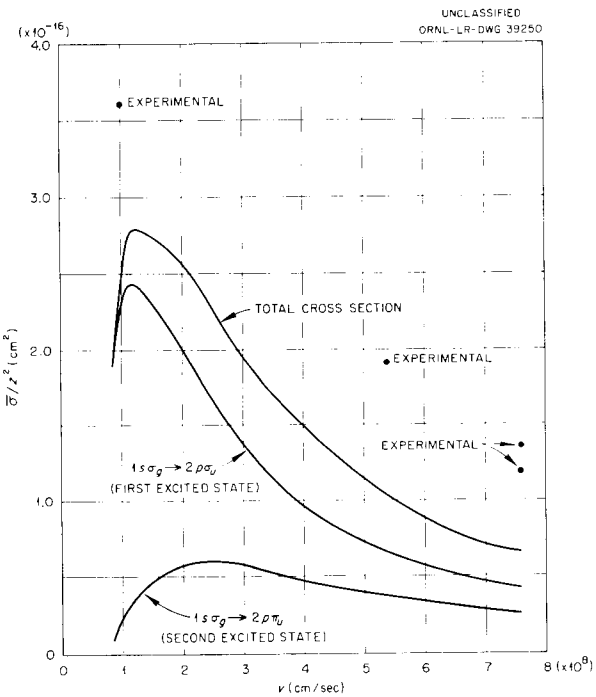

Fig. 7.6.1. Calculated and Experiment Cross Sections ($\times 1/Z^2$) for Dissociation of D_2^+ Molecule.

The experimental and theoretical results are found to agree within a factor of 2 over the velocity range considered. However, the Born approximation cross section is much more reliable at the high velocities than at the low velocities, and thus the agreement at low velocities may be erroneous.

To obtain a better estimate of the low-velocity cross section a semiclassical calculation which treats only distant collisions is being carried out.[1] In the calculation the incident particle of charge ze is treated as a classical point charge moving along a straight line trajectory. It is assumed that only the ground state and first excited state of the molecule need be considered, and it is further assumed that, for the distant collisions considered, the interaction potential may be expanded and only the dipole term retained.

With these assumptions the calculation consists in solving a set of coupled differential equations on the Oak Ridge Analog Computer. To date, it has been found that the machine error is so large that the results obtained are not meaningful; however, it is hoped that by revising the method of computation most of this error may be eliminated.

DISTRIBUTION OF ION SPECIES OUTSIDE THE CARBON ARC

Experimental information is now available which gives the per cent dissociation of the D_2^+ molecule and the distribution of the carbon ion species as functions of distance outside the carbon arc. In an effort to explain these results theoretically an attempt is being made to calculate the distribution on the basis of nonlinear diffusion theory.

---

[1] R. G. Alsmiller, Jr., *Thermonuclear Project Semiann. Rep. Jan. 31, 1959*, ORNL-2693, p 40.

7.7 DIFFUSION OF PLASMA PARTICLES ACROSS A MAGNETIC FIELD

A. Isihara A. Simon

A previous calculation by one of us[1] of the rate of diffusion of like charged particles across a magnetic field has been generalized. No a priori assumption as to the relative magnitude of certain terms need be made, and spatial density gradients are permitted in both directions perpendicular to the field. The final result agrees with that given earlier. Details will be available in a forthcoming ORNL report.

[1] A. Simon, *Phys. Rev.* **100**, 1557 (1955).

7.8 COHERENT RADIATION FROM A PLASMA

E. G. Harris A. Simon

The "collisionless Boltzmann equation" or "Vlasov equation" may be deduced by beginning with the Liouville equation and treating both the plasma particles and the electromagnetic field in a complete statistical fashion. The only approximation involved is the assumption that all pair correlations vanish. The result of integrating over the coordinates of all field oscillators and all but one particle is the Vlasov equation. The result of integrating over all particle coordinates and over the coordinates of all but one field oscillator is a corresponding equation which has some interesting implications for plasma radiation.

We expand the vector potential in a series of orthogonal vector functions which are periodic on some surface bounding our system. Thus

$$\vec{A} = \sum_{\lambda} q_{\lambda}(t)\, \vec{A}_{\lambda}(\vec{r}) \quad , \tag{1}$$

where $\vec{A}_{\lambda}$ satisfies the equations

$$\nabla^2 \vec{A}_{\lambda} + \frac{\omega_{\lambda}^2}{c^2} \vec{A}_{\lambda} = 0 \quad , \tag{2}$$

$$\nabla \cdot \vec{A}_{\lambda} = 0 \quad . \tag{3}$$

In the Coulomb gage the Hamiltonian for the complete system of charged particles and electromagnetic field is:

$$H = \sum_{k} \frac{1}{2m_k} \left[\vec{p}_k - \frac{e_k}{c} \sum_{\lambda} q_{\lambda} \vec{A}_{\lambda}(\vec{q}_k) \right]^2 + \sum_{\lambda} \left(\frac{1}{2} p_{\lambda}^2 + \frac{\omega_{\lambda}^2}{2} q_{\lambda}^2 \right) + \sum_{i>k} \frac{e_i e_k}{r_{ik}} . \tag{4}$$

Liouville's equation is now:

$$\frac{\partial f^{N,\infty}}{\partial t} + \{ f^{N,\infty}, H \} = 0 \quad , \tag{5}$$

where the braces denote a Poisson bracket and where $f^{N,\infty} = f^{N,\infty}(\vec{q}_k, \vec{p}_k, \vec{q}_{\lambda}, \vec{p}_{\lambda})$ is the phase space distribution function of the system. The superscript on f reminds us that there are N particles and a (denumerable) infinity of field oscillators.

The result of integrating Eq. (5) over the coordinates of all field oscillators and all but the kth particle (assuming that all pair distribution functions may be written as a product of one-particle functions) is:

$$\frac{\partial f^k}{\partial t} + \vec{v}_k \cdot \frac{\partial f^k}{\partial \vec{q}_k} + \frac{e_k}{m_k c} \frac{\partial f^k}{\partial \vec{v}_k} \cdot \left\{ -\sum_{\lambda} \vec{A}_{\lambda}(\vec{q}_k) \cdot \int f^{\lambda} p_{\lambda}\, dq_{\lambda} dp_{\lambda} + \sum_{\lambda} \vec{v}_k \times [\nabla_k \times \vec{A}_{\lambda}(\vec{q}_k)] \int f^{\lambda} q_{\lambda}\, dq_{\lambda} dp_{\lambda} - \sum_{i \neq k} e_i \frac{\partial}{\partial \vec{q}_k} \int \frac{1}{r_{ik}} f^i\, d\vec{q}_i d\vec{v}_i \right\} = 0 \quad , \tag{6}$$

which may be shown to be identical to the Vlasov equation. The result of integrating over all coordinates but the λth field oscillator is:

$$\frac{\partial f^{\lambda}}{\partial t} + p_{\lambda} \frac{\partial f^{\lambda}}{\partial q_{\lambda}} - \omega_{\lambda}^2 q_{\lambda} \frac{\partial f^{\lambda}}{\partial p_{\lambda}} + \frac{\partial f^{\lambda}}{\partial p_{\lambda}} \sum_{k} \frac{e_k}{c} \int \vec{v}_k \cdot \vec{A}_k(\vec{q}_k)\, f^k\, d\vec{q}_k d\vec{v}_k = 0 \quad . \tag{7}$$

It should be noted that Eq. (7) represents a denumerable infinity of equations, one for each oscillator.

One can now define the entropy for the radiation field as:

$$S_\gamma = -K \sum_\lambda \int f^\lambda \ln f^\lambda \, dp_\lambda dq_\lambda \ . \qquad (8)$$

It is an immediate consequence of Eq. (7) that $dS_\gamma/dt = 0$. Hence the entropy of the electromagnetic field is a constant of the motion.

We can now show that a consequence of this result is that a plasma obeying the Vlasov equation can radiate only coherently. Suppose there is no radiation present initially. In this case we have complete information on each oscillator; its coordinate and momentum are zero. Thus

$$f^\lambda = \delta(p_\lambda)\, \delta(q_\lambda) \qquad (\text{all } \lambda) \ ,$$

and one finds

$$S = -K \sum_\lambda 2 \ln \delta(0) \ . \qquad (9)$$

If we excite all oscillators in a completely coherent manner (meaning that each oscillator has a unique value of its coordinate and momentum) we have

$$f^\lambda = \delta(p_\lambda - \alpha_\lambda)\, \delta(q_\lambda - \beta_\lambda) \qquad (\text{all } \lambda) \ ,$$

and once again

$$S = -K \sum_\lambda 2 \ln \delta(0) \ .$$

If, however, even one oscillator has a probability spread of its coordinates or momentum (some disorder) then the entropy will increase as shown by the following trivial example.

Let the distribution function of the jth oscillator be:

$$f^j(p_j q_j) = \delta(q_j - \alpha_j) \cdot \left[\frac{1}{2} \delta(p_j - \beta_j) + \frac{1}{2} \delta(p_j - \gamma_j) \right] \ .$$

Then it is easy to show that

$$S = -K \sum_\lambda 2 \ln \delta(0) + K \ln 2 \ .$$

Hence, in general, a plasma obeying the Vlasov equation may emit only completely coherent radiation.

Further details of these calculations may be found in a forthcoming ORNL report.

7.9 CRITICAL CURRENT FOR BURNOUT IN AN OGRA-TYPE DEVICE

A. Simon

A complete algebraic analysis has been obtained for the variation of the steady-state ion density n_+ with injected current I in an OGRA-type fusion device (i.e., a device based on trapping of ions by breakup of energetic molecular ions on collision with either the background gas or trapped ions). The most general variation of n_+ with I is shown to be an S-curve with at most three roots of n_+ for a given input I. A physical interpretation of these three roots is given. In addition algebraic expressions are obtained for the two currents (an upper and lower critical current) at which the bends in the S-curve occur. It will be necessary to attain the larger current in order to build up a high-density plasma from a lower point, but once the high density has been achieved it may be maintained by the steady injection of any current larger than the lower critical current.

In two previous publications,[1,2] an expression was derived for the critical current at which formation of a plasma by high-energy injection will begin. This previous expression was for a case in which the trapping mechanism (although not specified in detail) was localized and did not depend on either the neutral gas in the device, the trapped ion density, or the dimensions of the system. A trapping mechanism of this sort is provided by the arc in DCX.[3]

[1] A. Simon, *Phys. Fluids* 1, 495 (1958).

[2] A. Simon, *Phys. Fluids* 2, 336 (1959).

[3] C. F. Barnett *et al.*, *Proc. U.N. Intern. Conf. Peaceful Uses Atomic Energy, 2nd, Geneva, 1958* 31, 298 (1958).

The situation is quite different in a proposed fusion device such as OGRA.[4] Here the injected molecular ions have a long mean free path L before they strike the injector snout, and trapping occurs by virtue of the dissociation of the molecule on collision with either the background gas (cross section σ_B^0), the trapped ions (σ_B^+), or other molecular ions in transit (σ_B^{2+}). Nevertheless, one might suspect on physical grounds that a critical current also exists in this case, and indeed such an expression has been found. This result is somewhat more complex than in the case of DCX because of a feedback which is inherent in the gas-breakup scheme. The onset of neutral burnout results in a reduction of the neutral breakup centers as well as an increase of the ion breakup centers and hence has a back effect on the input trapped current.

A complete algebraic analysis of the steady-state equations has been achieved in the case where one can neglect the contribution of the molecular ions to burnout or to breakup of other molecules as compared with the effect of the trapped ions and the neutral gas. (This is a highly valid approximation in almost all cases of interest.) The total mean free path λ of the injected molecular ions is then:

$$\frac{1}{\lambda} = \frac{1}{L} + \hat{N}_0 \sigma_B^0 + n_+ \sigma_B^+ \ , \tag{1}$$

where $\hat{N}_0$ is the average neutral density external to the plasma region and n_+ is the trapped energetic ion density. (It has been assumed that the slow ions resulting from ionization of the neutrals in the plasma region contribute equally to breakup as do the neutrals themselves. The sum of the slow ion and neutral densities in the plasma interior should remain equal to the external neutral density even after burnout.) The probability that a molecule will break up after a path length x is then

$$p(x) = e^{-x/\lambda} \frac{dx}{\lambda_B} \ , \tag{2}$$

where

$$\frac{1}{\lambda_B} = \hat{N}_0 \sigma_B^0 + n_+ \sigma_B^+ \ . \tag{3}$$

Hence the percentage trapping is found by integrating Eq. (2) over all space. The result is

$$\% \text{ B.U.} = \frac{\lambda}{\lambda_B} = \frac{\hat{N}_0 \sigma_B^0 L + n_+ \sigma_B^+ L}{1 + \hat{N}_0 \sigma_B^0 L + n_+ \sigma_B^+ L} \ . \tag{4}$$

This leads to the following steady-state equation for the ion density:

$$\frac{I}{V} \frac{\hat{N}_0 \sigma_B^0 L + n_+ \sigma_B^+ L}{1 + \hat{N}_0 \sigma_B^0 L + n_+ \sigma_B^+ L} = \frac{\hat{N}_0 n_+ \sigma_{cx} v}{1 + \frac{\bar{l} v}{v_0} n_+ \sigma_d^+} + n_+^2 \sigma_c v P \ , \tag{5}$$

where

$$N_0 = \frac{\left(\frac{\Gamma}{\theta}\right) I + N_0}{1 + \left(\frac{\sigma}{\theta}\right) \frac{n_+ \sigma_d^+ v V}{\left(1 + \frac{\bar{l} v}{v_0} n_+ \sigma_d^+\right)}} \ . \tag{6}$$

Here I is the injected (number) current of molecular ions, V the plasma volume, $\bar{l}$ the mean chord length of the plasma volume, v the energetic ion velocity, and v_0 the neutral atom velocity. The charge-exchange cross section is denoted by σ_{cx}, the sum of the charge-exchange and ionization cross sections is denoted by σ_d^+ ($\sigma_d^+ = \sigma_i + \sigma_{cx}$), and σ_c is the effective 90° Coulomb scattering cross section. Finally, the pumping speed of the system is denoted by θ, N_0 is the initial neutral density before the beam is turned on, Γ is the fraction of input molecular ions which come back as neutrals ($\Gamma \leqq 2$), σ is the fraction of slow ions which do *not* return to the system as neutrals after striking the walls, and P is the usual mirror loss probability.

Equations (5) and (6) combined constitute an implicit equation in the variables n_+ and I. Thus we have

$$f(n_+, I) = 0 \ . \tag{7}$$

It can be shown that I is uniquely determined by a choice of n_+, and conversely that there are either three or one real positive values of n_+ for any

[4] I. V. Kurchatov, *J. Nuclear Energy* 8, 168 (1958).

given I. As a result, the variation of n_+ with I has the general form shown in Fig. 7.9.1, whereas the corresponding curve for DCX has the form shown in Fig. 7.9.2.

The multiple roots occurring in Fig. 7.9.1 have a straightforward physical interpretation.[5] In region 1 neutral burnout has set in. The steady-state solution is achieved by balance between charge-exchange loss of the trapped ions and feed by breakup of the molecular ions on the neutral background (mirror loss is negligible). The second solution (in region 2) corresponds to the point at which the ion density has risen and the neutral density has fallen so that the breakup on the ions now is the same as the previous breakup on the neutral gas. The charge-exchange loss remains the same since it is proportional to the product $n_0 n_+$ (where n_0 is the average neutral density in the plasma region) and since, after burnout, $n_0 \sim 1/n_+$. The final root (of region 3) corresponds to the point at which mirror loss becomes more important than charge-exchange loss. It is clear that roots 1 and 3 are stable while root 2 will be unstable.

An implicit equation for the upper critical current (UCC in Fig. 7.9.1) has been found and is as follows:

$$I_{UCC} = \frac{\left(\frac{\Gamma}{\theta} I + N_0\right) \sigma_{cx} v V \left(\frac{\phi - 1}{\phi}\right) \left[1 + \Lambda \sigma_\beta^0 L + \left(\frac{\phi - 1}{K}\right) \sigma_B^+ L\right]}{K \left[\Lambda \sigma_B^0 L + \left(\frac{\phi - 1}{K}\right) \sigma_B^+ L\right]} , \tag{8}$$

where

$$\phi = \left[\left(\frac{\Gamma}{\theta} I + N_0\right) \frac{\sigma_B^0 \sigma}{\sigma_B^+ \theta} \sigma_d^+ v V\right]^{1/2} , \tag{9}$$

$$K = \left(\frac{\bar{l}}{v_0} + \frac{\sigma}{\theta} V\right) v \sigma_d^+ , \tag{10}$$

$$\Lambda = \left(\frac{\Gamma}{\theta} I + N_0\right) \left[1 + (\phi - 1) \frac{\bar{l} v \sigma_d^+}{v_0 K}\right] \frac{1}{\phi} . \tag{11}$$

[5] A recent paper by I. N. Golovin (Harwell, April 1959, unpublished) states that Kuznetsov and co-workers have obtained numerical results indicating a behavior of this sort.

UNCLASSIFIED
ORNL-LR-DWG 39282

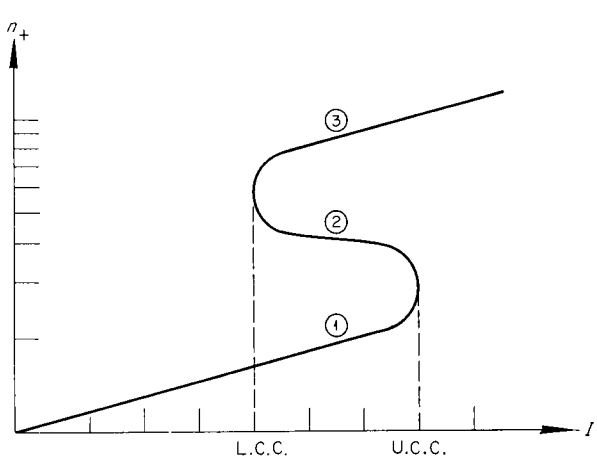

Fig. 7.9.1. Variation of Trapped Energetic Ion Density with Current of Injected Molecular Ions for an OGRA-Type Device.

UNCLASSIFIED
ORNL-LR-DWG 39283

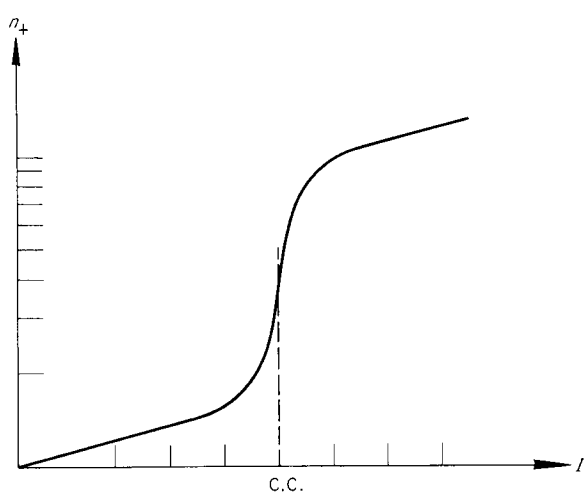

Fig. 7.9.2. Variation of Trapped Energetic Ion Density with Current of Injected Molecular Ions for a DCX-Type Device.

The corresponding plasma density is $(\phi - 1)/K$. This equation for I_{UCC} can be solved quite readily by numerical means. It will be necessary to inject this UCC in order to attain a high plasma density when the density is being increased from a low point.

In some cases there will not be a solution of the above equations, which means that burnout is not possible. The condition for which burnout is impossible is that

$$\frac{\Gamma\sigma_{cx}}{\sigma_d^+} \geqq \sigma + \frac{\theta\bar{l}}{Vv_0} . \qquad (12)$$

The approximations which are involved in the derivation of Eqs. (8) through (12) will break down if the resulting value of ϕ [as defined in Eq. (9)] is not larger than unity. In this case, no simple expression equivalent to Eq. (8) has been found and we must deal with the general solutions of Eq. (5). Numerical studies have so far indicated that the characteristic curve is still S-shaped in this region although it is much steeper and seems to be tending toward a DCX-shape.

A simple expression has also been derived for the lower critical current (LCC in Fig. 7.9.1). This is

$$I_{LCC} \cong \frac{\left(\frac{\Gamma}{\theta} I + N_0\right)\sigma_{cx} v V}{K\left[1 - \frac{3}{2\delta}\left(\frac{1}{\sigma_B^+ L} - \frac{1}{K}\right)\right]} , \qquad (13)$$

where

$$\delta = \left\{\left[\frac{I}{V} - \left(\frac{\Gamma}{\theta} I + N_0\right)\frac{\sigma_{cx} v}{K}\right]\frac{1}{3\sigma_c v P}\right\}^{1/2} . \qquad (14)$$

The corresponding plasma density is given by δ. Once a high plasma density has been obtained, it may be maintained by steady injection of a current larger than the LCC.

Details of these algebraic calculations and a summary of numerical results will be given in a future publication. I am greatly indebted to R. C. Gilbert and R. E. Hester for calling my attention to the possibility of multiple roots in the gas breakup case.

7.10 MOTION OF A NEUTRALIZED BEAM OF CHARGED PARTICLES ACROSS A MAGNETIC INDUCTION

D. J. Rose[1]

Work at the Massachusetts Institute of Technology by S. Frankenthal and the writer, on the passage of a beam across a magnetic field, has been extended. A summary of the simple theory follows.

Consider Fig. 7.10.1, where a beam of ions and electrons is injected in the positive y direction, across an induction B_z. The beam is of thickness d in the x direction, and is indefinitely wide in the z direction. Density of both ions and electrons is n (per unit volume), and all particles have velocity v. Therefore the beam has no net current.

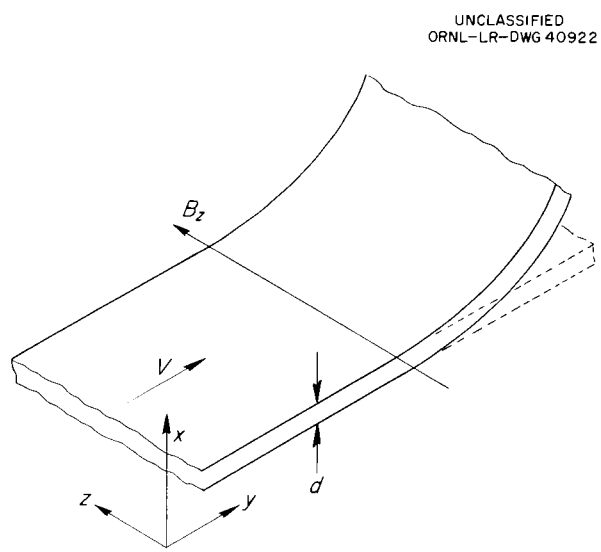

Fig. 7.10.1. Nomenclature for a Flat Beam in a Magnetic Induction.

[1]Consultant from Massachusetts Institute of Technology. An exact division of the locale of the work cannot be made. Most of the development described through sec 7.10.2 was done at the Massachusetts Institute of Technology, and most of that described in secs 7.10.3 and 7.10.4 was done at Oak Ridge National Laboratory.

As the beam starts to split, a space-charge field builds up, and the (now separated) current sheets give rise to an additional magnetic induction between them. The field energy can arise at the expense of the kinetic energy of the particles. If the beam is dense, the particle energy may be negligibly disturbed by these processes. We may state a simple criterion for whether the beam separates completely or not. If it splits by an amount $\delta (< d)$, the net surface charge density is $n\delta$ on each sheet, and the field between is $n\delta q/\epsilon_0$. The central (neutral) portion of the beam will pass straight across if $n\delta q/\epsilon_0 = VB$, the motional electric field. Then

$$\frac{ndq}{\epsilon_0} > VB \tag{1}$$

is the qualitative criterion for the beam being able to generate sufficient electric field to permit its core to progress unimpeded. In terms of singly charged ions, this criterion may be rewritten

$$\text{amp/meter} > 1.7 \times 10^{-3} \frac{BU}{M} , \tag{2}$$

where B = webers/m^2, U = energy in ev, and M = molecular weight. At U = 100 ev, B = 0.1 weber/m^2, and H^+, one obtains 17 ma/m.

It turns out that the perturbation $\Delta B \approx (V^2/C^2)B$, so that the charge motion is determined well enough by the ambient B and the space-charge electric field E.

7.10.1 THE EQUATIONS OF MOTION

Let us now look at the motion of an individual particle, and search for a formulation in which the beam makeup is independent of y and z.

A particular ion (or electron) is identified by its maximum excursion x_0 (see Fig. 7.10.2) into the beam on its successive gyrations. Let all "x_0" particles have the same total energy $H(x_0)$. Then

$$\frac{m\dot{x}^2}{2} + \frac{m\dot{y}^2}{2} + q\,\phi(x) = H(x_0) , \tag{3}$$

where

$$E = -\frac{d\,\phi(x)}{dx} . \tag{4}$$

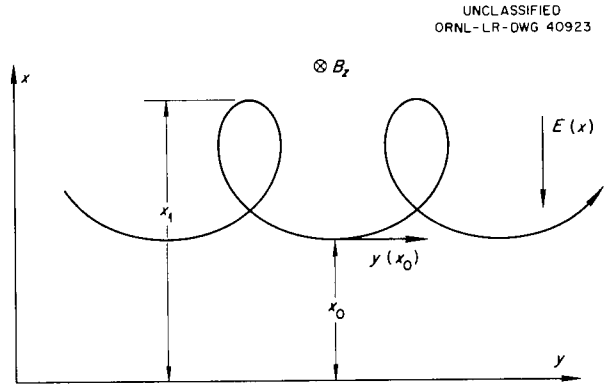

Fig. 7.10.2. Motion of a Charged Particle in a Magnetic Induction.

In addition,

$$m\ddot{y} = -qB_z\dot{x} , \tag{5}$$

$$m\ddot{x} = q[E(x) + B_z\dot{y}] , \tag{6}$$

from which Eq. (3) is also readily derived. If diamagnetism be neglected, then B_z = constant, and

$$\dot{y}(x) = \dot{y}(x_0) - \omega_b(x - x_0) , \tag{7}$$

$$\dot{x}^2 = 2\omega_b\,\dot{y}(x_0)(x - x_0) - \omega_b^2(x - x_0)^2 - \frac{2q}{m}[\phi(x) - \phi(x_0)] . \tag{8}$$

Here,

$$\dot{y}(x_0) = \left[\frac{2\,H(x_0)}{m} - \frac{2q\,\phi(x_0)}{m}\right]^{1/2} \tag{9}$$

is the velocity of the particle at x_0, and

$$\omega_b = \frac{qB}{m} , \tag{10}$$

the cyclotron frequency.

The equations of motion may be further reduced by changing to a coordinate space measured in terms of the Larmor radius of the particle, as it is at x_0:

$$\begin{Bmatrix} x \\ y \end{Bmatrix} = \frac{\dot{y}(x_0)}{\omega_b} \begin{Bmatrix} \eta \\ \zeta \end{Bmatrix} , \tag{11}$$

$$\dot{\zeta} = \omega_b[1 - (\eta - \eta_0)] \ , \tag{12}$$

$$\dot{\eta}^2 = \omega_b \left\{ 2(\eta - \eta_0) - (\eta - \eta_0)^2 - \frac{\phi(\eta) - \phi(\eta_0)}{U(\eta_0)} \right\} \ , \tag{13}$$

where

$$U(\eta_0) = \frac{m\,\dot{y}^2(x_0)}{2q} \ . \tag{14}$$

In considering the motion of just one particle, we can set $\eta_0 = 0$, $\phi(\eta_0) = 0$, and solve for the motion if $\phi(\eta)$ is known. Equation (13) is integrable if

$$\phi = 2kU_0(\eta - A\eta^2 + D\eta^3) \ , \tag{15}$$

where $U_0 = U(\eta_0)$. One finds:

1. $K = 0$: no field, circular motion,
2. $K \neq 0$, $A = 0$, $D = 0$: circular motion plus well-known $E \times B$ drift in y direction,
3. $K \neq 0$, $A \neq 0$, $D = 0$: elliptical motion, plus drift in y direction,
4. $K \neq 0$, $A \neq 0$, $D \neq 0$: higher-order cyclic motion in terms of elliptic functions, plus drift.

For example, if K, $A \neq 0$, one has

$$\eta = \left(\frac{1 - K}{1 - 2KA}\right)[1 + \sin\omega(t - t_0)] \ , \tag{16}$$

$$\zeta = \frac{\omega_b K(1 - 2A)}{1 - 2A}\,t + \frac{1 - K}{1 - 2KA\sqrt{1 - 2KA}}\cos\omega(t - t_0) \ , \tag{17}$$

where

$$\omega^2 = \omega_b^2(1 - 2KA) = \omega_b^2 - \omega_p^2 \ , \tag{18}$$

and

$$\omega_p^2 = \frac{ne^2}{m\epsilon_0} \tag{19}$$

is the plasma frequency.

In this approximation, there are two limits: $K \leqq 1$, $A \leqq 0.5$, for proper solutions. Figure 7.10.3 is intended to make the matter clear. The speed

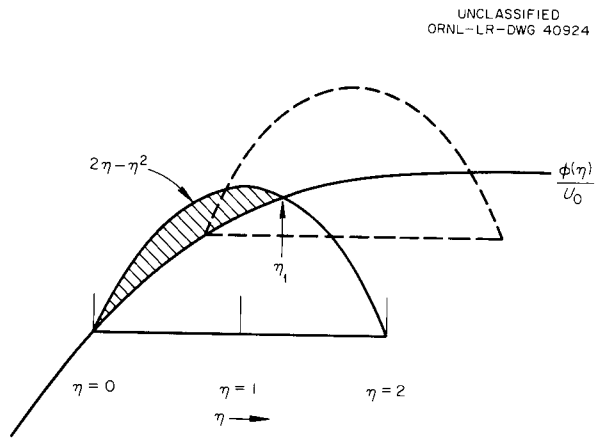

Fig. 7.10.3. The Quantity $[2\eta - \eta^2 - (\phi\eta/U_0)] \propto \dot{\eta}^2$.

$\dot{\eta}$ is proportional to the square root of the height of the shaded area. Thus the particle turns around at $\eta = 0$ (i.e., x_0 of Fig. 7.10.2) and η_1 (x_1 of Fig. 7.10.2). The case $K > 1$ corresponds to $d\phi/d\eta > 2U_0$ at $\eta = 0$. In such a case, the particle gyrates downward instead of upward. It belongs to a different class and should have been counted as a particle which originated at some smaller value of x_0. The case $A > 0.5$ corresponds to the potential turning around and going negative, in such a way that there is no crossing η_1 (or x_1). The particle therefore runs away, and such cases are not of physical interest here. Figure 7.10.3 may be used for further interpretation of Eq. (13). The potential $\phi(\eta)$ is a fixed (although largely unknown) function. The parabola $2\eta - \eta^2$ can be thought of as a template which can be slid up and down the potential curve, depending on the value of η_0 (or x_0). For the outermost particle, for example, one must have $E = 0$ or $d\phi/d\eta = 0$ at its turning around point, and at all larger values of η. Thus it can be positioned along the $\phi(\eta)$ curve as shown by the dotted curve. One sees that the excursion of the outermost particle must lie between one and two Larmor radii. That particle therefore executes loops in the laboratory system, as shown in Fig. 7.10.2; but interior particles may only undulate.

Returning now to Eqs. (16) and (17), one sees that in the moving system, the particle executes elliptic gyrations, in accordance with assumption 3 above.

7.10.2 DRIFT VELOCITY AND DENSITY

We return to x-y space, since the η-ζ co-ordinate system, which depends on $\dot{y}(x_0)$, is not necessarily the same for all particles. One may transform Eq. (6) to a system moving in the y direction:

$$y = s + v_0(x_0)t \ ; \tag{20}$$

then

$$m\ddot{x} = q\left\{E(x) + [\dot{s} + v_0(x_0)]B_z\right\} \ . \tag{21}$$

If $v_0(x_0)$ is chosen for a particular particle so that it executes a closed orbit in the moving system, one has

$$\oint \ddot{x}\, dt = \oint \dot{x}\, dt = \oint \ddot{s}\, dt = \oint \dot{s}\, dt = 0 \ , \tag{22}$$

the integrals being taken over a cycle of the orbital motion. The first three integrals are zero for any choice of v_0, but the last depends on the correct choice. Applying this to Eq. (21), one has

$$v_0(x_0) = -\frac{\oint E(x)\, dt}{B_z\, \tau(x_0)} \ , \tag{23}$$

where

$$\tau(x_0) = \oint \frac{dx}{\dot{x}(x,x_0)} \equiv 2\int_{x=x_0}^{x=x_1} \frac{dx}{\dot{x}(x, x_0)} \tag{24}$$

is the period.

One discovers the density at any point x by noting that an "x_0" particle spends a fraction of its time,

$$f = \frac{2\, dx}{\tau(x_0)\, \dot{x}(x,x_0)} \ , \tag{25}$$

in $(x, x + dx)$, where the factor of 2 comes from its travel up and down.

Now let there be a flux $\Gamma(x_0)\, dx_0$ of "x_0" particles in $(x_0, x_0 + dx_0)$. The mean forward velocity is $v_0(x_0)$, so their density is

$$\frac{\Gamma(x_0)\, dx_0}{v_0(x_0)}$$

per unit area. The particles are actually seen in $(x, x + dx)$ with probability f, so that

$$dn\,(x, x_0)\, dx\, dx_0 = \frac{2\,\Gamma(x_0)\, dx\, dx_0}{v_0(x_0)\, \tau(x_0)\, \dot{x}(x, x_0)} \ . \tag{26}$$

Then

$$n(x) = \int \frac{2\,\Gamma(x_0)\, dx_0}{v_0(x_0)\, \tau(x_0)\, \dot{x}(x, x_0)} \ . \tag{27}$$

The limits of integration are chosen to include all particles which are capable of reaching point x. These limits are, of course, given by the two roots of Eq. (8), solved for x_0.

So far, we have been discussing the ions only, but an identical development applies to the motion of the electrons. Thus Eq. (27) and its equivalent for electrons may be put into Poisson's equation, to give a nonlinear integral equation defining the potential ϕ.

7.10.3 DRIFT VELOCITY OF A WEAK BEAM

Consider a weak beam, in the sense that inequalities (1) and (2) are not satisfied. Then the positive and negative parts of the beam are completely separated. Furthermore, suppose that all particles have substantially the same value of x_0, so that the integration of Eq. (27) is avoided, and $d^2\phi/dx^2$ is determined by charges of one kind only. The flux of particles of one kind is Γ (and the current is $e\Gamma$ amp/m), and the general appearance of the beam is shown in Fig. 7.10.4.

UNCLASSIFIED
ORNL-LR-DWG 40925

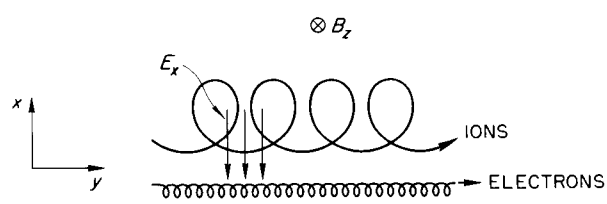

Fig. 7.10.4. Weak Ion Beam Moving to Right.

We are interested in the forward drift velocity, v_0, of the beam, determined by Eq. (23). The factor $E(x)$ is determined by an integration over $n(x)$ from (26) or (27), modified to suit. We see that since the average value of $E(x)$ is involved, the detailed shape can be somewhat in error without affecting v_0 appreciably. Thus a fortiori one can be naive about $n(x)$, by substituting a simple expression for $\dot{x}(x)$. We make the assumption that the potential term is negligible in Eq. (8), corresponding to the inability of the beam to polarize sufficiently and travel unimpeded across

the field. In that case (with $x_0 = 0$ for convenience), we have

$$n(x) = \frac{\epsilon_0}{e}\frac{dE}{dx} = \frac{2\Gamma}{v_0 \tau \left[2\omega_b \dot{y}(0)\, x - \omega_b^2 x^2\right]^{1/2}} . \quad (28)$$

This integrates simply, and we set $E = 0$ at the extreme of the motion $x = 2\,\dot{y}(0)/\omega_b$. Then

$$E = -\left(\frac{2e\Gamma}{\epsilon_0 v_0 \tau \omega_b}\right)\left\{\frac{\pi}{2} + \sin^{-1}\left[1 - \frac{\omega_b(x)}{\dot{y}(0)}\right]\right\} . \quad (29)$$

Then v_0 is given by Eq. (23), with x expressed as a function of time:

$$x = \frac{\dot{y}(0)}{\omega_b}\left[1 - \sin \omega_b (t - t_0)\right] , \quad (30)$$

$$v_0 = \frac{2e\Gamma}{\epsilon_0 v_0 \tau^2 \omega_b B_z} \; 2\int_{-\pi/2\omega_b}^{+\pi/2\omega_b} \left(\frac{\pi}{2} + \omega_b t\right) dt . \quad (31)$$

The limits are chosen (or phase adjusted) so that the inverse time is taken over its principal range of values. One finds

$$v_0 = \left(\frac{e\Gamma}{2\epsilon_0 B_z}\right)^{1/2} = \left[\frac{\text{(amperes/meter) of one sign}}{2\epsilon_0 B_z}\right]^{1/2} . \quad (32)$$

For a numerical example, suppose $e\Gamma = 1$ amp/m, $B_z = 1$ weber/m^2. Then $v_0 \approx 2.5 \times 10^7$ cm/sec. This drift might be of the order of $1/10$ of the injection velocity of ions. Thus an extreme slowing of a beam in a magnetic induction hardly seems possible.

One may check that the neglect of ϕ in Eq. (8) is not important. If one substitutes the expansion (15) for ϕ, with $D = 0$ for convenience, one finds exactly the same velocity v_0. While the field E is altered, the period τ is altered in a corresponding way, and the two effects cancel. Thus the average field is the same, and one suspects that Eq. (32) is somewhat better than the original assumptions. It may be checked also that (32) should be a good approximation provided that the drift velocity $v_0 \ll \dot{y}(0)$, the maximum speed of the particles.

Note that Eq. (32) should give the maximum possible slowing down for a beam. For example, suppose the beam is stronger, so that larger fields can be developed in its interior. Then the outside parts will drift forward with a velocity roughly corresponding to (32), but the inner core will move faster. In the limit of a very strong beam, the core will cross the field with a velocity close to $\dot{y}(0)$, with slight undulating motion of the particles.

7.10.4 SPECULATIONS REGARDING THE MOTION OF A BEAM ACROSS A MAGNETIC INDUCTION

In general, it is impossible to solve for the motions of a polarized beam in its interaction with its environment, but it is interesting to speculate on what may happen.

For example, in Fig. 7.10.4, the ions move in the electric field determined by their own space charge, and the fact that the field lines end on free electrons is of no particular account. One might therefore imagine a "*Gedanke*" experiment in which the electrons are replaced by a conducting plate. The lines of force from the ions then end on the image charge on the plate, and the ions go on as before.

It has been proposed that the ions could be slowed down very much by stripping off the electrons, as in Fig. 7.10.5. Of course, an ion cannot be permanently trapped this way, because an orbit coming from "outside" must eventually return outside in a d-c situation. But the ions in Fig. 7.10.5 are probably not very much slowed down either, for the same electric field lines that caused the ions to reach the vicinity of the obstacle will be distorted as shown, giving an $E \times B$ drift around the plate. Then the ions will probably turn around the corner and travel down. More intriguing is the idea of putting a second plate above the ions, but intercepting nothing. The lines of E are then more or less symetrically

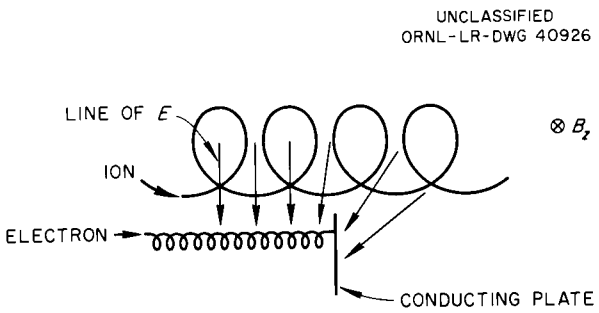

Fig. 7.10.5. Beam Moving to Right with Electrons Intercepted by an Obstacle.

disposed, and the beam may be slowed appreciably. If the beam be D_2^+, a suitably placed arc might then have a very good chance of dissociating the ions and actually trapping them.

Finally, suppose a polarized beam is heading for an infinitely conducting plate, as in Fig. 7.10.6, and suppose that interparticle collisions cannot occur. Since an electric field cannot exist in the conductor, the beam cannot travel through it, and we are constrained to look for some motion that does not lead to trapping of the beam where it reaches the plate. The only solution which appears likely is that the plate develops image charges as shown; the beam splits into two parts, running up and down the surface. There will be a force on the plate, arising from the momentum change in the beam.

It is interesting to speculate whether this effect could be observed if a large cylindrical arc plasma

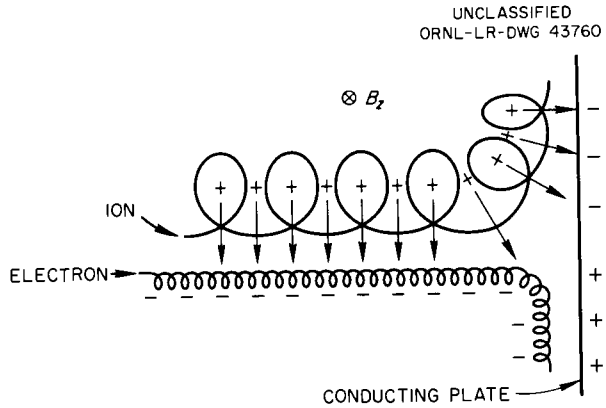

Fig. 7.10.6. Polarized Beam Incident on a Conducting Plate.

were substituted for the conducting plate. Under ideal conditions, one might imagine the beam to separate, pass around the arc plasma, and re-form on the other side. It is not known at present whether an arc would be well enough defined or collision-free.

ACKNOWLEDGMENT

It is a pleasure to acknowledge stimulating discussions with J. S. Luce and others in regard to the general problems described. In particular, Luce made a number of valuable suggestions regarding the slowing down of the ions as a condition for their efficient dissociation by an arc.

8. ENGINEERING SCIENCES GROUP

W. F. Gauster

The following work in the field of engineering sciences in support of the Thermonuclear Project was initiated, is in progress, or was completed.

1. At the request of the Engineering Sciences Group, a tabulation of rotational symmetrical magnetic fields (flux-density components B_z and B_r, magnetic potential A, and rA for calculating field lines) produced by semi-infinite circular current sheets was done by the Mathematics Panel of ORNL. The tables[1] (about 140 pages) will be issued soon.

2. The application of series of Legendre polynomials to magnetic field problems has been studied,[2] and the Mathematics Group of the Thermonuclear Experimental Division will write a new code for Oracle computation (see Sec 8.1). It is expected to use, in special cases, the Legendre polynomial series instead of the Oracle code based on elliptic integrals.[3]

3. Hydraulic and heat transfer studies for the design of large magnet coils are being done (see Sec 8.3) since the semiempirical data, as available in the literature, cannot be applied reliably to specific designs. Special calculations were made for the long solenoids for arc studies (the solenoids are to be designed by the Engineering Group of the Thermonuclear Experimental Division). Heat transfer test facilities have been built.

4. Graphical methods for designing magnetic fields and ion-beam trajectories were used extensively (see Sec 8.2). The starting point for this kind of work is either numerical field values, supplied by Oracle calculations of the Mathematics Group, or data taken from measurements on existing magnet coils. Extensive supporting work has been done with new coil types and with boosting arrangements for existing coil systems. Graphical determination of ion-beam trajectories has been done especially for DCX-1 and DCX-EPA (hollow arc).

5. The "Field Simulator" (resistor network, which simulates a rotational symmetrical magnetic field) has been completed, and some initial difficulties have to be overcome.

6. During this report period, work has been done for DCX-2 (see Sec 14.2). Using the method described previously,[4] approximate numerical values for the geometrical dimensions and the magnetic field properties of a DCX-2 machine have been calculated, based on a simplified containment condition for the 5-Mev alpha particles expected to be produced. Recent studies concern the application of calculations with Legendre polynomials to the design of DCX-2.

7. The proceedings of the Symposium on Magnetic Field Design in Thermonuclear Research held in Gatlinburg, Tennessee, on December 11 and 12, 1958, have been edited and will be issued soon.

---

[1] A. C. Downing and N. B. Alexander, *Tables for a Semi-Infinite Circular Current Sheet*, ORNL-2828 (to be published).

[2] M. W. Garrett, *J. Appl. Phys.* 22, 1091–1107 (1951).

[3] M. Rankin, *Thermonuclear Project Semiann. Rep. Jan. 31, 1959*, ORNL-2693, p 111.

[4] W. F. Gauster, *Thermonuclear Project Semiann. Rep. Jan. 31, 1959*, ORNL-2693, p 109–11.

8.1 COMPUTATION OF MAGNETIC FIELDS AND ION-BEAM TRAJECTORIES

M. Rankin W. F. Gauster

An extension of the Oracle elliptic integral code for calculating magnetic quantities has been made for long solenoid fields. Studies of the special-purpose advantages of using series of Legendre polynomials for designing magnetic fields have been made. Midplane ion beam trajectories have been calculated, and a code to use a stored table of magnetic quantities, rather than an analytic

representation, is being written. A fast, reliable graphical method for locating grid sources giving orbits with desired properties has been developed.

Previously a report was given on Oracle calculation of magnetic fields and vector potential.[1] The code involved uses complete elliptic integrals of the first and second kind for calculating the flux-density components B_z and B_r, the vector potential A, and the quantity rA (rA = constant is the equation of a magnetic field line) produced by a single circular loop. For magnet coils of any cross section, a certain number of such coaxial loops replace the actual windings. In general, a few hundred loops are sufficient for this purpose, and the Oracle working time required is reasonable (approximately one second for ten loops per space point).

In some special cases, for instance for long solenoids for arc studies (see Sec 8.3), the number of loops becomes very high. Here it is advisable to consider groups of windings, which occur repeatedly in the same form, and to put the field values of one unit in the "memory" of the Oracle; then the resulting magnetic field is calculated by superimposing as many units as necessary. In this way the Oracle working time is reduced considerably. Such a code has been written by G. R. North.

It is planned to develop an additional Oracle code based on a series of Legendre polynomials instead of elliptic integrals. Using spherical coordinates (see Fig. 8.1.1), the magnetic quantities produced by a coaxial loop can be expressed, as is well known, by a series of Legendre polynomials. For instance,

$$B_z = \frac{\pi I_j \sin^2 \alpha_j}{5R_j} \sum_{k=1}^{\infty} P_k'(\cos \alpha_j)\, P_{k-1}(\cos \theta) \left(\frac{r}{R_j}\right)^{k-1} ,$$

where I_j is the product of current (in amperes) and the number of turns; $P_n(\cos \theta)$ represents the Legendre polynomial of nth degree; r and R_j are measured in centimeters, and the flux density B_z in gauss.

The following advantages can be expected from such a code:

1. Using any point on the axis as the origin, the field values can be represented as functions of r and z, showing the performance of the quantities concerned in the whole zone of convergence. The code based on elliptic integrals yields values at one point of the desired location. Such series of Legendre polynomials show easily which degree of homogeneity can be achieved with a certain magnetic coil arrangement.

2. Integration of series of Legendre polynomials leads again to series of the same kind. Therefore, a code of the magnetic quantities produced by current sheets and thick solenoids has to consider the corner points only.[2] It is not necessary to approximate the actual winding by a loop arrangement distributed over the coil cross section.

It is expected that such a new code can be advantageously applied for special cases.

For calculating the trajectories of ion beams in the midplane of magnetic mirror fields for DCX experiments, the Oracle code developed for the study of ion orbits and containment properties of DCX[3] has been applied. The calculation of θ was added to the code; r and θ are computed as

UNCLASSIFIED
ORNL-LR-DWG 40927

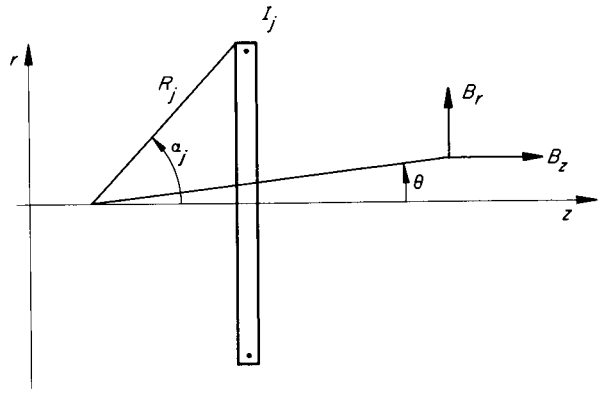

Fig. 8.1.1. Spherical Coordinates Used in Calculation of the Magnetic Quantities Produced by a Coaxial Loop.

[1] M. Rankin, *Thermonuclear Project Semiann. Rep. Jan. 31, 1959*, ORNL-2693, p 111.

[2] A. Gray, *Phil. Mag.* [5]33, 62 (1892); A. Gray, *Absolute Measurements in Electricity and Magnetism*, 2d ed., pp 201–6, 796–97, Macmillan, London, 1921; M. W. Garrett, *J. Appl. Phys.* 22, 1091–1107 (1951).

[3] M. Rankin and T. K. Fowler, *Thermonuclear Project Semiann. Rep. Jan. 31, 1959*, ORNL-2693, p 18–24.

functions of time. This parametric representation of the motion avoids the singularity which occurs at the breakup point in the time-independent form of calculation.[4] By time-reversing the code, a trajectory may be followed backward to its entry position into the liner as well as forward to its collision point with the liner.

For some experimental problems the present code is inadequate due to the fact that it uses an analytical representation of the magnetic quantities. This is a good approximation to the DCX field only up to r in the neighborhood of 12–14 in. A new code is now being written which will use a stored table of actual DCX magnetic quantities.

A special problem is to find for a DCX experiment the location of a grid source in such a way that atomic ion orbits of desired precession occur. This demand determines the angle between the radius to the magnetic field center and the beam middle trajectory at the focal point. Now the ion beam can be followed up toward the source; however, the location of the grid of the ion source is yet unknown. It has to be considered that the two trajectories, which represent the beam boundaries, start perpendicular to the grid at the points concerned. For instance, in the case of a straight grid, the trajectory tangents at the starting points are parallel and, therefore, also parallel to the middle trajectory of the beam. This geometrical property is sufficient to determine the source position.

It would be possible to work out an Oracle code to perform the procedure mentioned above. This is, however, a case where a graphical method for designing ion-beam trajectories produces fast, reliable results (see Sec 8.2).

[4]R. J. Mackin, Jr., *The ORNL Thermonuclear Program*, ORNL-2457, p 156 (Jan. 15, 1958).

8.2 GRAPHICAL METHODS FOR DESIGNING MAGNETIC FIELDS AND ION-BEAM TRAJECTORIES

R. L. Brown

D. L. Coffey

Graphical design of magnetic fields and of ion-beam trajectories has been used extensively. The following examples illustrate the methods used.

8.2.1 BOOSTER COILS FOR THE LONG SOLENOID FACILITY AND FOR DCX-1

Magnetic measurements of the long solenoid facility for arc studies revealed an axial mirror ratio of slightly greater than two.[1] To obtain a more uniform midplane field with a smaller mirror ratio, two compact booster coils (designed by E. S. Bettis) were inserted in the long solenoid symmetrically about the midplane.

The field of the booster coils, when combined with the field of the solenoid, yields an axial field as shown in Fig. 8.2.1. The current in the booster coils is so adjusted that a reasonably uniform field results. The axial midplane field strength of the booster coil may be increased by a factor of 3 by raising the current to its full rating of 7000 amp. The booster coils have been installed and are in operation.

Extensions of the same long arc facility have been studied. One method is to extend the field of the solenoid by installing additional coils at one end. Three such coils (DCX-EP-A design) may be added as shown in Fig. 8.2.1. The resultant axial field is between 6.4 and 4.5 kilogauss over a distance exceeding 15 ft.

Several proposals were made to extend the field of DCX-1 so that a longer arc might be used. One such proposal is to add one coil on either end as shown in Fig. 8.2.2. These additional coils are of the same type as the existing coils but will be operated with only half the rated current, that is, 3000 amp. Under these conditions, the axial field will be not less than 10 kilogauss for a length of 7 ft. Mechanical designs are now in progress.

8.2.2 ION TRAJECTORIES AND GRAPHICAL DETERMINATION OF ION SOURCE LOCATION

An ion, moving in a trajectory orthogonal to the magnetic field lines (as in the midplane of a mirror coil system), will be deflected according

[1]J. F. Potts *et al.*, *Thermonuclear Project Semiann. Rep. Jan. 31, 1959*, ORNL-2693, Fig. 2.5.2.

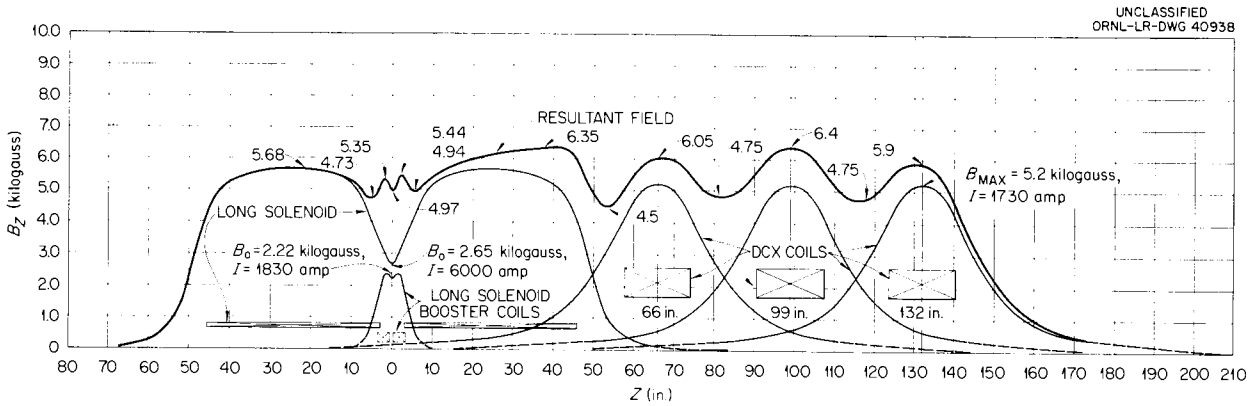

Fig. 8.2.1. Long Solenoid Arc Facility Resultant Axial Field with Booster Coils and Three DCX Coils.

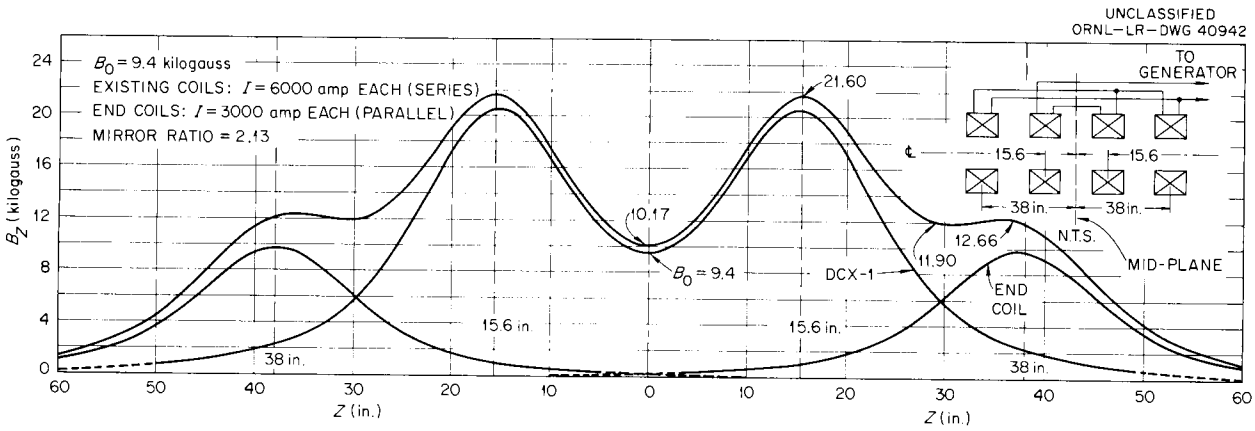

Fig. 8.2.2. DCX-1 with Combined Fields of Additional Coils.

to the relation

$$\rho = \frac{1.798\sqrt{AE}}{nB} ,$$

where A is the mass number, E the energy in kev, n the number of electron charges, B the magnetic field strength in kilogauss, and ρ the radius of curvature in inches.

An ion trajectory in a magnetic field without sharp gradients is closely approximated over a short path by a circle. By adjusting the radius of curvature in appropriate steps the complete ion path may be traced. Experience shows that, in general, sufficient precision is achieved when the rotationally symmetrical magnetic field is divided in circular ring zones of 1 in. radial thickness. The flux density B of each zone is assumed constant and equal to the actual value at the middle of this zone. Two examples of this kind of graphical work will be given.

DCX-1 Design for Precessing H_1^+ Orbit

In order to reduce charge-exchange losses of the trapped ion beam in DCX-1, it was suggested to inject H_2^+ ions with 600 kev energy into a precessing orbit. In the magnetic field produced by the rated coil current of 6000 amp the arc is positioned to cross the midplane at a distance of 5.3 in. from the magnetic center. The tangent to the ion beam at the arc is assumed to be orthogonal to the radius. Since 5.3 in. is the radius of a stable orbit of D_1^+ ions of 300 kev, the lighter H_1^+ ions will precess. The radius of the circle which contains the precessing orbit will be 5.3 in. The circle with smaller radius (r = 1.8 in.), which limits the precession zone on the inner side, has been found graphically (see Fig. 8.2.3).

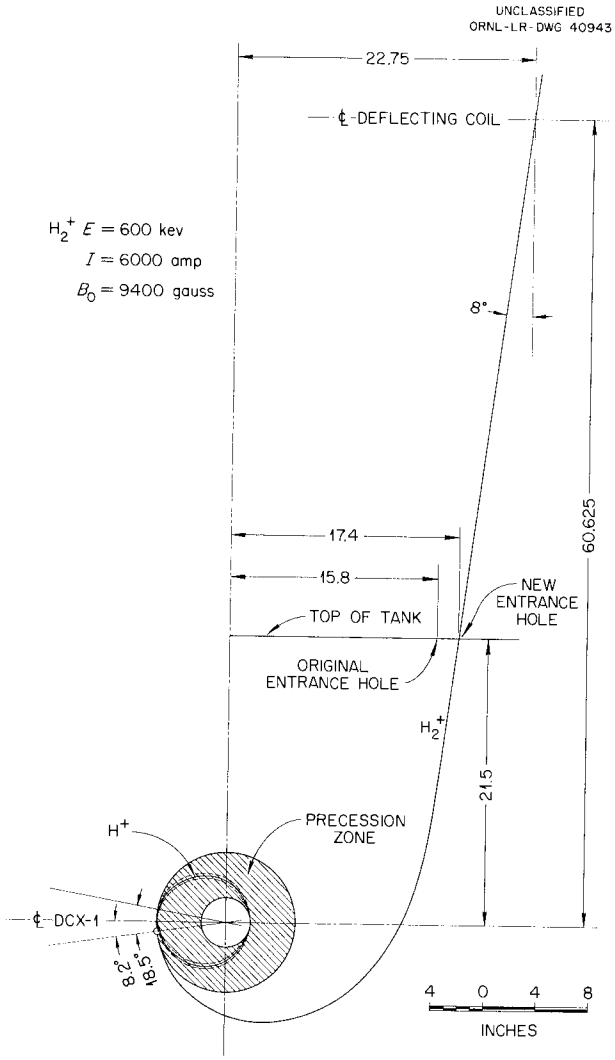

Fig. 8.2.3. DCX-1 Beam Entry and Precession Orbit.

In order to find the number of revolutions of an H_1^+ ion before it reaches the arc again, the angle between two successive aphelion positions is determined (see Sec 7.3). This can be done with higher precision by using auxiliary orbits which represent the boundaries of a narrow beam, focused at the arc. The precession angle is approximately 18.5°, corresponding to 19 to 20 turns before the arc is reached again.

Figure 8.2.3 also shows the H_2^+ trajectory with the position of the existing analyzing magnet on top of the DCX-1 vacuum chamber unchanged. It is only necessary to move the entrance hole, on top of the tank, by 1.6 in. The assumption was made that the H_2^+ trajectory is a straight line outside the tank. The arc must be positioned at an angle of 8.2° below the horizontal through the magnetic center. The analyzing magnet deflects the H_2^+ beam about 8° from the vertical.

Trajectory Design for Arc Wall Experiments

Another example of plotting ion-beam trajectories is shown in Fig. 8.2.4. The arc wall experiment (see Sec 4.2) in DCX-EP-A uses D_3^+ ions, which are dissociated by the arc wall into D_1^+ ions and other particles. A plot of the D_1^+ orbit shows (see Fig. 8.2.4) that a precession zone can be achieved which stays inside the arc wall and which should reduce charge exchange losses in the arc wall. The D_3^+ beam is produced by a grid source, the position of which must be determined.

The first step in finding the source position is to find the exact shape of the hollow arc in the midplane. Since the position (½ in. above the magnetic axis) and the radius of the analyzer cathode and anode (which are 10 in. outside the coil centers) are known, the shape of the hollow arc in the midplane is found by following field lines from the circumference of the electrodes to the midplane. The breakup point F is assumed to be ⅛ in. above the center circle of the arc wall. Starting from F, the D_3^+ beam can be followed up in the direction of the grid source. The position of the source, however, is yet unknown. Figure 8.2.4 shows the geometrical loci A, B, and C of the centers of curvature of the trajectories a, b, and c. If the position of the grid is determined in a proper way, the centers of curvature of the three beams a, b, and c, have to be located on the straight line through the grid. This property is sufficient to find the ion source position. Figure 8.2.4 also shows the trajectories of D_1^+ and D_2^+ ions leaving the ion source, the broken-up D_2^+ ion trajectory, and finally the unbroken D_3^+ ion beam.

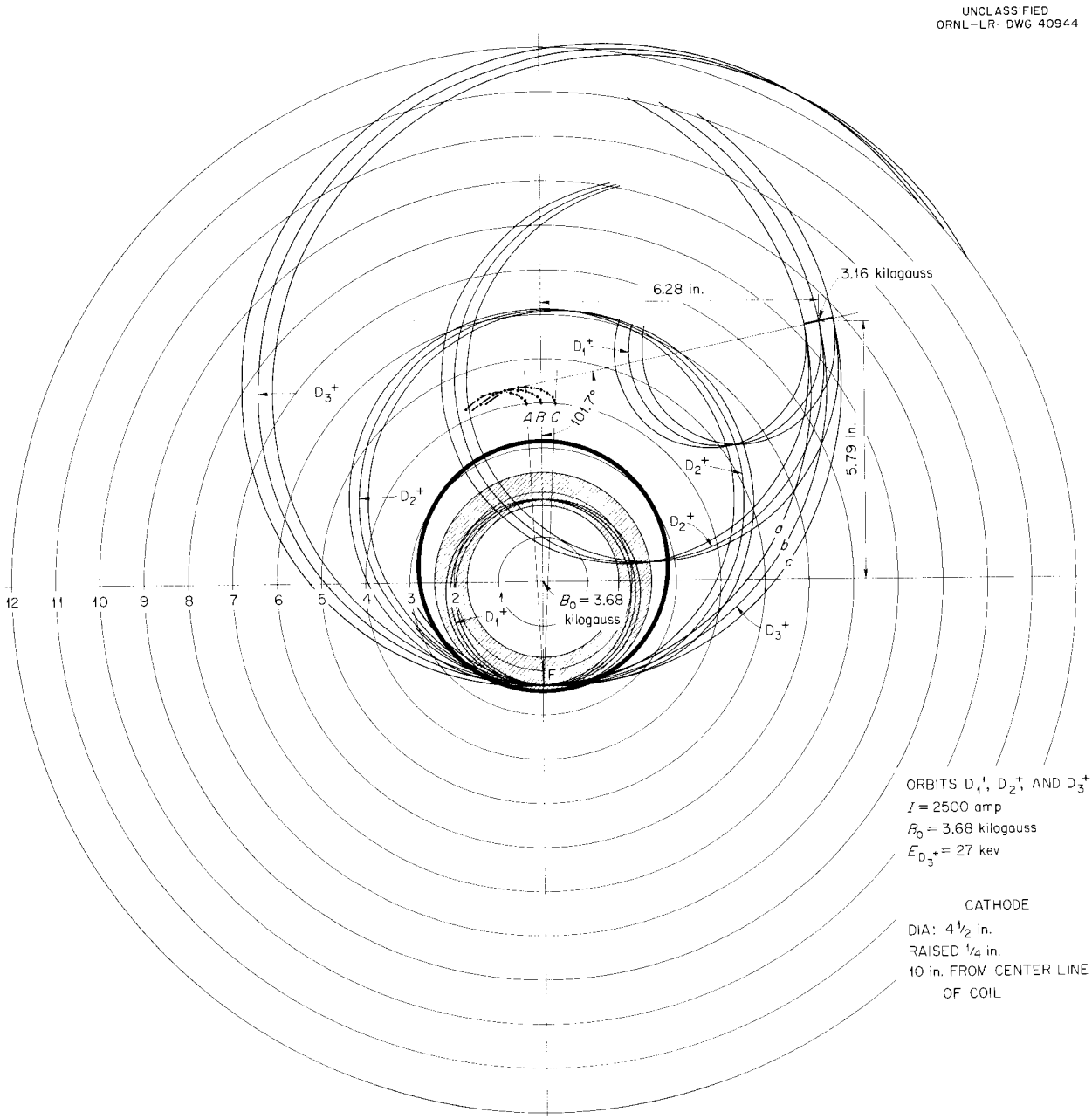

Fig. 8.2.4. Location of Source Position for DCX-EPA-1 Showing Precession Within the Unsymmetric Arc Wall.

8.3 DESIGN OF LONG SOLENOIDS FOR ARC STUDIES

W. F. Gauster J. N. Luton, Jr.

Arc studies require long solenoids with approximately homogeneous magnetic fields. Since flux densities of the order of 25 kilogauss and lengths of 10 ft or more are desirable, the necessary power is high; and it was decided to design the solenoids to match existing 6-Mw d-c power supplies. The field strength produced by any coil arrangement depends strongly on the copper volume, and a practical compromise has to be made between good efficiency and a reasonable copper weight. Around 5 tons for a 10-ft solenoid, and 10 tons for a 14-ft solenoid seems to be reasonable. When a considerable number of observation portholes is desired, the design requirements differ from those appropriate to only a small number of holes. Furthermore, the variation of the magnetic field strength in the solenoid should not be too high, that is, the influence of the portholes and the reduction of the flux density at the solenoid ends must be held within prescribed limits. Finally, sufficient cooling must be provided.

8.3.1 COPPER WEIGHT DIAGRAM

The starting point for calculating a long solenoid is Fabry's equation: [1]

$$H_0 = G \sqrt{\frac{P\lambda}{\rho a_1}} \quad , \tag{1}$$

where

P = power in watts,

λ = space factor = ratio of copper cross section to total cross section, including insulation and free interspaces = copper volume/solenoid volume,

ρ = copper resistivity in ohm-cm,

a_1 = inside radius of the coil in cm,

G = Fabry factor (dimensionless),

H_0 = maximum magnetic field strength in oersteds, having the same numerical value as B_0 (flux density) in gauss.

[1] C. Fabry, *L'Éclairage Électrique* **17**, 133–41 (1898).

A good approximation for calculating the maximum field strength is achieved when the actual conductor cross section is considered to be evenly distributed over the appropriate area. Under this assumption, for a rectangular coil with uniform current density:

$$G = \frac{\sqrt{2\pi}}{5} \sqrt{\frac{\beta}{\alpha - 1}} \ln \frac{\alpha + \sqrt{\alpha^2 + \beta^2}}{1 + \sqrt{1 + \beta^2}} \quad , \tag{2}$$

where

$$\alpha = \frac{a_2}{a_1} = \frac{\text{outside solenoid radius}}{\text{inside solenoid radius}} \quad ,$$

$$\beta = \frac{b}{a_1} = \frac{\text{half solenoid length}}{\text{inside solenoid radius}} \quad .$$

When $\beta = 10$, a good approximation (error smaller than 2%) is:

$$G = \frac{\sqrt{2\pi}}{5} \sqrt{\frac{\alpha - 1}{(\alpha + 1)\beta}} \quad . \tag{3}$$

For a solenoid 10 ft long with $a_1 = 6$ in. and $a_2 = 14.5$ in., the Fabry factor is close to 0.1. For a solenoid 14 ft long with $a_1 = 5.59$ in. and $a_2 = 13.9$ in., $G = 0.082$. In the first case, however, the space factor λ is only 0.40, since four observation gaps 4 in. wide are arranged in each of the three sections (see Fig. 8.3.1). In the second case (see Fig. 8.3.2) the space factor is approximately 0.80. These data show that it is necessary to make the windings as thick as possible in order to achieve a reasonable efficiency.

Figure 8.3.3 is a diagram showing the copper weight as a function of the maximum flux density B_{max} (in kilogauss), the outside radius a_2 (in inches), and the length $2b$ (in feet). Power, space factor, and inner radius are fixed; all other solenoid parameters are allowed to vary. With such a "catalog" of information available, the operating group can make a reasonable choice of solenoid length, weight, and field. Figure 8.3.3 was drawn for the solenoid type shown in Fig. 8.3.2. Point A in Fig. 8.3.3 indicates the data of the particular solenoid which was chosen. End compensation is not desired for this solenoid.

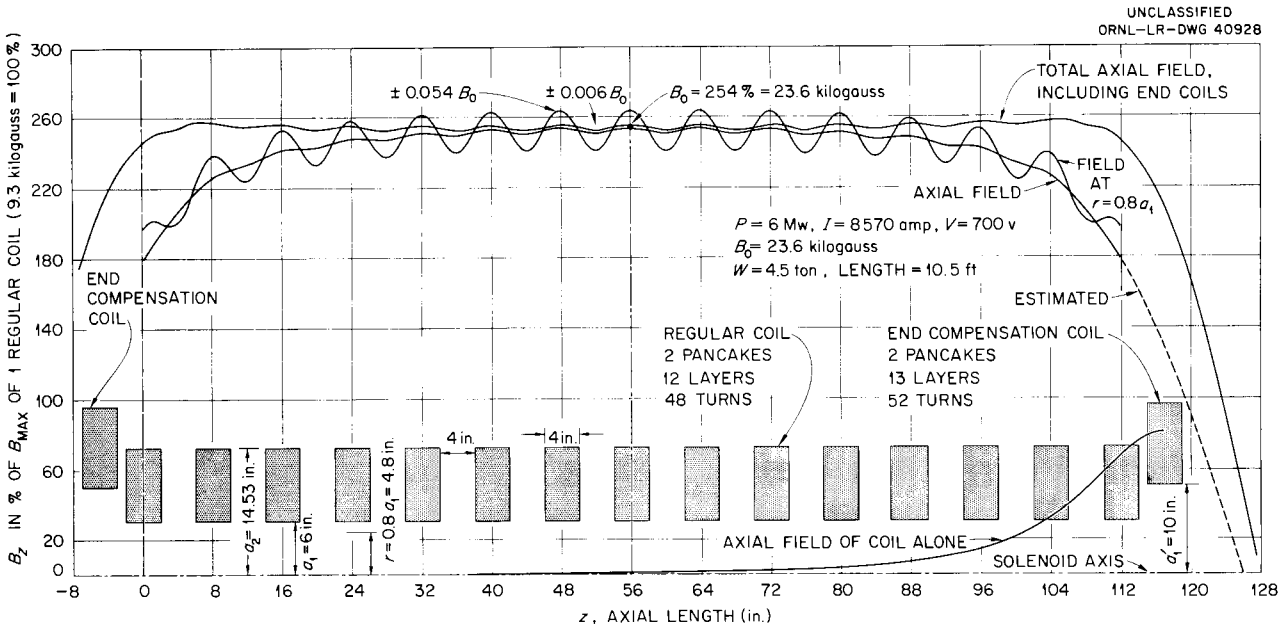

Fig. 8.3.1. Cross Section and Field Shape of 10-ft Solenoid.

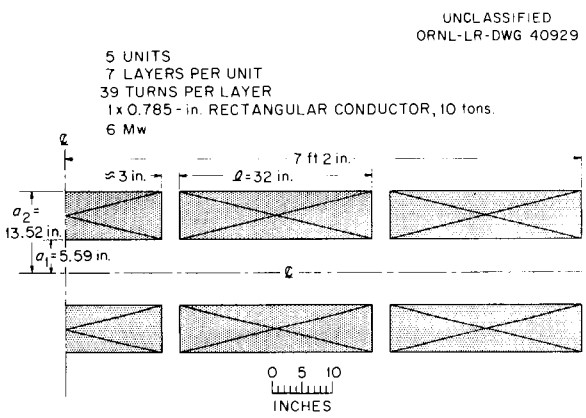

Fig. 8.3.2. Cross Section of 14-ft Solenoid.

8.3.2 VARIATION OF MAGNETIC FIELD STRENGTH IN THE SOLENOID

The Mathematics Group of TED made an Oracle calculation of the axial component B_z of the magnetic field strength at the axis and at a line parallel to the axis having a distance from the axis $r = 0.8a$. For the 10-ft solenoid, the field strength distribution is shown in Fig. 8.3.1. (The Oracle calculation was based on double pancake coils with 14 layers each, matched without end compensation to a 5-Mw power supply. The revised situation is 12 layers per coil with the solenoid including end compensation matched to 6 Mw. There is very little difference in the magnetic fields produced, and the detailed Oracle calculation has not yet been repeated.) The field variation at the axis is only about 1%. At the $0.8a$ line, the fluctuation is between 4.5 and 6%. The comparative uniformity is due to the shortness of the individual coils and gaps, and to the depth of the windings.

In order to compensate the end effects, an additional coil is provided at each end. The axial field of the end coil was approximated by means of Lyle's theorem and added to the field of the regular coils, as shown in Fig. 8.3.1. The field strength over a range of 8½ ft inside the solenoid is well compensated. The total power of 6 Mw is divided into 5 Mw for the 15 regular coils and 1 Mw for the pair of compensation coils. The arrangement of the end coils fits the mechanical demands of the design made by the Engineering Group of the TED.

8.3.3 COOLING PROBLEMS

Because individual coils of the 10-ft solenoid were to be only 4 in. in axial length, it was decided to use hollow rectangular conductors fabricated into pancakes (a pancake being a pair of concentric spirals in parallel planes), which

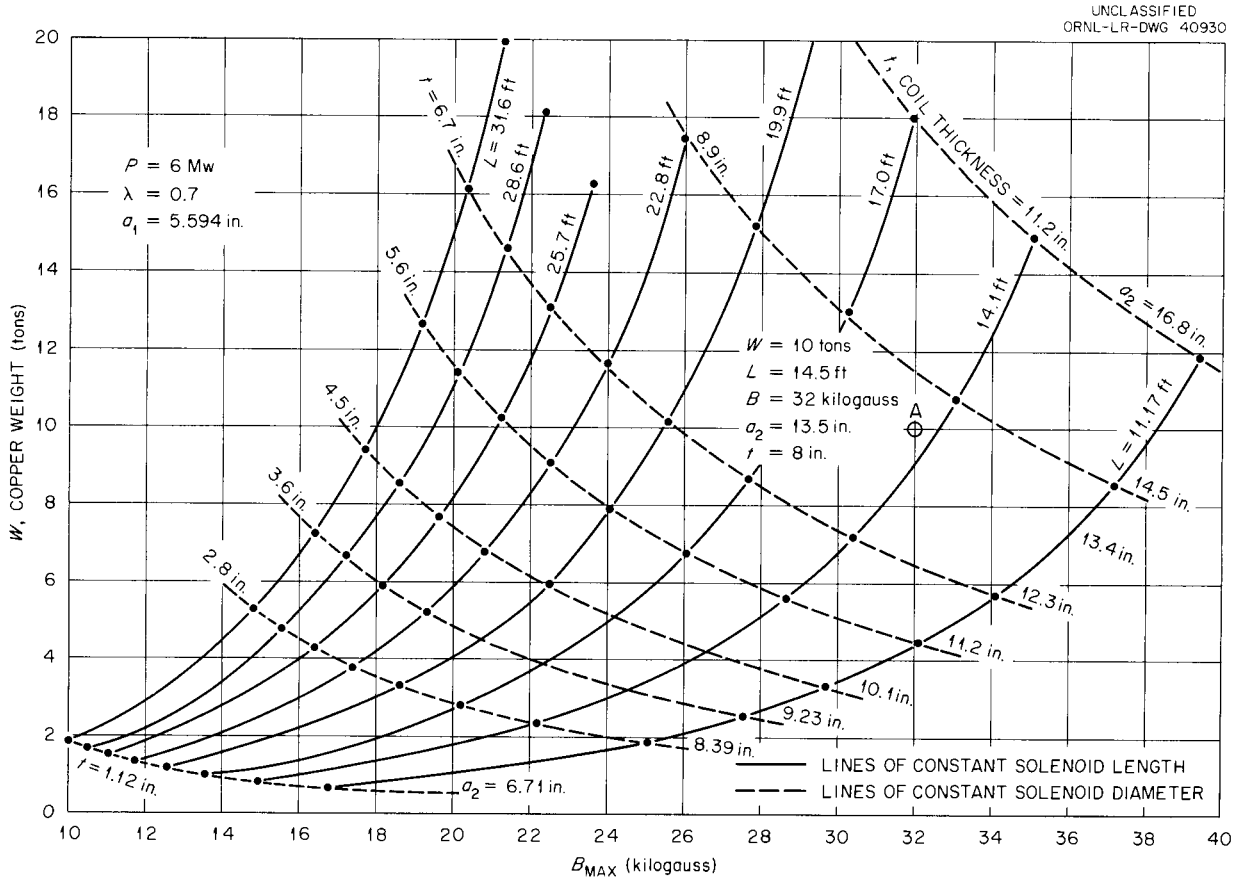

Fig. 8.3.3. Copper Weight Diagram for Long Solenoids.

is the same construction used in DCX-EP-A1. The desired coil thickness resulted in a water path so long that proper cooling was doubtful. The path length was then cut in half by introducing water at the center of the spiral and permitting it to flow outward through both halves of the pancake. This changes the water temperature rise by a factor of $(1/2)^{3/2}$, or 0.35, and makes the pancake design feasible for considerably thicker coils.

The 14-ft solenoid is made up of five sections, each 32 in. long. This makes it impossible to introduce water to the center of any but the end pancakes without encroaching upon the solid cylindrical space inside the copper, which is reserved for experimentation. Having only one water path per pancake (water entrance and exit at the outer radius) did not provide sufficient cooling. The design was then changed to solid rectangular conductors wound in concentric helices of different radii, with the longer side of the conductor cross section perpendicular to the coil axis. Cylindrical cooling passages are provided between conductor layers to provide water flow parallel to the axis. This is exactly as in the Bettis-type DCX-1 coils, except that the water comes in one end, makes one pass only over the copper, and leaves at the other end.

9. CROSS SECTION EXPERIMENTS

C. F. Barnett R. A. Gibbons D. P. Hamblen
L. A. Massengill H. Postma J. A. Ray

The cross section experiments in the Thermonuclear Experimental Division are of two types – "high energy" and "crossed beam." The cross sections to be measured are of fundamental importance in explaining the dissociation and loss mechanisms in the DCX. Equipment for both types has been designed and constructed, and improvements and systematic checks are being made.

9.1 HIGH-ENERGY CROSS SECTION EXPERIMENTS (100–600-kev ION BEAM)

The cross sections of most immediate interest are:

1. $H_2^+ + \text{gas} \rightarrow H^+ + H^0 + \text{gas}$
   or $2H^+ + e + \text{gas}$,
2. $H_3^+ + \text{gas} \rightarrow H_2^+ + H^0 + \text{gas}$
   or $H^+ + H_2 + \text{gas}$,
3. $HeH^+ + \text{gas} \rightarrow He + H^+ + \text{gas}$
   or $He^+ + H + \text{gas}$,
4. $H_2^+ + \text{gas}$ vs $D_2^+ + \text{gas}$ (and possible cross section changes due to increased vibrational distances in D_2^+) ,
5. $H^0 + \text{carbon arc} \rightarrow H^+ + e$,
6. $H_3^+ + \text{carbon arc} \rightarrow \text{dissociation}$,
7. $H^+ + \text{carbon arc} \rightarrow H^0$.

The cross sections for dissociation of diatomic hydrogen ions in target gases of hydrogen, helium, nitrogen, and argon over an energy range of 100 to 600 kev will be the first quantities to be investigated. The measurements of Barnett[1] and Fedorenko[2] are in disagreement in the narrow region of overlap (500 kev), and this experiment will extend the earlier measurement of Barnett into the lower energies to permit closer comparison. Competing charge-exchange processes complicate the measurement at the lower energies.

The experimental setup is similar to that described by Stier and Barnett[3] except that the first gas cell is not used, and an additional detector is installed to measure the deflected beam. The H_2^+ beam from the accelerator supply of DCX is incident upon a differentially pumped target cell containing gas at a pressure sufficiently low to avoid multiple collisions. The emerging products from the gas cell – H_2^+, H^0, H^+ – are electrostatically separated to analyze the components of the resulting beam. An axial secondary-electron detector and Faraday cup (i.e., one detector with two functions) and another detector identical to the axial one but mounted horizontally 1 in. away are used to analyze the neutral and charged particles of the emergent beam. Table 9.1.1 illustrates the currents to be measured (some measurements are repeated by different methods to provide calibration or consistency checks).

The cross section can then be calculated from the following relations:

$$\frac{I_1}{I_0} = \frac{\sigma_{d_1}}{\sigma_{d_T}} \left(1 - e^{-\sigma_{d_1} xn}\right) ,$$

$$\frac{I_2}{I_0} = \frac{\sigma_{d_2}}{\sigma_{d_T}} \left(1 - e^{-\sigma_{d_2} xn}\right) ,$$

where

x = particle path length in gas,

n = density of target gas,

σ_{d_1} = dissociation via $H_2^+ \rightarrow 2H^+ + e$,

σ_{d_2} = dissociation via $H_2^+ \rightarrow H^+ + H^0$,

$$\sigma_{d_T} = \sigma_{d_1} - \sigma_{d_2} .$$

[1] C. F. Barnett, *The ORNL Thermonuclear Program*, ORNL-2457, p 126–27 (Jan. 15, 1958).

[2] N. V. Fedorenko, *J. Exptl. Theoret. Phys. (U.S.S.R.)* 2, 385 (1959).

[3] P. M. Stier and C. F. Barnett, *Phys. Rev.* 103, 896–907 (1956).

Measurements await reduction of the base pressure in the gas cell and the release of the DCX 600-kev accelerator. Substitution of different ion beams while using the same equipment will allow the sequential investigation of the cross sections for processes 2–4. Substitution of the carbon arc described by Barnett, Mackin, and Ray[4] for the target gas cell will permit the completion of measurements of this list of cross sections.

[4]C. F. Barnett, R. J. Mackin, Jr., and J. A. Ray, *The ORNL Thermonuclear Program*, ORNL-2457, p 128–32 (Jan. 15, 1958).

Table 9.1.1. Currents To Be Measured and Detectors Used in 100–600-kev Cross Section Measurements

Detector	Electrostatic Deflection	Measurement
1. Axial Faraday cup	None	$I_{H_2^+} + I_{H^+}$
2. Axial secondary electron detector	Yes	I_{H^0}
3. Off-center Faraday cup	Yes	$I_{H_2^+}$
4. Off-center Faraday cup	Yes	I_{H^+}
5. Off-center secondary electron detector	Yes	I_{H^+}

Total incident H_2^+ beam: $I_0 = I_{H_2^+} + I_{H^+} + I_{H^0}$

Total reactions proceeding via $H_2^+ \rightarrow H^+ + H^+ + e$: $I_1 = \dfrac{I_{H^+} - I_{H^0}}{2}$

Total reactions proceeding via $H_2^+ \rightarrow H^0 + H^+$: $I_2 = I_{H^0}$

9.2 CROSSED-BEAM CROSS SECTION EXPERIMENTS (5–50-kev ION BEAM)

The cross sections of most immediate interest in the lower energy region are:

1. $H_2^+ + e \rightarrow H^+ + H^0 + e$
   or $2H^+ + 2e$,
2. $H_2^+ + H^+ \rightarrow H^0 + 2H^+$
   or $3H^+ + e$,
3. $H^0 + H^+ \rightarrow 2H^+ + e$,
4. $H_2^+ + C^+, C^{++}, C^{+++} \rightarrow$ dissociation .

Common to all these proposed investigations is the necessity for producing and crossing beams of particles.

The cross section for dissociation of the hydrogen diatomic ion by electrons is the first quantity to be measured by the crossed-beam method. An analyzed H_2^+ beam is crossed at right angles by an electron beam in a collision chamber. A solenoidal magnetic field in this chamber confines the electrons to paths perpendicular to the H_2^+ beam and also analyzes the dissociation products according to charge and mass. A movable secondary-electron detector and Faraday cup analyze the neutral and charged particles of the emergent beam (in the fashion outlined in the preceding section) to give the cross section for the two modes of dissociation ($H_2^+ + e \rightarrow 2H^+ + 2e$; $H_2^+ + e \rightarrow H^+ + H^0 + e$).

A steady background current produced by particles from H_2^+ dissociating on the gases of the vacuum system (10^{-7} mm Hg) is 100 times larger than the expected current from the $H_2^+ + e$ dissociation, and so it is necessary to chop the

electron beam electronically and to use phase-sensitive detectors for the dissociated particles. The resulting modulated current will arise mainly from the desired interaction. The background under these conditions will arise from stochastic processes, beam noise, and pressure fluctuations of the background gas.

We are operating with a 20-kev H_2^+ beam of 30 μa and a 10-ev electron beam of 6 ma in a pressure range of $0.9-1 \times 10^{-7}$ mm Hg. At present the beams have inhomogeneities in both space and energy that make them unacceptable for cross section measurements. Refinements are being introduced into the equipment for the purpose of improving the quality of the beams. If this can be done, successful development of the crossed-beam technique will permit completion of the measurement of the other cross sections listed and an extension of the measurements to higher energies may also be possible.

10. DIFFUSION OF DEUTERIUM IN COPPER

M. T. Robinson[1] A. L. Southern[1]
W. R. Willis[2]

Among the problems associated with the walls of a thermonuclear device is the rate at which "cold" deuterium, produced by slowing down of "hot" ions in the wall and subsequent diffusion, is returned to the plasma. As an aid in analyzing this problem, experiments are being performed on the rate of diffusion of deuterium in deuteron-irradiated copper. Only a brief summary of the results to date is presented here. The current Solid State Division Annual Report[3] should be consulted for details.

[1]Solid State Division.

[2]Consultant.

[3]*Solid State Ann. Prog. Rep. Aug. 31, 1959*, ORNL-2829 (in press).

10.1 EXPERIMENTAL PROCEDURE AND RESULTS

Briefly, the experiment consists in irradiating a copper target, typically about 0.020 in. thick, maintained at a constant temperature by a circulating alcohol stream, with a beam of 176-kev deuterons produced from the Cockcroft-Walton accelerator at the High Voltage Laboratory, and monitoring the neutrons produced from the $D(d,n)He^3$ reaction. The incident deuterons are slowed to thermal energies within the target, their mean range being about 1.63 μ, and subsequently diffuse throughout the volume of the metal. The observed neutron counting rate, $P(t)$, is related to the deuterium concentration in the target by

$$P(t) = a \int_0^\infty \sigma\left[\frac{E(x)}{E_0}\right] Q(x,t)\, dx \ , \qquad (1)$$

where a is a proportionality constant, involving the deuteron beam current, the counting geometry and efficiency, and other factors; $Q(x,t)$ is proportional to the deuterium concentration in the target; $\sigma[E(x)/E_0]$ is proportional to the cross section for the $D(d,n)He^3$ reaction; $E(x)$ is the deuteron energy within the target; E_0 is the incident deuteron energy; t is time; and x is the penetration coordinate measured normal to the target surface.

A typical experimental curve is shown in Fig. 10.1.1. The observations have been corrected for background and for counter dead-time losses. From the viewpoint of fitting Eq. (1) to a set of data, the experimental curve may be divided into three regions:

1. **$0 \leqq t \leqq \sim 1000$ sec:** Almost any reasonable diffusion model can be fitted to the data in this region. The diffusion process itself, described by a parameter $\delta = D/R^2$, where D is the diffusion coefficient and R is the deuteron range, is rate-controlling.
2. **~ 1000 sec $\leqq t \leqq \sim 2500$ sec:** This region is very sensitive to the choice of the model. Diffusion alone is not rate-determining.
3. **$t > \sim 2500$ sec:** This region is sensitive to the model only in the respect that models suggesting rapid attainment of a steady state are ruled out.

The curves in region 3 may all be readily fitted by assuming the target to be infinitely thick beyond the deuteron range. In this case, it may be readily shown that Eq. (1) may be reduced to

$$P(t) = a(1 - bt^{-1/2} + Ct^{-3/2} \ldots) \ . \qquad (2)$$

An empirical equation of this sort fits all the experimental observations to date for $t > \sim 1500$ sec. Elimination of the third term in Eq. (2) is satisfactory for $t > \sim 2500$ sec. The assumption of infinite thickness is entirely reasonable since the ratio of target thickness to deuteron range is about 300 at the very least. The coefficient b can be shown to have the form

$$b = \frac{1+\gamma}{\delta^{1/2}} \ , \qquad (3)$$

where γ is a surface resistance and δ is the diffusion parameter. If γ is taken as zero, that is, if

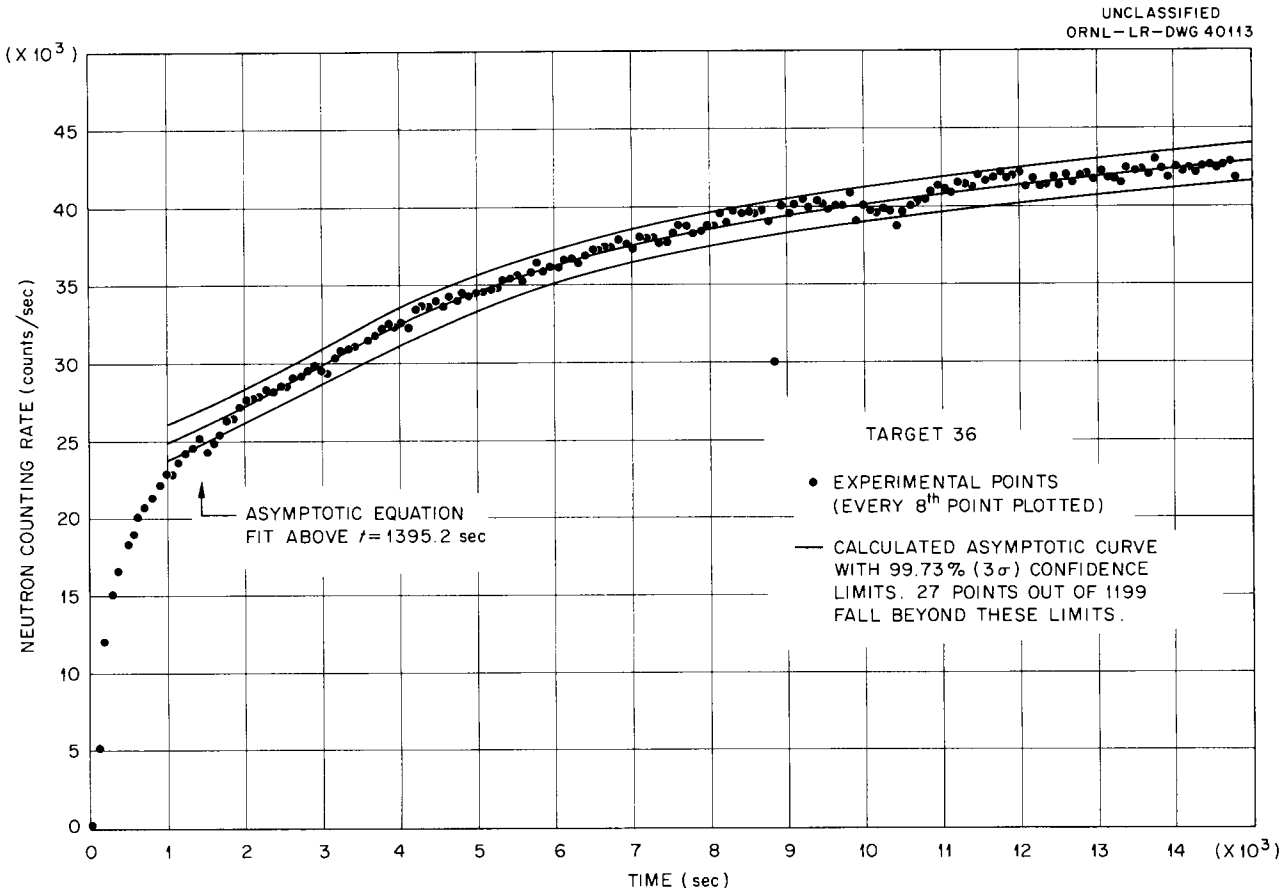

Fig. 10.1.1. Typical Curve for Diffusion of Deuterium in Copper.

every deuterium atom reaching the irradiated surface escapes immediately into the gas phase, the experimental curves in region 2 cannot be well fitted at all. Introduction of nonzero values of γ, however, greatly improves the agreement. Typical results are shown in Table 10.1.1.

The most recent refinement in the diffusion model is to introduce a parameter β to describe the dispersion of the deuteron range (the "straggle"). No computations are yet available to determine whether this change results in any improvement in the fitting of the experimental data.

The significance of the values of γ obtained may be illustrated by noting that $1/\delta$ is approximately the mean time required for a deuterium atom to diffuse from the end of the deuteron range to the irradiated surface. The mean time for that escape of the atom into the gas phase is, roughly, γ/δ. Hence, whatever surface effects cause γ to be nonzero have a major effect on retention of deuterium by the targets.

Other experiments, not yet analyzed in detail, show that the neutron counting-rate curves depend on target temperature in the expected sense. No quantitative interpretation is yet possible. There seems also to be a possibility that δ is somewhat dependent on the deuteron beam current, suggesting that internal strains in the metal are responsible for at least part of the diffusion observed.

Table 10.1.1. Relation of Surface Resistance and Diffusion of Deuterium in Copper

Target	Surface Resistance, γ	Diffusion Parameter, δ (sec^{-1})	Agreement Index* (%)
34	0	$(3.55 \pm 0.05) \times 10^{-3}$	2.48
	1.40 ± 0.05	$(1.39 \pm 0.04) \times 10^{-2}$	1.38
36	0	$(1.34 \pm 0.03) \times 10^{-3}$	5.73
	6.47 ± 0.28	$(2.80 \pm 0.17) \times 10^{-2}$	3.32

*The agreement index is defined as

$$\left[\frac{\sum w(P_{obs} - P_{calc})^2}{\sum w P_{obs}^2}\right]^{1/2} \times 10^2\% ,$$

where w is the weight of an observation, and the summations extend over all observations.

11. SPUTTERING AND SURFACE PHYSICS

O. C. Yonts D. E. Harrison, Jr.[1]

11.1 NEW EQUIPMENT

During the past six months part of our time has been devoted to development and testing on the following new equipment.

11.1.1 DOUBLE ACCELERATION ION SOURCE

A double acceleration ion source has been built and tested. This source was designed to give high-current beams of H^+ and D^+ ions up to energies of 70 kev. Total source emissions of approximately 100 ma have been obtained, but at present only about 10 ma is available at the target.

11.1.2 SINGLE ACCELERATION ION SOURCE

A new single acceleration source, also for H^+ and D^+ ions, was successfully operated with voltages to 40 kev and ion beams of 150–200 ma at the target. This source is shown in Fig. 11.1.1 without shields and with only the 90° baffle in place. Data taken with this system are shown in Fig. 11.1.2 and discussed below.

11.1.3 VACUUM ANALYZER

A small vacuum analyzer in the form of a 180° mass spectrometer has been completed and is now undergoing preliminary tests. Ultimately it will be installed in large operating vacuum systems to provide partial-pressure information on the background gas. Vacuum analysis has recently taken on new significance in the sputtering work.

[1]Permanent address: Engineering Physics Department, University of Toledo, Toledo, Ohio.

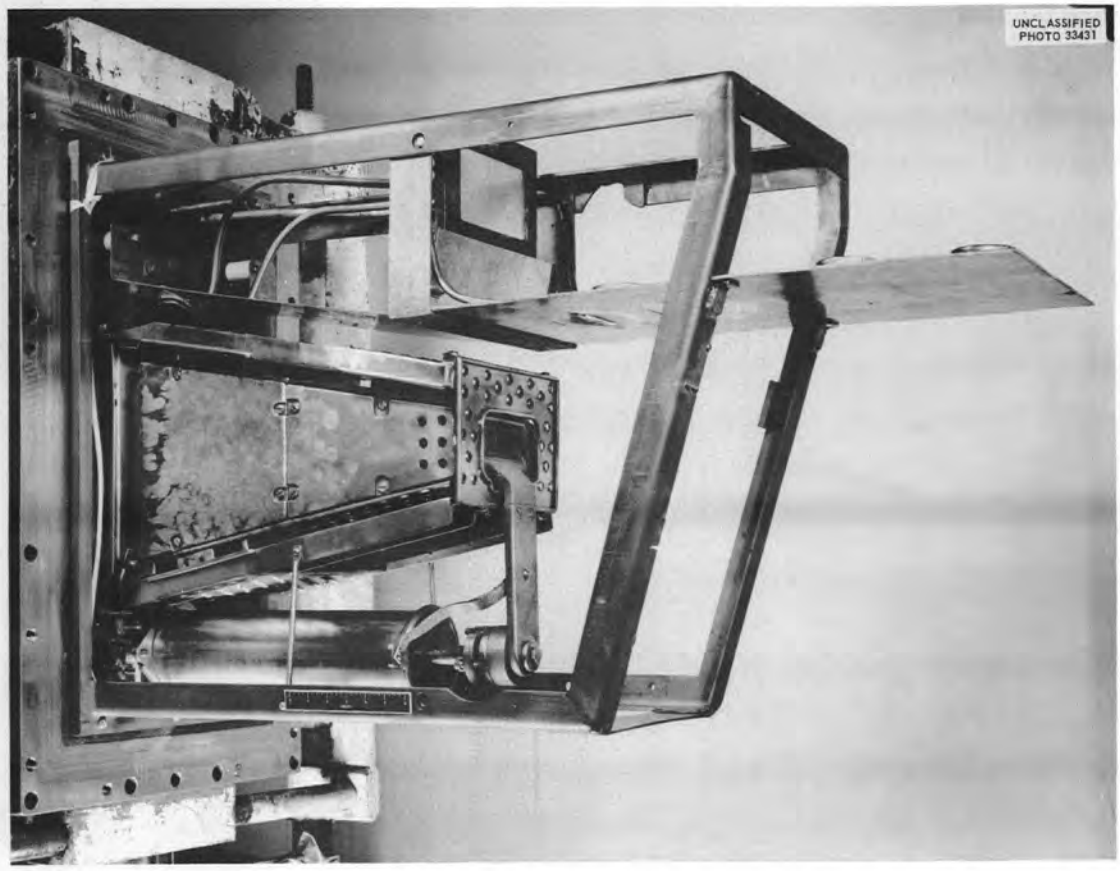

Fig. 11.1.1. Ion Source and Target Assembly for Sputtering with Light Ions.

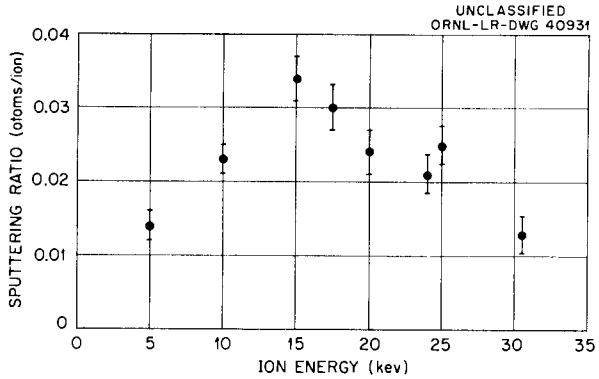

Fig. 11.1.2. Sputtering of Aluminum by Helium.

11.2 SPUTTERING DATA

11.2.1 HELIUM ON ALUMINUM OXIDE

Using the source and target assembly shown in Fig. 11.1.1, a sputtering-ratio vs ion-energy curve for helium bombarding an aluminum target was obtained (See Fig. 11.1.2). No attempt was made to remove the aluminum oxide surface layer, which should be self-renewing for these sputtering ratios at a tank pressure of 4×10^{-5} mm Hg. Also, no allowance has been made for helium which may remain in the target. Current densities were varied in the range from 2 to 8 ma/cm^2, but no variations in the sputtering ratio could be detected.

11.2.2 HELIUM ON COPPER

Some additional data have been obtained for the helium-vs-copper system. These are shown in Fig. 11.2.1, plotted with earlier data for this system. These earlier measurements were made in 1956.

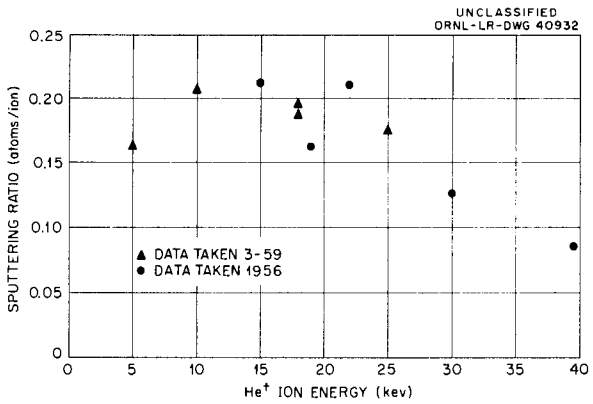

Fig. 11.2.1. Sputtering of Copper by Helium.

11.2.3 ARGON ON COPPER

Enough data have now been obtained on argon bombarding copper at 30 kev to reveal an unexpected pressure effect. As shown in Fig. 11.2.2, the sputtering ratio decreases with increasing pressure. Further tests indicate that this effect cannot be attributed to an increased positive ion current caused by additional low-energy argon

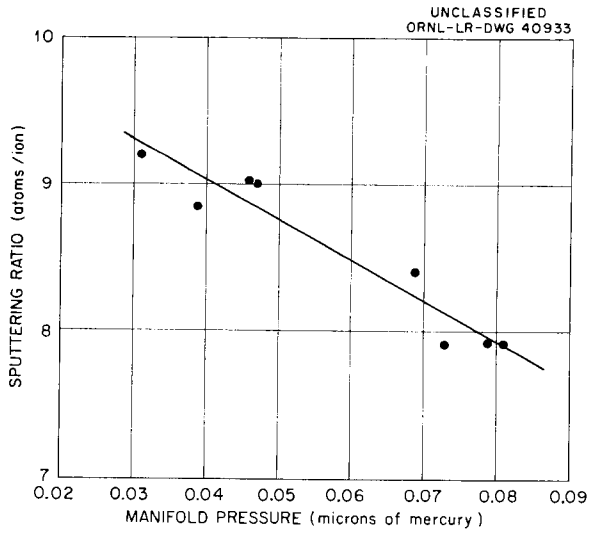

Fig. 11.2.2. Sputtering Ratio vs Pressure; Argon on Copper, 30 kev.

ions produced in the target plasma at higher pressure. This effect may also be present, but it cannot account for our total variation.

We feel that the decreased sputtering ratio is caused by a self-renewing surface film which re-forms as rapidly as it is removed by the bombarding ions. A rough model for the physical adsorption of some unknown material is adequate to interpret the experimental results. Several possible candidates for the adsorbed material are now being investigated.

11.2.4 MISCELLANEOUS SPUTTERING DATA

Some sputtering data have been obtained on other ion-metal combinations (see Table 11.2.1). Of these results only the deuterium on titanium requires comment. For this system the target actually gained 219 mg when bombarded with 170 mg of deuterium ions. This weight gain is evident from even a superficial examination of the target surface, which is swollen and cracked or crazed very much like a mud flat dried in the sun, rather than pitted or etched like other targets. This appearance can be explained as an expansion of the metal lattice to accommodate milligram quantities of additional material. By comparison, titanium bombarded by He^+ has a characteristic etched appearance and there is no visible evidence of adsorption. Apparently a surface compound of titanium deuteride is being formed, but more work must be done on this interesting system.

This program has been ably assisted by J. P. Wood, H. L. Huff, and E. F. Leach.

Table 11.2.1. Miscellaneous Sputtering Data

Ion	Target Metal	Energy (kev)	Sputtering Ratio
He^+	Titonium	20	0.014
D^+	Titanium	24	(~200 mg weight gain)
D^+	Aluminum	24	0.008
A^+	Hardened copper	35	7.15*

*Average of two determinations.

12. METALLURGY

R. E. Clausing J. W. Tackett

The study of the feasibility of using fusible metal seals in ultrahigh vacuum systems has been continued. The major areas under active investigation include studies of the compatibility of fusible alloys with the valve body materials and of the possible use of sintered metal compacts as a reservoir for the sealant alloy.

The evolution of gas from graphite upon heating in a vacuum is being studied. Data have been obtained which allow comparison of several grades of graphite and a partial evaluation of the effects of exposure of vacuum-degassed graphite to air.

12.1 OUTGASSING OF GRAPHITE

The release of gas from graphite during heating in vacuum is being studied at a pressure of 5×10^{-5} mm Hg and temperatures to 2100°C. The results of the first tests are not intended to provide accurate measurements of the outgassing but rather to serve as a means of comparing grades of graphite, degassing treatments, and handling procedures.

Figure 12.1.1 is a block diagram of the apparatus used in this study. The graphite specimen is 0.175 × 0.175 × 0.500 in. and is heated by direct electrical resistance. Water-cooled electrical contacts are arranged so that the specimen temperature is uniform within 20°C. The test cell is water-cooled, and the specimen temperature is determined with an optical pyrometer. The pressure drop across the known conductance (0.4 liter/sec for air at room temperature) provides a measure of the gas evolved. For these experiments the pressure P_1 was held constant at 5×10^{-5} mm Hg (as indicated on ion gage No. 1)

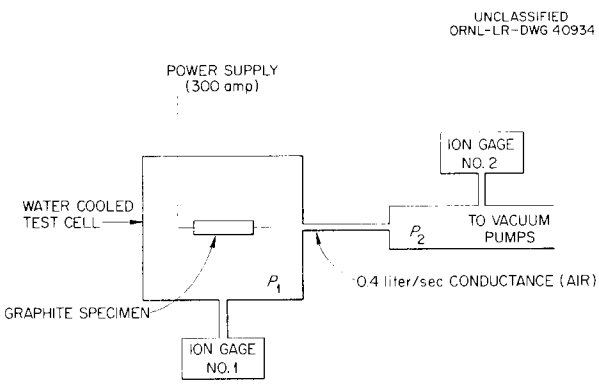

Fig. 12.1.1. Schematic Diagram of Apparatus Used to Study the Outgassing of Graphite.

by varying the temperature of the graphite specimen. Both temperature and time are recorded, and the formula below, derived from the theory of molecular flow, is used to determine the approximate quantity of gas evolved:

$$q = S(P_1 - P_2)t \quad , \tag{1}$$

where

q = total gas evolved at time t in liters of gas at 1 mm Hg,

S = flow conductance between the test cell and ion gage No. 2, in liters/sec,

P_1 = pressure in test cell (held constant), in mm Hg,

P_2 = pressure in pump manifold, in mm Hg,

t = time, in sec.

The quantity Q, defined as the volume of gas evolved per unit volume of graphite, is then calculated as shown below. The units of Q are atmospheric cubic centimeters of gas per 100 cm^3 of graphite or, more simply, volume per cent.

$$Q = q \times \frac{100}{V} \quad , \tag{2}$$

where V = volume of the graphite specimen in cubic centimeters.

Since V, S, P_1, and P_2 are constant during an experiment we can insert their values and obtain:

$$Q = t \times 0.4 \times (5 \times 10^{-5}) - (5 \times 10^{-6}) \times \frac{100}{0.251} \quad ;$$

$$Q = 0.00944 \times t \text{ vol \% } (t \text{ in sec}) \quad ,$$

or

$$Q = 0.58 \times T \text{ vol } \% \ (T \text{ in min}) \ . \qquad (3)$$

Table 12.1.1 is a listing of the relative amounts of gas evolved by various grades of graphite and the results of short exposures to air after vacuum degassing. The values given are calculated on the basis of air; that is, the ion gages and conductance are calibrated for air. These values may be somewhat low, since hydrogen is expected to constitute a portion of the evolved gas. These values, however, should provide a reasonable basis for comparison inasmuch as the gases evolved from various specimens are probably similar. It should be noted that the specially prepared ATJ contains the least gas and that an exposure to air for 1 hr results in re-adsorption of 50% of the original gas content.

Data not included here show that there is very little gas evolved above 2100°C and that between 50 and 75% of the gas is evolved below 1000°C for most specimens tested.

A mass spectrometer will be added to the system in the near future to provide more accurate data and to determine the species of gas evolved as a function of temperature and previous history.

Table 12.1.1. Outgassing of Several Grades of Graphite

Type of Graphite	Gas Evolved Upon Heating to 2100°C* (vol %)
C-18	54, 134, 48, 74
AGOT III	65, 71, 58, 57
Speer's Moderator No. 1	25, 30, 29, 24
Speer's Moderator No. II	18, 16, 22, 17, 17
Special ATJ**	15
Special ATJ exposed to air 1 hr after vacuum degassing	8
AGOT III exposed to air 20 min after vacuum degassing	8

*The values given are the results of individual tests.
**This graphite was chlorinated and partially protected from air during the cooling period.

12.2 GETTER TESTING

The experiment described previously[1] has been slightly modified and adapted to measure the adsorption of nitrogen on tungsten (a well-known system) as a means of perfecting procedures and techniques for such measurements. As soon as these experimental techniques are satisfactorily developed attention will be directed toward measurements using evaporated metal films.

[1]R. E. Clausing, J. W. Tackett, and J. D. Hudson, *Thermonuclear Project Semiann. Rep. Jan. 31, 1959*, ORNL-2693, p 91.

12.3 VALVE AND FLANGE DEVELOPMENT

In the development of high-vacuum valves and flanges to be used in thermonuclear experimental apparatus, various types of demountable joints as well as various seal materials have been investigated. A preliminary study described previously[1,2] showed that: (1) satisfactory high-vacuum demountable flanges have been made utilizing both metal-gasket and welded-seal techniques, (2) a large high-vacuum remotely operated valve can be made using a solidified-metal seal, and (3) high-vacuum valves utilizing a metal seal which is liquid at room temperature are unreliable when present materials and techniques are used.

In connection with the solidified-metal seal investigation, many different demountable joint

[2]*Ibid.*, p 86–90.

designs have been studied in an attempt to determine the most suitable designs. Of the designs studied thus far, the type showing the most promise utilizes a sump-type joint. Two methods for making this type of joint are being investigated. The first method, previously described,[1,2] utilizes a circumferential pool of the filler metal as the joint seal (Fig. 12.3.1). The second method employs a sintered metal compact impregnated with an alloy filler metal which serves as the sealant material. Figure 12.3.2 is a drawing of a possible joint design using this technique. The joint is closed by bringing the two portions (*A*) and (*B*) together, as shown in Fig. 12.3.2*b*, and then heating the joint to a temperature just above the "flowpoint" of the filler metal. The capillary attraction within the compact retains the liquid alloy in the joint area and prevents undesirable flow of the filler metal on the base metal. Figure 12.3.3 shows a typical joint between an impregnated compact and an Inconel plate. If it is necessary to supply additional filler metal to the joint the sintered compact joint may be compressed. The sintered joint has a decided advantage over the sump type in that it can be made and broken in the horizontal as well as the vertical position.

Sintered compacts have been made using coarse metal powders (> 100 mesh) of type 316 stainless

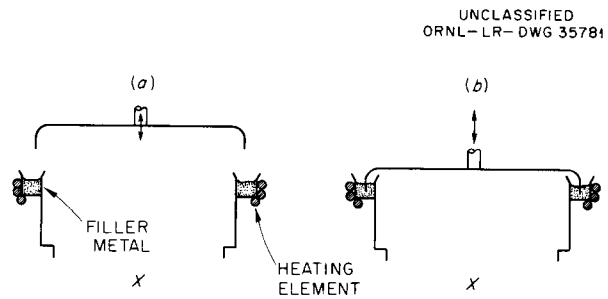

Fig. 12.3.1. Demountable Joint Using Circumferential Pool of Filler Metal as Seal.

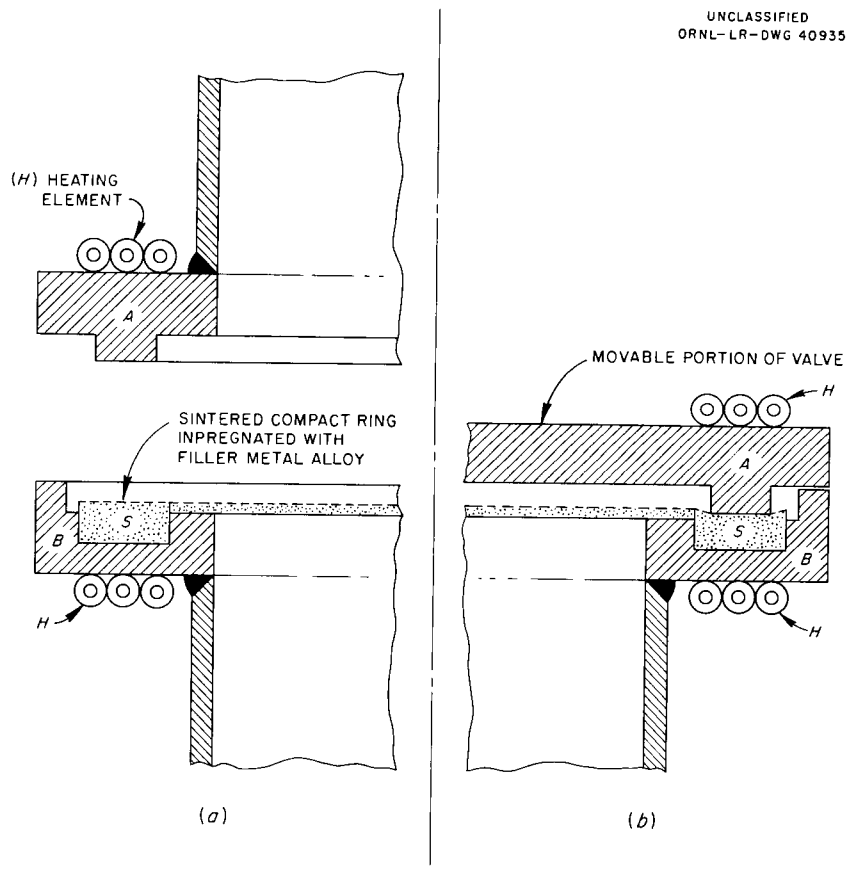

Fig. 12.3.2. Cross-Section View of Demountable Joint Which Utilizes an Impregnated Sintered Compact as the Seal Material. (*a*) Open, (*b*) closed. Note sintered compact may be slightly compressed when valve is closed.

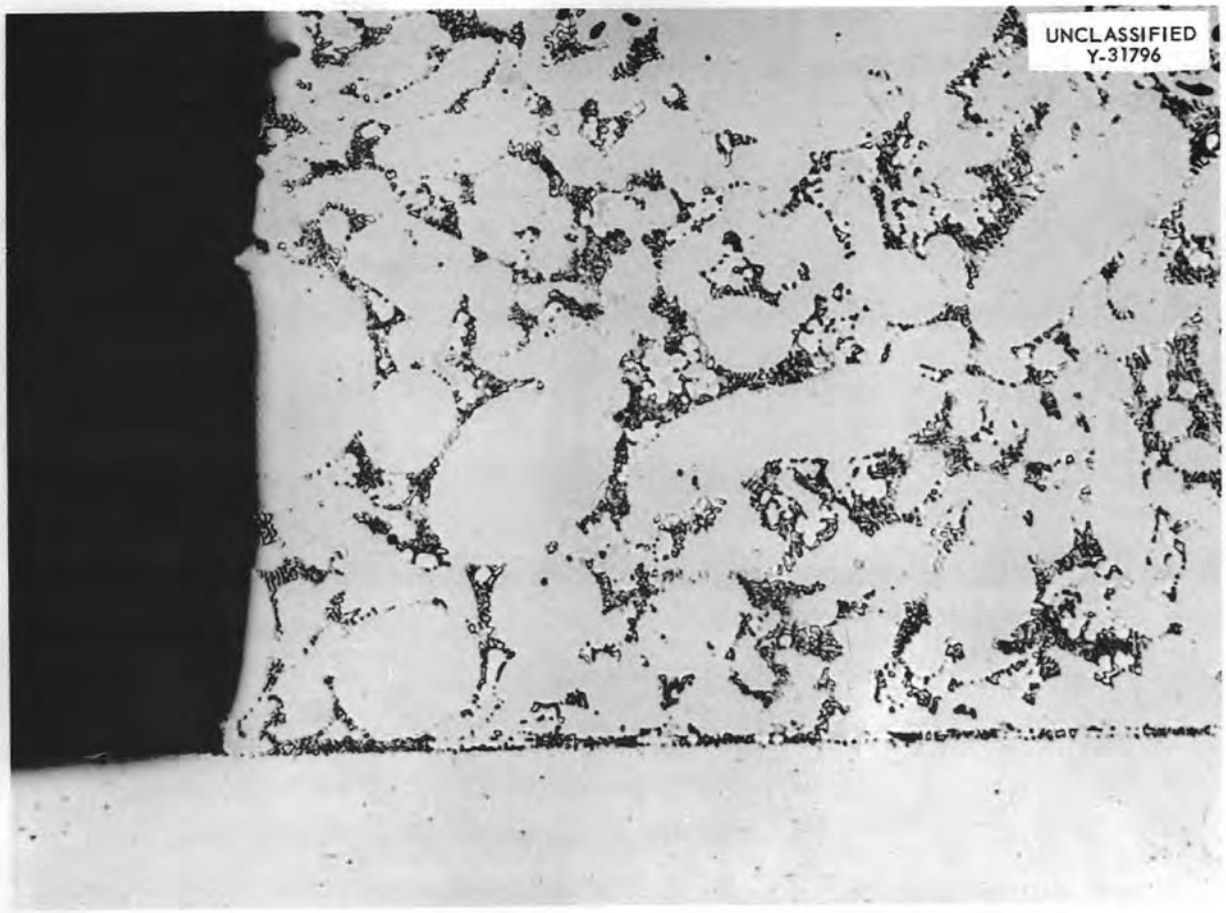

Fig. 12.3.3. Photomicrograph of a Typical Joint Between an Inconel Plate and a Sintered Metal Compact Impregnated with an Alloy Filler Metal.

steel, Inconel, nickel, and iron. The compacts were sintered without compaction to provide as much void space as possible (50%-dense compacts were easily obtained using this method). Various methods of impregnating the metal compact with brazing alloy have been studied. The most satisfactory method tried consists of heating the compact to the temperature required for the filler metal to wet the powder compact before applying the filler metal. Other factors being investigated include:

1. particle size and distribution,
2. method of forming the compact (i.e., rolling, swaging, etc.),
3. compatability of the filler metal and the compact,
4. axial pressure during brazing of the joint.

It is also planned to investigate the use of sintered compacts made of metal fibers instead of metal powders. Fiber compacts may have a definite advantage over powder compacts in that fiber compacts can be made with densities as low as 10% and in addition are strong and flexible.

Two classes of brazing alloys are being examined as a result of the somewhat different conditions encountered in the operation of valves as compared with the use of flanges. The valve-seal material must have a vapor pressure $<10^{-8}$ mm Hg at a temperature just above melting, and the melting point of the seal material should be >400 but $<550°C$. However, for flange-seal materials the vapor pressure need only be $<10^{-8}$ at 400°C, the melting point of the filler metal can be somewhat higher than 400°C, and an oxidation-resistant filler alloy is preferable.

Because the filler alloy serving as the sealant material must be at a temperature above the solidus while a joint of this type is being opened or closed, a study has been initiated to establish the compatibility of candidate filler alloys in contact with compact materials and joined members at a temperature just above the melting point of the alloys. In connection with the flange-seal investigation, several candidate alloy compositions containing Ag, Cu, In, and Sn were prepared and their melting points and wetting characteristics determined and compiled. A typical example of the information obtained is shown in Table 12.3.1. Also, because it is desirable to utilize commercially available materials, a 61 Ag–24 Cu–15 In alloy (Handy and Harman Permabraze 610) has been considered as a flange-seal material. The temperatures shown in Table 12.3.1 are those necessary for initially wetting the base material or compact material and do not indicate the temperatures which are necessary for subsequent opening or closing of the joint. The low-melting, low-vapor-pressure alloys listed in Table 12.3.2 are being evaluated as potentially useful alloys for both valve and flange applications.

Table 12.3.1. Wetting Characteristics of Various Metals in Vacuum (10^{-5} mm Hg) by a Filler Alloy

Alloy No. 2: 28.9% In–35.24% Ag–31.4% Cu–4.76% Sn
Melting point: 550°C

Base Metal	Brazing Temperature (°C)	Wetting Characteristics	Bond
Nickel	630	Good	Poor
Copper	630	Fair	Good
Copper	750	Good	Good
Inconel	870	Fair	Good
Inconel	920	Good	Good
Niobium	920	Good	Poor
Niobium	970	Good	Good
Tungsten	920	Fair	Poor
Tungsten	970	Good	Fair
Molybdenum	920	Good	Poor
Molybdenum	970	Good	Good
304 stainless steel	920	Good	Good
Tantolum	1020	Fair	Good

Table 12.3.2. Melting Points of Potentially Useful Alloys for Valve and Flange Applications

Alloy	Melting Point (°C)
Eutectics	
Ge–Al (46 wt % Al)	424
Au–Ga (31.5 % Ga)	451
Au–Al (3.8% Al)	525
Au–Al (8.5% Al)	569
Au–Cu (33% Cu)	548
Ag–Al (29.5% Al)	566
Intermetallic Compounds (open maximum)	
Au–Sn (37.7% Sn)	418
Au–Ga (26.1% Ga)	470
Au–Ga (41.6% Ga)	490
Puritectics (Amalgaren)	
Sn–Cu (41% Cu)	415

13. VACUUM TESTS

C. E. Normand

13.1 DIFFUSION PUMP PERFORMANCE

Measurements of the performance of various diffusion pumps of interest in the Sherwood program have been continued. In addition to the three pumps previously reported (MCF-1400 and PMC-1440 by Consolidated Electrodynamics Corporation, and DO-4001 by Leybold), tests have now been completed on the following types of pumps: Leybold DO-501 (6 in.), Edwards F903 (9 in.), and Consolidated MCF-700 (6 in.) and PMC-4100 (nominal 10 in.). A re-evaluation of the MCF-1400 pump, extended to include certain modifications, has also been completed. Reports covering the first six of these investigations have been issued, and reports on the remaining two are now in preparation.

The principal characteristics of all the pumps thus far examined are listed in Table 13.1.1. For convenient comparison, listing is in order of increasing pump size.

Attention is called to the very good over-all performance of the PMC-type pumps and to the better-than-average performance of the Edwards F903.

Two major modifications of the MCF-1400 pump were made during the course of its investigation. The water-cooled top shield, described in the previous report[1] as an effective means of reducing

[1] C. E. Normand, *Thermonuclear Project Semiann. Rep. Jan. 31, 1959*, ORNL-2693, p 70.

Table 13.1.1. Summary of Diffusion Pump Characteristics

	Leybold DP-501	CEC MCF-700	CEC PMC-1440	Edwards F903	CEC MCF-1400	CEC MCF-1400 Mod.	CEC PMC-4100	Leybold DO-4001
Pump diameter, in.	$5\frac{7}{8}$	6	$7\frac{1}{4}$	9	10	10	$11\frac{3}{16}$	$13\frac{3}{4}$
Intake aperture, in.^{2}	27.1	28.3	41.3	63.6	78.5	78.5	98.3	148
Heater power for air, w								
Low	1000	700	1060	1500	1500	1400	1400	1500
Medium	1100	800	1800	2500	3100	3000	3400	3000
High	1500	>950	2150	2750	4800	4200	6000	3700
Speed, air at 10^{-5} mm Hg and medium power, liters/sec	420	~600	950	1320	1440	1450	2300	3000
Limiting fore pressure at medium power, μ	75	45	400	400	125	260	400	110
Ultimate pressure at medium power, mm Hg	5.5×10^{-7}	4.5×10^{-7}	5×10^{-7}	3.5×10^{-7}	1.1×10^{-6}	1.1×10^{-6}	4.5×10^{-7}	3×10^{-7}
Oil backstreaming rate at medium power, cc/hr	0.17		0.043	0.30	8.2	0.047	0.19	>0.054
Heater power for hydrogen	1100	960		3250	3400	3800	3400	3100
Speed, hydrogen at 10^{-5} mm Hg, liters/sec	~800	~800 ± 60		>2250	2300	2000	4500	3100
Ratio: $\frac{\text{speed, air}}{\text{intake aperture}}$	15.5	21.2	23.0	20.8	18.3	18.5	23.9	20.3

oil backstreaming, was again installed over the top jet cap. Then, in an attempt to reduce pressure variations resulting from irregular boiling, and to provide operating vapor at higher pressure and temperature, a new type of heater was installed.

The novel feature of this heater was its design to supply heat from above rather than below the surface of the oil in the boiler. This was accomplished by hard-soldering Calrod heating elements to a grid of heavy nickel-plated copper fins projecting downward into the boiler reservoir. To provide room for this heater without altering the jet assembly or its location in the pump barrel the bottom of the pump boiler was lowered 3 in. Fractionation within the pump boiler was thereby eliminated; but it was hoped that this might be compensated by operating the lower pump barrel at somewhat higher temperature. To this end, aluminum heat shielding was placed around the boiler and the lower pump barrel.

The principal effects of this change in heaters were a slight reduction in operating power, a twofold increase in limiting fore pressure, and a reduction by about one-half in the oil backstreaming rate at medium operating power. Eruptive boiling, with its accompanying pressure surges, was completely eliminated at all powers.

The effectiveness of the water-cooled shield in reducing oil backing was determined, both with the original heater and with the modified design. The following backstreaming rates were observed at about 3000 w operating power:

Heater	Backstreaming Rate (cc/hr)
Original, no shield	8.2
Modified, no shield	4.2
Original, with shield	0.098
Modified, with shield	0.047

13.2 TESTS OF VAC-ION PUMP

A new series of measurements is being made on the Va-1415 Vac-Ion pump. The pumping of air, hydrogen, and helium has been re-examined, and the pumping of nitrogen, methane, and propane has been measured. In general, performance characteristics of the pump appear to be essentially as previously reported;[1] that is, (1) the pumping speed decreases with increasing pressure; (2) adjustment to equilibrium, following a pressure increase, is very slow; (3) the maximum throughput is low; and (4) both pumping speed and throughput are very low for the inert gases.

For a pump having these characteristics, it is almost impossible to make reliable speed measurements. On the basis of many measurements we list in Table 13.2.1 our best estimates of pumping speeds at several pressures for the different gases studied. Also listed in the table is the apparent maximum throughput for each gas.

Table 13.2.1. Speed and Maximum Throughput for Vac-Ion Pump

Pressure (mm Hg)	Air	H_2	N_2	CH_4	C_3H_8	He
			Speed (liters/sec)			
2×10^{-5}	155	190	110	110	60	10.8
7×10^{-6}	155	225	120	130	70	4 to 9
3×10^{-6}	150	270	125	135	100	1 to 3
			Maximum Throughput (micron liters/sec)			
	3.9	16.8	5.3	6.6	2.5	0.8

13.3 PURGING AND FRACTIONATION IN A DIFFUSION PUMP

All diffusion pump oils contain initially, or soon acquire in service, some high-vapor-pressure impurities. If these impurities remain in the oil and are allowed to pass indiscriminately to all stages of the pump, some find their way into the high-vacuum region and adversely affect the ultimate pressure attainable.

Two methods of dealing with the problem are widely used. In one, the oil, as it is recycled through the pump, is more or less effectively purged of its volatile impurities as it passes through the lower part of the pump barrel, that is, between the lower vapor jet and entrance to the boiler. This is accomplished by maintaining this region at sufficiently high temperature; and the net effect is a continuous discharge of high volatiles at the fore-vacuum line. Another method is to construct the boiler with a number of concentric compartments through which the returning oil flows in sequence. The more volatile constituents are vaporized largely in the outermost compartments and the vapor from these compartments goes only to the lowest pump jet, the jet farthest removed from the high-vacuum region. Thus, succeeding compartments supply vapor of progressively higher purity to succeeding jets until at the uppermost (high-vacuum) jet the vapor may be quite free of contaminants.

The effectiveness of purging and fractionation as they are applied in a 4-in. MCF-300 pump using Convoil-20 pump fluid have been under observation for a number of weeks.

The degree of purging is varied simply by varying the rate of flow of the pump cooling water. The two rates of flow commonly employed are the maximum attainable through the $\frac{1}{4}$-in. copper cooling coil and the minimum flow that can be readily adjusted. At these rates of flow the cooling water is discharged at temperatures of about 20 and 60°C, respectively. The corresponding distributions of temperature over the pump wall have not yet been determined; however, a distinct change in ultimate pressure indicated that the purging action is significantly different under these two conditions.

No feasible way has occurred to us of changing the pump from fractionating to nonfractionating. A somewhat exaggerated indication of the effect of fractionation can be quite simply realized, however. This is done by installing a bypass line between the oil seal separating the boiler from the fore-vacuum region and the center compartment of the boiler. Closing a valve in the bypass line causes oil to return to the boiler in the normal way and be fractionated as it passes from the periphery toward the center of the boiler. On opening the bypass valve, the returning oil enters the center compartment of the boiler and is fractionated in reverse order. The difference in ultimate pressure under these two conditions of operation is certainly an upper limit to the effect of fractionation vs nonfractionation.

The ultimate pressures observed after prolonged (24 hr or more) operation under four conditions of purging and fractionation are (in units of 10^{-6} mm Hg):

1. reverse fractionation, full cooling: $p = 8$,
2. direct fractionation, full cooling: $p = 3.0$,
3. reverse fractionation, reduced cooling: $p = 2.1$,
4. direct fractionation, reduced cooling: $p = 1.9$.

It is of interest to note that the ultimate pressure is substantially reduced either by fractionation or by purging. Under the conditions of these tests, the greater effect is produced by purging. It is not safe to assume, however, that this will always be the case.

14. DCX-2

14.1 DCX-2 COIL DESIGN EXERCISE

P. R. Bell R. L. Fredrickson R. J. Mackin, Jr.

In order to acquire a certain amount of perspective regarding magnetic field synthesis, the authors undertook an exercise in designing a coil layout for DCX-2. The procedure, for the most part, followed intuitive lines, but the results were sufficiently encouraging to warrant their inclusion in this report.

It was considered that one purpose of DCX-2 might be a study of particle and plasma containment under a broad range of circumstances. One aim of the design, therefore, was to provide a wide choice of field shapes all consistent with a mirror ratio of 3.5.

The configuration which resulted from the exercise consists of a pair of mirror coils and three pairs of booster coils arranged as shown in Fig. 14.1.1. The variety of field shapes is to be achieved by adjusting the relative currents in the individual pairs of coils.

Table 14.1.1 gives a set of relative current values and other parameters, and Fig. 14.1.2 shows the field shape resulting from each one. The 3.5 mirror ratio was retained only approximately in the calculations.

One note on design procedure will be given. The arrangement with the most nearly uniform field was arrived at by making the midplane field as uniform a function of radius as possible. This was done by adjusting the relative currents (and here only the two inner booster-coil pairs were considered, and they were given equal current) so that the total field at a radius of 18 in. (corresponding to the peak of the booster-coil field) equaled the total field at the axis. The

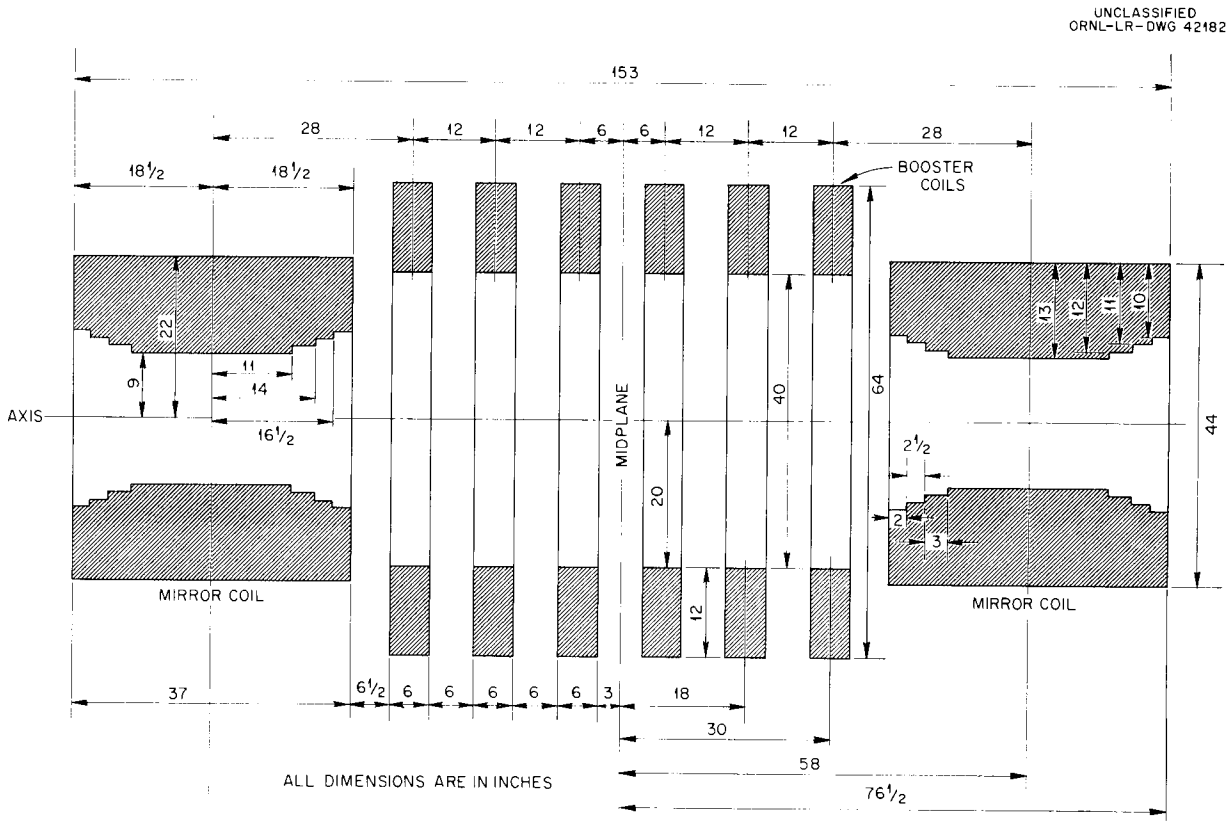

Fig. 14.1.1. Proposed DCX-2 Coil Arrangement.

Table 14.1.1. Parameters Used in DCX-2 Coil Design Exercise

	Case I	Case II	Case III	Case IV
$B_1:B_2:B_3$*	1:1:0	1:1:1	1:1:4	0:1:4
$B_m:B_2$	13.5:1	15.75:1	21.56:1	13.0:1
MR	3.6	3.63	3.56	3.53
Flux density, kilogauss				
B_m	59.5	59.0	55.7	53.5
B_1	4.41	3.74	2.58	0
B_2	4.41	3.74	2.58	4.11
B_3	0	3.74	10.30	16.44
Power, Mw				
P_m	7.18	7.06	6.31	5.85
P_1	0.497	0.360	0.170	0
P_2	0.497	0.360	0.170	0.434
P_3	0	0.360	1.158	6.36
Current density, amp/in.^{2}				
i_m	1.642×10^4	1.63×10^4	1.54×10^4	1.48×10^4
i_1	8.46×10^3	7.19×10^3	4.95×10^3	0
i_2	8.46×10^3	7.19×10^3	4.95×10^3	7.9×10^3
i_3	0	7.19×10^3	1.97×10^4	3.16×10^4
I_2/I_m	0.0821	0.0704	0.0515	0.0852

*Subscripts 1, 2, 3, and m refer to booster coils 1, 2, 3, and mirror coil, respectively.

B_i = field at center of symmetry of ith coil due to ith coil alone.

MR = mirror ratio.

P_i = power of ith coil.

i_i = current density in ith coil.

I_2/I_m = ampere-turns ratio of 2nd booster coil to mirror coil.

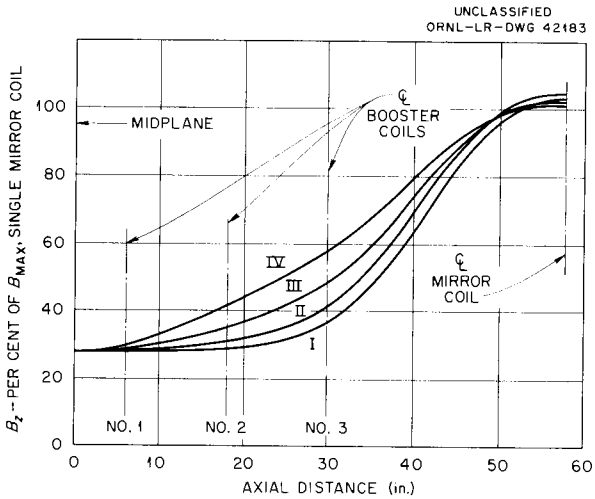

Fig. 14.1.2. Shape of Fields Resulting from Proposed DCX-2 Coils.

resulting field was uniform to 1.3% out to $r = 18$ in. in the midplane, and to 3% out to 20 in. along the axis. Under the booster coils (at $z = 6$ and 18 in.) the variations in the axial field out to 18 in. were 2% and 5%, respectively.

Reflection on the general problem of designing booster coils for field uniformity in a mirror-machine midplane suggests that best results are achieved not by adjusting for cancellation of field derivatives at the axis but by adjusting, as above, for equality in field values between the center point and some point far from the center.

It is often true that this step will improve uniformity over a volume, but this must be checked in individual cases. The Legendre polynomial expansion, which will be discussed by W. F. Gauster in the next section, provides a convenient vehicle for making the check. That section will give, in general, the basis for a more general approach to field synthesis.

14.2 MAGNETIC COIL DESIGN FOR DCX-2

W. F. Gauster M. W. Garrett[1]

14.2.1 SHORT REVIEW OF KNOWN METHODS OF MAGNETIC FIELD SYNTHESIS

The problem of finding a coil arrangement which produces magnetic fields of certain properties ("magnetic field synthesis") is a difficult one, even if restricted to rotationally symmetrical fields. The simplest special case is the generation of a homogeneous field. The principles of the Helmholtz coil and of Maxwell's three- and four-coil galvanometer are well known.[2] A great number of publications deal with refining or extending these principles to coil arrangements with relatively large coil cross sections,[3] higher numbers of coils,[4] or coil systems for generating magnet fields of extremely good homogeneity.[5]

Another problem is to produce a rotationally symmetrical magnetic mirror field with a certain mirror ratio, and with an extended middle zone of good homogeneity. One approach[6] consists of selecting a special solution of Laplace's equation in cylindrical coordinates that satisfies the requirements of uniformity in the central region and of a rapid rise along the axis farther away from the center. The desired field can be produced by placing a current sheath of appropriate variable surface-current density along a field line, and surrounding the whole arrangement by a steel shell of high magnetic permeability. The great advantage of this approach is that all necessary data can be exactly calculated in advance, and no succeeding adjustment of the precalculated numbers becomes necessary.

For large mirror coils, as needed for DCX machines, this field-synthesis method cannot

[1] Consultant, Swarthmore College.

[2] J. C. Maxwell, *A Treatise on Electricity and Magnetism*, 3d ed., vol II, p 356–59, Oxford University Press, London, 1946.

[3] M. W. Garrett, *J. Appl. Phys.* **22**, 1091 (1951).

[4] L. W. McKeehan, *Rev. Sci. Instr.* **7**, 150–53, 178–79 (1936).

[5] A. E. Ruark and M. F. Peters, *J. Opt. Soc. Am.* **13**, 205–12 (1926).

[6] D. C. White, *Quarterly Progress Report*, p 16, Research Laboratory of Electronics, Massachusetts Institute of Technology, July 15, 1957; S. Frankenthal, *Quarterly Progress Report*, p 9, Research Laboratory of Electronics, Massachusetts Institute of Technology, Apr. 15, 1959.

be used because:

1. a steel shell would geometrically interfere with the molecular ion beam to be introduced into the magnetic mirror, with the electrodes of the vacuum arc used for the breakup of the molecular ions, and with the vacuum system;
2. a thin current sheet has a very low Fabry factor; the power demand becomes high, and the cooling difficult.

Any modification of the original principle of the approach, such as omitting all or part of the magnetic shell, or providing a winding of sufficient thickness instead of a thin current sheet, invalidates the basic assumptions on which the method is based.

14.2.2 USE OF ZONAL HARMONICS IN THE DESIGN OF MAGNETIC MIRROR FIELDS

The simplest, and in many cases the most efficient, practical way to find a coil arrangement which produces a desired magnetic field starts with an intelligent guess of an appropriate coil configuration. By changing the current distribution and, when necessary, the geometrical dimensions of the first concept, the desired magnetic field will be approached in successive approximations. An analog computer ("Field Simulator")[7] will be very useful for this purpose. Or, as shown previously,[8] field data computed separately by means of an electronic computer for the different parts of the coil arrangement can be superimposed in order to check the degree of approximation reached.

In the following, a mathematical procedure is described which is very similar to the treatment of coil arrangements for the generation of highly uniform fields, as mentioned in Sec 14.2.1.

A problem in the synthesis of a magnetic mirror field may be formulated by assigning certain desired boundary values in an appropriate way. For instance, the axial component B_z of the flux density at any axial point inside the zone of convergence may be written in the following form:

$$B_{z0}(z) = \sum_{k=0}^{\infty} A_k z^k \quad . \tag{1}$$

Where the field has a plane of symmetry through the origin, the coefficients A_k of odd order vanish.

In a source-free region, a scalar magnetic potential exists, and:

$$B_z = -\frac{\partial \phi}{\partial z} \; ; \tag{2}$$

ϕ, and therefore B_z, satisfies the Laplace equation, and from a well-known theorem,

$$B_z(r,\theta) = \sum_{k=0}^{\infty} A_k P_k(\cos\theta)\, r^k \quad . \tag{3}$$

Here r and θ are polar coordinates of the field point, and $P_k(\cos\theta)$ is the Legendre polynomial of order k. Equation (3) describes the field within a source-free sphere, and reduces to Eq. (1) as a boundary condition along the axis.

As described in Sec 8.1 of this report, the axial component of the magnetic field, generated by an arbitrary system of coaxial thick solenoids, can be represented within a sphere whose center lies at an arbitrary axial point and which contains no sources of the field, by an infinite series of zonal harmonics. For example:

$$B_z^{+}(r,\theta) = \sum_{k=0}^{\infty} M_k P_k(\cos\theta)\, r^k \quad . \tag{4}$$

The coefficients M_k can be calculated *in closed form* from the coordinates of the coil system.[3]

If a particular system of coils has n independently adjustable parqmeters (currents, dimensions, or axial positions of the coils), then it should be possible, by varying these parameters, to satisfy n conditions that may be imposed upon the field. One condition is expressed by the choice of the mirror ratio. The other $(n-1)$ conditions serve to match as well as possible the functions B_z^{+} [Eq. (4)] and B_z [Eq. (3)]. A mathematical method to do this in a systematic way is being worked out. For this kind of numerical work the use of an electronic computer is mandatory. As mentioned in Sec 8.1, an Oracle code for this purpose will be developed.

---

[7] K. E. Wakefield, *A Resistance Analogue Device for Studying Axially Symmetric Magnetic Fields*, NYO-7313 (Dec. 13, 1956).

[8] W. F. Gauster, *Thermonuclear Project Semiann. Rep. Jan. 31, 1959*, ORNL-2693, p 103–4.

14.2.3 INFLUENCE OF NONUNIFORM CURRENT DENSITY DISTRIBUTION ON THE MACHINE DATA

In the preceding semiannual report some basic considerations on the design of the magnetic coils for DCX-2 were made in order to obtain initial numerical data for this machine.[9] A simplified containment calculation for 5-Mev alpha particles was made, and a mirror ratio of 3.5 was assumed. At this time no consideration was given to the details of the field configuration. The machine was matched to a 15-Mw power supply, and, for simplified calculations, wedge-shaped coils with uniform current density were considered. It was anticipated that a more realistic design of DCX-2 should use other coil shapes with more favorable current density distributions.

In the preceding report a major step has been taken towards finding a shape of the coil arrangement suitable for the desired field configurations. The current density in the windings was also assumed to be uniform.

In connection with the initial study on wedge-shaped coils, an investigation was made of the influence of different current density distributions on the data of a DCX-2 machine. Table 14.2.1 shows how greatly the current density distribution influences these data. Similar calculations will be made for the new mirror and booster coils.

[9] W. F. Gauster, *ibid.*, p 109–11.

Table 14.2.1. Influence of Current Density Distribution on Initial Data of DCX-2 Machine*

	Current Density Uniform	Current Density Inversely Proportional to Distance from Axis	Current Density Inversely Proportional to Square of Distance from Axis
a_1, inner coil radius, in.	11.8	10.8	10.2
a_2, outer coil radius, in.	29.0	25.5	25.0
z_0, distance from coil center to midplane, in.	45.0	37.6	34.0
r_{max}, maximum distance of 5-Mev alpha-particle orbit from axis, in.	20.3	18.2	17.5
W, copper weight of each mirror coil, tons (2000 lb)	11.2	7.7	7.2
B_c, flux density at center of the midplane, kilogauss	15.3	17.5	18.3
B_{max}, flux density at the center of the mirror coils, kilogauss	53.6	61.25	64.0
i_{max}, maximum current density amp/in.$^2 \times 10^4$	1.2	2.66	4.5

*W. F. Gauster, *Thermonuclear Project Semiann. Rep. Jan. 31, 1959*, ORNL-2693, Fig. 9.1.1, p 110.

15. DESIGN AND CONSTRUCTION GROUP

E. S. Bettis

Work of the Design and Construction section is of a support character, inasmuch as it is not concerned with research. Work of the section can, therefore, be reported in a summary manner.

The design group report runs from February 1 to August 1, 1959:

Jobs received	121
Jobs completed	93
Jobs now in progress	10
Backlog not working	18
Average backlog	25
Actual drawings completed	383

The Fabrication Group is responsible for scheduling and expediting work through the various machine shops doing work for the Sherwood program. The number of jobs processed through the shops since April 1, when this group was organized, is divided into two groups. There were 449 jobs requiring 16 man hours or less per job. There were 135 jobs requiring from 16 to 1000 man hours per job to complete.

During this period, an average of 35 men of machinist classification were employed in Sherwood work.

Work on the new building, 9201-2, has proceeded without incident. The lump-sum contractor will finish the offices and laboratories ahead of schedule. The 50,000-kva transformer is now installed, and the cooling-tower rebuilding job has been completed. The four motor generator foundations have been finished, and two of the three motor generator sets to be installed immediately have been dismantled from 9201-5 and moved to the crane bay of 9201-2.

Installation of the four Beta tanks is going well and will be completed on schedule October 15.

Engineering of the move of the PIG facility has been completed to the point where it can be turned over to Y-12 field engineering forces.

Engineering of the services (electrical, water, air, etc.) in the crane bay has been initiated. Every phase of the relocation to Building 9201-2 is now under way.

INTERNAL DISTRIBUTION

1. R. G. Alsmiller
2. C. F. Barnett
3. M. C. Becker
4. P. R. Bell
5. C. E. Bettis
6. E. S. Bettis
7. D. S. Billington
8. E. P. Blizard
9. C. W. Blue
10. R. L. Brown
11. C. E. Center (K-25)
12. R. A. Charpie
13. R. E. Clausing
14. D. L. Coffey
15. F. L. Culler
16. R. A. Dandl
17. R. C. Davis
18. S. M. DeCamp
19. J. L. Dunlap
20. H. O. Eason
21. R. S. Edwards
22. L. B. Emlet (K-25)
23. J. L. Fowler
24. T. K. Fowler
25. J. E. Francis
26. J. H. Frye, Jr.
27. W. R. Gambill
28. W. F. Gauster
29. J. H. Gibbons
30. R. A. Gibbons
31. W. R. Grimes
32. E. Guth
33. D. P. Hamblen
34. C. S. Harrill
35. C. C. Harris
36. A. Hollaender
37. A. S. Householder
38. H. C. Hoy
39. R. P. Jernigan, Jr.
40. W. H. Jordan
41. C. P. Keim
42. M. T. Kelley
43. G. G. Kelley
44. R. J. Kerr
45. R. L. Knight
46. F. A. Knox
47. J. A. Lane
48. N. H. Lazar
49. G. F. Leichsenring
50. T. A. Lincoln
51. S. C. Lind
52. R. S. Livingston
53. J. S. Luce
54. J. N. Luton
55. J. R. McNally, Jr.
56. R. J. Mackin
57. W. D. Manly
58. E. R. Mann
59. F. T. May
60. C. Michelson
61. K. Z. Morgan
62. O. B. Morgan
63. J. P. Murray (Y-12)
64. R. V. Neidigh
65. J. H. Neiler
66. M. L. Nelson
67. J. Neufeld
68. C. E. Normand
69. C. E. Parker
70. D. Phillips
71. J. F. Potts
72. M. Rankin
73. H. Postma
74. R. G. Reinhardt
75. P. M. Reyling
76. M. T. Robinson
77. P. W. Rueff
78. W. K. Russell
79. H. E. Seagren
80. E. D. Shipley
81. A. Simon
82. M. R. Skidmore
83. M. J. Skinner
84. G. M. Slaughter
85. A. H. Snell
86. W. L. Stirling
87. R. F. Stratton, Jr.
88. R. A. Strehlow
89. J. A. Swartout
90. E. H. Taylor
91. A. Tell
92. R. E. Toucey
93. R. M. Warner
94. H. L. Watts
95. A. M. Weinberg
96. E. R. Wells
97. T. A. Welton
98. G. K. Werner

99. G. C. Williams
100. C. E. Winters
101. W. L. Wright
102. O. C. Yonts
103. D. Alpert (consultant)
104. W. B. Ard, Jr. (consultant)
105. A. A. Blank (consultant)
106. W. R. Chambers (consultant)
107. W. H. Cramer (consultant)
108. E. Creutz (consultant)
109. J. W. Flowers (consultant)
110. M. W. Garrett (consultant)
111. O. G. Harrold (consultant)
112. E. G. Harris (consultant)
113. R. Hefferlin (consultant)
114. W. Kerr (consultant)
115. E. D. Klema (consultant)
116. H. Lewis (consultant)
117. F. E. Low (consultant)
118. H. Mott-Smith (consultant)
119. W. B. Pardo (consultant)
120. H. K. Reynolds (consultant)
121. H. S. Robertson (consultant)
122. D. J. Rose (consultant)
123. L. P. Smith (consultant)
124. H. S. Snyder (consultant)
125. P. M. Stier (consultant)
126. J. D. Trimmer (consultant)
127. C. H. Weaver (consultant)
128. Sherwood Reading File (P. R. Bell)
129. Sherwood Reading File (V. Glidewell)
130. Biology Library
131. Health Physics Library
132. Reactor Experimental Engineering Library
133–135. Central Research Library
136–285. Laboratory Records Department
286. Laboratory Records, ORNL R.C.
287. ORNL – Y-12 Technical Library, Document Reference Section

EXTERNAL DISTRIBUTION

288. N. E. Bradberry, Los Alamos Scientific Laboratory
289. H. D. Smythe, Princeton University
290. E. Teller, University of California, Lawrence Radiation Laboratory
291. W. A. Fowler, California Institute of Technology
292. R. R. Wilson, General Atomics, La Jolla
293. S. Chandrasekhar, Yerkes Observatory, Williams Bay, Wisconsin
294. S. C. Brown, Massachusetts Institute of Technology
295. D. W. Kerst, General Dynamics Corporation, San Diego, California
296. R. F. Post, University of California, Lawrence Radiation Laboratory
297. M. B. Gottlieb, Princeton University
298. J. A. Phillips, Los Alamos Scientific Laboratory
299. E. P. Gyftopoulos, Massachusetts Institute of Technology
300–301. Division of Research and Development, AEC, ORO (1 copy each to H. M. Roth and R. B. Martin)
302–303. Controlled Thermonuclear Branch, AEC, Washington (1 copy each to A. E. Ruark and H. S. Morton)
304. Oak Ridge Operations Office
305–898. Given distribution as shown in TID-4500 (15th ed.) under Controlled Thermonuclear Processes category (75 copies – OTS)